Fraunhofer ISE

FRAUNHOFER INSTITUTE FOR SOLAR ENERGY SYSTEMS ISE

Johannes Gutmann

PHOTONIC LUMINESCENT SOLAR CONCENTRATORS

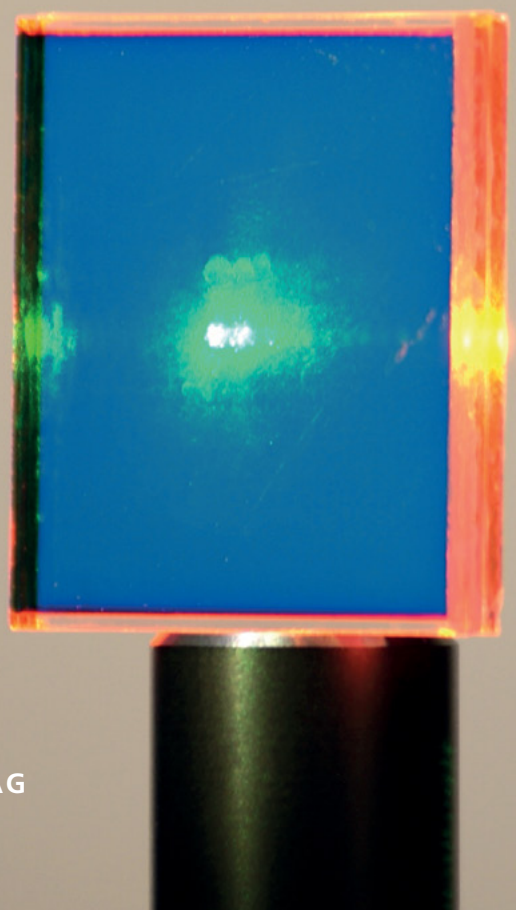

FRAUNHOFER VERLAG

Fraunhofer Institute for Solar Energy Systems ISE

Photonic luminescent solar concentrators

Johannes Gutmann

FRAUNHOFER VERLAG

Contact:
Fraunhofer Institute for Solar Energy Systems ISE
Heidenhofstrasse 2
79110 Freiburg
Phone +49 761/4588-5150
Fax +49 761/4588-9342
E-Mail info@ise.fraunhofer.de
URL www.ise.fraunhofer.de

Bibliographic information published by Die Deutsche Nationalbibliothek

Die Deutsche Bibliothek lists this publication in the Deutsche Nationalbibliografie; detailed bibliografic data is available in the Internet at www.dnb.de.

D 25

Zugl.: Freiburg, Univ., Diss., 2014

Printing and Bindery:
Mediendienstleistungen des
Fraunhofer-Informationszentrum Raum und Bau IRB, Stuttgart

Printed on acid-free and chlorine-free bleached paper.

All rights reserved; no part of this publication may be translated, reproduced, stored in a retrieval system, or transmitted in any form or by any means, electronic, mechanical, photocopying, recording or otherwise, without the written permission of the publisher.

Many of the designations used by manufacturers and sellers to distinguish their products are claimed as trademarks. The quotation of those designations in whatever way does not imply the conclusion that the use of those designations is legal without the consent of the owner of the trademark.

© by Fraunhofer Verlag, 2015, ISBN 978-3-8396-0833-3
Fraunhofer Information-Centre for Regional Planning and Building Construction IRB
P.O. Box 80 04 69, D-70504 Stuttgart
Nobelstrasse 12, D-70569 Stuttgart
Phone +49 (0) 7 11/9 70-25 00
Fax +49 (0) 7 11/9 70-25 07
E-Mail: verlag@fraunhofer.de
URL www.verlag.fraunhofer.de

Research in Micro-optics
Volume 16

Edited by Prof. Dr. Hans Zappe

Department of Microsystems Engineering - IMTEK
University of Freiburg
Georges-Köhler-Allee 102
Germany

Research in Micro-optics

Edited by Prof. Dr. Hans Zappe

Previously published:

Volume 1: **Silicon based tunable optical filters**
Dennis Hohlfeld - 2005

Volume 2: **Deformable polymer membrane devices**
Christoph Friese - 2007

Volume 3: **Dynamic and static diffractive optical elements**
Carsten Glasenapp - 2007

Volume 4: **Pneumatic micro-optics**
Armin Werber - 2007

Volume 5: **Controlled tilting micro-mirrors**
David Kallweit - 2008

Volume 6: **Tunable micro-external cavity laser**
Eva Geerlings - 2008

Volume 7: **Tunable liquid micro-optical systems based on electrowetting**
Florian Krogmann - 2008

Volume 8: **Integrated micro-optics for endoscopic optical coherence tomography**
Khaled Aljasem - 2010

Volume 9: **Positions-Encoder mit replizierten und mittels diffraktiver optischer Elemente codierten Maßstäben**
Thomas Samland - 2011

Volume 10: **Tunable microfluidic multi-chamber membrane lenses**
Daniel Mader - 2011

Volume 11: **Tunable optofluidic apertures**
Philipp Müller - 2012

Volume 12: **Spectroscopy inside the cavity of a two mode laser**
Benjamin Scherer - 2012

Volume 13: **Thermo-pneumatic micro-lenses**
Wei Zhang - 2013

Volume 14: **Highly flexible micro-bench system for endoscopic micro-probes**
Niklas Weber - 2013

Volume 15: **Photonische Vermessung der Arterienausdehnung mittels eines mikrooptischen Sensorsystems**
Dominic Ruh - 2014

Volume 16: **Photonic luminescent solar concentrators**
Johannes Gutmann - 2014

Photonic luminescent solar concentrators

How photonic crystals affect the emission and guiding of light

Johannes Gutmann

Dissertation zur Erlangung des Doktorgrades der Technischen Fakultät der Albert-Ludwigs-Universität Freiburg im Breisgau

Examiner:	Prof. Dr. Hans Zappe
Co-Examiner:	PD Dr. Andreas Gombert
Dean:	Prof. Dr. Georg Lausen
Date of examination:	October 14, 2014

Contents

Abstract **v**

Zusammenfassung **vii**

1 Introduction **1**
1.1 Motivation . . . 1
1.2 State of the art . . . 3
1.3 Scope of this work . . . 6
1.4 Organization of this thesis . . . 8

2 Theory **11**
2.1 Light . . . 11
2.1.1 Photonic crystals . . . 12
2.1.2 Light at interfaces . . . 14
2.2 Light-matter interaction . . . 16
2.2.1 Transition rates and Einstein coefficients . . . 16
2.2.2 Emission rate: Fermi's golden rule . . . 18
2.2.3 Local absorption . . . 20
2.2.4 Photoluminescence . . . 21

3 Modeling methods **23**
3.1 Local density of photon states . . . 23
3.1.1 LDOS in photonic crystals from eigenmodes . . . 24
3.1.2 Sampled LDOS in homogeneous media . . . 27
3.1.3 Example: 1D, 2D, and 3D (L)DOS of Bragg stack . . . 29
3.1.4 Fractional LDOS . . . 31

3.2 Model of fluorescent emission 35
3.2.1 Emitter model 35
3.2.2 Emission spectrum, PLQY and fluorescence lifetime 39
3.2.3 Detected spectrum 41
3.3 Propagation of light 44
3.3.1 Transfer and scattering matrix methods 44
3.3.2 Incoherent treatment of thick layers 46
3.3.3 Ray tracing light in LSCs 48
3.3.4 Angular pattern of light out-coupled at edge face 51

4 Experimental methods 53
4.1 Fabrication of multilayer structures 53
4.1.1 Spin coated multilayer structures 54
4.1.2 Thin film filters bonded with a dye-doped layer 63
4.2 Fabrication of opal structures 66
4.3 Characterization 71
4.3.1 Reflectance, transmittance, absorptance and concentrator quantum yield 71
4.3.2 Spectroscopic ellipsometry 74
4.3.3 Angular resolved photoluminescence 75
4.3.4 Integrated photoluminescence 78

5 Effect of photonic crystals on emission 81
5.1 Modeling results 81
5.1.1 Local density of photon states (LDOS) 81
5.1.2 Emission spectrum, PLQY and fluorescence lifetime 83
5.1.3 Light guiding efficiency 86
5.1.4 Detected emission: Angular resolved surface PL 89
5.2 Experimental results and comparison to theory 92
5.2.1 Angular resolved surface PL 94
5.2.2 Angular resolved edge PL 100
5.2.3 Integrated PL 105

6 Effect on concentrator performance 111
6.1 Modeling results for multilayer structures 111
6.1.1 Absorption of incident light 111
6.1.2 Overall concentrator performance 117
6.2 Experimental results 124
6.2.1 Multilayer structures 124
6.2.2 Opal structures 128

7 Conclusion and outlook 131

Appendix **135**
A.1 Derivation of the wave equation 135
A.2 Definitions of polarization at interfaces and in photonic crystals . . 136
A.3 Fresnel equations 138
A.4 Effect of the LDOS on the line shape of individual transitions . . . 138
A.5 Propagation of probability distributions 139
A.6 Multilayer structure with single dye-doped layer 141

References **145**

Notation **163**

List of Figures **172**

List of Tables **173**

Acknowledgments **175**

Curriculum vitae **177**

Publications **179**

Abstract

This work presents a comprehensive theoretical and experimental investigation of photonic luminescent solar concentrators (PLSC). In these devices, the luminescent material is embedded in a photonic crystal to tailor the emission of light. This way the major loss mechanisms of conventional luminescent solar concentrators (LSC) can be mitigated, namely the escape cone and reabsorption.

By combining the theory of photonic crystals and light-matter interaction, a novel modeling method was developed that allows for the *quantitative* calculation of the photonic-crystal-induced changes in the emission characteristics. The effects on the absorption, emission and guiding of light were combined in an analytical model to predict the overall performance of PLSCs. In particular, PLSCs realized from 1D-periodic Bragg stacks and 3D-periodic opals were studied.

As shown in the calculations, these photonic crystals feature only rather small variations in the density of photon states. Therefore only little spectral redistribution and small changes in the emitter's quantum yield were obtained. The anisotropy of the dispersion relation, however, leads to strong directional redistribution of emission. As a result, *measured* spectra in experiments can be heavily distorted as typically only a subset of modes is detected, which explains previously not fully understood observations in literature. I show that in PLSCs, this directional redistribution can drastically improve the efficiency of light guiding.

It is shown theoretically that opals are not able to outperform conventional LSCs due to a lower light guiding efficiency. The Bragg stack, however, was identified as a very promising candidate for PLSCs: due to directional redistribution of emission within the photonic band gap, the light guiding is strongly enhanced, leading to a reduction of escape cone losses by 60% for a typical luminescent dye. At the same time the calculated absorption of incident light was found to be increased as well, which results in an estimated system efficiency 2.1-times larger than in a comparable conventional LSC.

To study the predicted effects experimentally, new fabrication processes were developed to obtain Bragg stacks and opals with embedded fluorescent dyes. While the realization of defect-free opals was found to be challenging, Bragg stacks with up to 29 layers and a peak reflectance of 98.9% were obtained using an optimized spin coating process. Focusing on the promising Bragg stack, a very good agreement between theoretical calculations and experimental results was obtained in photoluminescence measurements with directional resolution. With the help of appropriate experiments and reference samples, it was shown that the observed spectral and directional redistribution indeed originates from the photonic crystal's influence on the emitter, as predicted in the calculations.

In a proof-of-principle experiment, the desired guiding of light to the edge faces was demonstrated for a Bragg stack PLSC. A reliable quantitative investigation of the predicted improvements in the quantum yield of the concentrator, however, was limited by the weak absorption of the samples. In future work, the fabrication process needs to be further optimized to embed additional dye layers.

To conclude, the very good agreement between emission experiments and calculations confirms the theoretical treatment presented in this work, which provides fundamental insight into and understanding of the relevant physics of luminescent emission in photonic structures. Besides the application in PLSCs, the findings of this work are of large interest for other applications that deal with the emission of light, for example to model and design photonic crystal lasers and efficient light-extraction structures in light emitting diodes.

Keywords: luminescence, fluorescence, photonic crystals, Bragg stack, opal, light-matter interaction, Fermi's golden rule, solar energy, photovoltaics, luminescent solar concentrator

Zusammenfassung

Die vorliegende Dissertation untersucht das Konzept photonischer Fluoreszenzkonzentratoren theoretisch wie auch experimentell. In diesen Konzentratoren wird der Fluoreszenzstoff in einen photonischen Kristall eingebettet, um die Emissionscharakteristik zu beeinflussen. Dadurch können die in herkömmlichen Fluoreszenzkonzentratoren dominierenden Verluste verringert werden, insbesondere die unvollständige Lichtleitung im Verlustkegel und Reabsorption.

Durch die Kombination der Theorie von photonischen Kristallen und der quantenmechanischen Licht-Materie-Wechselwirkung wurden die grundlegenden physikalischen Effekte herausgearbeitet, die in solchen Strukturen auftreten. Erstmals wurde der Einfluss des photonischen Kristalls auf das Emissionsverhalten eines fluoreszenten Farbstoffs *quantitativ* modelliert und die Auswirkungen auf die Effizienz der Konzentratoren berechnet. Konkrete Betrachtungen wurden dabei für 1D-periodische Bragg-Stapel und 3D-periodische Opale angestellt.

Die Berechnungen zeigen, dass in beiden Strukturen die photonische Zustandsdichte nur geringe Variationen aufweist und dadurch geringe Auswirkungen auf die spektrale Verteilung der Emission und auf die Quanteneffizienz des Emitters zu erwarten sind. Durch die anisotropen Dispersionsrelationen tritt jedoch eine signifikante Umverteilung der Emission bezüglich der Abstrahlungsrichtung auf. Dadurch können im Allgemeinen Messungen der Photolumineszenz trotzdem starke spektrale Veränderungen aufweisen, da typischerweise nur ein Teil aller emittierter Moden detektiert wird. Mit dieser Erkenntnis können bislang teilweise unverstandene Beobachtungen in der Literatur erklärt werden. Für die Anwendung des Fluoreszenzkonzentrators spielt die richtungsmäßige Umverteilung eine zentrale Rolle, da so die Effizienz der Lichtleitung erheblich gesteigert werden kann.

Die theoretischen Betrachtungen zeigen, dass der Opal auf Grund einer gegenüber herkömmlichen Fluoreszenzkonzentratoren geringeren Lichtleiteffizienz für

diese Anwendung wenig aussichtsreich ist. Sehr vielversprechend ist hingegen der Bragg-Stapel, für welchen eine erhebliche Verbesserung der Lichtleitung erzielt werden konnte. Dadurch reduzieren sich die Verluste im klassischen Verlustkegel um 60%. Gleichzeitig kann eine verstärkte Absorption von einfallendem Licht erzielt werden, wie Simulationen zeigen. Als Folge dieser vorteilhaften Effekte fällt die berechnete Gesamteffizienz eines beispielhaften Bragg-Stapels mehr als doppelt so hoch aus wie die eines vergleichbaren konventionellen Fluoreszenzkonzentrators.

Zur experimentellen Überprüfung wurden spezielle Verfahren entwickelt, um sowohl Bragg-Stapel als auch Opale mit eingebettetem Farbstoff herzustellen. Während die defektfreie Herstellung von Opalen eine große Herausforderung darstellt, konnten Bragg-Stapel mit bis zu 29 Lagen und einem Reflektionsgrad von 98.9% durch Rotationsbeschichtung realisiert werden. An Hand der vielversprechenden Bragg-Stapel konnten die Ergebnisse der theoretische Modellierung der Emission im Experiment nachgewiesen werden: Durch winkelaufgelöste Photolumineszenzmessungen, welche sensitiv auf die spektrale und richtungsmäßige Umverteilung der Abstrahlung sind, wurde eine sehr gute Übereinstimmung gefunden. Mittels geeigneter Experimente und Referenzproben wurde gezeigt, dass die beobachteten Effekte tatsächlich wie vorhergesagt auf Grund des Einflusses der photonischen Kristalle auf die Emission des Farbstoffs auftreten.

Bei der Messung der Konzentrator-Quanteneffizienz konnte erstmals die gewünschte Funktionalität in einem photonischen Fluoreszenzkonzentrator nachgewiesen werden: Einfallendes Licht wird absorbiert und daraufhin emittiertes Licht wird zu den Kanten geleitet. Wegen der schwachen Absorption der Proben war jedoch eine quantitative Überprüfung der vorhergesagten Steigerung der Gesamteffizienz nicht zuverlässig möglich. Hierfür muss in Zukunft der Herstellungsprozess weiter optimiert werden, um zusätzliche Farbstoffschichten einzubetten.

Zusammenfassend lässt sich sagen, dass die sehr gute Übereinstimmung der berechneten und gemessenen Emissionscharakteristiken die in dieser Arbeit vorgestellten theoretischen Überlegungen und Modellierungsmethoden bestätigt. Insbesondere die theoretischen Betrachtungen liefern einen wichtigen Beitrag zum grundlegenden Verständnis des Einflusses einer umgebenden Struktur auf die Abstrahlung von Licht. Neben der Anwendung als Fluoreszenzkonzentrator sind die Ergebnisse und Methoden dieser Arbeit auch für andere Anwendungen von hohem Interesse, die sich mit der Emission von Licht beschäftigen, wie z.B. in Lasern und Leuchtdioden.

Stichwörter: Lumineszenz, Fluoreszenz, Photonische Kristalle, Bragg-Stapel, Opal, Licht-Materie-Wechselwirkung, Fermis goldene Regel, Solarenergie, Photovoltaik, Fluoreszenzkonzentrator

Chapter 1 Introduction

1.1 Motivation

The transformation of the world's energy system towards renewable energy sources is a major challenge of our time: currently the energy supply is based on fossil fuels that are limited, involve risks for ecosystems (see the Gulf of Mexico oil spill in 2010, for example) and threads to human health, and cause severe climate changes [1]. The renewable energy source with the biggest potential is the radiation from the sun: theoretically, in 1.5 hours the earth receives the amount of energy mankind consumes in one year [2]; even the sustainably usable potential is more than 20 times larger than the current consumption [3]. For electric power generation, the technology of photovoltaics, i.e. the direct conversion from light to electricity, has made enormous progress in the past decades in terms of efficiency and cost due to experience curve effects.

One approach to further reduce the cost of photovoltaic systems is to concentrate the sunlight onto small solar cells to save semiconductor material, i.e. resources and costs. This can be achieved with luminescent solar concentrators (LSC), which are flat plates that concentrate incident light on its edge faces. In contrast to mirror and lens based concentrator systems, LSCs are capable of concentrating not only direct but also diffuse radiation and therefore have no need for tracking. Furthermore, they provide novel application possibilities such as building integrated photovoltaics [4] with colorful and semi-transparent designs (see Fig. 1.1 (a)), or flexible modules [5, 6].

In detail, an LSC is a plate of a transparent matrix (e.g. glass or polymer) that is doped or coated with a luminescent material, as illustrated in Fig. 1.1 (b). The luminescent material absorbs incident light and emits at longer wavelengths. Most

(a) Different LSCs

(b) Cross-section of a conventional LSC

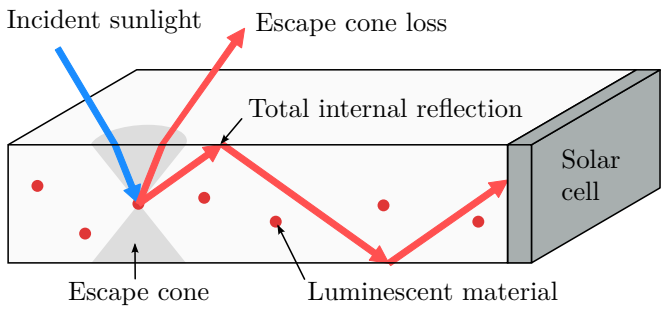

Figure 1.1: Luminescent solar concentrators (LSC) are semi-transparent plates doped or coated with a luminescent material. They concentrate incident light on their edge faces, as shown in (a) for different luminescent materials [Photograph courtesy of Luca Greco, Fraunhofer ISE]. The cross-section of an LSC in (b) reveals, that most of the emitted light is trapped inside the LSC plate and it is thus guided to the edge faces, where small solar cell convert the concentrated light into electricity.

of the emitted light is trapped inside the plate by total internal reflection (TIR). Consequently, it is guided to the plate's edge faces. With a surface area larger than the edge faces, a concentration of light can be achieved. The concentrated light can then be converted to electricity by small solar cells attached to the edge faces.

The concentration of light, however, is not perfect. The performance of conventional LSCs suffers from several loss mechanisms:

- Not all emitted light is trapped by TIR: within the escape cone defined by the critical angle, light can exit the LSC and is lost. Typically, emission of the luminescent material can be assumed to be isotropic [7], thus the fraction of light in the loss cone is given by

$$1 - \sqrt{1 - (n_{\text{out}}/n_{\text{in}})^2} \tag{1.1}$$

  from geometrical considerations [8], where n_{out} and n_{in} are the refractive indices of the surrounding medium and the LSC plate, respectively. Typically, $n_{\text{out}} = 1$ (air) and $n_{\text{in}} = 1.5$ (polymer), thus 25.5% of emitted light is lost.

- Furthermore, the propagation of emitted light through the LSCs suffers from parasitic absorption of the matrix material, and from scattering within the LSCs. These losses increase with the path length to the edge faces and therefore with the concentrator size.

- Additionally, emitted light can be reabsorbed on its path towards the edge faces by another molecule of the same luminescent species. This occurs when

the absorption and emission spectra of the luminescent material overlap. Reabsorbed photons are not necessarily lost, as they can be emitted again. This reemitted light, however, is also subject to the escape cone loss. Therefore, reabsorption limits the performance of large size LSCs, as the probability of reabsorption increases with the path length.

- Moreover, (re)absorbed photons may be lost due to non-radiative decay processes in the luminescent material. In other words: not every absorbed photon results in emission of a photon. The ratio of emitted photons and absorbed photons is defined as the photoluminescence quantum yield (PLQY) and depends on the luminescent material as discussed below.

1.2 State of the art

Luminescent solar concentrators

LSCs for solar energy harvesting were proposed at the end of the 1970s [9, 10], while the principle of trapping fluorescent light was studied earlier for scintillation counters [11, 12]. In the 1980s, LSCs were extensively investigated both in theory and experiments. Fundamentally, the performance of LSCs was theoretically studied using optics [13] and thermodynamics [14–17]. Practically, the design of concentrator system was investigated in detail including the geometrical form of LSC plates [10], the stacking of multiple LSCs with different luminescent materials to cover a broad spectral range of absorption [10], the use of mirrors and reflectors at the back surface and at certain edge faces (e.g. [18]), placing solar cell at the back surface instead of the edge faces [19], tapering the plate's edges to further increase concentration [20, 21], and using thin luminescent films on transparent substrates ("thin film LSC") instead of homogeneously doped bulk LSCs [22].

A main focus of research, however, were and still are the luminescent materials as they strongly influence the performance of an LSC. In the beginning of LSC research, mainly organic dyes and rare earth ions were studied. Organic dyes are complex molecules that feature broad absorption spectra and high PLQYs above 95% in the visible spectrum, also when embedded in polymers such as Poly(methyl methacrylate) (PMMA) [7, 23, 24]. In the near-infrared (NIR), however, the PLQY of such molecules is limited for fundamental reasons [7]. Typically the absorption and emission spectra exhibit a significant overlap, thus promoting reabsorption-related losses. Utilized energy transfer [25, 26] from one dye to a second one can help to reduce these losses in LSCs [27–29]. Using phosphorescence instead of fluorescence also reduces reabsorption as a result of the larger Stokes shift but it is typically associated with a lower PLQY [28].

As an alternative, lanthanide ions like Nd^{3+}, Yb^{3+} [30, 31] or other ions like Cr^{3+} or $[UO_2]^{2+}$ [32, 33] were studied. They are very stable and can be embedded

in glass as they resist the high temperatures that occur during the fabrication of glass. Their absorption and emission spectra typically feature several lines that are relatively narrow. The small overlap reduces reabsorption, but only a small part of the incident light can be absorbed in such LSCs. To broaden the absorption spectra, energy transfer from one ion ("sensitizer") to another ion ("emitter") was investigated [30, 31].

With the rise of nanotechnology, luminescent semiconductor nano-crystals in form of quantum dots [34–41] and nano rods [42, 43] have been studied in the last decade for the use in LSC. The broad absorption spectrum as well as the emission can be tuned by the nano-crystal's size and geometry. Up to now, however, the PLQY of these materials is rather poor ($< 60\%$) when embedded in solid matrices like polymers [44].

Consequently, organic dyes are the preferred luminescent species for LSCs with high performance. Recently, researchers reported novel materials with promising features such as large Stokes shifts, which might help to reduce reabsorption while maintaining broad band absorption and high PLQY in future LSCs [45–48].

The best performing LSC systems were realized in the past few years due to the progress in solar cells from III-V semiconductors whose electric band gaps are well suited to convert the emitted light to electricity. In 2008, Goldschmidt et al. realized a stack of two plates with different organic dyes, attached to GaInP and GaAs solar cells. They achieved a power conversion efficiency of 6.9%, which was a record at that time [49, 50]. Shortly later, Slooff et al. reported an efficiency of 7.1% for a system of two organic dyes mixed in one PMMA plate with GaAs solar cells on all four edges [51]. Using (cheaper) solar cells of crystalline silicon, Desmet et al. recently published a system efficiency of 4.4% for a stack of two plates, which is lower than the other values due to the lower electronic band gap of silicon and the therefore lower output voltage [52].

These record efficiencies were achieved for rather small systems of several cm^2. Larger systems that would be necessary for commercial applications suffer from reabsorption as well as from parasitic absorption and scattering. To increase the efficiency of (large) LSCs, Smestad et al. proposed to put a frequency-selective reflector on their top surface [53]. Such a reflector should reflect the emitted light to the reduce escape cone loss, while transmitting light in the spectral range of the luminescent material's absorption. This concept was investigated theoretically and experimentally by different groups [16, 54–58]. Goldschmidt et al. obtained a relative gain in system efficiency of 20% in experiments [59]. However, parasitic reflection, especially at oblique incidence, limits the possible gain by such filters. Furthermore, longer path lengths due to propagation at steep angles increase path-length-dependent losses such as reabsorption or scattering.

In consequence, Goldschmidt et al. proposed the concept of "*photonic* luminescent solar concentrators" (PLSC) [60], which is investigated in this work in detail. PLSCs aim at tackling the major shortcomings of conventional LSCs: in-

stead of using a plate of homogeneous material with macroscopic thickness, the luminescent material is embedded into a photonic structure (Fig. 1.2 (a), (b)). Such a structure features a variation of the refractive index on the length scale of the wavelength of light. Therefore, the emission of light is subject to photonic effects, which can be utilized to increase the concentrator performance by (i) restricting emission to in-plane directions, thus circumventing the escape cone loss, (ii) tailoring the emission spectrum to reduce the overlap of absorption and emission spectra to mitigate reabsorption, and (iii) enhancing radiative decay rates to increase the PLQY.

Recently, other researchers followed this route of using photonic effects: Giebink et al. proposed an LSC with a thin luminescent film that is resonantly coupled to the underlying substrate via a low-refractive-index layer in between. By varying the thickness of the luminescent film over the sample, the propagation of the emitted light inside the substrate can be de-coupled from the luminescent film to avoid reabsorption [61]. Rousseau and Wood calculated that patterning such a luminescent film can increase the guided photon flux [62].

Photonic crystals and their influence on emission of light

In PLSCs, photonic effects are utilized to tailor the emission characteristics of the luminescent material. For the first time, Purcell pointed out in 1946 that the rate of spontaneous emission is affected by the light source's environment, specifically inside resonant cavities [63]. The introduction of photonic crystals 40 years later [64, 65] has drawn particular attention to this phenomenon. Being nanostructures with a periodic modulation of the refractive index, photonic crystals offer fascinating means for the manipulation of light [66]. In particular, photonic crystals influence the emission of photons by embedded light sources as already pointed out in the pioneering works of Yablonovitch [64] and Bykov [67]. As a result of a modified local density of photon states (LDOS), the emitter's electronic transition probability for spontaneous emission is altered as described in detail in Sec. 2.2.2. Several researchers reported on the calculation of the LDOS in photonic crystals using different approaches, as discussed in Sec. 3.1.

In experiments, various light sources (rare earth ions [68, 69], organic dye molecules [70–72], semiconductor quantum dots [73–76] and quantum wells [77]) were embedded in different photonic crystals to study the emission properties. Furthermore, biological samples were investigated, such as wings of butterflies that feature fluorescent materials within photonic structures [78, 79]. The shape of the measured emission spectra was found to be strongly modified, which was attributed to suppression of emission inside photonic band gaps and enhancement at band edges. However, for the fluorescence lifetime, which is directly related to the emission probability, only little effect was observed in time-resolved measurements of "weak" photonic crystals, featuring no complete i.e. no omnidirectional

band gaps [70–72]. In contrast, photonic crystals with complete band gaps (e.g. woodpile or diamond structures from high permittivity materials) significantly influenced the lifetime when emitters were embedded [75, 76].

Up to now, the experimental results have been compared only qualitatively to theoretical calculations of the LDOS, e.g. by comparing the emission spectrum with the LDOS spectrum [72]. However, a quantitative theoretical treatment of the influence of the photonic crystal on the emission of a fluorescent material is missing in current literature. In this work, I fill this gap and present a comprehensive model that combines the theoretical LDOS in photonic crystals with a rate-equation model for fluorescent emitters to quantitatively calculate the different effects. This approach allows modeling of characteristics observable in experiments, such as the emission spectrum, the PLQY and the fluorescence lifetime (see Sec. 3.2).

1.3 Scope of this work

The objective of this thesis is to investigate the novel concept of a "*photonic* luminescent solar concentrator" (PLSC) in both theory and experiment. As mentioned above, the idea of PLSCs is to mitigate the major loss mechanisms in conventional LSCs by embedding the luminescent material in a photonic crystal. The photonic crystal allows influencing the directional and spectral distribution of the emitted light to reduce the losses in the escape cone and due to reabsorption.

In this work, two different photonic crystals were considered, as proposed in Ref. 60: on one hand, the so-called *Bragg stack* of alternating high- and low-refractive-index layers features an one-dimensional periodicity, as illustrated in Fig. 1.2 (a). The thickness of the layers d_j is given by the Bragg condition $\lambda_{\text{design}} = d_j/4n_j$ where j indexes the two materials with refractive indices n_j, and λ_{design} denotes the center wavelength of the (first) photonic band gap, where a reflection peak occurs for incident light. On the other hand, small dielectric spheres close-packed in a face-centered cubic (fcc) arrangement provide three-dimensional periodicity, see Fig. 1.2 (b). This photonic crystal is called *opal* according to the gemstone that exhibits the same structure [80].

The luminescent material is embedded in one or several layers of the Bragg stack and inside the spheres of the opal. While the PLSC concept is independent of the type of luminescent materials, this work focuses on fluorescent organic dyes as they have proven to yield the best LSC performance. The presented theoretical and experimental treatments, however, allow adaptation to other emitter species.

Due to the small feature sizes, light inside photonic crystals must be considered as waves (not rays), which are reflected and scattered at the many interfaces in the structure and interfere with each other. As a result, the propagation of light is different from plane waves in homogeneous media. Technically, the photon dispersion relation $\omega(\boldsymbol{k})$, which relates the frequency ω and the wave vector $\boldsymbol{k}$,

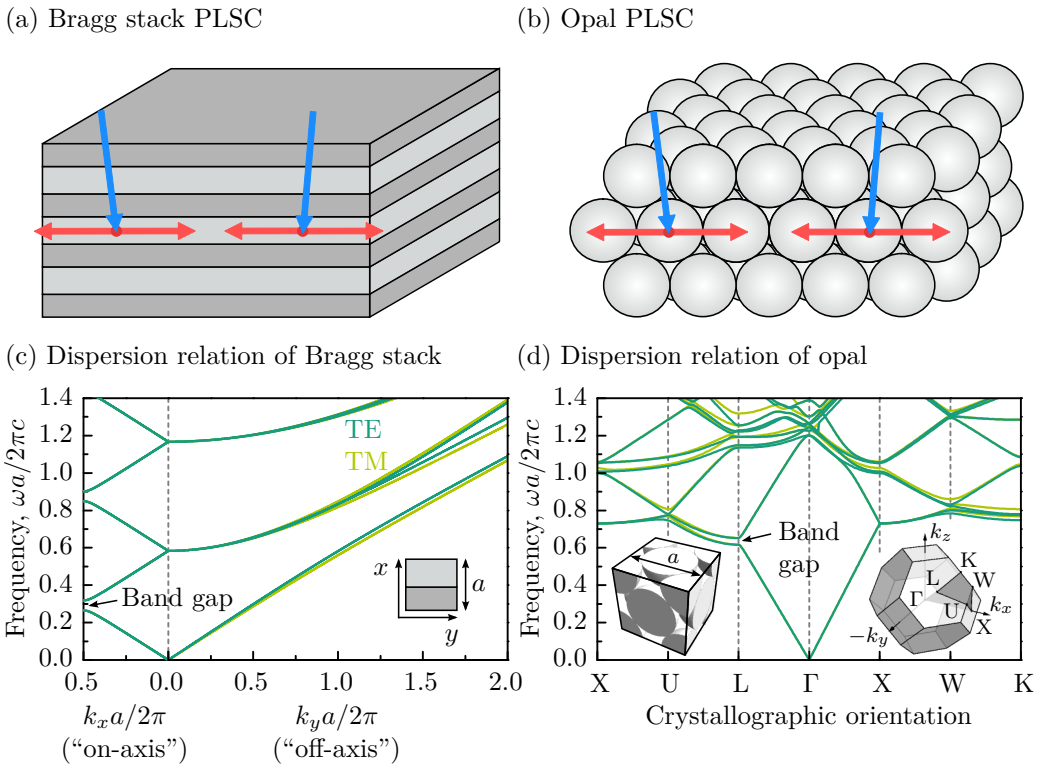

Figure 1.2: To tackle the major shortcomings of conventional LSCs, the luminescent material is embedded into photonic crystals to influence its emission characteristics. Here, such *photonic* LSCs (PLSCs) are studied in form of (a) the one-dimensional Bragg stack and (b) the 3D-periodic opal that consists of an close-packed arrangements of spheres. The dispersion relation of the Bragg stack features a photonic band gap in on-axis direction, see (c). As shown for different directions of the first Brillouin zone in (d), the opal's dispersion relation exhibits a band gap in L-direction, i.e. normal to the top/bottom surface. In both cases, the absence of photon states in direction of the classical escape cone leads to suppression of emission in these directions, thus reducing escape cone losses.

becomes strongly non-linear in photonic crystals, as shown in Fig. 1.2 (c), (d).[1] As a consequence, photons with certain energies may not be allowed to propagate in certain directions. Analogously to solid-state physics, such forbidden photon states give rise to photonic band gaps, as indicated in the figure.

The absence of photon states in a certain direction implies that photons cannot be emitted in this direction, as explained in detail in Sec. 2.2.2. In the PLSC, this effect is utilized to reduce escape cone losses by suppressing emission towards

[1] For the calculation of the dispersion relations, the refractive indices $n_{\mathrm{lo}} = 1.5$, $n_{\mathrm{hi}} = 2$ (Bragg stack) and $n_{\mathrm{sphere}} = 1.5$, $n_{\mathrm{void}} = 1$ (opal) were used according to the (experimental) realizations investigated in this work.

the top and bottom surface: in direction of the classical escape cone, both Bragg stack (x-direction) and opal (crystallographic L-direction) feature a band gap, as shown in Fig. 1.2 (c), (d). Instead, light is emitted in in-plane directions, which is beneficial for the concentrator performance.

Being a central part of this work, the general interaction of a photonic crystal and an embedded fluorescent emitter was studied in theory to promote the understanding of the relevant processes. Based on these fundamentals, a modeling method was developed to quantitatively calculate the effects on the emission. Besides PLSCs, this novel theoretical framework could be applied also to other applications such as lasers [81–87] and (organic) light emitting diodes (LED) [88–92], where emitted light needs to be extracted efficiently. Furthermore, the overall performance of (P)LSCs was modeled considering the changes in absorption of incident light as well as path-length-dependent losses due to reabsorption.

I will show in the following that all the desired benefits mentioned above can be achieved with the Bragg stack PLSC: the escape cone loss can be reduced as the light guiding efficiency is strongly enhanced, the emitted spectrum can be reshaped to reduce reabsorption, and the PLQY can be slightly increased. Additionally, absorption of incident light can also be enhanced, due to slow light modes. All these effects promise large concentrators with superior efficiency.

Based on theoretical calculations, the opal PLSC, however, is expected not to perform better than conventional LSCs due to a less efficient guiding of emitted light. Therefore, advanced investigations were focused on the Bragg stack concept.

Both Bragg stack and opal were analyzed in experiments. Through developing and evaluating different fabrication approaches, samples with embedded luminescent material were realized. The samples were characterized using different, partly newly developed optical measurements methods to study absorption, emission and concentrator performance. By comparing the dye's emission characteristics from calculations and experiments, a very good agreement was found, which confirms the theoretical models developed in this work.

1.4 Organization of this thesis

In the following Chapter 2, I briefly introduce the theoretical backgrounds of photonic crystals, luminescence and light-matter interaction. Based on this theory, the different modeling methods and approaches developed and applied in this work are presented in Chapter 3. Being a key quantity, it is shown how the local density of photon states can be calculated in photonic crystals. To quantify the changes in emission induced by the photonic crystal, I propose a rate-equation model for broad-band fluorescent emitters.

Chapter 4 introduces the fabrication and characterization methods used in this work to experimentally investigate the PLSC concept. In detail, processes were

developed for the fabrication of multilayer and opal samples with embedded luminescent dyes. Furthermore, the most important characterization methods are presented.

The results of theoretical calculations and experiments are presented in Chapter 5 and 6 in two parts: Chapter 5 deals with the effects of the photonic crystal on the fluorescent emission. Calculations for the influence of the Bragg stack and opal on the emitted spectra, the PLQY, and the light guiding efficiency are presented. Being very sensitive to photonic effects, the angular resolved photoluminescence from the sample surface was chosen to compare theoretical calculations with experimental measurements of the fabricated devices.

Chapter 6 is focused on the effects of the photonic crystal on the overall performance of PLSC devices. Therefore, the absorption of incident light is studied in simulations and is combined with the modifications of emission from Ch. 5 in an overall performance model that accounts for reabsorption losses. Using this model, the different effects of the photonic crystal are combined to predict the concentrator quantum yield. Both absorptance and concentrator quantum yield are accessible in measurements. Thus, experimental results for the fabricated samples are discussed and compared to the theoretical calculations.

In the concluding Chapter 7, the main results are summarized and discussed. In a brief outlook, perspectives arising from the findings of this work are presented.

Chapter 2

Theory

THIS chapter introduces the theory of the physics relevant for this work. First, the existence and propagation of light in homogenous media and photonic crystals, and its behavior at boundary interfaces are discussed. As the key quantity for the interaction with matter, the local density of photon states is derived. In the second part, the absorption and emission of light by matter in a photonic environment, and the phenomenon of luminescence are discussed in detail.

2.1 Light

Light in form of waves can be described by the well-known Maxwell equations. Using an harmonic ansatz for the time dependency of the fields, the wave equation for the stationary magnetic field $\boldsymbol{H}$

$$\boldsymbol{\nabla} \times \left(\frac{1}{\varepsilon(\boldsymbol{r})} \boldsymbol{\nabla} \times \boldsymbol{H}(\boldsymbol{r}) \right) = \left(\frac{\omega}{c} \right)^2 \boldsymbol{H}(\boldsymbol{r}) \tag{2.1}$$

can be derived for a dielectric material that is non-magnetic, free of charges and currents, and that features no material dispersion (see Appendix A.1). Note, that the relative permittivity $\varepsilon(\boldsymbol{r})$ can vary in space. This wave equation can be read as an hermitian eigenvalue problem, where $(\omega/c)^2$ (with frequency ω and the speed of light in vacuum c) is the eigenvalue and the field $\boldsymbol{H}(\boldsymbol{r})$ is the eigenvector [66].

For homogeneous media with constant permittivity $\varepsilon \neq \varepsilon(\boldsymbol{r})$, the solution to this problem are the plane waves

$$\boldsymbol{H}(\boldsymbol{r}) = \boldsymbol{H}_0 \, \mathrm{e}^{i\boldsymbol{k}\boldsymbol{r}}, \tag{2.2}$$

with wave vector $\boldsymbol{k}$ that is related to the frequency ω by the linear dispersion relation $\omega = (c/n)\,|\boldsymbol{k}|$ through the refractive index $n = \sqrt{\varepsilon}$.

2.1.1 Photonic crystals

Photonic crystals feature a periodic modulation of the relative permittivity ε (and the refractive index n). Analogous to "real" crystals in solid state physics, their spatial structure can be described by a Wigner-Seitz unit cell (WSC) [93]. With a lattice vector $\boldsymbol{R}$ being a linear combination of the primitive lattice vectors, the translation symmetry can thus be expressed as $\varepsilon(\boldsymbol{r}) = \varepsilon(\boldsymbol{r} + \boldsymbol{R})$.

Equation (2.1), which in the field of photonic crystals is sometimes called "master equation", can therefore be solved according to the Bloch theorem using the ansatz

$$\boldsymbol{H}_{b,\boldsymbol{k}}(\boldsymbol{r}) = e^{i\boldsymbol{k}\boldsymbol{r}}\boldsymbol{u}_{b,\boldsymbol{k}}(\boldsymbol{r}) \tag{2.3}$$

with the function $\boldsymbol{u}_{b,\boldsymbol{k}}(\boldsymbol{r}) = \boldsymbol{u}_{b,\boldsymbol{k}}(\boldsymbol{r} + \boldsymbol{R})$ being periodic on the crystal lattice. In this way, the wave vector $\boldsymbol{k}$ and the band index b are introduced. Inserting this ansatz in Eq. (2.1) yields

$$(i\boldsymbol{k} + \boldsymbol{\nabla}) \times \frac{1}{\varepsilon(\boldsymbol{r})}(i\boldsymbol{k} + \boldsymbol{\nabla}) \times \boldsymbol{u}_{b,\boldsymbol{k}}(\boldsymbol{r}) = \left(\frac{\omega(\boldsymbol{k})}{c}\right)^2 \boldsymbol{u}_{b,\boldsymbol{k}}(\boldsymbol{r}), \tag{2.4}$$

which is again an hermitian eigenvalue problem. This problem can be solved numerically using the plane wave expansion method, as implemented in the MIT Photonic-Bands (MPB) package that was used for the calculations in this work [94].

In photonic crystals, the dispersion relation $\omega(\boldsymbol{k})$ becomes anisotropic and nonlinear. Typically, it is studied along certain directions in $\boldsymbol{k}$-space, as shown in the "band diagrams" in Fig. 1.2 (c), (d). In fact, in this reciprocal space a first Brillouin zone (FBZ) can be constructed in the same way as in solid state physics. For the fcc lattice of the opal, the established crystallographic orientations are used to refer to major direction in its FBZ, as shown in Fig. 1.2 (d).[1]

In the dispersion relation, photonic band gaps become visible, such as at the border of the FBZ in on-axis direction of the Bragg stack, and in L-direction of the opal, see Fig. 1.2 (c), (d). They result from the fact that for wave vectors $\boldsymbol{k}$ in this direction there are no solutions $\boldsymbol{H}_{b,\boldsymbol{k}}(\boldsymbol{r})$ to Eq. (2.1) that have frequencies inside the gap. At the edges of band gaps, the dispersion relation is typically bent. These "flat band" conditions give rise to slow light modes as the group velocity $\boldsymbol{v}_{\mathrm{g}} = \boldsymbol{\nabla}_{\boldsymbol{k}}\,\omega(\boldsymbol{k})$ decreases [96, 97].

When a band gap exists in all directions, it is called complete or omnidirectional. The photonic crystals studied in this work feature incomplete band gaps due relatively small refractive index contrasts.[2] For the desired directional redistribution in PLSCs, however, incomplete band gaps are needed so that emission is

[1] For a better understanding of the opal's FBZ I recommend to build a 3D model according to the template from Ref. 95, p. 175.

[2] In some publications, the term "band gap" is used only for complete band gaps and incomplete band gaps are called "stop bands".

inhibited only in certain, lossy, directions, and gets redirected in other directions (e.g. in-plane).

To study emission inside photonic crystals, it is necessary to examine the local density of photon states (LDOS) that appears in Fermi's golden rule (see Sec. 2.2.2). Mathematically, the LDOS is defined via [98]

$$\rho(\boldsymbol{r},\omega) = \sum_b \int_{\mathrm{FBZ}} |\boldsymbol{E}_{b,\boldsymbol{k}}(\boldsymbol{r})|^2 \, \delta(\omega - \omega_{b,\boldsymbol{k}}) d\boldsymbol{k}, \tag{2.5}$$

which can be understood as "counting" all photon states in the FBZ with a certain frequency, weighted with the mode's[3] individual field distribution.[4] It is the field term $|\boldsymbol{E}_{b,\boldsymbol{k}}(\boldsymbol{r})|^2$ that introduces the spatial dependence of the LDOS.

In contrast, the (total) density of states (DOS)

$$\varrho(\omega) = \sum_b \int_{\mathrm{FBZ}} \delta(\omega - \omega_{b,\boldsymbol{k}}) d\boldsymbol{k} \tag{2.6}$$

counts all states with same weights.

The DOS and LDOS are connected via spatial integration over the Wigner-Seitz unit cell [98, 99]:

$$\varrho(\omega) = \int_{\mathrm{WSC}} \varepsilon(\boldsymbol{r}) \rho(\boldsymbol{r},\omega) d\boldsymbol{r}. \tag{2.7}$$

Even in photonic crystals with weak refractive index contrast, the LDOS typically depends strongly on the actual emitter position $\boldsymbol{r}$, and differs significantly from the DOS [98, 100]. For the emission process, the LDOS is the relevant quantity rather than the DOS, as discussed in Sec. 2.2.2.

Furthermore, a fundamental "sum rule" was found [101, 102], which states that the total number of photon states is conserved and a reduction of the LDOS for some region of the spectrum must be compensated by an enhancement at other frequencies.

In general, both DOS and LDOS vanish in complete band gaps, and they are enhanced at band edges due to the flattening of the bands. In photonic crystals with incomplete band gaps, the DOS and typically also the LDOS do not drop to zero as there are modes with frequencies in the band gap in other directions, as observed for the Bragg stack and the opal (see Sec. 3.1.1).

[3] Throughout this work, the terms "state" and "mode" are used as equivalents, denoting a solution to Eq. (2.1)

[4] Note that in literature the field $\boldsymbol{E}_{b,\boldsymbol{k}}$ in Eq. 2.5 is typically normalized so that the integral of its energy density in the WSC is unity ($\int_{\mathrm{WSC}} \varepsilon(\boldsymbol{r}) \, |\boldsymbol{E}_{b,\boldsymbol{k}}(\boldsymbol{r})|^2 \, d\boldsymbol{r} = 1$), which was also done in this work. Thus, the in this way defined LDOS and DOS both have no units.

2.1.2 Light at interfaces

In the previous section, homogeneous or periodic media were considered to be extended infinitely. In reality, however, finite systems have boundaries to other media. In general, light at such interface has to obey the following criteria to be able to couple from one medium to the other: (i) conservation of the frequency ω (conservation of energy), and (ii) conservation of the wave vector component $\boldsymbol{k}_{\parallel}$ parallel to the interface as a result of translational symmetry [66, 103].

For plane waves at the interface of two homogeneous materials, these criteria and the linear dispersion relation yield Snell's law of refraction, stating

$$n_{\mathrm{i}} \sin(\phi_{\mathrm{i}}) = n_{\mathrm{t}} \sin(\phi_{\mathrm{t}}), \tag{2.8}$$

where n_{i}, n_{t} denote the refractive indices of the medium of incidence and transmission, respectively, and ϕ_{i}, ϕ_{t} are the corresponding propagation angles defining the $\boldsymbol{k}$-vectors in both media, as shown in Fig. 2.1 (a). When $n_{\mathrm{i}} > n_{\mathrm{t}}$, total internal reflection (TIR) occurs for incident angles larger than the critical angle $\phi_{\mathrm{c}} = \sin^{-1}(n_{\mathrm{t}}/n_{\mathrm{i}})$, determining the escape cone loss in conventional LSCs.

In contrast, light in photonic crystals is described as Bloch modes, i.e. their fields are products of a plane wave and a periodic Bloch function $\boldsymbol{u}$. As there is no trivial dispersion relation $\omega(\boldsymbol{k})$, it is necessary to consider $\boldsymbol{k}_{\parallel}$, rather than the angle φ_k of a mode's wave vector inside the photonic crystal. In fact, the angle φ_k is not suitable to express the propagation direction of light in photonic crystals: the propagation direction of electromagnetic energy is given by the group velocity $\boldsymbol{v}_g$ that generally does not point in the same direction as $\boldsymbol{k}$ in photonic crystals.[5] This effect is known in literature as "beam steering" [66, 104–106].

Consequently, the condition for out-coupling of light from photonic crystals to a homogeneous medium is given by

$$|\boldsymbol{k}_{\parallel}| \leq \omega\, n_{\mathrm{out}}/c, \tag{2.9}$$

where n_{out} is the refractive index of the surrounding medium, see Fig. 2.1 (b). Typically, only part of the photonic crystal's modes meet this condition, the other modes are guided inside the photonic crystal (similar to total internal reflection). For modes that are able to couple out, the wave vector $\boldsymbol{k}_{\mathrm{out}}$ of the out-coupled plane wave is given by the components parallel and perpendicular to the interface

$$\boldsymbol{k}_{\mathrm{out},\parallel} = \boldsymbol{k}_{\parallel}, \tag{2.10}$$

$$\boldsymbol{k}_{\mathrm{out},\perp} = \sqrt{(\omega\, n_{\mathrm{out}}/c)^2 - |\boldsymbol{k}_{\mathrm{out},\parallel}|^2}\ \ \boldsymbol{n}/|\boldsymbol{n}|, \tag{2.11}$$

where $\boldsymbol{n}$ is the normal vector of the interface.

[5] The group velocity $\boldsymbol{v}_g$ is a normal to the iso-frequency curve (surface in 3D). In photonic crystals the iso-frequency curve (surface) is no longer simply a circle (sphere) due to the non-linear dispersion relation, as shown in Fig. 2.1 (b) for an arbitrary case. Therefore, the direction of the normal does not necessarily coincide with $\boldsymbol{k}$ as in homogeneous media.

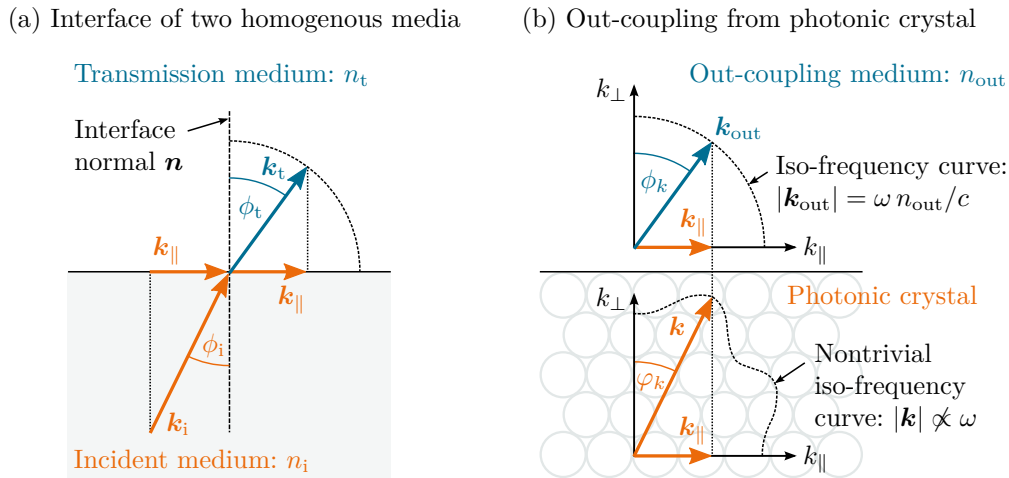

Figure 2.1: Light at interfaces has to obey the conservation of frequency (i.e. energy) and of the interface-parallel wave vector component $\boldsymbol{k}_\parallel$. (a) For an interface of two homogenous media, the propagation angles of the incident and transmitted plane waves are therefore connected via the refractive indices of the two materials, which is known as Snell's law of refraction. (b) At interfaces between a photonic crystal and a homogeneous medium, there is no general connection between the angles of the wave vectors due the non-linear dispersion relation. Instead, the wave vector $\boldsymbol{k}_{out}$ of out-coupled light is given by $\boldsymbol{k}_\parallel$ and the frequency ω. Similar to total internal reflection in refraction, however, not all modes in the photonic crystal are able to couple out.

The considerations above yield the propagation direction of the out-coupled light. The field amplitudes or the fractions of power that are transmitted or reflected at the interface, however, are determined by the boundary conditions of the electromagnetic fields at the interface, including the polarization of the incident light. Note that the definitions of polarizations are different for interfaces and in photonic crystals, as explained in Appendix A.2.

At interfaces between two homogeneous materials, the continuity of the tangential field components [107] yield the well-known Fresnel equations for the reflectance and transmittance, as listed in Appendix A.3. At the interface of a photonic crystal, however, the reflected and transmitted field amplitudes depend on the exact surface termination and require a detailed investigation of Maxwell's equations at the interface. In this work, the worst case scenario for a (P)LSC was examined: all modes that are able to couple out are assumed to be lost. With a non-zero out-coupling efficiency, this assumption corresponds to a large concentrator where light may interact many times with the surfaces while bouncing through the concentrator.

2.2 Light-matter interaction

Light and matter interact: most prominently light can get absorbed by matter, and matter can emit light. While photons are annihilated and created during these processes, energy is conserved as matter (for example an atom or a molecule) changes from one to another state with different energy. Einstein introduced rate-equations for these transitions based on the quantum theory of light, as shown in the following. Subsequently, the influence of a photonic environment on the transition rates of absorption and emission is discussed in detail. In the last part of this section, the phenomenon of luminescence is introduced, where absorbed and emitted photons typically have different energies.

2.2.1 Transition rates and Einstein coefficients

In his fundamental work, Einstein considered the transitions between two discrete energy level of an atom [108]. Let there be N_{tot} atoms with the two energy levels $\mathcal{E}_{\mathrm{i}}$, $\mathcal{E}_{\mathrm{f}}$ ($\mathcal{E}_{\mathrm{i}} < \mathcal{E}_{\mathrm{f}}$) of the respective states i (ground state), f (excited state), which have the degeneracies $\mathcal{G}_{\mathrm{i}}$, $\mathcal{G}_{\mathrm{i}}$. Through absorption of a photon an atom undergoes a transition from state i to state f, while emission of a photon corresponds to the transition of an excited atom to the lower state i. In both cases, conservation of energy requires the photon to have the energy $\hbar\omega_{\mathrm{fi}} = \mathcal{E}_{\mathrm{f}} - \mathcal{E}_{\mathrm{i}}$.

There are three types of transitions: absorption, stimulated emission, and spontaneous emission, as indicated in Fig. 2.2. While spontaneous emission requires no external influence,[6] absorption and stimulated emission result from an incoming photon. This incoming photon can be described in terms of the spectral energy density $u(\omega)$.

To model the probability of these transitions, Einstein introduced coefficients $\mathcal{B}_{\mathrm{if}}$, $\mathcal{B}_{\mathrm{fi}}$, $\mathcal{A}_{\mathrm{fi}}$. In case of absorption, the transition probability P_{ABS} is proportional to $u(\omega_{\mathrm{fi}})$, and depends on the Einstein coefficient $\mathcal{B}_{\mathrm{if}}$ via

$$P_{\mathrm{ABS}} = \mathcal{B}_{\mathrm{if}}\, u(\omega_{\mathrm{fi}}). \tag{2.12}$$

Similarly, the probability of stimulated emission is described by

$$P_{\mathrm{STE}} = \mathcal{B}_{\mathrm{fi}}\, u(\omega_{\mathrm{fi}}) \tag{2.13}$$

with Einstein coefficient $\mathcal{B}_{\mathrm{fi}}$. The transition probability of spontaneous emission is given by the Einstein coefficient $\mathcal{A}_{\mathrm{fi}}$:

$$P_{\mathrm{SPE}} = \mathcal{A}_{\mathrm{fi}}. \tag{2.14}$$

[6] In quantum electrodynamics, where not only atomic levels but also the electromagnetic field is quantized, spontaneous emission can be explained with zero-point fluctuations of the vacuum (arising from Heisenberg's uncertainty relation). In this picture, virtual photons trigger the transition.

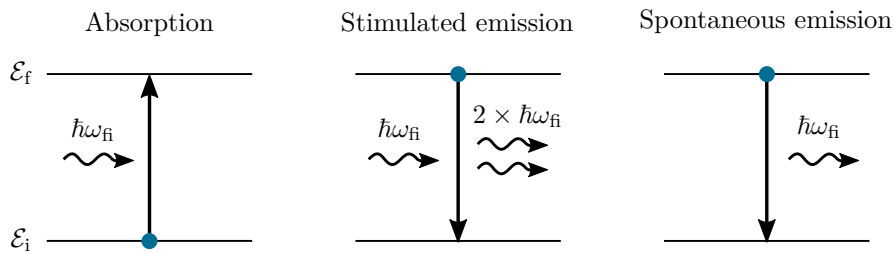

Figure 2.2: An atom can absorb light through the transition from one state to another with higher energy $\mathcal{E}$. Such an excited atom can decay via stimulation by an incident photon (stimulated emission) or spontaneously. The rates, at which these three transitions occur, can be described with the Einstein coefficients as described in the text.

In real atoms or molecules, energy levels are not perfectly discrete due to homogeneous broadening (e.g. natural broadening) or inhomogeneous broadening (e.g. Doppler broadening). To account for these effects, line shape functions can be used to describe the spectral shape of the transitions. The shape of such a function $g_\mathrm{l}(\omega)$ depends on the broadening mechanism (e.g. Lorentzian for natural broadening, Gaussian for Doppler broadening [109]), while the spectral integral of $g_\mathrm{l}(\omega)$ is normalized to unity ($\int_0^\infty g_\mathrm{l}(\omega)d\omega = 1$). The probability of the transition is then given by the spectral integral of the product of the Einstein coefficient and the line shape function: for example for spontaneous emission $P_\mathrm{SPE} = \int_0^\infty \mathcal{A}_\mathrm{fi}\, g_\mathrm{l}(\omega)d\omega = \mathcal{A}_\mathrm{fi}$.

The rate Γ of an atomic transition is given by the product of the transition probability and the population of the corresponding state N_i or N_f, i.e. the number of atoms found in the respective state. Accordingly,

$$\Gamma_\mathrm{ABS} = N_\mathrm{i}\, P_\mathrm{ABS}, \qquad \Gamma_\mathrm{STE} = N_\mathrm{f}\, P_\mathrm{STE}, \qquad \Gamma_\mathrm{SPE} = N_\mathrm{f}\, P_\mathrm{SPE}. \tag{2.15}$$

In steady-state, absorption is balanced with emission. Thus,

$$\Gamma_\mathrm{ABS} = \Gamma_\mathrm{STE} + \Gamma_\mathrm{SPE} \qquad \Leftrightarrow \qquad \frac{N_\mathrm{f}}{N_\mathrm{i}} = \frac{\mathcal{B}_\mathrm{if}\, u(\omega_\mathrm{fi})}{\mathcal{B}_\mathrm{fi}\, u(\omega_\mathrm{fi}) + \mathcal{A}_\mathrm{fi}}. \tag{2.16}$$

At the same time, the population of the states in thermal equilibrium according to Boltzmann is given by

$$\frac{N_\mathrm{f}}{N_\mathrm{i}} = \frac{\mathcal{G}_\mathrm{f}}{\mathcal{G}_\mathrm{i}} \exp\left(-\frac{\hbar\omega_\mathrm{fi}}{k_\mathrm{B}\vartheta}\right) \tag{2.17}$$

with the Boltzmann constant k_B and Temperature ϑ. Comparison of Eqs. (2.16) and (2.17) yields

$$u(\omega_\mathrm{fi}) = \frac{\mathcal{A}_\mathrm{fi}/\mathcal{B}_\mathrm{fi}}{(\mathcal{B}_\mathrm{if}/\mathcal{B}_\mathrm{fi})\, \frac{\mathcal{G}_\mathrm{i}}{\mathcal{G}_\mathrm{f}} \exp\left(\frac{\hbar\omega_\mathrm{fi}}{k_\mathrm{B}\vartheta}\right) - 1}. \tag{2.18}$$

On th other hand, the spectral energy density $u(\omega)$ is given in general by the product of the photon energy $\hbar\omega$, the density of photon states $\varrho(\omega)$, and the Bose-Einstein distribution (as photons are bosons):

$$u(\omega) = \hbar\omega\, \varrho(\omega)\, \frac{1}{\exp\left(\frac{\hbar\omega}{k_\mathrm{B}\vartheta}\right) - 1}. \tag{2.19}$$

With the DOS for the case of a homogeneous medium, this equation yields the well-known Planck's law for the black body radiation, as often stated in textbooks at this point. In this work, photonic structures are considered that have a disturbed DOS, therefore the general case needs to be discussed.

Comparing Eqs. (2.18) and (2.19) reveals

$$\mathcal{B}_\mathrm{if} = \frac{\mathcal{G}_\mathrm{f}}{\mathcal{G}_\mathrm{i}} \mathcal{B}_\mathrm{fi}, \tag{2.20}$$

$$\mathcal{A}_\mathrm{fi} = \hbar\omega_\mathrm{fi}\, \varrho(\omega_\mathrm{fi}) \mathcal{B}_\mathrm{fi}. \tag{2.21}$$

Thus the Einstein coefficients of absorption and stimulated emission differ only by the ratio of the energy level's degeneracies; for non-degenerate levels $\mathcal{B}_\mathrm{if} = \mathcal{B}_\mathrm{fi}$. The Einstein coefficient for spontaneous emission $\mathcal{A}$ and the $\mathcal{B}$-coefficients are related by the DOS.

While $\mathcal{B}_\mathrm{if}$ and $\mathcal{B}_\mathrm{fi}$ are material properties determined by the states' quantum mechanical wave functions, the probability of spontaneous emission additionally depends on the DOS. Thus the rate of spontaneous emission can be influenced by the surrounding structure, it is no inherent property of the emitting atom.

In non-homogeneous media, the spectral energy density and also the relevant photonic states depend on the atom's position in space. Thus the local absorption due to the local field distribution, as well as the local density of photon states (LDOS) need to be considered as discussed in the following.

2.2.2 Emission rate: Fermi's golden rule

The mechanisms that determine the transition rates, i.e. the Einstein coefficients, can be revealed by a quantum mechanical analysis of the atom-field interaction. In the following, I will present a brief summary of the concepts and the main results that are relevant for this work, while a detailed derivation can be found in textbooks like Refs. 110–112.

Using time-dependent perturbation theory, the absorption and emission of light is considered as a perturbation $\mathcal{V}_\mathrm{fi}$ in the Hamiltonian of the emitter's Schrödinger equation. As a consequence, the probability to find the emitter either in its ground or excited state (i.e. the populations N_i, N_f) can be solved as a function of time. Depending on the intensity of the light field, the two regimes of *weak coupling* and *strong coupling* are distinguished. Strong coupling applies to high fields such

as found in powerful laser beams, and it can cause oscillations in the populations (so-called Rabi oscillations). In this work, I consider the weak coupling regime, reflecting the relatively low intensities in PLSCs. This regime is characterized by $N_\mathrm{i} >> N_\mathrm{f}$, i.e. that the excited state population is relatively small. As a result, a steady-state for the populations and transition rates is found that is consistent with Einstein's treatment [109].

Furthermore, a relation between the transition probability of spontaneous emission P_SPE and the local density of photon states $\rho(\boldsymbol{r}, \omega)$ can be found that is known as Fermi's golden rule [99, 113]:

$$P_\mathrm{fi}(\boldsymbol{r}) = \frac{2\pi}{\hbar} \left|\langle \mathrm{f}|\mathcal{V}_\mathrm{fi}|\mathrm{i}\rangle\right|^2 \rho(\boldsymbol{r}, \omega_\mathrm{fi}), \tag{2.22}$$

where the matrix element $\langle \mathrm{f}|\mathcal{V}_\mathrm{fi}|\mathrm{i}\rangle$ of the transition from state f to state i (in braket notation) is determined by the interaction part $\mathcal{V}_\mathrm{fi}$ of the Hamiltonian coupling the emitter to the electromagnetic field.

Accordingly, the probability for the radiative transition is proportional to the LDOS $\rho(\boldsymbol{r}, \omega_\mathrm{fi})$, as a photon with energy $\hbar\omega_\mathrm{fi}$ can be emitted only if there is an appropriate photon state it can populate. Note, that it is the LDOS, not the DOS, that determines the transition probability: given a mode with a field pattern being zero at a certain position (due to a node, for example), an emitter at that position cannot excite this mode. Consequently, the transition probability (i.e. in Einstein's picture the $\mathcal{A}$-coefficient) becomes a function of $\boldsymbol{r}$.

Furthermore, the transition probability depends on the emitter's dipole orientation arising from $\langle \mathrm{f}|\mathcal{V}_\mathrm{fi}|\mathrm{i}\rangle$. In this work emission from an ensemble with randomly oriented dipole moments is considered. However, the influence of the emitter orientation could be easily implemented in the proposed model following Ref. 114.

When an emitter is embedded in a photonic environment, the rate of spontaneous emission mainly changes due to the modified LDOS. The influence of the surrounding on the electronic configuration of the emitter, i.e. on $\langle \mathrm{f}|\mathcal{V}_\mathrm{fi}|\mathrm{i}\rangle$, can be neglected as the typical feature size of photonic structures in the range of 100 nm is much larger than the range of the interaction forces that determine the emitters wave functions.

In the extreme case, spontaneous emission is fully suppressed if the structure features a complete band gap at the transition frequency. This is not the case for the photonic crystals investigated in this work. Due to their incomplete bandgaps, emission is partly suppressed in certain spatial direction, while enhanced in others. Even though the (total) transition rate is not changed significantly, this effect of directional redistribution can strongly improve the light guiding in PLSCs, as shown in Sec. 5.1.

2.2.3 Local absorption

In Einstein's picture, absorption of light by matter is described by the microscopic coefficient $\mathcal{B}$. Coming from the phenomenological side, absorption can be quantified using the absorption coefficient α, the imaginary part of the complex refractive index $\kappa = \alpha\lambda_0/4\pi$, or the imaginary part of the relative permittivity $\varepsilon'' = 2n\kappa$. These rather macroscopic quantities can be linked with Einstein's $\mathcal{B}$-coefficient, given the number of emitters in a certain volume [115].

For light traveling through homogeneous media, the loss in intensity[7] I due to absorption can be described via the well-known Lambert-Beer law:

$$I(x) = I_0\,\mathrm{e}^{-\alpha x}, \tag{2.23}$$

where x is the propagation direction of light and I_0 denotes the initial intensity (at $x = 0$).

In non-homogenous media like photonic crystals, interference of waves traveling in different directions result in a certain distribution of the electromagnetic energy, for example in form of nodes and anti-nodes of standing waves. Furthermore, the absorption coefficient may vary spatially as the structure consists of different materials. To determine the amount of light absorbed by an atom or molecule at a certain position $\boldsymbol{r}$, the spatial field distribution needs to be considered.

Based on Poynting's theorem, the power absorbed in the infinitesimal volume dV at position $\boldsymbol{r}$ can be expressed as [116]

$$d\mathcal{P}_{\mathrm{ABS}}(\boldsymbol{r}) = \frac{1}{2}\,\omega\,\varepsilon_0\,\varepsilon''(\boldsymbol{r})\,|\boldsymbol{E}(\boldsymbol{r})|^2\,dV. \tag{2.24}$$

Accordingly, the local absorption is proportional to the imaginary part of the relative permittivity $\varepsilon''(\boldsymbol{r})$ and to the magnitude of the local electric field $|\boldsymbol{E}(\boldsymbol{r})|^2$. This expression is consistent with Einstein's treatment, where the transition rate depends on the spectral energy density u, which is also proportional to $|\boldsymbol{E}|^2$ [109].

In this work, the concept of local absorption is used to calculate the absorptance by emitters at certain positions in PLSCs (see Sec. 6.1.1). Considering non-homogenous media under external illumination of intensity I_0, the local absorptance, i.e. the fraction of incident light absorbed within the distance dx in propagation direction x, is given by

$$\frac{dA}{dx}(\boldsymbol{r}) = \frac{1}{I_0}\frac{1}{2}\,\omega\,\varepsilon_0\,\varepsilon''(\boldsymbol{r})\,|\boldsymbol{E}(\boldsymbol{r})|^2 = \frac{1}{I_0}\alpha(\boldsymbol{r})\,I(\boldsymbol{r}) \tag{2.25}$$

in units of 1/m. Accordingly, local absorption is directly proportional to the intensity

$$I(\boldsymbol{r}) = \frac{1}{2}\,\varepsilon_0\,c\,n(\boldsymbol{r})\,|\boldsymbol{E}(\boldsymbol{r})|^2 \tag{2.26}$$

of plane waves.

[7] The term intensity is used for the power per area (with units $\mathrm{W/m^2}$), which is sometimes also referred to as "irradiance".

2.2.4 Photoluminescence

In general, luminescence is the emission of photons not resulting from heat radiation, but from a transition from an excited state to a lower-energy state. In particular, photoluminescence is defined by the excitation via absorption of photons. Typically, such materials are characterized by a spectral separation of absorption and emission: light is emitted at longer wavelengths than previously absorbed, as shown in Fig. 2.3 (a) for a typical fluorescent dye. This spectral difference is known as the Stokes shift (named after the 19th century scientist Sir G. G. Stokes) and arises from non-radiative internal conversion processes before emission.

The phenomenon of photoluminescence is divided into two categories, particularly for organic dyes: fluorescence and phosphorescence, depending on the electronic structure of the material and therefore the decay dynamics. Fluorescence describes the emission from an excited singlet state, thus return to the ground state is spin-allowed. Consequently, emission rates are rather high (around 10^8 s^{-1} [117]), i.e. the average time between excitation and decay - the *lifetime* - is in the range of nanoseconds. Phosphorescence, in contrast, is characterized by the decay from an excited triplet state. As the transition to the ground state is forbidden, the decay happens much slower. Typical lifetimes range from milliseconds to seconds, or even longer as known from "glow-in-the-dark" materials [117].

(a) Typical absorption and emission spectra of a fluorescent dye

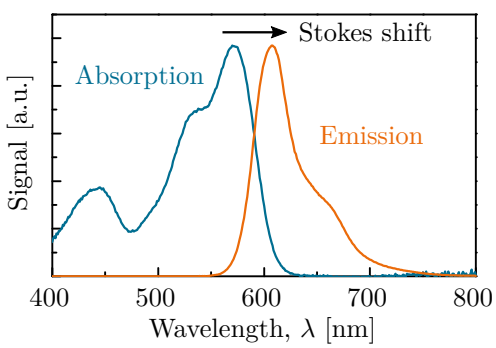

(b) Energetic structure of a fluorescent dye

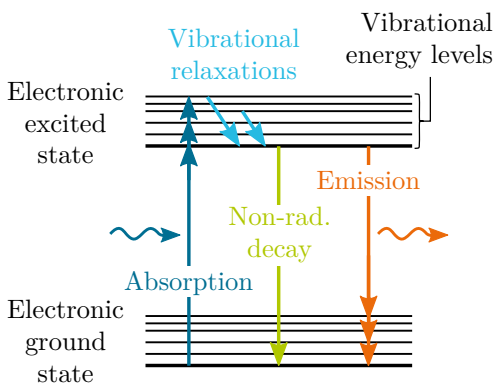

Figure 2.3: In luminescent materials, light is typically emitted at smaller energies, i.e. longer wavelengths, compared to the previously absorbed light. As an example, the spectra of the organic dye "Lumogen F Red 300" are shown in (a), where the spectral separation of absorption and emission, known as the Stokes shift, is visible. The reason for this phenomenon are non-radiative internal conversion processes in the material as illustrated in (b): while light can excite the material into different energetic levels of the excited state, fast vibrational relaxations occur so that emission can be assumed to originate only from the lowest level of the excited state.

There are different material classes that exhibit photoluminescence, and that are therefore interesting for the application in LSCs, such as lanthanide ions, semiconductor nano-crystals, and organic dyes. As mentioned in Sec. 1.3, this work focuses on fluorescent organic dyes as they have shown best results in terms of the performance of LSCs.

These organic molecules typically feature rather complex energetic structures that can be described by an electronic ground state and one (or more) excited states, as illustrated in Fig. 2.3 (b). These electronic states are split up into a number of vibrational energy levels, which are further subdivided into rotational energy levels of the molecule. As a result, absorption and emission spectra are relatively broad.

The absorption of a photon with appropriate energy promotes the molecule from its ground state to one of the vibrational levels of an electronic excited state. This excited molecule subsequently undergoes vibrational relaxations to the lowest level of the (first) excited state. From this level, it can radiatively (or non-radiatively) decay to one of the ground state levels. Therefore, emitted photons have lower energy than the absorbed ones (Stokes shift). As the vibrational transitions ($\sim 10^{-12}$ s) are much faster than the radiative decay ($\sim 10^{-9}$ s), emission can be assumed to originate only from the lowest level of the excited state [117].

Not all excited molecules emit a photon when decaying to the ground state: non-radiative decay, also referred to as *quenching*, can occur for example through energy transfer to other atoms or molecules in the vicinity [25]. Being a key characteristics of luminescent materials, the photoluminescence quantum yield (PLQY) Φ denotes the ratio of emitted to absorbed photons, i.e. the probability that a photon is emitted after a photon was absorbed. Given the transition rates of absorption Γ_{ABS} and spontaneous emission Γ_{SPE}, the PLQY is thus defined as

$$\Phi = \frac{\Gamma_{\mathrm{SPE}}}{\Gamma_{\mathrm{ABS}}}. \tag{2.27}$$

As mentioned above, the fluorescence lifetime is a measure for the decay dynamics. In lifetime experiments, the decay of fluorescence is analyzed after the excitation has been turned off. Given that return to the ground state is possible through either spontaneous emission (with transition probability P_{SPE}) or non-radiative decay (transition probability P_{NRD}), the corresponding differential equation for the population of the excited state “2”

$$\dot{N}_2(t) = -N_2(t)\,(P_{\mathrm{SPE}} + P_{\mathrm{NRD}}) \tag{2.28}$$

can be solved with the exponential ansatz $N_2(t) = N_2(0)\,e^{-t/\tau}$, where

$$\tau = (P_{\mathrm{SPE}} + P_{\mathrm{NRD}})^{-1} \tag{2.29}$$

is called fluorescence lifetime.

Chapter 3

Modeling methods

Several modeling methods were developed in this work to theoretically investigate the influence of a photonic crystal on the fluorescent emission and light guiding. As a key quantity, the photonic crystal's local density of photons states (LDOS) was obtained from eigenmode calculations, as described in the first part of this chapter. In the second part, a rate equation model for fluorescent emitters is proposed that allows calculating the LDOS-induced changes in the emitted and detected spectra, the photoluminescence quantum yield, and the fluorescence lifetime. In the last part, different methods are presented that deal with the propagation of light in finite structures. They allow for modeling realistic structures and were used to predict certain measurement results for comparison with experiments.

3.1 Local density of photon states

The local density of photon states (LDOS) of a certain structure can be obtained using different approaches. For ideal, i.e. infinitely extended photonic crystals, the LDOS can be calculated from the eigenmodes [72, 98, 100, 118], as mentioned in Sec. 2.1.1. Finite and non-periodic structures can be treated with the Green's function approach [114, 119–121], the transfer matrix [122] and scattering matrix method [79] or using finite-difference time-domain (FDTD) calculations [123, 124]. These methods, however, require typically much more computational effort than the efficient eigenmode approach, as all emitted modes need to be considered in extensive three-dimensional calculations to obtain the LDOS. An additional advantage of the eigenmode approach is that it allows the extraction of directional information since each eigenmode belongs to a certain wave vector $\boldsymbol{k}$. Thus, a

specific *fractional* LDOS (FLDOS) can be calculated from a subset of all modes.

For these reasons, I obtained the LDOS in this work from the photonic crystal's eigenmodes. In the following, the corresponding numerical approach is presented, focusing on the 1D-periodic Bragg stack and the 3D-periodic opal that were introduced in Sec. 1.3. Subsequently, the appropriate "sampled" LDOS in homogeneous media is derived theoretically for comparison with the photonic-crystal LDOS to obtain the changes in the transition rates of an emitter. In the third part, numerical results for the Bragg stack are presented as an example that helps to understand the distribution of eigenmodes in such a structure. The last part of this section explains the calculation of the FLDOS from eigenmodes.

3.1.1 LDOS in photonic crystals from eigenmodes

An eigenmode is obtained from numerically solving the master equation (Eq. (2.1)) for a certain wave vector $\boldsymbol{k}_j$ as an input, yielding its frequency $\omega_{b,\boldsymbol{k}_j}$ and field distribution $\boldsymbol{H}_{b,\boldsymbol{k}_j}(\boldsymbol{r})$ for the band b. To calculate the LDOS of the photonic crystal $\rho^{\mathrm{PC}}(\boldsymbol{r},\omega)$ from such eigenmodes, the integral from Eq. (2.5) is translated to the sum $\hat{\rho}^{\mathrm{PC}}(\boldsymbol{r},\omega)$ over discrete wave vectors $\boldsymbol{k}_j$:[1]

$$\hat{\rho}^{\mathrm{PC}}(\boldsymbol{r},\omega) = \sum_{b} \sum_{\boldsymbol{k}_j \in K_{b,\omega}} |\boldsymbol{E}_{b,\boldsymbol{k}_j}(\boldsymbol{r})|^2$$
$$\text{with } K_{b,\omega} = \left\{ \boldsymbol{k} \in \mathrm{FBZ} \;\middle|\; \omega - \Delta\omega/2 \leq \omega_{b,\boldsymbol{k}} < \omega + \Delta\omega/2 \right\} \tag{3.1}$$

and the binning width $\Delta\omega$. In this "histogramming" approach all the sampled eigenmodes, of which the frequency $\omega_{b,\boldsymbol{k}_j}$ lies within a certain frequency bin, are counted with their individual distribution of the electric field $|\boldsymbol{E}_{b,\boldsymbol{k}_j}(\boldsymbol{r})|^2$. Analogously, the sampled DOS $\hat{\varrho}^{\mathrm{PC}}(\omega)$ is given by the sum

$$\hat{\varrho}^{\mathrm{PC}}(\omega) = \sum_{b} \sum_{\boldsymbol{k}_j \in K_{b,\omega}} 1. \tag{3.2}$$

Rather than calculating only some modes along certain directions (as for the dispersion relations in Fig. 1.2 (c), (d)), for the (L)DOS one needs to consider all FBZ wave vectors $\boldsymbol{k}_j$ on an equidistant grid in $\boldsymbol{k}$-space.[2] Accordingly, a finite set of eigenmodes needs to be calculated, depending of the discretization of the FBZ in reciprocal space. Here, the FBZ of the opal and the Bragg stack were sampled in different ways for an efficient computation of the LDOS, as shown in the following.

[1] Alternatively, the integrals for the LDOS and DOS could be discretized using the tetrahedron method by linearly interpolating the dispersion relation [98, 125, 126]. The histogramming method used here, however, is more comprehensible and allows for convenient calculation of the FLDOS as explained later (Sec. 3.1.4).

[2] It is possible to use only wave vectors of an irreducible symmetry element of the FBZ (such as the one indicated in the inset of Fig. 1.2 (d)). However, this requires an additional transformation as the fields do not necessarily exhibit the same symmetry as the $\boldsymbol{k}$-vectors [118].

Opal (full-3D)

For the opal, the whole FBZ was sampled in all three dimensions to simplify the evaluation of LDOS and FLDOS. The discretization of the opal's FBZ is illustrated in Fig. 3.1 (a) with a very large spacing Δk for the purpose of illustration. The finer the grid, i.e. the smaller Δk, the higher the resolution and accuracy of $\hat{\rho}(\boldsymbol{r}, \omega)$ since the binning noise is reduced. As a trade-off between accuracy and computational effort, I calculated all modes within the FBZ with $\Delta k = 0.1/a$ (resulting in 994233 $\boldsymbol{k}$-vectors) up to the 8th band to obtain all states with normalized frequency $\omega a/2\pi c < 1$ and used a binning width of $\Delta\omega = 0.01\ 2\pi c/a$. The 3D unit cell was discretized using $16 \times 16 \times 16$ points.

Bragg stack (quasi-3D)

To calculate the LDOS of the Bragg stack efficiently, I exploited the structure's in-plane symmetry: as indicated in Fig. 3.1 (b), the reciprocal space was sampled only in one quadrant of the two-dimensional xy-plane rather than in all three dimensions. To obtain the 3D LDOS, each mode was weighted with the circumference of a circle around the x-axis through the point described by its $\boldsymbol{k}_j$. This length is given by $2\pi k_{j,y}$ ($k_{j,y}$ being the y-component of $\boldsymbol{k}_j$). It quantifies how

(a) Discretized FBZ of opal

(b) Quasi-3D LDOS of Bragg stack through weighting of 2D-sampled $\boldsymbol{k}$-space

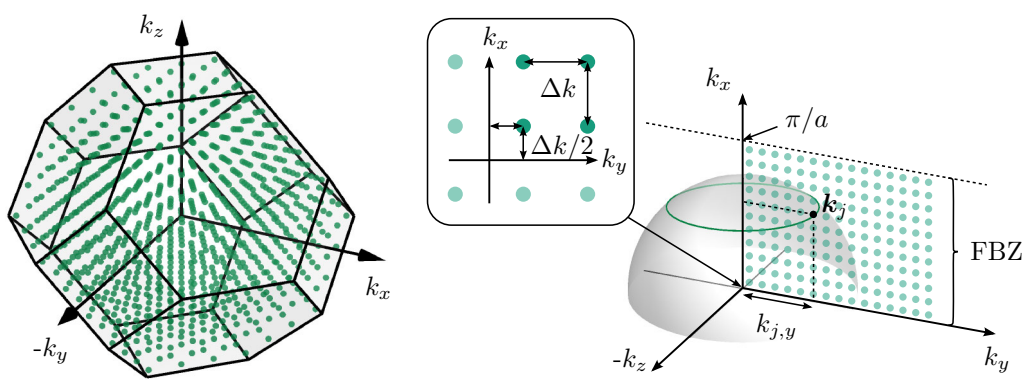

Figure 3.1: To calculate the LDOS in photonic crystals, their eigenmodes were computed on a finite and equidistant grid in reciprocal space. For the opal, the full FBZ was sampled, as shown in (a). For the Bragg stack, only the wave vectors in one quadrant of the two-dimensional xy-plane were calculated to reduce computational efforts, see (b). Due to the structure's in-plane symmetry, the "quasi-3D" LDOS was obtained from weighting each mode with the circumference of a circle around the x-axis through its $\boldsymbol{k}_j$. This length quantifies the number of equivalent modes in the 3D $\boldsymbol{k}$-space. In both (a) and (b), a grid spacing Δk much larger than in the calculations was used for the purpose of illustration.

many modes equivalent to this wave vector $\boldsymbol{k}_j$ would exist in full-3D calculations, all of them having the same field distribution $|\boldsymbol{E}_{b,\boldsymbol{k}_j}(\boldsymbol{r})|^2$. Accordingly, the "quasi-3D" (q3D) LDOS $\hat{\rho}^{\mathrm{PC}}_{\mathrm{q3D}}(\boldsymbol{r},\omega)$ and DOS $\hat{\varrho}^{\mathrm{PC}}_{\mathrm{q3D}}(\omega)$ are given by

$$\hat{\rho}^{\mathrm{PC}}_{\mathrm{q3D}}(\boldsymbol{r},\omega) = \sum_b \sum_{\boldsymbol{k}_j \in K_{b,\omega}} 2\pi \tilde{k}_{j,y} \, |\boldsymbol{E}_{b,\boldsymbol{k}_j}(\boldsymbol{r})|^2, \tag{3.3}$$

$$\hat{\varrho}^{\mathrm{PC}}_{\mathrm{q3D}}(\omega) = \sum_b \sum_{\boldsymbol{k}_j \in K_{b,\omega}} 2\pi \tilde{k}_{j,y}, \tag{3.4}$$

where the normalized wave vector $\tilde{k}_{j,y} = k_{j,y}\, a/2\pi$ was used for weighting to obtain $\hat{\rho}^{\mathrm{PC}}_{\mathrm{q3D}}$ and $\hat{\varrho}^{\mathrm{PC}}_{\mathrm{q3D}}(\omega)$ normalized with respect to the unit cell size a (cf. Eqs. (3.12) and (3.13)). Benchmarking this quasi-3D approach with full-3D calculation yielded the same LDOS and DOS results at a much lower computational effort but with a higher accuracy. Furthermore, all calculations were consistent with the relation of the LDOS and the DOS given by Eq. (2.7).

Please note, that sampling only one quadrant of the xy-plane requires to consider the symmetry-induced multiplicity: the smallest $\boldsymbol{k}_j$ of the grid should not lie at $x = y = 0$. Instead it needs to be shifted by $\Delta k/2$, as shown in the inset of Fig. 3.1 (b). Otherwise the $\boldsymbol{k}_j$-vectors lying on the axes have double the multiplicity of the other $\boldsymbol{k}_j$-vectors yielding erroneous results, especially at small frequencies.

For most Bragg stack calculations in this work, $\Delta k = 0.001\ 2\pi/a$ was used to sample the $\boldsymbol{k}$-space up to the FBZ border at $k_x = \pi/a$. As the FBZ is not restricted in y-direction, wave vectors in this direction were sampled according to the condition $|\boldsymbol{k}| \leq 1.2\ 2\pi/a$. In this way, all modes with normalized frequency $\omega a/2\pi c < 0.58$ were obtained, considering the first two bands of both polarizations. Histogramming was performed with a binning width of $\Delta\omega = 0.001\ 2\pi c/a$. The 1D unit cell was discretized using 32 points.

LDOS ratio

To calculate the changes in emission induced by a photonic crystal, the ratio $\gamma(\boldsymbol{r},\omega)$ of the LDOS in a photonic crystal and the LDOS in a homogeneous medium was calculated:

$$\gamma(\boldsymbol{r},\omega) = \frac{\hat{\rho}^{\mathrm{PC}}(\boldsymbol{r},\omega)}{\hat{\rho}^{0}(\omega)}, \tag{3.5}$$

where $\hat{\rho}^{0}(\omega)$ is the corresponding "sampled" LDOS in a homogeneous medium, as presented in the following section. The homogeneous-medium LDOS does not depend on $\boldsymbol{r}$. As it depends on the refractive index, however, the local $n = n(\boldsymbol{r})$ needs to be chosen for comparison in the corresponding material. The LDOS ratio $\gamma(\boldsymbol{r},\omega)$ is as an input parameter to the rate-equation model of fluorescent emission, as presented in Sec. 3.2.

3.1.2 Sampled LDOS in homogeneous media

To investigate the photonic crystal's influence on an emitter, the LDOS in the photonic crystal needs to be compared to that in a homogeneous medium, which serves as a reference for undisturbed emission. Therefore, it needs to be considered, that the LDOS in the photonic crystal is obtained from a finite set of eigenmodes as explained above. Consequently, calculating the LDOS in homogeneous media needs to account for the discretization of $\boldsymbol{k}$-space. In the following, the appropriate expressions for the homogeneous-medium (L)DOS are derived for the full-3D calculations of the opal as well as for the quasi-3D approach used for the Bragg stack.

Full-3D calculations (opal)

Considering the three-dimensional $\boldsymbol{k}$-space, the number of sampled modes $M(k_\mathrm{g})$ with $|\boldsymbol{k}| \leq |\boldsymbol{k}_\mathrm{g}| = k_\mathrm{g}$ can be approximated by the ratio of the volume of a sphere with radius k_g and the volume of one sampled mode that is given by a cube with side length of Δk:

$$M(k_\mathrm{g}) = 2\frac{\frac{4}{3}\pi k_\mathrm{g}^3}{\Delta k^3}, \tag{3.6}$$

where the factor of two accounts for the two linearly independent polarizations.

From this equation and using the linear dispersion $\omega = (c/n)\,k$ in homogeneous media, the density of states (per angular frequency ω) is given by

$$\varrho^0(\omega) = \frac{dM(k(\omega))}{d\omega} = \frac{dM(k(\omega))}{dk}\frac{dk(\omega)}{d\omega} = \frac{8\pi k^2(\omega)}{\Delta k^3}\frac{n}{c} = \frac{8\pi n^3}{c^3\Delta k^3}\,\omega^2, \tag{3.7}$$

depending quadratically on ω.

The *local* density of states $\rho^0(\omega)$ can be derived from this DOS using Eq. (2.7):

$$\rho^0(\omega) = \frac{1}{n^2}\,\varrho^0(\omega) = \frac{8\pi n}{c^3\Delta k^3}\,\omega^2. \tag{3.8}$$

1D and 2D LDOS and DOS

In the example in Sec. 3.1.3, also the 1D and 2D (L)DOS are discussed. In homogeneous media, they can be obtained similar to the 3D (L)DOS: in 1D one needs to consider the number of modes along a line: $M_\mathrm{1D}(k_\mathrm{g}) = 4k_\mathrm{g}/\Delta k \rightarrow \varrho^0_\mathrm{1D}(\omega) = 4n/c\Delta k$ and $\rho^0_\mathrm{1D}(\omega) = 4/nc\Delta k$. Consequently, the resulting 1D DOS and LDOS are independent of ω.

In 2D, the modes within a circle need to be considered: $M_\mathrm{2D}(k_\mathrm{g}) = 2\pi k_\mathrm{g}^2/\Delta k^2 \rightarrow \varrho^0_\mathrm{2D}(\omega) = 4\pi n^2\omega/c^2\Delta k^2$ and $\rho^0_\mathrm{2D}(\omega) = 4\pi\omega/c^2\Delta k^2$. Thus the 2D (L)DOS increases linearly with ω.

Quasi-3D calculations (Bragg stack)

For comparison with the quasi-3D (L)DOS calculations of the Bragg stack, the corresponding quasi-3D (L)DOS in a homogeneous medium needs to be computed using the same conversion: from the modes in the 2D $\boldsymbol{k}$-space, the 3D (L)DOS is obtained by weighting each mode with its individual $2\pi\tilde{k}_y = a\,|\boldsymbol{k}|\sin\varphi_k$, where φ_k denotes the internal angle as depicted in Fig. 2.1 (b). Due to the linear dispersion relation $\omega \propto |\boldsymbol{k}|$, the homogeneous-medium modes within a certain frequency interval have equal magnitute $k = |\boldsymbol{k}|$ and lie on a circle in the 2D xy-plane, uniformly distributed with respect to θ_k. Consequently, the average weight of these equivalent modes is given by

$$\frac{1}{\pi/2}\int_{0^\circ}^{90^\circ} a\,k\sin\varphi_k\,d\varphi_k = \frac{2a}{\pi}k = \frac{2an}{\pi c}\omega. \tag{3.9}$$

Accordingly, the theoretical quasi-3D DOS is obtained as the product of the 2D DOS from above and this average weighting factor:[3]

$$\varrho^0_{\mathrm{q3D}}(\omega) = \frac{\pi n^2\omega}{c^2\Delta k^2} \times \frac{2an}{\pi c}\omega = \frac{2an^3}{c^3\Delta k^2}\,\omega^2 \tag{3.10}$$

The corresponding LDOS $\rho^0_{\mathrm{q3D}}(\omega)$ can again be obtained by dividing the DOS $\varrho^0_{\mathrm{q3D}}(\omega)$ by n^2, thus

$$\rho^0_{\mathrm{q3D}}(\omega) = \frac{2an}{c^3\Delta k^2}\,\omega^2. \tag{3.11}$$

Conversion of the (L)DOS to another denominator

Note that the (L)DOS is typically stated as the (L)DOS per normalized frequency $\tilde{\omega} = \omega a/2\pi c$, not per ω as in the derivations above. Accordingly, the LDOS is commonly plotted versus $\tilde{\omega}$, see for example Fig. 3.2. When converting the (L)DOS from ω to $\tilde{\omega}$ or other quantities like ν or λ, not only the ω in the equation needs to replaced, but also the corresponding differential needs to be considered. For instance, the quasi-3D DOS of the Bragg stack per $\tilde{\omega}$ is thus given by

$$\begin{aligned}\varrho^0_{\mathrm{q3D},\tilde{\omega}}(\tilde{\omega}) &= \frac{dM}{d\tilde{\omega}} = \frac{dM}{d\omega} \times \frac{d\omega}{d\tilde{\omega}} \\ &= \varrho^0_{\mathrm{q3D}}(\omega = 2\pi c\,\tilde{\omega}/a) \times \frac{2\pi c}{a} = \frac{16\pi^3 n^3}{a^2\Delta k^2}\,\tilde{\omega}^2.\end{aligned} \tag{3.12}$$

When in this equation also the $\boldsymbol{k}$-grid spacing Δk is written in normalized units ($\Delta\tilde{k} = \Delta k\,a/2\pi$), it becomes visible that this DOS is independent of the unit cell size a due to weighting with $\tilde{k}_y$ instead of k_y (see Eq. (3.3)):

$$\varrho^0_{\mathrm{q3D},0,\tilde{\omega}}(\tilde{\omega}) = \frac{4\pi n^3}{\Delta\tilde{k}^2}\,\tilde{\omega}^2. \tag{3.13}$$

[3] Here, the 2D LDOS was divided by 4 since in the LDOS calculations for the Bragg stack only one quadrant of the xy-plane was sampled for symmetry reasons.

Frequency-binning of the homogeneous-medium (L)DOS

To compare the homogeneous-medium (L)DOS to the "binned" LDOS of the photonic crystal from histogramming, the theoretical (L)DOS needs to be binned as well to obtain accurate results. Due to the non-linear dependence on ω, the 3D (L)DOS needs to be integrated within the corresponding frequency bins. As an example, the binned theoretical 3D LDOS for the opal calculations (see Eq. (3.8)) is thus given by

$$\hat{\rho}^0(\omega) = \int_{\omega-\Delta\omega/2}^{\omega+\Delta\omega/2} \rho^0(\omega)\, d\omega = \frac{8\pi n\, \Delta\omega}{c^3 \Delta k^3} \left(\omega^2 + \frac{\Delta\omega^2}{12} \right). \tag{3.14}$$

The 1D and 2D (L)DOS, however, can simply be multiplied with $\Delta\omega$ for binning due to the non-quadratic dependence on ω.

3.1.3 Example: 1D, 2D, and 3D (L)DOS of Bragg stack

To promote the understanding of the eigenmode distribution in a Bragg stack, the one-, two-, and three-dimensional LDOS and DOS are shown in Fig. 3.2. As an example, a Bragg stack with refractive indices $n_{\mathrm{lo}} = 1.5$, $n_{\mathrm{hi}} = 2$ was used corresponding to the investigated PLSC structure. Although the 1D and 2D (L)DOS have no physical meaning with regard to Fermi's golden rule, they help to understand the resulting 3D LDOS that determines an emitter's transition rates.

For the 1D LDOS, $\boldsymbol{k}$-space was sampled only on the k_x-axis (in on-axis direction).[4] The 2D LDOS was obtained as in Eq. (3.3), but without the weighting factor $2\pi\tilde{k}_{j,y}$. The DOS in homogenous media were calculated as explained above, using the Bragg stack's volume-averaged effective refractive index

$$n_{\mathrm{eff}} = \int_{\mathrm{WSC}} n(\boldsymbol{r})\rho(\boldsymbol{r},\omega) d\boldsymbol{r} = \frac{2 n_{\mathrm{lo}} n_{\mathrm{hi}}}{n_{\mathrm{lo}} + n_{\mathrm{hi}}} = 1.714\,. \tag{3.15}$$

In 1D, the LDOS in homogeneous media is constant with respect to ω, Similar, the LDOS and DOS of the Bragg stack are constant apart from the band gap: within the band gap ($0.265 < \omega a/2\pi c < 0.318$) no modes exist at all, thus both LDOS and DOS drop to zero. At the band edges, however, the DOS is strongly enhanced: the singularity at the edge arises from the flat bands from the dispersion relation, see Fig. 1.2 (c). The LDOS is enhanced at the lower-frequency band edge inside the high-refractive-index material and at the upper-frequency band edge inside the low-refractive-index material. This distribution is a result of the spatial distribution of the electromagnetic fields of the "slow light" modes at the band edges: it is well known that modes at the lower band edge concentrate in the n_{hi}

[4] In contrast to the other Bragg stack calculations, an increased $\boldsymbol{k}$-space resolution of $\Delta k = 10^{-5}\, 2\pi/a$ was used to obtain satisfactory accuracy of the 1D LDOS.

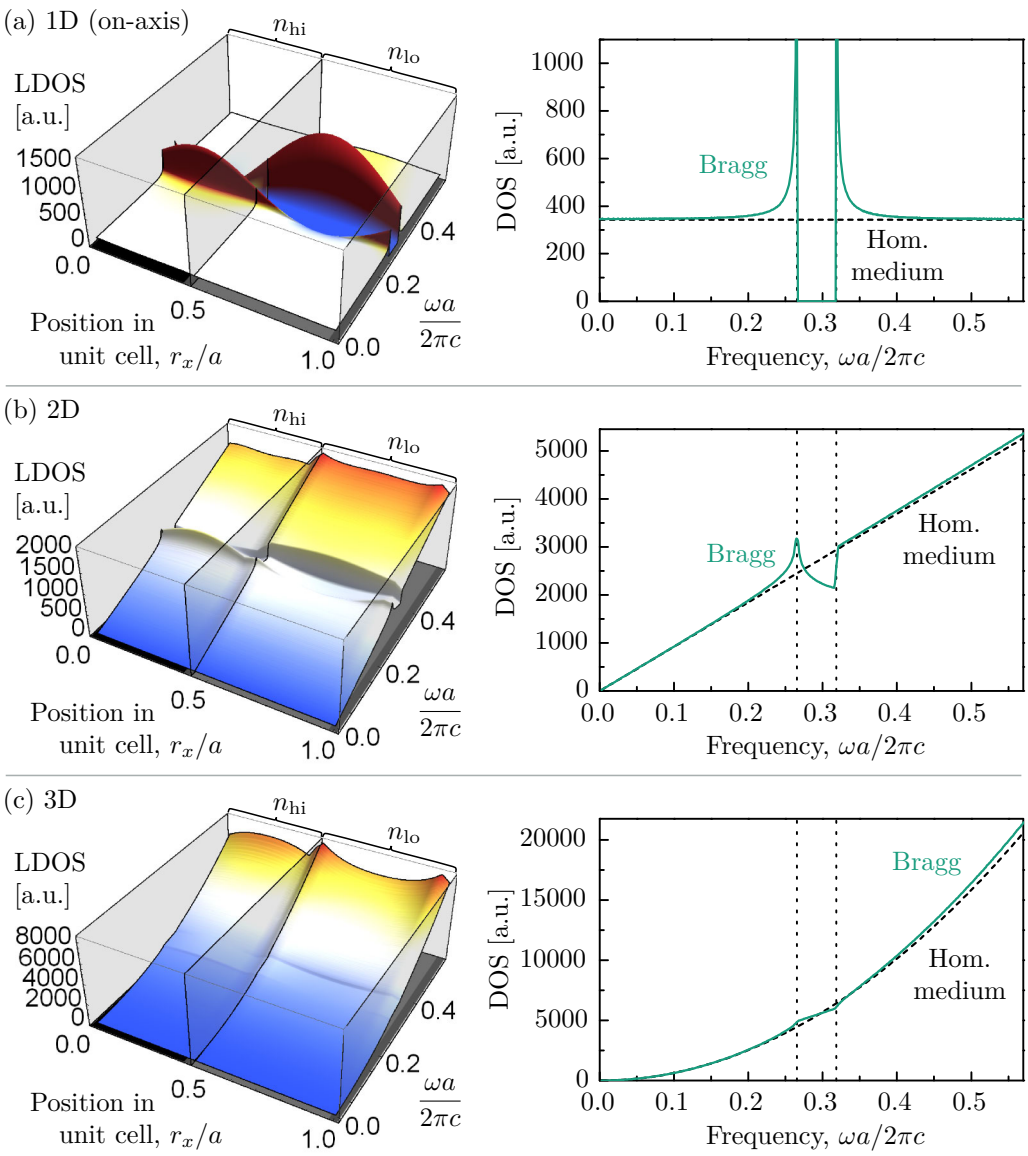

Figure 3.2: The 1D, 2D, and 3D LDOS and DOS of the Bragg stack help to understand the distribution of eigenmodes. Though, only the 3D LDOS has physical meaning with regard to Fermi's golden rule. (a) The 1D (L)DOS in on-axis direction drops to zero within the band gap due to the absence of modes. The enhancement at the band edges arises from the band flattening and occurs differently in the high- and low-refractive-index material, according to the field concentration of the modes near the lower and upper band edge. In (b) 2D and (c) 3D, the influence of the band gap vanishes as many off-axis modes contribute to the (L)DOS. Apart from the band gap, the DOS in 1D, 2D, and 3D agrees well with the DOS of homogeneous media with the Bragg stack's effective refractive index.

regions (*dielectric modes*) while the ones above the band gap have a larger fraction of their energy in the n_{lo} regions (*air modes*) [66].

As in theory, the 2D (L)DOS of the Bragg stack increases linearly with ω apart from the band edges. The influence of the band gap, however, strongly decreases: along the off-axis directions, numerous modes exist with frequencies within the band gap that contribute to the (L)DOS in the same way as the on-axis modes. As a result, the (L)DOS is reduced only slightly. The spatial distribution of the LDOS at the band edges corresponds to the 1D on-axis LDOS that, however, is strongly attenuated. Inside the gap, more modes exist at the lower- than at the upper-frequency band edge. This asymmetry arises from the shift of the band gap to higher frequencies for wave vectors tilting from on-axis to off-axis directions, which reduces the number of modes with frequencies near the upper-frequency band edge.

In 3D, both DOS and LDOS of the Bragg stack feature the quadratic dependence on ω as expected from theory. The band gap vanishes even more than in 2D, as there are much more off-axis modes, which do not experience any band gap, than on-axis modes. In the calculation these off-axis modes are counted with much larger weights $2\pi\tilde{k}_y$. For (fluorescent) emission, it is the 3D LDOS that is the relevant quantity. For emitters in the low-refractive-index layers, results are discussed in detail in Sec. 5.1.1.

3.1.4 Fractional LDOS

For the change in emission rates according to Fermi's golden rule, the LDOS of *all* eigenmodes of the photonic crystal is relevant, as the emitter will emit in all those modes. Only some of these modes, however, are able to escape from the photonic crystal and merely few modes are typically detected in common setups for photoluminescence measurements.

To model the light guiding efficiency, i.e. the fraction of emitted light that is guided inside the photonic structure, or to theoretically calculate the results to expect from PL measurements, a subset $F_{b,\omega}$ of all modes needs to be considered that satisfies certain conditions, as explained below. Accordingly, a *fractional* LDOS[5] (FLDOS) $\hat{\rho}_{\mathrm{f}}^{\mathrm{PC}}$ is defined by restricting the LDOS analysis from Eq. (3.1) to $F_{b,\omega} \subset K_{b,\omega}$:

$$\hat{\rho}_{\mathrm{f}}^{\mathrm{PC}}(\boldsymbol{r},\omega) = \sum_{b} \sum_{\boldsymbol{k}_j \in F_{b,\omega}} |\boldsymbol{E}_{b,\boldsymbol{k}_j}(\boldsymbol{r})|^2, \tag{3.16}$$

and analogous for the quasi-3D LDOS from Eq. (3.3).

In the following, I discuss the calculation of $\hat{\rho}_{\mathrm{f}}^{\mathrm{PC}}$ for the two cases mentioned above that are relevant in the context of this work: the light guiding efficiency and

[5] I use the term "fractional" LDOS (FLDOS) as introduced in Ref. 72 and used in Refs. 127, 128. With the same meaning, also other terms like the "reduced" DOS [103] are found in literature.

the theoretical angular resolved surface PL. The concept of the FLDOS presented here and the combination with the emitter model in Sec. 3.2.3, however, can be used similarly for other cases.

Light guiding efficiency

Most relevant for the LSC application is the fraction of the emitted light that is trapped in the concentrator as it is not able to couple out. In photonic crystals the out-coupling depends on the eigenmode's wave vector component $\boldsymbol{k}_{\parallel}$ parallel to the surface of interest, as discussed in Sec. 2.1.2. The subset of eigenmodes that are not able to escape from the photonic crystal is thus given by

$$F_{b,\omega} = \left\{ \boldsymbol{k} \in K_{b,\omega} \;\middle|\; |\boldsymbol{k}_{\parallel}| > \omega_{b,\boldsymbol{k}}\, n_{\mathrm{out}}/c \right\}. \tag{3.17}$$

As for (P)LSCs the surrounding medium is typically air, $n_{\mathrm{out}} = 1$ was used in the calculations. The surface-parallel wave vector $\boldsymbol{k}_{\parallel}$ can be calculated by the projection of $\boldsymbol{k}$ on the considered surface specified by its normal $\boldsymbol{n}$ according to

$$\boldsymbol{k}_{\parallel} = \boldsymbol{k} - \frac{\boldsymbol{k}\cdot\boldsymbol{n}}{\boldsymbol{n}\cdot\boldsymbol{n}}\,\boldsymbol{n}. \tag{3.18}$$

The light guiding efficiency (LGE) σ^{PC} in a photonic crystal is consequently defined as the ratio of the FLDOS of these guided modes to the LDOS of all emitted modes:

$$\sigma^{\mathrm{PC}}(\boldsymbol{r},\omega) = \frac{\hat{\rho}_{\mathrm{f}}^{\mathrm{PC}}(\boldsymbol{r},\omega)}{\hat{\rho}^{\mathrm{PC}}(\boldsymbol{r},\omega)} \tag{3.19}$$

The LGE is thus a local quantity in the same way as the LDOS and the FLDOS, i.e. it depends on the location of the emitter in the WSC. Note, that the LGE is always referred to a certain surface of out-coupling that needs to be specified. In Sec. 5.1.3 results for the LGE of the opal and Bragg stack are presented.

For emission in a homogeneous medium with refractive index n_{in} the LGE σ^0 is determined by TIR. It is the fraction not lost in the escape cone, thus

$$\sigma^0 = \sqrt{1 - \left(\frac{n_{\mathrm{out}}}{n_{\mathrm{in}}}\right)^2}, \tag{3.20}$$

which is typically 74.5% in conventional LSCs ($n_{\mathrm{in}} = 1.5$, $n_{\mathrm{out}} = 1$).

Angular resolved surface PL

To compare theory and experiment of the emission in photonic crystals, the PL escaping from a sample's surface was measured as a function of the detection angle, as described in Sec. 4.3.3. To obtain the corresponding spectra from theory, the

FLDOS was calculated according to the measurement setup and used as an input to the modeling of the detected emission spectrum, as presented in Sec. 3.2.3.

Therefore, the FLDOS was obtained by selecting the modes, that lie within a detection cone with half-angle θ_d that is tilted by the detection angle ϕ_d with respect to the surface normal, as illustrated in Fig. 3.3. First, to escape at all from the photonic crystal at the surface, the criterion $|\boldsymbol{k}_\parallel| > \omega\, n_\mathrm{out}/c$ needs to be satisfied.

Second, the wave vector of the out-coupled light $\boldsymbol{k}_\mathrm{out}$, as given by Eq. (2.10) and (2.11), needs to lie within the detection cone. This can be checked by comparing the cone's half-angle θ_d with the angle included between $\boldsymbol{k}_\mathrm{out}$ and the direction vector $\boldsymbol{d}$ of the cone using their dot product via

$$\sphericalangle(\boldsymbol{k}_\mathrm{out}, \boldsymbol{d}) = \cos^{-1}\left(\frac{\boldsymbol{k}_\mathrm{out}\cdot\boldsymbol{d}}{|\boldsymbol{k}_\mathrm{out}| \times |\boldsymbol{d}|}\right) \leq \theta_\mathrm{d}. \tag{3.21}$$

The subset of modes fulfilling these conditions, contributes to the FLDOS for a given detection angle ϕ_d. This evaluation, however, is only applicable for full-3D calculations, as done for the opal.

For the quasi-3D approach of the Bragg stack calculations, the FLDOS calculation needs to consider the three-dimensionality of the detection cone. To obtain

(a) Detection cone in 2D plane (b) Evaluation scheme for quasi-3D FLDOS

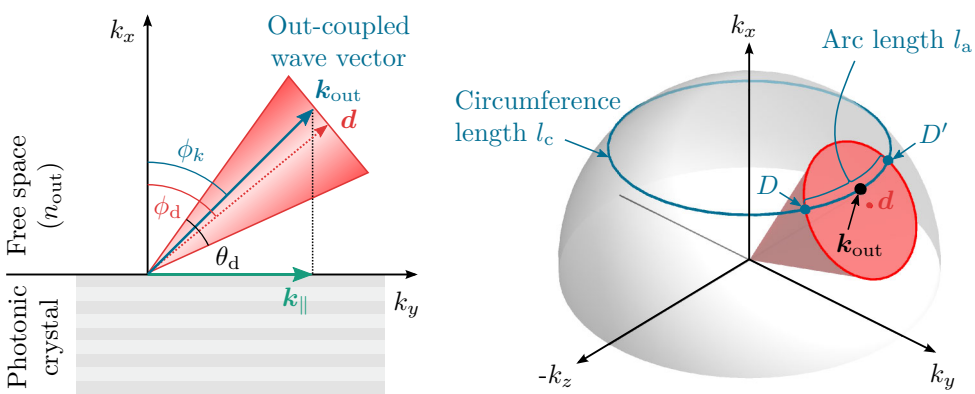

Figure 3.3: To calculate theoretical results for the angular resolved PL measurements, the FLDOS were calculated for the modes within the corresponding detection cones. For the quasi-3D evaluation of the Bragg stack, first all modes of the 2D xy-plane were selected that are able to couple out and lie inside the cone, as shown in (a). As illustrated in (b), these modes contribute to the FLDOS according to the ratio of the arc length l_a and the circumference length l_c, which gives the detectable fraction of the symmetric modes along the circumference. In both (a) and (b), a large half-angle θ_d of the detection cone was chosen for illustration purposes. In experiments and calculations, it was $\theta_\mathrm{d} = 0.6°$.

the appropriate quasi-3D FLDOS, the out-coupled modes need to be selected, which lie within the detection cone in the xy-plane, see Fig. 3.3 (a). These modes can be found by simply checking

$$\phi_\mathrm{d} - \theta_\mathrm{d} < \phi_k < \phi_\mathrm{d} + \theta_\mathrm{d}, \tag{3.22}$$

where $\phi_k = \sin^{-1}(|\boldsymbol{k}_\parallel|/|\boldsymbol{k}_\mathrm{out}|)$ is the angle of $\boldsymbol{k}_\mathrm{out}$ with respect to the surface normal. According to the experiments, light escaping from the surface parallel to yz-plane (plane with surface normal in on-axis direction) is considered as illustrated in Fig. 3.3 (a). Given a selected $\boldsymbol{k}_\mathrm{out}$ in the xy-plane within the detection cone, not all of the symmetric $\boldsymbol{k}$ along the circumference are being detected, only those that lie in the 3D cone (see Fig. 3.3 (b)). The detectable fraction of the symmetric modes is given by the fraction of the circumference that lies within the cone. Thus, the length of the arc was calculated that is defined by the intersection points D and D' of the circumference and the cone boundary.[6] The ratio of this arc length l_a and the total circumference length l_c gives the fraction of detectable symmetry modes. Accordingly, the quasi-3D FLDOS is determined by

$$\hat{\rho}^\mathrm{PC}_\mathrm{f,q3D}(\boldsymbol{r},\omega) = \sum_b \sum_{\boldsymbol{k}\in F_{b,\omega}} \frac{l_\mathrm{a}}{l_\mathrm{c}} \times 2\pi\tilde{k}_y \, |\boldsymbol{E}_{b,\boldsymbol{k}}(\boldsymbol{r})|^2, \tag{3.23}$$

where $F_{b,\omega}$ contains the selected modes according to Eq. (3.22).

To predict the detected spectra in PL measurements for conventional LSCs, the corresponding FLDOS was also calculated for undisturbed emission in a homogeneous medium with refractive index $n_\mathrm{in} = 1.5$. In this case, the angular FLDOS distribution does not depend on the frequency ω because at the interface light is classically refracted according to Snell's law due to the linear dispersion relation in homogeneous media. Corresponding to an arbitrary frequency, a finite set of $\boldsymbol{k}$-vectors on the xy-plane with same $|\boldsymbol{k}|$ was constructed, with uniform distribution of their internal angles representing the isotropy of emission.[7]

On this set of modes, the same selection procedure was performed as above for the Bragg stack's quasi-3D FLDOS, yielding the subset F. Due to the frequency-independence mentioned above, it is convenient to calculate the ratio of FLDOS and LDOS

$$\chi := \frac{\hat{\rho}^0_\mathrm{f}(\omega)}{\hat{\rho}^0(\omega)} \tag{3.24}$$

that holds for every ω. Accordingly, this ratio for the quasi-3D treatment here is

[6] Technically, the points of intersection were obtained from solving for the angles, by which the $\boldsymbol{k}_\mathrm{out}$-vector needs to be rotated around the x-axis to intersect with the edge of the detection cone, i.e. to find D so that the included angle between D and $\boldsymbol{d}$ is θ_d.

[7] Here, 90000 $\boldsymbol{k}$-vectors with internal angles from 0–90° were used (although only modes with angles up to the critical angles are able to escape).

given by

$$\chi = \frac{\sum_{\boldsymbol{k}\in F_{b,\omega}} (l_\mathrm{a}/l_\mathrm{c}) \times 2\pi\tilde{k}_y}{\sum_{\boldsymbol{k}\in F_{b,\omega}} 2\pi\tilde{k}_y}. \tag{3.25}$$

For other detection configurations less complex than the oblique detection cone considered here, simple analytical expressions can be found. For instance, the fraction of the LDOS detected in a cone normal to the surface is given by $\chi = 1 - \sqrt{1 - (\sin(\theta_\mathrm{d})\, n_\mathrm{out}/n_\mathrm{in})^2}$ from geometric reasoning. This expression yields the same result as Eq. (3.25) for the case of $\phi_\mathrm{d} = 0°$.

Note that only tiny fractions of all emitted modes are detected with the experimental setup used in this work (e.g. $\chi = 2.4 \times 10^{-5}$ for $\phi_\mathrm{d} = 0°$), due to the small half-angle $\theta_\mathrm{d} = 0.6°$ of the detection cone. By varying ϕ_d, this characterization method therefore allows for accurately probing the photonic crystal's effect on emission and compare it to theoretical calculations, which can be obtained by combining the FLDOS with the emitter model as described in Sec. 3.2.3. Results of both theory and experiments and presented and discussed in Sec. 5.1.4.

Summary of Section 3.1

In this section, I showed how the LDOS of a photonic crystal can be obtained from its eigenmodes, and proposed the very efficient quasi-3D approach for 1D-periodic structures like the Bragg stack. The LDOS example demonstrated that an incomplete band gap typically does not heavily alter the (3D) LDOS. Such band gaps can, however, strongly influence the FLDOS that was derived above in terms of the light guiding efficiency and the detected emission in PL measurements. By deriving the appropriate theoretical LDOS and FLDOS in homogenous media, the *changes* in LDOS and FLDOS induced by a photonic crystal were determined, which serve as inputs to the emitter model presented in the following.

3.2 Model of fluorescent emission

To calculate the influence of the photonic crystal on the emission of a fluorescent dye, I propose in the following a rate equation model for such emitters. It combines the electronics transitions and the changes of the LDOS to quantitatively calculate the experimentally observable modifications of emission in terms of emission spectrum, photoluminescence quantum yield and fluorescence lifetime.[8]

3.2.1 Emitter model

Fluorescent dye typically feature rather complex energetic structures as discussed in Sec. 2.2.4. To study their emission inside photonic crystals I propose a model

[8] Parts of this section are adopted from my publication, Ref. 129.

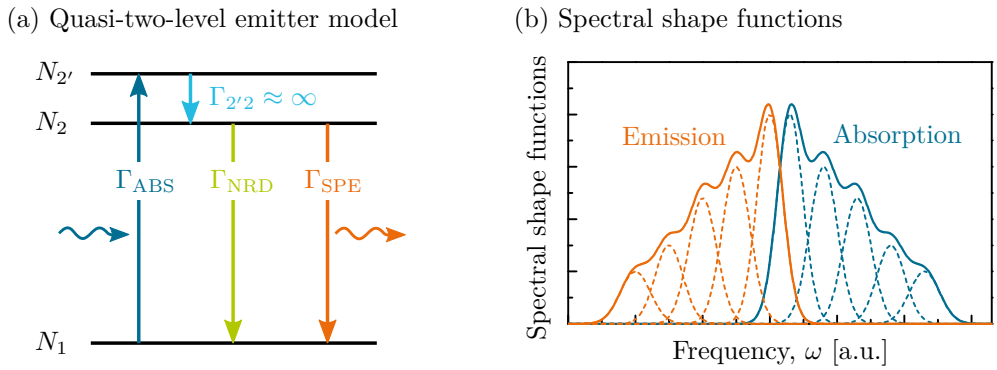

Figure 3.4: To study the influence of a photonic crystal on the emission of a fluorescent dye, its electronic structure was modeled with a quasi-two-level rate-equation model, as shown in (a). As indicated in (b) for a fictive dye, the numerous individual transition from and to vibrational and rotational energy levels (dashed curves) are aggregated in "spectral shape functions" (solid curves) to account for the spectral widths of absorption and emission. The linewidths of the individual transitions are typically much smaller than illustrated (see Appendix A.4).

with a reduced electronic structure, as shown in Fig. 3.4 (a). This quasi-two-level model consist of a ground state (with population N_1) and an excited state, which is split up in state 2 and state $2'$ to account for the Stokes shift. Due to quasi-instantaneous vibrational relaxation (transition rate $\Gamma_{2'2} \approx \infty$), however, all excited emitters are assumed to be in state 2, thus $N_{2'} = 0$.

To account for the numerous vibrational levels and thus the spectral widths of absorption and emission, "spectral shape functions" were employed (comparable to line shape functions used for single atomic transitions).[9] These functions aggregate all transitions to the different energy levels of the ground state (for emission) and of the excited state (for absorption), as illustrated in Fig. 3.4 (b).

Transition probability of emission

Following Einstein's treatment of transition rates (see Sec. 2.2.1), the rate of spontaneous emission Γ_{SPE} is the product of the population N_2 and the transition probability P_{SPE}. Using the spectral shape function $g^0(\omega)$ of emission, this transition probability is given by

$$P^0_{\mathrm{SPE}} = \int \mathcal{A}^0_{21} g^0(\omega) d\omega, \tag{3.26}$$

[9] I use the term "spectral shape function" to avoid confusion with the classical understanding of line shape functions (for example from the line broadening of discrete atomic transitions). Technically, the spectral shape function can be implemented analogously since it describes just the sum of numerous different transitions.

with the corresponding Einstein coefficient $\mathcal{A}_{21}^0$. The spectral shape function is normalized via $\int g^0(\omega)d\omega = 1$ analogous to a classical line shape function (see Sec. 2.2.1). The superscript "0" denotes undisturbed emission in a homogeneous medium as a reference case. The function $g^0(\omega)$ can be obtained from appropriate PL measurements,[10] using a confocal setup, for example, to minimize reabsorption artifacts. For that purpose, the PL spectrum needs to be obtained as "*photons* per second (per area per frequency interval)" corresponding to the units of the transition rates. In this work, this was achieved by spectral calibration of the used measurement setup.

Inside a photonic crystal, the spontaneous emission probability is modified via the LDOS ratio $\gamma(\boldsymbol{r}, \omega)$ (Eq. (3.5)) according to Fermi's golden rule (Eq. (2.22)):

$$P_{\mathrm{SPE}}^{\mathrm{PC}}(\boldsymbol{r}) = \int \mathcal{A}_{21}^0 g^0(\omega)\gamma(\boldsymbol{r}, \omega)d\omega = \psi(\boldsymbol{r})P_{\mathrm{SPE}}^0, \tag{3.27}$$

where the emission probability enhancement factor

$$\psi(\boldsymbol{r}) = \int g^0(\omega)\gamma(\boldsymbol{r}, \omega)d\omega \tag{3.28}$$

is introduced that describes the absolute change in the transition probability.

The spectral shape function

$$g^{\mathrm{PC}}(\boldsymbol{r}, \omega) := \frac{\gamma(\boldsymbol{r}, \omega)}{\psi(\boldsymbol{r})} g^0(\omega) \tag{3.29}$$

describes the spectral distribution of the emitted light and is defined so that $\int g^{\mathrm{PC}}(\boldsymbol{r}, \omega)d\omega = 1$. Note that inside a photonic crystal the emission probability and the emitted spectrum depends on the emitter location $\boldsymbol{r}$ as a result of the *local* density of states.

In Eq. (3.27) the rather small effects of the photonic crystal on natural broadening and Lamb shift of each individual transition within the emission spectrum are neglected as the total spectral shape is typically much broader than these effects (see Appendix A.4).

The spontaneous emission rate $\Gamma_{\mathrm{SPE}}^{\mathrm{PC}}(\boldsymbol{r}) = N_2^{\mathrm{PC}} P_{\mathrm{SPE}}^{\mathrm{PC}}(\boldsymbol{r})$ is a measure of the intensity of emission ("number of photons per second"). It includes the number of excited emitters N_2^{PC} that might be different from N_2^0. The steady-state population of the electronic states, however, depends also on the rate of absorption, as discussed in the following.

Influence of absorption on transition rates

According to Sec. 2.2.1, the absorption rate is given by $\Gamma_{\mathrm{ABS}} = N_1 \mathcal{B}_{12'} u(\omega_{12'})$.[11] While the corresponding Einstein coefficient $\mathcal{B}_{12'}$ does not change due to LDOS

[10] For conversion to wavelengths: $g_\lambda(\lambda) = g_\omega(\omega(\lambda)) \times d\omega/d\lambda = g_\omega(\omega(\lambda)) \times |-2\pi c/\lambda^2|$

[11] In fact, accounting for the typically broad absorption spectra as well as for broad-band excitation: $\Gamma_{\mathrm{ABS}} = N_1 \int \mathcal{B}_{12'}(\omega)u(\omega)d\omega$

effects, the excitation through the spectral energy density $u(\omega)$ depends on many factors: where does the light come from (from outside a finite photonic crystal, for example) and how is the electromagnetic field distribution within the photonic crystal as a function of $\boldsymbol{r}$? The modified local spectral energy density $u^{\mathrm{PC}}(\omega, \boldsymbol{r})$ in photonic crystals could be calculated only for a specific geometry, for example using numerical methods like finite-difference time-domain [130, 131], rigorous coupled wave analysis [132] or the scattering matrix formalism [133].

Assuming such calculations yield a local absorption probability enhancement of $\beta(\boldsymbol{r}) = u^{\mathrm{PC}}(\omega_{12'}, \boldsymbol{r})/u^0(\omega_{12'})$,[12] we can express the transition rates of an emitter inside a photonic crystal as

$$\Gamma^{\mathrm{PC}}_{\mathrm{ABS}} = \beta(\boldsymbol{r})(N_1^{\mathrm{PC}}/N_1^0)\,\Gamma^0_{\mathrm{ABS}}, \tag{3.30}$$

$$\Gamma^{\mathrm{PC}}_{\mathrm{SPE}} = \psi(\boldsymbol{r})(N_2^{\mathrm{PC}}/N_2^0)\,\Gamma^0_{\mathrm{SPE}}, \tag{3.31}$$

$$\Gamma^{\mathrm{PC}}_{\mathrm{NRD}} = (N_2^{\mathrm{PC}}/N_2^0)\,\Gamma^0_{\mathrm{NRD}}, \tag{3.32}$$

with the non-radiative decay rate $\Gamma_{\mathrm{NRD}} = N_2 P_{\mathrm{NRD}}$, whose transition probability P_{NRD} is not influenced by the photon LDOS as it represents electronic transitions without emission of a photon (that would require a photon state). Assuming a relatively low spectral energy density (weak-coupling regime), stimulated emission processes are neglected.

When comparing the steady state rates

$$\Gamma^0_{\mathrm{ABS}} = \Gamma^0_{\mathrm{SPE}} + \Gamma^0_{\mathrm{NRD}}, \tag{3.33}$$

$$\Gamma^{\mathrm{PC}}_{\mathrm{ABS}} = \Gamma^{\mathrm{PC}}_{\mathrm{SPE}} + \Gamma^{\mathrm{PC}}_{\mathrm{NRD}}$$

$$\Leftrightarrow \beta(\boldsymbol{r})\frac{N_1^{\mathrm{PC}}}{N_1^0}\Gamma^0_{\mathrm{ABS}} = \frac{N_2^{\mathrm{PC}}}{N_2^0}(\psi(\boldsymbol{r})\Gamma^0_{\mathrm{SPE}} + \Gamma^0_{\mathrm{NRD}}), \tag{3.34}$$

we find the change of the ground and excited state populations:

$$\frac{N_1^{\mathrm{PC}}}{N_1^0} = \frac{1}{\xi(\boldsymbol{r})(1 - N_1^0/N_{\mathrm{tot}}) + N_1^0/N_{\mathrm{tot}}} \approx 1, \tag{3.35}$$

$$\frac{N_2^{\mathrm{PC}}}{N_2^0} = \frac{\xi(\boldsymbol{r})}{1 + (\xi(\boldsymbol{r}) - 1)\,N_2^0/N_{\mathrm{tot}}} \approx \xi(\boldsymbol{r}) \tag{3.36}$$

$$\text{with } \xi(\boldsymbol{r}) = \frac{\beta(\boldsymbol{r})}{1 + \Phi^0(\psi(\boldsymbol{r}) - 1)}, \tag{3.37}$$

with PLQY $\Phi^0 = \Gamma^0_{\mathrm{SPE}}/\Gamma^0_{\mathrm{ABS}}$ and $N_{\mathrm{tot}} = N_1 + N_2$. The approximations in Eqs. (3.35) and (3.36) correspond to the weak-coupling regime, where $N_1^0 \gg N_2^0$ [109]. In fact, the approximations are equal to the zeroth-order Taylor expansion around $N_1^0 = N_{\mathrm{tot}}$ (Eq. (3.35)) and $N_2^0 = 0$ (Eq. (3.36)).

[12] With broad-band: $\beta(\boldsymbol{r}) = \int \mathcal{B}_{12'}(\omega) u^{\mathrm{PC}}(\omega, \boldsymbol{r}) d\omega / \int \mathcal{B}_{12'}(\omega) u^0(\omega) d\omega$

These results for the populations yield the change in transition rates due to the photonic crystal

$$\Gamma^{\mathrm{PC}}_{\mathrm{ABS}}/\Gamma^{0}_{\mathrm{ABS}} \approx \beta(\boldsymbol{r}), \tag{3.38}$$

$$\Gamma^{\mathrm{PC}}_{\mathrm{SPE}}/\Gamma^{0}_{\mathrm{SPE}} \approx \frac{\psi(\boldsymbol{r})\beta(\boldsymbol{r})}{1+\Phi^{0}(\psi(\boldsymbol{r})-1)}, \tag{3.39}$$

$$\Gamma^{\mathrm{PC}}_{\mathrm{NRD}}/\Gamma^{0}_{\mathrm{NRD}} \approx \frac{\beta(\boldsymbol{r})}{1+\Phi^{0}(\psi(\boldsymbol{r})-1)}. \tag{3.40}$$

Note that all three transition rates and also the populations in a photonic crystal are functions of the emitter position $\boldsymbol{r}$, although not explicitly denoted.

Hence, the absolute intensity of emission depends on the enhancement of the probabilities of absorption $\beta(\boldsymbol{r})$ and emission $\psi(\boldsymbol{r})$ as well as on the quantum yield Φ^0 of the emitter. In the absence of non-radiative decay channels ($\Phi^0 = 1$), the rates of both absorption and emission would be enhanced by the same factor $\beta(\boldsymbol{r})$. This factor $\beta(\boldsymbol{r})$ depends on the specific geometry, the source of excitation and needs to be obtained separately as mentioned above. Independent of the absorption rate, however, one can calculate how many of the absorbed photons are emitted, i.e. the PLQY inside the photonic crystal Φ^{PC}, as shown in the following.

3.2.2 Emission spectrum, PLQY and fluorescence lifetime

Emission spectrum

Spontaneous emission from emitters with broad emission spectra may be spectrally redistributed in a photonic crystal, as excited emitter can decay to different ground state levels: emission at frequencies with a relatively low LDOS ratio is suppressed and instead light is emitted at frequencies with higher LDOS ratios. The spectral distribution of the emitted light is given by the spectral shape function. Based on the undisturbed emission spectrum $g^0(\omega)$ as an input parameter, the emission spectrum in the photonic crystal $g^{\mathrm{PC}}(\boldsymbol{r},\omega)$ was calculated for the Bragg stack and the opal, as presented in Sec. 5.1.2.

In the photonic crystal, the emission spectrum depends on the exact emitter position. To model a particular spatial distribution of emitters, the emission spectrum for each emitter positions needs to be calculated individually. In general it is not correct to first average the LDOS over all relevant $\boldsymbol{r}$, and to subsequently use this averaged LDOS for further calculations. Due to differences in local absorptance ($\beta(\boldsymbol{r})$) and PLQY, the amount of emission, i.e. the rate $\Gamma^{\mathrm{PC}}_{\mathrm{SPE}}(\boldsymbol{r})$ and thus the contribution to the ensemble's emission spectrum varies with position $\boldsymbol{r}$. Accordingly, the emitted spectrum $g^{\mathrm{PC}}_{\mathrm{tot}}(\omega)$ from multiple emitters at different $\boldsymbol{r}_j$

is given by the sum

$$g_{\mathrm{tot}}^{\mathrm{PC}}(\omega) = \varkappa \sum_j \beta(\boldsymbol{r}_j) \frac{\Phi^{\mathrm{PC}}(\boldsymbol{r}_j)}{\Phi^0} g^{\mathrm{PC}}(\boldsymbol{r}_j, \omega) \tag{3.41}$$

where the normalization factor $\varkappa$ ensures $\int g_{\mathrm{tot}}^{\mathrm{PC}}(\omega) d\omega = 1$, and $\Phi^{\mathrm{PC}}/\Phi^0$ denotes the change in PLQY of an emitter inside the photonic crystal as discussed in the following.

Photoluminescence quantum yield

As the transition rates of radiative and non-radiative decay are modified in the photonic crystal, also the PLQY changes. In general, we can write Eq. (2.27) for the steady state $\Gamma_{\mathrm{ABS}} = \Gamma_{\mathrm{SPE}} + \Gamma_{\mathrm{NRD}}$ as

$$\Phi = \frac{\Gamma_{\mathrm{SPE}}}{\Gamma_{\mathrm{ABS}}} = \frac{P_{\mathrm{SPE}}}{P_{\mathrm{SPE}} + P_{\mathrm{NRD}}}. \tag{3.42}$$

Applying this equation to the cases of a homogeneous medium and the photonic crystal, we find

$$\Phi^{\mathrm{PC}}(\boldsymbol{r}) = \frac{\psi(\boldsymbol{r}) P_{\mathrm{SPE}}^0}{\psi(\boldsymbol{r}) P_{\mathrm{SPE}}^0 + P_{\mathrm{NRD}}} = \frac{\Phi^0 \psi(\boldsymbol{r})}{1 + \Phi^0(\psi(\boldsymbol{r}) - 1)}. \tag{3.43}$$

When the undisturbed PLQY Φ^0 of a fluorescent species in homogeneous media is known, the modified quantum yield in a photonic crystal environment can be described solely by the emission probability enhancement factor $\psi(\boldsymbol{r})$, which is independent of the absorption process.

Note that the PLQY inside the photonic crystal depends on the emitter location $\boldsymbol{r}$. To calculate the PLQY $\Phi_{\mathrm{tot}}^{\mathrm{PC}}$ of a group of emitters, the individual $\Phi^{\mathrm{PC}}(\boldsymbol{r}_i)$ need to be averaged, weighted with the local absorption:

$$\Phi_{\mathrm{tot}}^{\mathrm{PC}} = \frac{\sum_j \Phi^{\mathrm{PC}}(\boldsymbol{r}_j)\, \beta(\boldsymbol{r}_j)}{\sum_j \beta(\boldsymbol{r}_j)}. \tag{3.44}$$

Furthermore, I want to mention that the PLQY is not only affected by the LDOS but also by the chemical environment of the emitter, for example due to quenching of the fluorescence (see e.g. [117, 134–138]). It is therefore necessary to determine Φ^0 under the same chemical conditions as in the photonic crystal (same host material for embedding).

Fluorescence lifetime

Due to the changes of the transition rates, also the fluorescence lifetime τ is different in photonic crystals. Using Eqs. (2.29) and (3.43), we can write

$$\tau = (P_{\mathrm{SPE}} + P_{\mathrm{NRD}})^{-1} = \Phi / P_{\mathrm{SPE}}. \tag{3.45}$$

Comparing the lifetime τ^{PC} inside a photonic crystal to the lifetime τ^0 in homogenous media, we find

$$\tau^{\mathrm{PC}}(\boldsymbol{r}) = \tau^0 \frac{1}{1 + \Phi^0(\psi(\boldsymbol{r}) - 1)}. \tag{3.46}$$

This means that the relative change in fluorescence lifetime depends only on the quantum yield Φ^0 and the emission probability enhancement factor $\psi(\boldsymbol{r})$, i.e. on the LDOS.

I want to emphasize the dependence on the quantum yield Φ^0: doing experiments with low quantum yield emitters will result in very small changes in lifetime, even if the photonic crystal provides a large LDOS effect. This can be one reason for the small changes in lifetime reported in previous studies [70, 71, 73], additional to small LDOS changes by the studied photonic crystals.

When studying multiple emitters, the observed decay kinetics arise from the sum of the individual decays of emitters at positions $\boldsymbol{r}_j$:

$$\Gamma^{\mathrm{PC}}_{\mathrm{tot}}(t) = \sum_j \Gamma^{\mathrm{PC}}_{\mathrm{SPE}}(\boldsymbol{r}_j)\, e^{-t/\tau^{\mathrm{PC}}(\boldsymbol{r}_j)} \approx \sum_j \frac{\psi(\boldsymbol{r}_j)\beta(\boldsymbol{r}_j)\Gamma^0_{\mathrm{SPE}}}{1 + \Phi^0(\psi(\boldsymbol{r}_j) - 1)}\, e^{-t/\tau^{\mathrm{PC}}(\boldsymbol{r}_j)} \tag{3.47}$$

Thus, the decay becomes non-single-exponential. To calculate the contribution of each emitter, i.e. the pre-exponential factors, local absorption needs to be considered.

3.2.3 Detected spectrum

In PL experiments, typically only a subset of all emitted modes is detected, depending on the specific measurements setup. To model the spectra obtained in such measurements, I introduce *fractional* transition rates and probabilities based on the fractional LDOS (FLDOS) of detectable modes presented in Sec. 3.1.4.

The fractional transition rate accounts only for those transitions, which emit modes that can be detected. Accordingly, in homogeneous media it is defined as

$$P^0_{\mathrm{SPE,f}} = \int \mathcal{A}^0_{21} g^0(\omega) \frac{\hat{\rho}^0_{\mathrm{f}}(\omega)}{\hat{\rho}^0(\omega)} d\omega = \chi P^0_{\mathrm{SPE}} \tag{3.48}$$

with the ratio χ of FLDOS and LDOS from Eq. (3.24), depending on the geometry of the measurement setup. For emission in homogeneous media, the spectral distribution of detected light $g^0_{\mathrm{f}}(\omega)$ is the same as for the emitted light $g^0(\omega)$ as χ is constant for all frequencies.

In photonic crystals, the fractional transition probability is given by

$$P^{\mathrm{PC}}_{\mathrm{SPE,f}}(\boldsymbol{r}) = \int \mathcal{A}^0_{21} g^0(\omega) \frac{\hat{\rho}^{\mathrm{PC}}_{\mathrm{f}}(\boldsymbol{r},\omega)}{\hat{\rho}^0(\boldsymbol{r},\omega)} d\omega = \chi\, \psi_{\mathrm{f}}(\boldsymbol{r}) P^0_{\mathrm{SPE}} \tag{3.49}$$

with

$$\psi_{\mathrm{f}}(\boldsymbol{r}) := \int g^0(\omega)\gamma_{\mathrm{f}}(\boldsymbol{r},\omega)d\omega \quad \text{and} \quad \gamma_{\mathrm{f}}(\boldsymbol{r},\omega) := \frac{\hat{\rho}_{\mathrm{f}}^{\mathrm{PC}}(\boldsymbol{r},\omega)}{\hat{\rho}_{\mathrm{f}}^{0}(\boldsymbol{r},\omega)}. \tag{3.50}$$

The shape of the detected spectrum from emission in a photonic crystal is thus

$$g_{\mathrm{f}}^{\mathrm{PC}}(\boldsymbol{r},\omega) = g^0(\omega)\frac{\gamma_{\mathrm{f}}(\boldsymbol{r},\omega)}{\psi_{\mathrm{f}}(\boldsymbol{r})}. \tag{3.51}$$

In contrast to the homogeneous medium case, this detected spectrum can differ very strongly from the spectral distribution of the totally emitted light $g^{\mathrm{PC}}(\boldsymbol{r},\omega)$, as it arises usually only from a small subset of all modes. Thus it can be more distorted in terms of suppressions due to band gaps and enhancements at band edges, when a band gap lies in the direction of detection. One can therefore not draw non-ambiguous conclusions about the emitted spectrum based on a measured spectrum that was obtained from only a narrow angular range. Furthermore, the detected spectrum depends on the exact measurement configurations: in the angular resolved surface PL measurements (see Sec. 4.3.3), for instance, $g_{\mathrm{f}}^{\mathrm{PC}}(\boldsymbol{r},\omega)$ typically varies with the detection angle ϕ_{d} due to the non-isotropic dispersion relation in photonic crystals.

The "intensity" of the detected signal ("number of photons per second") can be obtained from the corresponding fractional transition rates

$$\Gamma_{\mathrm{SPE,f}}^{0} = N_2^0 P_{\mathrm{SPE,f}}^{0} = \chi\,\Gamma_{\mathrm{SPE}}^{0}, \tag{3.52}$$

$$\Gamma_{\mathrm{SPE,f}}^{\mathrm{PC}}(\boldsymbol{r}) = N_2^{\mathrm{PC}} P_{\mathrm{SPE,f}}^{\mathrm{PC}}(\boldsymbol{r}) = \chi\,\psi_{\mathrm{f}}(\boldsymbol{r})\xi(\boldsymbol{r})\,\Gamma_{\mathrm{SPE}}^{0}. \tag{3.53}$$

Note that the fractional emission rate in the photonic crystal $\Gamma_{\mathrm{SPE,f}}^{\mathrm{PC}}(\boldsymbol{r})$ depends not only on the FLDOS (through $\psi_{\mathrm{f}}(\boldsymbol{r})$) but also on the LDOS via $\psi(\boldsymbol{r})$ in $\xi(\boldsymbol{r})$ as the population N_2^{PC} is determined by all transitions (not only the detected ones). Furthermore, the rates depend on the local absorption $\beta(\boldsymbol{r})$ in $\xi(\boldsymbol{r})$ that needs to be considered when multiple emitters at different positions are studied.

These fractional transition rates allow the comparison of the absolute values of the detected spectra, for example for different detection cone angles. The detected spectrum Π_{f} is given by the product of the fractional transition rate and the spectral shape function:

$$\Pi_{\mathrm{f}}^{0}(\omega) = \Gamma_{\mathrm{SPE,f}}^{0} \times g_{\mathrm{f}}^{0}(\omega), \tag{3.54}$$

$$\Pi_{\mathrm{f}}^{\mathrm{PC}}(\boldsymbol{r},\omega) = \Gamma_{\mathrm{SPE,f}}^{\mathrm{PC}}(\boldsymbol{r}) \times g_{\mathrm{f}}^{\mathrm{PC}}(\boldsymbol{r},\omega). \tag{3.55}$$

Accordingly, the expected results of angular resolved surface PL measurements were theoretically calculated, as presented in Sec. 5.1.4.

Table 3.1 summarizes the transition probabilities and rates as well as the spectral distributions (spectral shape functions) for both emitted and detected light as used in this work.

Table 3.1: Overview of the spontaneous emission transition probabilities and transition rates as well as the spectral distributions (spectral shape functions) for the totally emitted and the detected light, as used in the calculations.

	Transition probability	Spectral shape function	Transition rate ("intensity")
Emission in homogeneous medium	P^0_{SPE}	$g^0(\omega)$	Γ^0_{SPE}
Emission in photonic crystal	$P^{\mathrm{PC}}_{\mathrm{SPE}}(\boldsymbol{r}) = \psi(\boldsymbol{r}) P^0_{\mathrm{SPE}}$	$g^{\mathrm{PC}}(\boldsymbol{r},\omega) = g^0(\omega)\gamma(\boldsymbol{r},\omega)/\psi(\boldsymbol{r})$	$\Gamma^{\mathrm{PC}}_{\mathrm{SPE}}(\boldsymbol{r}) = \psi(\boldsymbol{r})\xi(\boldsymbol{r})\,\Gamma^0_{\mathrm{SPE}}$
Detected emission from homogeneous medium	$P^0_{\mathrm{SPE,f}} = \chi P^0_{\mathrm{SPE}}$	$g^0_{\mathrm{f}}(\omega) = g^0(\omega)$	$\Gamma^0_{\mathrm{SPE,f}} = \chi\,\Gamma^0_{\mathrm{SPE}}$
Detected emission from photonic crystal	$P^{\mathrm{PC}}_{\mathrm{SPE,f}}(\boldsymbol{r}) = \chi\,\psi_{\mathrm{f}}(\boldsymbol{r}) P^0_{\mathrm{SPE}}$	$g^{\mathrm{PC}}_{\mathrm{f}}(\boldsymbol{r},\omega) = g^0(\omega)\gamma_{\mathrm{f}}(\boldsymbol{r},\omega)/\psi_{\mathrm{f}}(\boldsymbol{r})$	$\Gamma^{\mathrm{PC}}_{\mathrm{SPE,f}}(\boldsymbol{r}) = \chi\,\psi_{\mathrm{f}}(\boldsymbol{r})\xi(\boldsymbol{r})\,\Gamma^0_{\mathrm{SPE}}$

Symbols

– LDOS ratio $\gamma(\boldsymbol{r},\omega) = \hat{\rho}^{\mathrm{PC}}(\boldsymbol{r},\omega)/\hat{\rho}^0(\boldsymbol{r},\omega)$, FLDOS ratio $\gamma_{\mathrm{f}}(\boldsymbol{r},\omega) = \hat{\rho}^{\mathrm{PC}}_{\mathrm{f}}(\boldsymbol{r},\omega)/\hat{\rho}^0_{\mathrm{f}}(\boldsymbol{r},\omega)$
– Fraction of detectable emission from homogeneous media $\chi = \hat{\rho}^0_{\mathrm{f}}(\boldsymbol{r},\omega)/\hat{\rho}^0(\boldsymbol{r},\omega)$, depending on detection setup geometry
– Emission probability enhancement factor $\psi(\boldsymbol{r}) = \int g^0(\omega)\gamma(\boldsymbol{r},\omega)d\omega$, for detected emission: $\psi_{\mathrm{f}}(\boldsymbol{r}) = \int g^0(\omega)\gamma_{\mathrm{f}}(\boldsymbol{r},\omega)d\omega$
– Excited-state population factor $\xi(\boldsymbol{r}) = \beta(\boldsymbol{r})/(1+\Phi^0(\psi(\boldsymbol{r})-1))$ with absorption probability enhancement factor $\beta(\boldsymbol{r})$

3.3 Propagation of light

In this section different modeling methods are presented that are related to the propagation of light in homogeneous and structured media with finite size. Besides the established transfer and scattering matrix methods, new theoretical models were developed to compute the optical properties of thick layers incoherently, to calculate the angular and spectral distribution of light escaping from samples with certain surface reflectivity, and to derive the angular distribution of light at the edges of an LSC.

3.3.1 Transfer and scattering matrix methods

The transfer and scattering matrix methods are well-known formalisms to calculate the optical properties of finite structures that consist of layers with certain thicknesses and (complex) refractive indices [133, 139–141]. While details can be found in literature, here I want to briefly illustrate the basic concepts.

Both matrix methods provide exact steady-state solutions to Maxwell's equations in layered media. Given incident light with certain angle of incidence from top and/or bottom as boundary conditions, the reflectance, transmittance and absorptance of a stack can be calculated. Furthermore, the local fields and thus the local absorptance can be extracted according to Eq. (2.25). Due to a wave-optical treatment based on perfectly coherent plane waves, interference effects due to reflections at all layer interfaces are considered.

In detail, the transfer matrix method examines the tangential field components $E_\parallel$ and $H_\parallel$ at each interface between layers of different refractive indices, as illustrated in Fig. 3.5 (a). These tangential field components are continuous across the interfaces, i.e. $E_\parallel$ and $H_\parallel$ are equal in both materials at the interface [107]. With the ansatz of a plane wave propagating in one direction and a second one in opposite direction, the fields in the layer are given by the sum of these two waves. Accordingly, the tangential field components $E_{\parallel,j}$ and $H_{\parallel,j}$ at one interface of the jth layer can be linked with $E_{\parallel,j+1}$ and $H_{\parallel,j+1}$ at the other interface via a *transfer* matrix $\boldsymbol{\mathcal{T}}_j$ via

$$\begin{pmatrix} E_{\parallel,j} \\ H_{\parallel,j} \end{pmatrix} = \boldsymbol{\mathcal{T}}_j \begin{pmatrix} E_{\parallel,j+1} \\ H_{\parallel,j+1} \end{pmatrix}. \tag{3.56}$$

The 2×2 matrix $\boldsymbol{\mathcal{T}}_j$ of layer j accounts for the phase shift due to propagation and for absorption in between the interfaces according to the thickness d_j and the complex refractive index $\tilde{n}_j$ of the layer, depending on the polarization of the considered fields. As the tangential field components are conserved at the interfaces, multiple layers can be connected by multiplying their matrices, e.g.

$$\begin{pmatrix} E_{\parallel,1} \\ H_{\parallel,1} \end{pmatrix} = \left[\prod_{j=1}^{J} \boldsymbol{\mathcal{T}}_j \right] \begin{pmatrix} E_{\parallel,J} \\ H_{\parallel,J} \end{pmatrix} \tag{3.57}$$

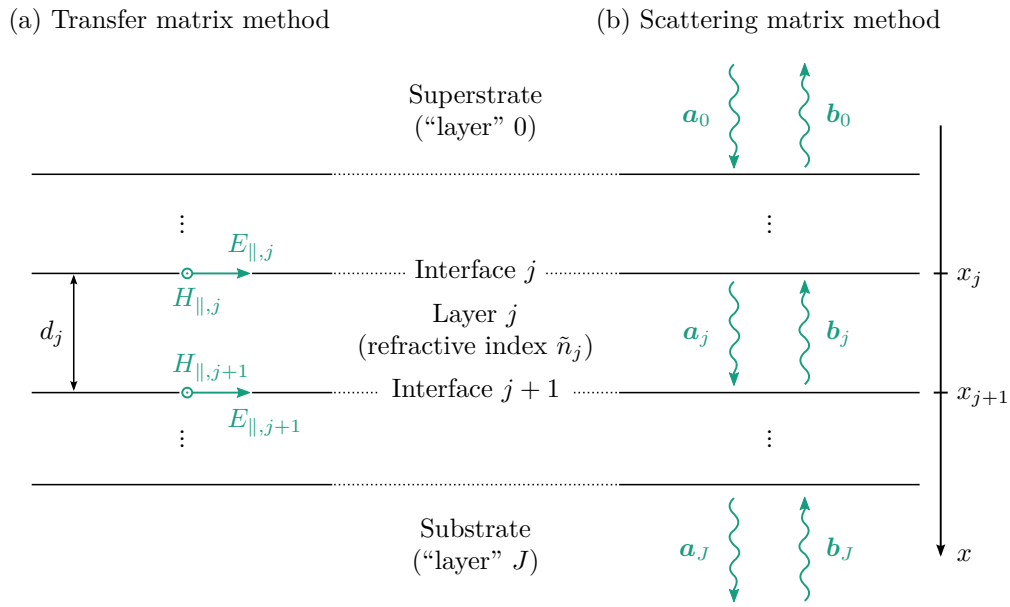

Figure 3.5: Both transfer and scattering matrix method provide the same exact solution of Maxwell's equations in layered stuctures, but with different mathematical treatments. (a) The transfer matrix method links the tangential field components $E_\parallel$ and $H_\parallel$ at the interfaces using a *transfer* matrix $\boldsymbol{\mathcal{T}}_j$ for each layer j accounting for propagation and absorption inside the layer. (b) In the scattering matrix method, the amplitudes $\boldsymbol{a}$ and $\boldsymbol{b}$ of forth and back propagating waves (from which the fields can be easily derived) are connected via a *scattering* matrix $\boldsymbol{\mathcal{S}}(j \to j+1)$ for each interface.

for the complete stack from superstrate to substrate.

In contrast, the scattering matrix approach considers the amplitudes $\boldsymbol{a}$ of the wave propagating in one direction and $\boldsymbol{b}$ of the wave in opposite direction inside the layers. The construction as two-component vectors allows solving for both polarizations at the same time. For these amplitudes, the components of the electric and magnetic fields can be easily derived.[13] According to the conservation of the tangential field components at the interfaces, a *scattering* matrix $\boldsymbol{\mathcal{S}}(j \to j+1)$ for interface j can be found to link the amplitudes in adjacent layers via

$$\begin{pmatrix} \boldsymbol{a}_{j+1} \\ \boldsymbol{b}_j \end{pmatrix} = \boldsymbol{\mathcal{S}}(j \to j+1) \begin{pmatrix} \boldsymbol{a}_j \\ \boldsymbol{b}_{j+1} \end{pmatrix}. \tag{3.58}$$

To link the amplitudes across multiple layers, such as with $\boldsymbol{\mathcal{S}}(0 \to J)$ for the complete stack, the scattering matrix is not given by a product of individual

[13] For instance, $E_{j,y}(x) = a_{j,y} \exp(i\,\tilde{n}_j k_{0,x}(x - x_j)) + b_{j,y} \exp(i\,\tilde{n}_j k_{0,x}(x_{j+1} - x))$ with $\boldsymbol{a}_j = (a_{j,y}, a_{j,z})^{\mathrm{T}}$, $\boldsymbol{b}_j = (b_{j,y}, b_{j,z})^{\mathrm{T}}$ according to the directions on-axis x and in-plane y, z (see Fig. 3.5).

matrices as in the transfer matrix method. Instead, it can be obtained recursively based on the thicknesses and refractive indices of the layers.

Both methods are mathematically different but physically equivalent treatments. As described in Refs. 133, 141, the scattering matrix method is numerically more stable than the mathematically more intuitive transfer matrix method. In this work, both methods were used for different problems in form of an self-written transfer matrix algorithm following Ref. 139 and an implementation of the scattering matrix method by Florian Bödicker [142].

3.3.2 Incoherent treatment of thick layers

In reality, samples typically contain or consist of a relatively thick layer (thickness $d >> \lambda$), such as conventional LSCs or samples with photonic structures on a (glass) substrate. To model their optical properties, the reflections from the back surface need to be considered. When using such thick layers in the transfer or scattering matrix method, the resulting spectra highly oscillate due to Fabry-Pérot resonances. These strong oscillations, however, are typically not observed in experiments due to the non-coherence of incident light as well as a limited spectral resolution of measurement setups. To compare the calculations with experiments, the simulated spectra could be smoothed by spectral averaging, which however is inexact and may introduce artifacts.

For a proper incoherent treatment of a thick layer, I traced the forth and back bouncing light as illustrated in Fig. 3.6. The total fractions of reflected, transmitted, and absorbed light R, T, and A are given by the superposition of the individual *power* (not field) terms and can be expressed using geometric series as

$$\begin{aligned} R &= R_1 + q^2 T_1 R_3 T_2 + q^4 T_1 R_3^2 R_2 T_2 + q^6 T_1 R_3^3 R_2^2 T_2 + \dots \\ &= R_1 + q^2 T_1 T_2 R_3 \sum_{j=0}^{\infty} (q^2 R_2 R_3)^j = R_1 + \frac{q^2 T_1 T_2 R_3}{1 - q^2 R_2 R_3}, \end{aligned} \tag{3.59}$$

$$\begin{aligned} T &= q T_1 T_3 + q^3 T_1 R_3 R_2 T_3 + q^5 T_1 R_3^2 R_2^2 T_3 + \dots \\ &= q T_1 T_3 \sum_{j=0}^{\infty} (q^2 R_2 R_3)^j = \frac{q T_1 T_3}{1 - q^2 R_2 R_3}, \end{aligned} \tag{3.60}$$

$$A = 1 - R - T, \tag{3.61}$$

where R_1 and T_1 denote the reflectance and transmittance at the top surface for incident light from above and R_2 and T_2 for light from opposite direction. Analogous, R_3, T_3 and R_4, T_4 are defined for the bottom surface, as shown in Fig. 3.6. The term $q = \exp(-\alpha d)$ models Lambert-Beer absorption from single-path propagation though the layer with absorption coefficient α.

For oblique incidence with incident angle ϕ_i, $T_j \to T_j(\phi_\mathrm{i})$, $R_j \to R_j(\phi_\mathrm{i})$, and $q \to \exp(-\alpha d/\sqrt{1 - (\sin(\phi_\mathrm{i})\, n_\mathrm{out}/n_\mathrm{in})^2})$ with refractive indices n_in of the thick

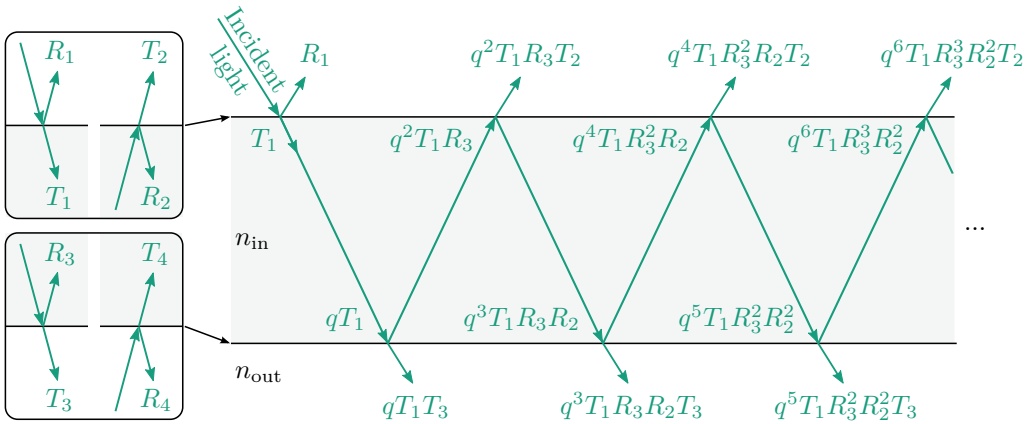

Figure 3.6: To calculate the reflectance, transmittance, and absorptance of a thick layer without interference effects (i.e. incoherently), the contributions of forth and back bouncing light to reflectance and transmittance need to be added (power terms, not fields). Tracing the individually ray as shown in the figure allows finding analytical expressions for the total reflectance, transmittance, and absorptance depending on the surfaces' reflectances and transmittances, which are given by Fresnel equations for simple dielectric interfaces or from the transfer/scattering matrix method if the surface represents a photonic multilayer structure, for example.

layer and n_{out} of the surrounding medium. Note that in this case R_2, R_3 and T_2, T_3 need to be calculated for the internal angle corresponding to ϕ_{i}.

For surfaces that are interfaces between two dielectrics, the R_j and T_j can be obtained from the (power) Fresnel equations (see Appendix A.3). Accordingly, $R_1 = R_2 = 1 - T_1 = 1 - T_2$ and $R_3 = R_4 = 1 - T_3 = 1 - T_4$, with $R_1 = R_3$ if the surrounding medium is the same at the top and bottom. This case corresponds to a conventional LSC, being a simple plate of PMMA or glass in air. Combining Eqs. (3.59) and (3.60), the absorption coefficient α can be expressed in term of R and T, which is useful to extract α from reflectance and transmission measurements, see Eq. (4.5).

More generally, the surfaces can also be understood as imaginary interfaces representing a photonic multilayer structure on a substrate, for example. The reflectances and transmittances at such surfaces are given by the optical properties of the multilayer structure that can be calculated separately, for axample with the transfer or scattering matrix method. In such cases, the reflectance R_1 and R_2 (as well as R_3 and R_4) are not necessarily equal, since absorption can appear within the multilayer structure, for example. The transmittances, however, are equal for reverse direction ($T_1 = T_2$, $T_3 = T_4$) due to reciprocity in optics (at least in non-magneto-optic materials) [143, 144].

Here in this work, this approach was used to calculate the local absorptance

in a multilayer stack on top of a thick glass substrate, as presented in Sec. 6.1.1 (Fig. 6.1 (a) shows the multilayer structure). The back side reflections were considered by performing two separate scattering matrix calculations: one where light was incident from the top (air), and one with incidence from the bottom of the stack (from glass). To obtain the total local absorptance inside the multilayer stack, the two resulting local absorptances were added, where the result for incidence from glass was weighted with the fraction of incident light that hits the top surface in Fig. 3.6.[14]

3.3.3 Ray tracing light in LSCs

In this work the spectrum of escaping light from the surface of a sample was studied angular resolved with the measurement setup presented in Sec. 4.3.3. The theoretical spectra for the PLSC and LSC were calculated using the FLDOS in combination with the emitter model as explained in Sec. 3.1.4 and 3.2.3. Using this approach, the efficiency of out-coupling is not considered: all modes that are able to couple are assumed to couple out, which is for example valid for conventional LSCs due to the small Fresnel reflectance of only 4% at the surfaces.

For a third type of samples named "TSR" (*triple stack reference*), consisting of an LSC with highly reflective filter structures on the top and bottom surfaces (see Fig. 5.6), however, the limited out-coupling efficiency due to the high reflectance needs to be considered. While emission inside the TSR is assumed to be isotropic, the out-coupled light varies with wavelength and angle due to the transmission function at the surface determined by the filters. To predict these spectral and angular resolved spectra, the emitted light was "ray-traced" as illustrated in Fig. 3.7 (a). This geometric optical approach corresponds to an incoherent treatment of the "thick" body of the sample, similar to the previous section.

An emitting dye layer was assumed in the center of a sample with thickness d, as realized with the fabrication method of filter bonding (Sec. 4.1.2). The exact vertical position of this dye layer, however, has no significant effect on the results, thus this model is also valid for the slightly asymmetric samples obtained from spin coating (Sec. 4.1.1). The reflectance R and the transmittance T at the interfaces are determined by the filter structures (see Fig. 3.7 (b)), and were calculated using the transfer matrix method. It was assumed that both interfaces are equal and no (re)absorption occurs (cf. Fig. 3.6 with $R_2 = R_3 = R$, $T_2 = T_3 = T$, and $q = 1$).

To model the light detected in the experiments, the rays exiting the sample within a spot with radius l_d were calculated. The corresponding total transmittance function $T_\mathrm{tot}(\lambda, \phi_\mathrm{d})$ for this light can be obtained by summing up the indi-

[14] This fraction is given by $q^2 T_1 R_3 + q^4 T_1 R_3^2 R_2 + q^6 T_1 R_3^3 R_2^2 + \ldots = \frac{q^2 T_1 R_3}{1 - q^2 R_2 R_3}$ with T_1, R_2 from the stack's reflectance (calculated with scattering matrix method) and R_3 according to the Fresnel equation for the glass-to-air interface on the back.

(a) Ray tracing model: angular resolved spectra of out-coupled light for certain detection spot size

(b) Reflectance and transmittance at surfaces (of TSR samples)

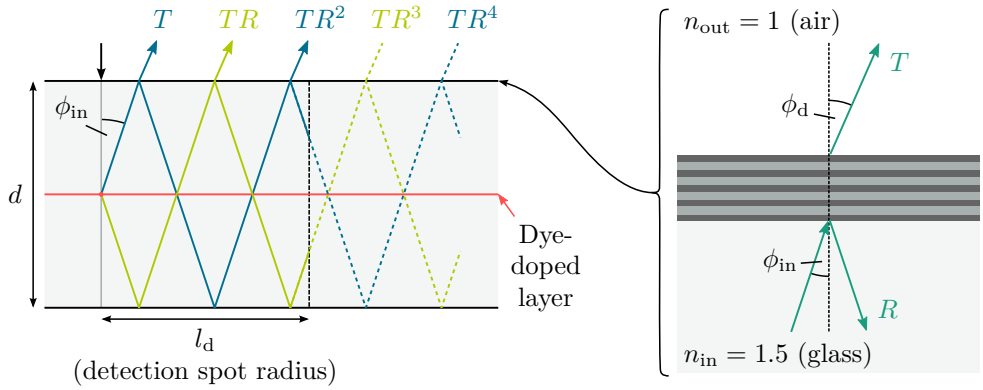

Figure 3.7: To model the angular resolved PL escaping from a finite surface spot, the emitted light was "ray-traced" inside the sample, as shown in (a). This is necessary for samples with highly reflective surfaces such as the TSR samples in this work (LSC with filters on top and bottom): light in the escape cone may exit the sample not directly at the first reflection event but after several times "bouncing" through the sample. For this purpose the reflectance and transmittance of the filters were used for the optical properties of the sample's surface, as indicated in (b).

vidual contributions within this spot, as shown in Fig. 3.7 (a). Thus,

$$T_{\text{tot}}(\lambda, \phi_{\text{d}}) = T \sum_{j=1}^{J_{\text{f}}} R^{2(j-1)} + TR \sum_{j=1}^{J_{\text{b}}} R^{2(j-1)} \tag{3.62}$$

with the two sums corresponding to the blue and green rays in Fig. 3.7 (a). The number of summands is given by

$$J_{\text{f}} = \left\lfloor \frac{l_{\text{d}}}{2d \tan \phi_{\text{in}}} + \frac{3}{4} \right\rfloor \quad \text{and} \quad J_{\text{b}} = \left\lfloor \frac{l_{\text{d}}}{2d \tan \phi_{\text{in}}} + \frac{1}{4} \right\rfloor, \tag{3.63}$$

where $\lfloor x \rfloor$ gives the greatest integer less than or equal to x.

Note that R, T and J_{f}, J_{b} depend on the angle of the emitted light. It must be distinguished between the internal angle ϕ_{in} and the external angle ϕ_{d} that are connected via Snell's law. As we want to model angular PL measurements that measure external angles, the transmission function is expressed in ϕ_{d} and R, T, J_{f}, J_{b} need to be calculated for the corresponding ϕ_{in}.

The detected angular resolved PL spectrum $\Pi_{\text{d}}(\lambda, \phi_{\text{d}})$ is the "filtered" angular emission spectrum $\Pi_0(\lambda, \phi_{\text{d}})$, given by the product

$$\Pi_{\text{d}}(\lambda, \phi_{\text{d}}) = \Pi_0(\lambda, \phi_{\text{d}}) \times T_{\text{tot}}(\lambda, \phi_{\text{d}}). \tag{3.64}$$

The angular emission spectrum $\Pi_0(\lambda, \phi_\mathrm{d})$ is the product of the undistorted emission spectrum $g^0(\lambda)$ and the angular distribution function $f_{\phi_\mathrm{d}}(\phi_\mathrm{d})$. In the case of isotropic emission, i.e. the uniform distribution of emission with respect to the internal angle ϕ_in, the angular distribution function is given by

$$f_{\phi_\mathrm{d}}(\phi_\mathrm{d}) = \frac{n_\mathrm{out}}{n_\mathrm{in}\sin^{-1}(n_\mathrm{out}/n_\mathrm{in})} \frac{\cos(\phi_\mathrm{d})}{\sqrt{1-\left(\frac{n_\mathrm{out}}{n_\mathrm{in}}\right)^2 \sin(\phi_\mathrm{d})}} \tag{3.65}$$

in terms of the external angle ϕ_d, as derived in Appendix A.5.

With this approach, also the angular integrated surface PL as well as the spectrum of light guided to the edge face ("edge PL") according to the experiments from Sec. 4.3.4 can be modeled. The integrated surface PL $\Pi_\mathrm{s}(\lambda)$ is given by the integral over the angular resolved surface $\Pi_\mathrm{d}(\lambda, \phi_\mathrm{d})$, weighted with $\sin\phi_\mathrm{d}$:

$$\Pi_\mathrm{s}(\lambda) = \int_{0^\circ}^{90^\circ} \sin(\phi_\mathrm{d})\, \Pi_\mathrm{d}(\lambda, \phi_\mathrm{d})\, d\phi_\mathrm{d}. \tag{3.66}$$

The weighting factor $\sin\phi_\mathrm{d}$ arises from the fact that the angular resolved measurement probes the escaping light only along a 2D plane. Given rotation symmetry with respect to the surface normal, the light detected at a certain "zenith" ϕ_d also escapes in other directions with same ϕ_d but other azimuthal angles that lie outside the detection cone. The larger ϕ_d, the smaller the detected fraction, which can be understood with the length of the circumference on a sphere similar to that in Fig. 3.3 (b). Accordingly, the "multiplicity" of the light detected at ϕ_d can be approximated by $\sin\phi_\mathrm{d}$ as the half-angle of the detection cone used in this work is quite small ($\theta_\mathrm{d} = 0.6^\circ$).

Note that an appropriate value for l_d needs to be used for the calculation of $\Pi_\mathrm{s}(\lambda)$: to obtain the spectrum of all light escaping from the whole sample surface (as in the integrated PL experiments), $\Pi_\mathrm{d}(\lambda, \phi_\mathrm{d})$ needs to be calculated for l_d given by the surface dimensions of the sample.

The (integrated) edge PL $\Pi_\mathrm{e}(\lambda)$ is determined by both the guided light due to TIR (given by the LGE σ^0) as well as the light in the escape cone that was not lost due to the filter's reflectance:

$$\Pi_\mathrm{e}(\lambda) = \underbrace{\sigma^0 g^0(\lambda)}_{\text{TIR guided}} + \underbrace{(1-\sigma^0)\, g^0(\lambda) \frac{\int_{0^\circ}^{90^\circ} \sin(\phi_\mathrm{d})\, \Pi_\mathrm{d}(\lambda, \phi_\mathrm{d})\, d\phi_\mathrm{d}}{\int_{0^\circ}^{90^\circ} \sin(\phi_\mathrm{d})\, \Pi_0(\lambda, \phi_\mathrm{d})\, d\phi_\mathrm{d}}}_{\text{Filter reflection}}. \tag{3.67}$$

Note that here $\Pi_\mathrm{d}(\lambda, \phi_\mathrm{d})$ needs to be calculated for the appropriate value of l_d given by the distance from point of excitation to the edge face.

3.3.4 Angular pattern of light out-coupled at edge face

In the experiments, the light guided to the samples' edge faces was measured as a function of the internal propagation angle using a glass half-cylinder coupled to the edge faces, as described in Sec. 4.3.3. The angular distribution of the light at the edge reveals interesting information about the light guiding mechanisms as discussed in Sec. 5.2.2. In general, this angular distribution is strongly non-uniform and depends on the type of concentrator (bulk or thin film LSC), its geometry (e.g. thickness), and the way of excitation (e.g. spot vs. full area excitation). It was studied previously in theory and experiments [18, 145–147].

Here, I want to derive the characteristic angular distribution of a thin film LSC resulting from excitation at a single point (using a laser as in the experiments in this work, for example) to motivate the measurement results. In detail, a sample of thickness d with a dye-doped layer on top is studied, that is excited at a point with distance l_e to the edge face, as illustrated in Fig. 3.8 (a). For a qualitative treatment, reabsorption and parasitic absorption were neglected.

The in-plane rays with isotropic angular distribution can be divided into different subsets: first, part of emission features angles within the escape cone (gray area in the figure). This fraction is assumed to be lost on the way to the edge face and does not contribute the angular distribution at the edge face. Second, the guided light exits at the edge face propagating up- or downwards, depending on the number of reflection events it encounters on the path through the concentrator, as indicated by the red ray bundles in Fig. 3.8 (a). The angles where the out-coupling direction flips, i.e. the angles of the limiting rays of the bundles, are given by

$$\phi_{\mathrm{d},j} = 90^\circ + \tan^{-1}\left(j\frac{d}{l_\mathrm{e}}\right) \qquad (j \in \mathbb{Z}). \tag{3.68}$$

The possible angles $\phi_{\mathrm{d},j}$ are limited by the bounds $\{\phi_\mathrm{c}, 180^\circ - \phi_\mathrm{c}\}$ due to the escape cone of TIR (with critical angle ϕ_c).

Accordingly, the angular distribution is given by a pattern of "on"/"off" regions, as shown in Fig. 3.8 (b) for different d/l_e ratio (i.e. different sample thicknesses). The smaller this ratio, i.e. the thinner the sample (d) and/or the longer the distance from excitation to the edge (l_e), the more "on"/"off" regions occur with smaller spacing due to the increasing number of possible reflection events on the way through the sample.

The asymmetry around $\phi_\mathrm{d} = 90^\circ$ arises from the modeled sample's asymmetry (dye layer on top). Shifting the vertical position of the dye layer moves the pattern on the ϕ_d axis, and it is symmetric for a dye layer in the center. The characteristic pattern spacing, however, is similar for all vertical positions. When the emitting dye is not confined in a single layer, but distributed in a volume as in bulk LSCs, for example, the "on"/"off" pattern is smoothed. The typical "oscillations", however, can still be observed as reported in Refs. 18, 146.

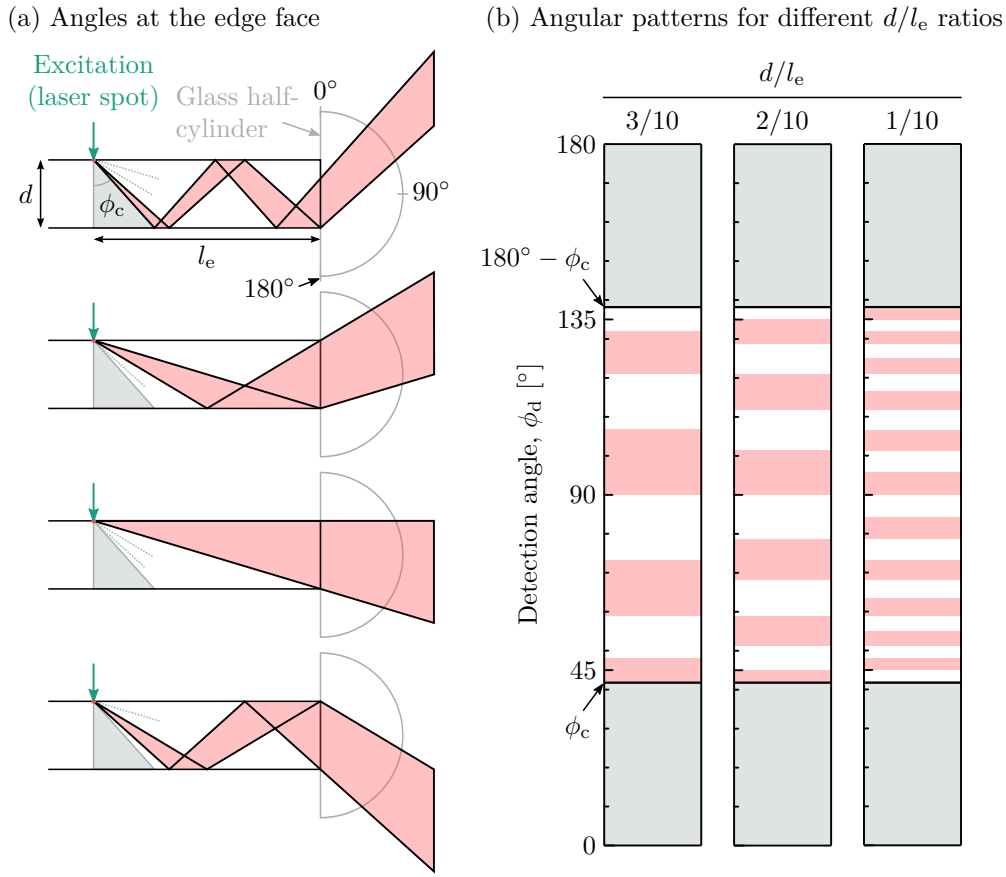

Figure 3.8: (a) At the edge face of a thin film LSC guided light exits up- or downwards, depending on the sample thickness d and distance l_e between the point of excitation and the edge face. (b) The angular distribution is thus determined by a "on"/"off" pattern, as shown for different thicknesses d with respect to l_e ($n_{in} = 1.5, n_{out} = 1$). Light emitted with angles within the escape cone (gray shaded areas) is lost on the way to the edge face.

Chapter 4

Experimental methods

BASED on the theoretical considerations it is expected that the embedding of a fluorescent dye in a photonic crystal changes the emission of light in terms of spectral and directional redistribution, and thus influences the performance of a PLSC. To examine these effects in experiments, several samples were fabricated and characterized. In the first part of this chapter, different approaches and newly developed processes for the fabrication of multilayer and opal photonic structures with embedded dyes are presented.[1] In the second part, the most important measurement methods and characterization setups used in this work are introduced.

4.1 Fabrication of multilayer structures

To fabricate photonic multilayer structures, thin layers (around 100 nm) of alternating high- and low-refractive-index materials need to be stacked. All materials should be transparent in the absorption and emission range of the dye to avoid parasitic absorption. Furthermore, the dye needs to be embedded in one or more layers of the stack. In this work the perylene-based Lumogen dyes from BASF were used as well-known LSC dyes with high photoluminescent quantum yield Φ (PLQY). In particular, the dyes Lumogen F Yellow 083 ($\Phi = 91\%$ [150]) and F Red 300 ($\Phi = 98\%$ [151]) were studied in detail. To remain the high PLQY the dyes were embedded in the polymer Poly(methyl methacrylate) (PMMA), which is known to be a stable host material for organic dyes [7, 152].

[1] The former diploma students I supervised during my PhD, Janina Posdziech and Janina Löffler, both significantly contributed to this part on the fabrication methods, see Refs. 148, 149.

(a) Spin coated multilayer structures

(b) Bonding of undoped filters with dye-doped polymer layer

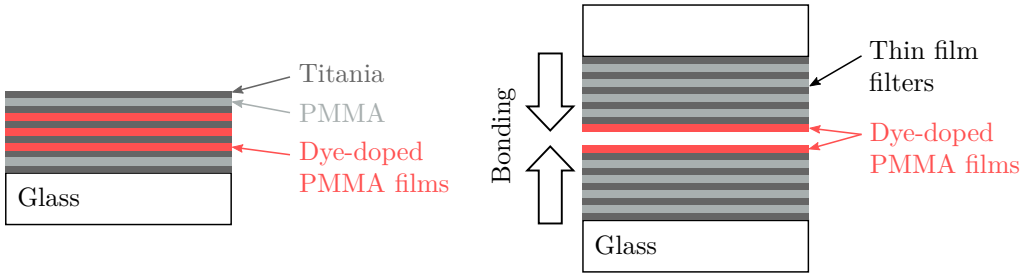

Figure 4.1: Sketches of the two approaches pursued in this work to fabricate dye-doped multilayer structures: (a) spin coating of alternating titania and PMMA layers, where the dye could be embedded in multiple polymer layers. (b) Second, thin film filters fabricated with conventional technologies were bonded together using a dye-doped polymer layer.

The use of dye-doped PMMA, however, is mostly incompatible with established thin film deposition technologies such as sputtering or chemical vapor deposition, e.g. due to high processing temperatures. Thus, two approaches were chosen in this work to fabricate multilayer structures with embedded dye layers.

On the one hand, a spin coating process was developed to deposit stacks of alternating layers (Fig. 4.1 (a)). Spin coating is a well-known process for the deposition of polymers. In this way, the dye can be easily embedded in one or more layers. The challenge of this approach is the deposition of high-refractive-index layers, which was solved by using a titania (titanium dioxide) sol-gel route as described below.

On the other hand, multilayer structures without dye were deposited using the established thin film technologies of plasma-enhanced chemical vapor deposition (PECVD) at Fraunhofer ISE and ion beam sputtering (IBS) at Laseroptik GmbH (Fig. 4.1 (b)). Subsequently, a dye-doped PMMA layer was spin coated on these “filters”, which were then bonded together using heat, pressure and vacuum, as described below.

4.1.1 Spin coated multilayer structures

Multilayer structures were fabricated by spin coating alternately PMMA and titania layers. It is important that the deposition of one layer does not dissolve or damage the previously deposited layer underneath. In this regard the solvents play a crucial role. Here, PMMA was dissolved in toluene, while an ethanol-based titania sol-gel was found to yield the best results. Stacks were spin coated on highly transparent glass substrates (Menzel-Gläser Superfrost Plus from Thermo Scien-

tific, cut to $25 \times 25 \times 1$ mm^3) after cleaning them with ethanol. The table-top spin coater G3P-8 from SCS was used inside a fume hood environment.

Low-refractive-index layers (PMMA)

For the low-refractive-index layers, PMMA (avg. $M_w \approx 350000$, Aldrich 445746) was dissolved in toluene (ROTISOLV HPLC, > 99.9%, Carl Roth 7346) under stirring for several hours at 60 °C. The resulting layer thickness and surface topography depend on several parameters. Most importantly, the thickness can be tuned with the polymer-to-toluene concentration ζ_p of the solution (in weight-%) and the spin speed Ω (in revolutions per minute (RPM)), as shown in Fig. 4.2 (a): the faster the substrate rotates and the lower the amount of PMMA in the solution, the thinner the layer. The resulting thickness d_p can be described well with the model $d_\mathrm{p}(\Omega, \zeta_\mathrm{p}) = 355\,\mathrm{nm}\,(\zeta_\mathrm{p}/\mathrm{w\%})^{1.60}\,(\Omega/\mathrm{RPM})^{-0.30}$, as adopted from Walsh and Franses [153]. The fit parameters were determined from a systematic variation for single PMMA layers on glass.

Furthermore, the influence of the acceleration (ramp up time) and the spinning duration (plateau time) were investigated. The acceleration time was found to have no effect on the layer thickness unless it is longer than 2 s. As also mentioned in Ref. 154, long acceleration times are expected to cause complete evaporation of the solvent before the final spinning speed has been reached. Thus the thickness is in this case not determined by the final speed. Due to the fast evaporation, the layer is formed after a few seconds of spinning. A variation of the spinning

(a) Film thickness vs. process parameters (b) Material dispersion of PMMA layer

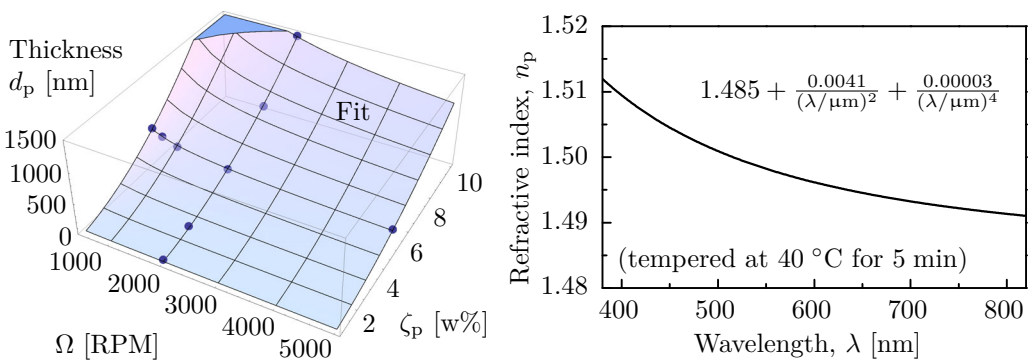

Figure 4.2: (a) The PMMA film thickness increases with decreasing spin speed Ω and increasing polymer-to-toluene concentration ζ_p. The experimental results (points) were fit with $d(\Omega, \zeta_\mathrm{p}) = 355\,\mathrm{nm}\,(\zeta_\mathrm{p}/\mathrm{w\%})^{1.60}\,(\Omega/\mathrm{RPM})^{-0.30}$ (plane). (b) The refractive index as a function of wavelength for the spin coated PMMA layers, modeled using the Cauchy approach. Both thickness and refractive index were extracted from spectroscopic ellipsometry measurements.

duration from 30 to 120 s showed that the layer thickness is not affected. Tempering the polymer films resulted in a slightly smaller layer thickness, indicating the evaporation of solvent residuals. Optical absorption measurements, however, revealed no influence of tempering on the optical quality of the films. The spin coating process parameters were optimized to obtain layers with low roughness (checked with atomic force microscopy), low waviness (measured using a stylus profilometer) and homogeneous thickness distribution over the sample.

The thickness was measured using spectroscopic ellipsometry. For that purpose the back surface of the glass substrate was roughened to minimize backside reflections. These thickness measurements could be confirmed by destructive profilometer measurements (by partly removing the polymer layer). Furthermore, the refractive index was extracted from the ellipsometry measurements. The material dispersion was fit using the *Cauchy* model as absorption was found to be negligible in the relevant spectral range of 400–1000 nm. The resulting refractive index $n_\mathrm{p}(\lambda) = 1.485 + 0.0041\ \mu\mathrm{m}^2/\lambda^2 + 0.00003\ \mu\mathrm{m}^4/\lambda^4$ is shown in Fig. 4.2 (b).

Dye-doped PMMA layers

The Lumogen dyes F Yellow 083 and F Red 305 (referred to as LY and LR, respectively) dissolved easily in the PMMA-toluene solution for the deposition of dye-doped layers. The concentration of the dye in the polymer, however, needs to be chosen carefully: on the one hand, the samples should absorb a large part of the incident light. As the total thickness of all dye-doped layers is limited for practical reasons, the highest dye concentrations possible are beneficial for the absorptance. On the other hand, high dye concentrations promote both reabsorption and self-quenching of luminescence and should be avoided with regard to the PLSC device performance.

Different theories exist for the phenomenon of self-quenching, i.e. the increase of non-radiative decays and thus the decrease of the PLQY: aggregation of single molecules [155], the formation of non-fluorescent dimers [156], energy transfer [157] and collisional interactions [158]. As only very few and incomplete data on self-quenching of the Lumogen dyes in PMMA are available [135, 159], samples with different dye concentrations were fabricated to study this effect.

A PMMA-to-toluene concentration of $\zeta_\mathrm{p} = 5$ w% was chosen and the dye concentrations ζ_dye (in weight-% with respect to the amount of PMMA in the solution) were varied. For the LY dye, concentrations up to only 5 w% could be achieved due to the solubility of the dye in toluene, whereas for LR solutions with up to $\zeta_\mathrm{dye} = 50$ w% could be prepared. This difference in toluene-solubility is consistent with literature[160]. The solutions were spun at 1000 RPM onto glass substrates so that a film thickness of roughly 500 nm was obtained.

As these samples represent thin film LSCs[22], the absorptance by the dye A_dye and the concentrator quantum yield (CQY) η were measured according to

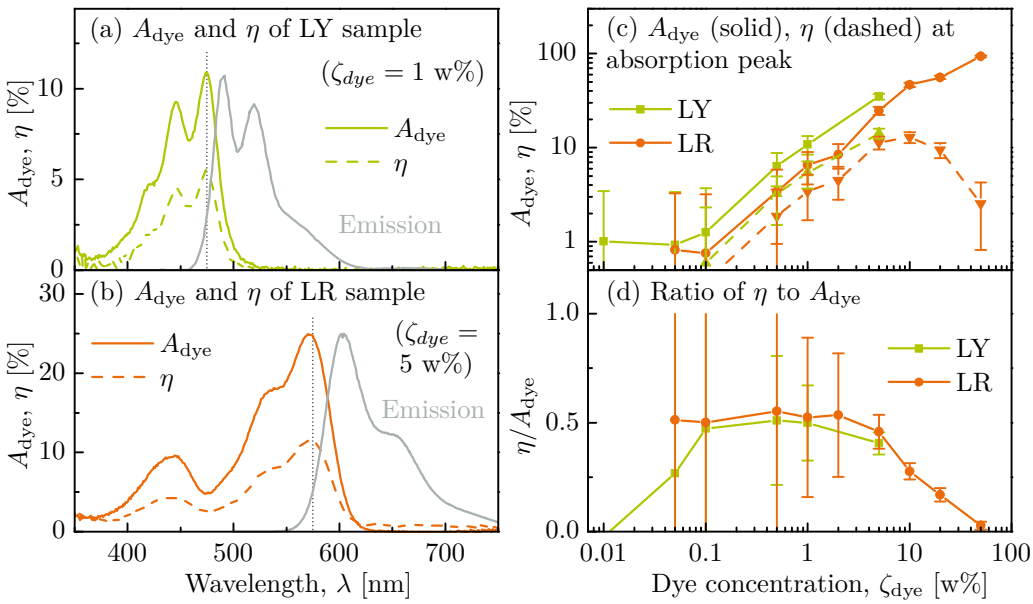

Figure 4.3: Typical dye absorptance curves (A_{dye}) for (a) Lumogen F Yellow 083 (LY) and (b) F Red 305 dye (LR) samples together with their concentrator quantum yield (η) and the dye's emission spectrum. (c) A_{dye} and η were evaluated at the corresponding peak absorption wavelength (dotted in (a), (b)) for different dye concentrations. (d) The ratio η/A_{dye} decreases for dye concentrations larger than 1–2 w%, indicating self-quenching of the luminescence. Error bars arise from the propagation of measurement uncertainties of the spectrophotometer setup.

Sec. 4.3.1. The CQY is a measure for the LSC performance and contains both reabsorption and self-quenching related losses. Figure 4.3 (a) and (b) show typical dye absorptance curves for an LY and an LR sample, respectively, along with their CQY and the corresponding photoluminescence spectrum. The LY dye covers the range from 400–500 nm and the LR dye the range 500–600 nm with significant absorption in the violet/blue (400–450 nm).

To investigate the effect of the dye concentration, A_{dye} and η were evaluated at the absorption peak wavelength (LY: 475 nm, LR: 575 nm, see dotted line in Figure 4.3 (a), (b)) and plotted in Figure 4.3 (c). As expected, the higher the dye concentration, the more light is absorbed in the layer. Also the collection efficiency increases as more photons are absorbed. For high concentrations, however, the two curves decouple. This can also be seen from their ratio η/A_{dye} in Figure 4.3 (d).[2] For dye concentrations higher than 1–2 w%, the ratio significantly decreases, in-

[2]Note that the error bars for small concentration values are large, as the used spectrophotometer setup has an absolute error of 1%, causing large uncertainties for small signals, especially when calculating ratios.

dicating self-quenching. The analysis of such high LY and LR concentrations in PMMA has not been reported before. Wilson, however, fabricated samples with much lower dye concentrations of up to 0.08 w% (LY) and 0.16 w% (LR) without observing quenching [159].

Based on this concentration study, the dye concentration $\zeta_{\text{dye}} = 1$ w% was chosen for the fabrication of PLSCs to avoid self-quenching. Further experiments were restricted to the LR dye due to the slightly higher PLQY and because the emission could be studied using a green excitation laser ($\lambda = 532$ nm).

High-refractive-index layers (titania)

To obtain spin coated layers with a high refractive index, a titania sol-gel process was used. In short, sol-gel processes are able to produce solid material from colloidal dispersions (*sol*) that form a network (*gel*). In the first stage, precursor molecules such as titanium isopropoxide undergo hydrolysis and polycondensation reactions to form colloids. Depending on solvents, catalysts, other additives and reaction conditions, the morphology of this solid phase ranges between discrete colloidal particles and networks [161]. Subsequent thermal treatment densifies the gel, thus increasing its refractive index. Heating first removes solvent residuals (drying). Higher temperatures of several 100 °C typically lead to sintering and growth of crystalline grains in the amorphous films.

In this work, a sol-gel process based on the recipe from Ref. 162 was optimized

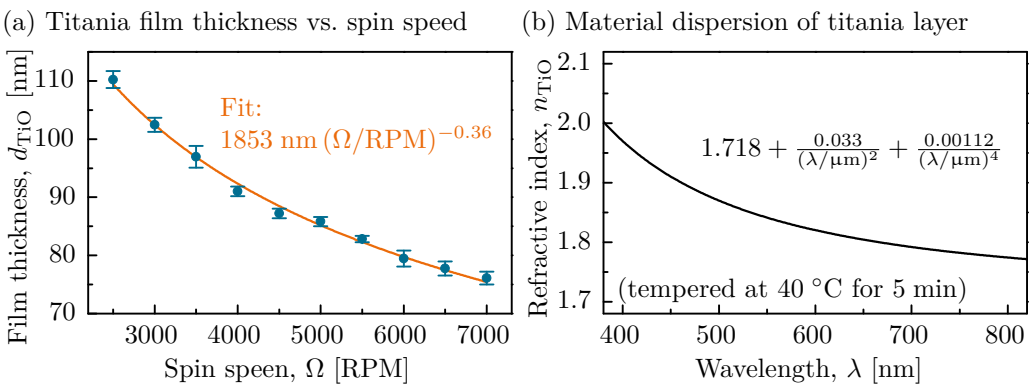

Figure 4.4: (a) The titania sol-gel film thickness reduced with increasing spin speed. Error bars indicate the standard deviation of thickness measurements at 9 different spots on the samples (on a 5 mm spaced square grid). The thickness model proposed by Walsh and Franses [153] was fit to the measurement data (orange line). (b) A titania refractive index of ca. 1.8 at $\lambda = 650$ nm was obtained (Cauchy model) using a low-temperature tempering process. Both thickness and refractive index were obtained using spectroscopic ellipsometry.

to obtain homogeneous, crack-free titania layers compatible with the deposition of PMMA layers. The titania sol was prepared by first mixing 0.574 mL of hydrochloric acid (2.0 M, Fluka 35327) with 20 mL of ethanol. Separately, 5.4 mL of the precursor titanium isopropoxide (Aldrich 377996) was mixed with 20 mL of ethanol. In both cases, pure ethanol (ROTIPURAN $\geq$ 99.8%, Carl Roth 9065) was used, as solvent-grade ethanol contains a significant amount of water, which drastically changes the kinetics of the reaction and thus the properties of the resulting titania gel. Finally, the mixture of hydrochloric acid and ethanol was added to the other mixture and stirred for 5 min.

As for the polymer films, the layer thickness d_{TiO} mainly depends on the spin speed Ω. The thickness results of a spin speed variation was fit with the function $d_{\mathrm{TiO}}(\Omega) = 1853\,\mathrm{nm}\,(\Omega/\mathrm{RPM})^{-0.36}$ (see Fig. 4.4 (a)). Tempering the titania layer decreased the thickness and increased the refractive index due to densification of the gel. Refractive indices of up to 2 (at $\lambda = 600$ nm) were obtained for temperatures of 300 °C. As the titania layers need to be optimized for stacking with PMMA layers, however, a relatively low temperature of 40 °C was chosen, as discussed below. Thus a refractive index of ca. 1.8 was obtained in the range of interest at 650 nm. The material dispersion was extracted from ellipsometry measurements by employing the Cauchy model as the absorption could be neglected for the relevant spectral range (400–1000 nm), yielding $n_{\mathrm{TiO}}(\lambda) = 1.718 + 0.033\ \mu\mathrm{m}^2/\lambda^2 + 0.00112\ \mu\mathrm{m}^4/\lambda^4$ (see Fig. 4.4 (b)).

Spin coated stacks

Based on the results for the single layers, stacks of alternating PMMA and titania layers were fabricated. For a given desired wavelength of the reflection peak $\lambda_{\mathrm{design}}$, the target film thicknesses are given by the Bragg condition $\lambda_{\mathrm{design}} = d/4n$. For the LR dye an optimum $\lambda_{\mathrm{design}} = 645$ nm was found in calculations (see Sec. 6.1.2), thus $d_{\mathrm{p}} = 108$ nm for PMMA and $d_{\mathrm{TiO}} = 90$ nm for titania. In general, the film thicknesses need to be controlled very well: a thickness variation of only 7.7%, i.e. 8 nm for PMMA and 7 nm for titania, corresponds to a shift of the stack's reflectance peak by 50 nm.

The stacks were spin coated on glass substrates, beginning with the titania layer. A PMMA bottom layer would have had no significant optical effect as the refractive indices of glass and PMMA are very similar. To obtain strong constructive interference, i.e. maximum peak reflectivity, the top $\lambda_{\mathrm{design}}/4$-layer (deposited last) should have the higher refractive index and should thus be made of titania. Consequently, the stacks had an odd total number of individual layers.

In first experiments with only few layers, the samples were tempered at 140 °C to obtain a high refractive index of titania. After this heating step, however, many cracks were found in the titania layers (see Fig. 4.5 (a)). This observation was attributed to the significant difference between the coefficients of thermal

(a) Titania on PMMA, tempered at 140 °C (b) Optical micrograph of four-layer stack

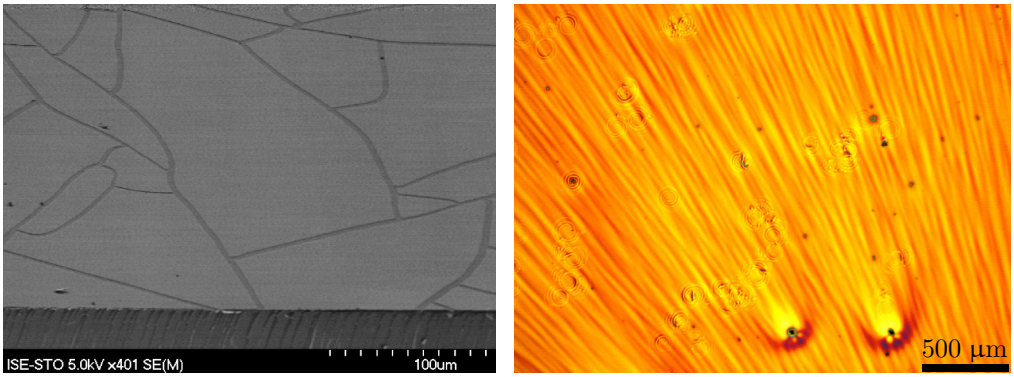

Figure 4.5: Several defects in the spin coated stacks were found for a non-optimized process: (a) shows a SEM graph of a titania layer on top of a PMMA layer. Tempering the sample for one hour at 140 °C caused many cracks in the titania layer as its coefficient of thermal expansion is much smaller than the one of PMMA. The cracks could be minimized by using lower temperatures. (b) The optical micrograph of a four-layer stack shows typical defects of spin coated films, most relevantly "striations" and "comets". Filtering the solutions before deposition and dynamic dispensing helped to reduce these effects.

expansion of PMMA (70–93 10^{-6} K^{-1} [163]) and titania (6–10 10^{-6} K^{-1} [164]): when heating the samples, the PMMA layers tend to expand more than the titania layers, thus stretching and breaking them. The crack density could be drastically reduced by lowering the temperature, at the expense of a slightly smaller refractive index of the titania layers. In the optimized process, the samples were tempered at 40 °C for 5 min after each layer deposition, mainly to remove solvent residuals.

Further optimization was done to increase the layer quality. The optical micrograph of a four-layer stack in Fig. 4.5 (b) shows typical defects of spin coated films, most relevantly "striations" and "comets", which are well-known in literature [154, 165]. These defects could be reduced by filtering the solutions prior to deposition (using MN 615 1/4 filter paper) and by dispensing the PMMA solution dynamically (on the already rotating sample), in contrast to the static dispensing of the titania sol.

When measuring the reflectance of the spin coated stacks, deviations from the expected reflectance were found. The reflectance peak was shifted, which means that the thicknesses of the individual layers in the stack were different from the expected thicknesses derived from the analysis of the single layers. A reason for the deviation could be that single layers were deposited on glass surfaces while the stack layers were deposited on underlying layers of PMMA or titania. The results of a thickness study of double layers of titania on PMMA and PMMA on titania, however, did not support this hypothesis. Furthermore, in several stack fabrication

experiments it was found that the reflectance peaks and thus the layer thicknesses were not reproducible to a satisfactory degree: within the same "batch" (same solutions, same day of processing) different samples with identical spin parameters featured the same optical properties. Differences, however, occurred for different batches (different solutions, other days of processing). The reproducibility was investigated in several experiments.

The strongest influence on the layer thicknesses originates from the solutions themselves. In a detailed study it was found that the titania sol "ages" over several days, probably due to on-going chemical reactions, leading to different layer thicknesses. Thus, later on the sol was synthesized just prior to the deposition. The PMMA solution was found to yield similar results even after one week of aging, but deviations were found after several weeks. A further influence on PMMA layer thickness could be that the polymer-to-toluene concentrations were not exactly identical in each experiment: since PMMA hardly dissolves in toluene, different techniques were used to support this process (ultrasonic bath, heating, stirring...). Another influence may have come from the temperature and humidity variation in the lab, which was not kept constant. For a detailed discussion of the processes and a comparison with simulations see Löffler [149].

The individual layer thicknesses inside a stack of several layers are not directly accessible: ellipsometry gives unreliable results due to the complex modeling, and SEM leads to degradation of the polymer layers (even at low voltages), making it hard to extract absolute measurements with high accuracy. Thus reflectance measurements of the stacks were used to find the optimum process parameters listed in Tab. 4.1. Increasing the spin speed for both materials decreased the peak

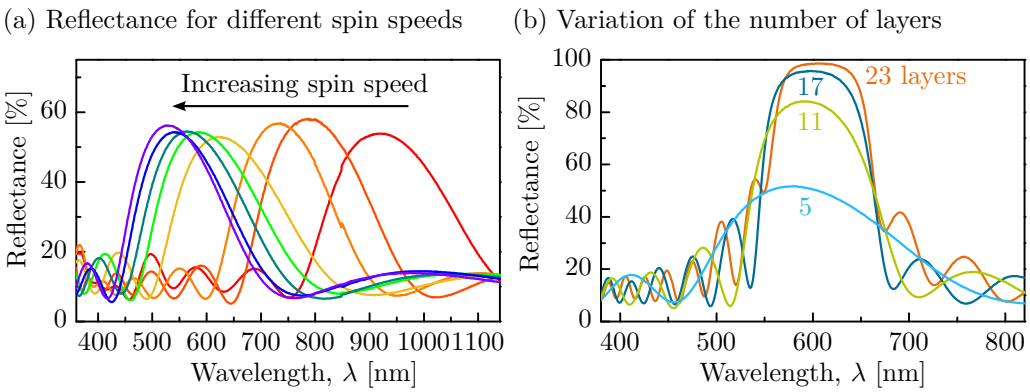

Figure 4.6: (a) The peak of reflectance shifts to shorter wavelengths for increasing spin speeds of titania and PMMA, indicating smaller layer thicknesses (results for 7-layer stacks). (b) Increasing the number of layers increases the absolute peak height of reflectance and improves the spectral selectivity.

Table 4.1: Spin coating process parameters for the deposition of multilayer stacks from PMMA and titania used to obtain a reflectance peak at $\lambda_{\text{design}} = 645$ nm (optimum for LR dye).

General	
Ramp up time (acceleration)	1 s
Spinning duration (plateau time)	60 s
Tempering	5 min at 40 °C after each layer
PMMA layers	
Spin speed Ω	3000 RPM
Polymer concentration ζ_{p}	2.5 w%
Dye concentration ζ_{dye}	1 w% (with respect to PMMA)
Dispensed volume	200 µL
Dispensing mode	dynamic
Titania layers	
Spin speed Ω	4500 RPM
Dispensed volume	300 µL
Dispensing mode	static

wavelength (Fig. 4.6 (a)). Here, the reflectance peak was varied from the blue to the NIR, but in principle it could be shifted even further for other applications. As expected, increasing the number of layers led to a higher reflectance, as shown in Fig. 4.6 (b). For more than 23 layers, the reflectance peaks at values close to 100% with high spectral selectivity, superior to other spin coated stacks reported in literature [154, 166–170].

Consequently, stacks with up to 29 individual layers were fabricated. In Figure 4.7 (a) an SEM graph of such a structure is shown. As mentioned above, the exact thickness could not be measured due to insufficient resolution and electron beam induced degradation and shrinkage of the polymer layers. Furthermore, breaking the sample to obtain a cross-section resulted in rough edges of the polymer layers. Nevertheless, from the SEM it can be seen that the individual layers are regularly distributed with homogeneous thicknesses throughout the stack.

Accordingly, dye-doped 29-layer stacks were fabricated. The dye LR was embedded in multiple layers to increase the samples' absorptance of incident light. As the photonic effects are reduced in the outer layers, only the inner 10 of the 14 PMMA layers were doped ($\zeta_{\text{dye}} = 1$ w%). Reflection measurements revealed a near-unity peak reflectance of 98.9% and a good match with the dye's emission spectrum (Fig. 4.7 (b)). These samples were used to study the effect of the photonic crystal on the dye's emission and the concentrator performance.

In this work the maximum layer number of 29 was chosen for practical reasons. In principle, more layers can be deposited using the spin coating process developed

(a) Cross-section of a 29-layer stack (b) Reflectance of optimized 29-layer stack

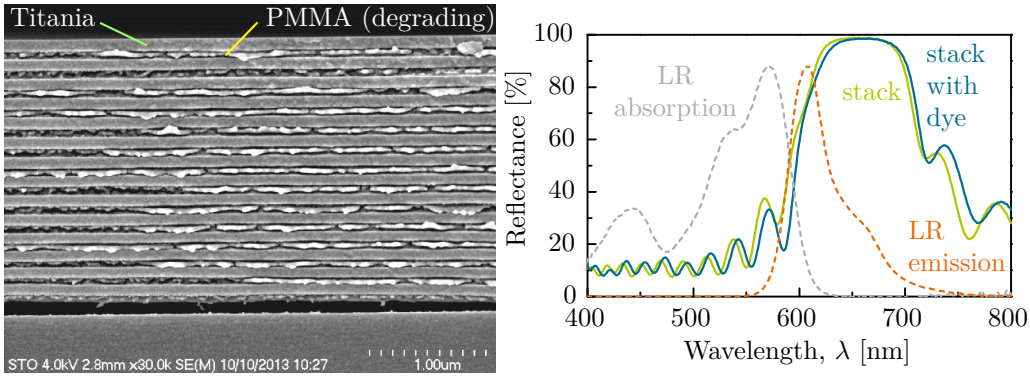

Figure 4.7: Spin coated stacks with up to 29 layers were fabricated. (a) The cross-section SEM image shows regularly and homogeneously distributed layers of titania and PMMA. The irregularities in the PMMA layers arise from the sample preparation through breaking. Exact thickness measurements of the layers were not possible due to the insufficient resolution and electron beam induced degradation and shrinkage of the polymer layers. (b) The reflectance of optimized 29-layer stacks with and without embedded dye matched the targeted characteristics, where the onset of reflection coincides with the cross-over of the dye's absorption and emission spectra.

in this work as no limitations were found in this regard. More layers would increase the absorptance and the strength of the photonic effect on emission. For further device optimization, the absorptance can be increased by depositing a $\lambda_{\text{design}}/8$ thick layer of PMMA on top of the top titania layer to reduce parasitic reflection of incident light in the dye's absorption range [139, 149].

4.1.2 Thin film filters bonded with a dye-doped layer

As an alternative to the spin coated stacks, multilayer structures were fabricated with established thin film technologies that allow for homogeneous films with good thickness control. To embed a dye in these "filters", two samples were bonded with a dye-doped layer in between, as illustrated in Fig. 4.1 (b).

As one option, filters with silicon oxide (SiO_2, $n \approx 1.5$) and silicon nitride (SiN_x, $n \approx 2$) were deposited using plasma-enhanced chemical vapor deposition (PECVD) in-house at Fraunhofer ISE. To optimize the optical properties of a 30-layer stack, i.e. to achieve low reflectance in the dye's absorption range and high reflectance in the emission range, an evolutionary algorithm was used. This way, the individual layer thicknesses were randomly varied in a iterative procedure to match the calculated reflectance with the targeted curve. When fabricating the optimized stack, a good agreement of the simulated and measured reflectance

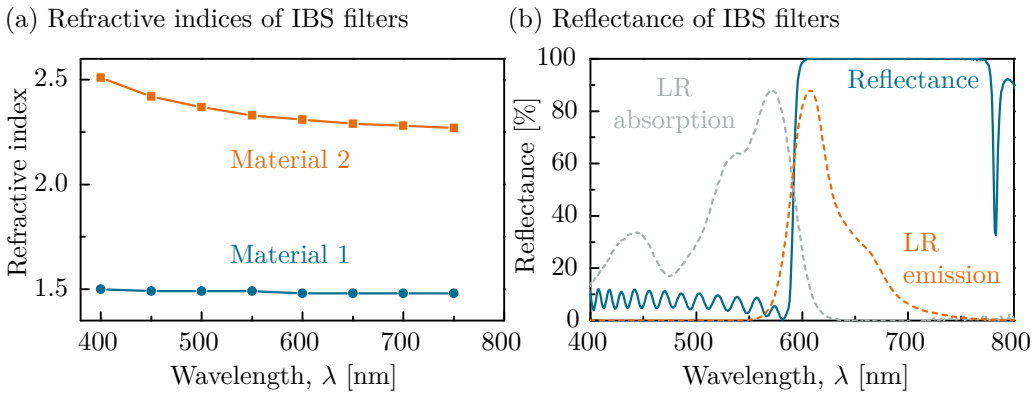

Figure 4.8: (a) The refractive indices of the two materials used to fabricate 33-layer stacks by ion beam sputtering (IBS) were specified by Laseroptik GmbH for certain wavelengths (lines are guides to the eye). (b) Due to the high refractive index contrast and the exact thickness control, the filters feature the desired low reflectance in the dye's absorption range, high reflectance in the emission range, and a steep transition at $\lambda = 600$ nm where the absorption spectrum crosses the emission spectrum.

could be obtained. Absorption measurements of the stacks, however, revealed large parasitic absorption of the stacks in the absorption range of the dye (up to 80% at $\lambda = 400$ nm). This absorption was caused by the SiN_x layers, even though process parameters optimized for low absorption were used. This finding could be confirmed in calculations using an advanced optical model for SiN_x including absorption (Tauc-Lorentz model). Details about these PECVD experiments can be found Ref. 149. In this work these samples were not considered further since the large parasitic absorption is detrimental to the use as PLSCs.

As another option, filters were fabricated externally at Laseroptik GmbH. Based on the specifications of the desired optical properties (low reflectance for $\lambda = 400$–600 nm, high reflectance for $\lambda = 600$–750 nm, no absorption in these ranges), Laseroptik GmbH designed and fabricated filters with 33 layers using ion beam sputtering (IBS). While the two materials used in the stack were not stated by the company, their refractive indices were specified for different wavelengths (Fig. 4.8 (a)). The stacks were deposited on the same $25 \times 25 \times 1$ mm^3 glass substrates as used for the spin coated stacks.

Due to the large refractive index contrast, high spectral selectivity of the reflectance was obtained for the filter's reflectance (Fig. 4.8 (b)). The steep transition from transmission to reflectance at $\lambda = 600$ nm matches very well with the crossover wavelength of the dye's absorption and emission spectrum. In the relevant spectral region $\lambda > 400$ nm no parasitic absorption was found, making it suitable for the application as PLSCs.

Bonding process

To incorporate the luminescent dye in these multilayer structures, two filters were bonded with a dye-doped layer in between. Such a bond needs to provide mechanical stability and good optical contact of the two filters. The thickness of the intermediate layer determines the strength of the photonic effect [171] and the absorptance of incident light. For comparing measurement results with calculations, a good control of the thickness is desired. As a trade-off between photonic effects and absorption of incident light, a target layer thickness of 800 nm was chosen.

Different approaches to establish such a bond were investigated: using silicone provided good optical contact but poor solubility for the dye. In-situ polymerization of the monomer methyl methacrylate (MMA) using the thermal initiator azobisisobutyronitrile (AIBN) also provided good optical contact. Both methods, however, offer no exact thickness control. As an alternative, dye-doped PMMA layers were deposited on the filters using spin coating followed by thermal bonding. This way, the thickness can be controlled over the thickness of the polymer layer. Best results were obtained using PMMA with $M_w \approx 120000$ (Aldrich 182230) with a polymer-to-toluene concentration of 10 w%. Films with 400 nm thickness were deposited on each of the two filters by spinning at 8000 RPM.

In a first experiment, these coated filters were bonded by heating on a hotplate at 180 °C with a weight of 800 g on top for 15 min. Better optical contact and a more reliable process, however, were found using the platen press P 200 MV from Dr. Collin GmbH at the Freiburg Materials Research Center (FMF). This machine allows evacuating the bonding chamber, which helped to reduce unwanted gas inclusions. Best results were obtained as follows: the samples were pre-heated to 100 °C before increasing the pressure to 10 MPa and holding it constant for 12 min. Subsequently, the temperature was slowly reduced stepwise to room temperature with pressure still being applied. To avoid damage to the samples (especially at the edges), two elastic polytetrafluoroethylene (PTFE) sheets were used between the platens and the samples.

The optical quality of the different bonding procedures was evaluated using reflectance measurements of glass samples bonded with undoped PMMA, as shown in Fig. 4.9 (a). An intact bond was indicated by a reflectance similar to that of a single glass substrate. In this case no optical interface was introduced inside the bonded sample where reflection occurs, as the refractive indices of glass and the bonding layer are similar. In samples without good contact, an additional reflecting interface was formed in between the two samples, resulting in higher reflectance, as shown for the hotplate process.

Best results were obtained for the platen press process with good optical contact and thickness control. As shown in Fig. 4.9 (b), however, the bond was not successful over the entire sample surface: interference fringes at the edges indicated poor optical contact. Furthermore, a slight extension of these regions after a cou-

(a) Reflectance of bonded glass samples (b) Photograph of bonded glass substrates

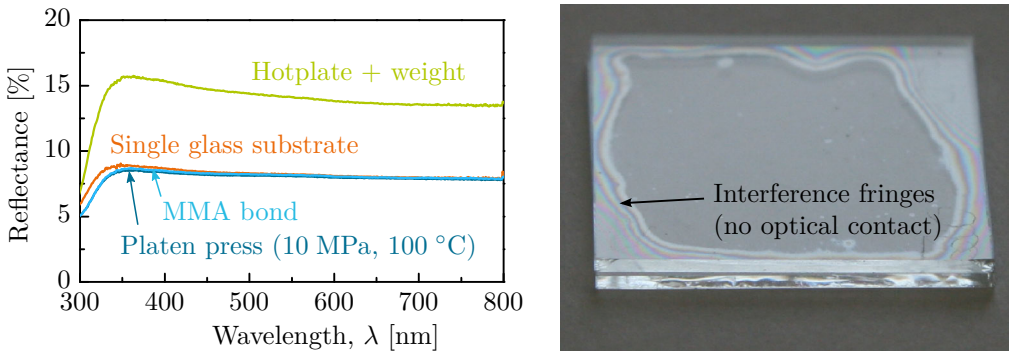

Figure 4.9: (a) Different bonding techniques were evaluated by measuring the reflectance of two glass substrates bonded with an undoped PMMA layer. Good optical contact is indicated by a reflectance similar to that of a single glass substrate (no additional reflecting interfaces inside). Best results were obtained for the platen press process, which also allows controlling the thickness of the bonding layer. (b) The bond was, however, not successful at the sample's edges, as seen from interference fringes.

ple of days was observed, presumably due to stress relief processes. To increase the long-term stability, further optimization of the bonding process is needed. For the characterization of the samples in this work in terms of emission and concentrator performance, however, the bond quality is sufficient as long as only the bonded regions are analyzed.

4.2 Fabrication of opal structures

In addition to multilayer photonic structures, opals were investigated as a potentially cost-effective approach to realize three-dimensional photonic crystals. Opals consist of colloids that are close-packed in a face centered cubic (fcc) arrangement. They can be obtained from the self-assembly of colloids using different techniques and have been studied intensively in literature [172–176].

Here, the organic dye Rhodamine B was embedded in PMMA colloids, synthesized by Lorenz Steidl within a cooperation with the group of Prof. Rudolf Zentel at University of Mainz: the colloids were fabricated by a two stage seeded polymerization under similar conditions as described for the preparation of large PMMA beads by surfactant-free emulsion polymerization [177]. In a first step PMMA colloids with a diameter of about 200 nm doped with Rhodamine B (about 30 mmol dye per kg polymer) were synthesized using potassium peroxodisulfate as an initiator [178]. A small portion of sodium dodecyl sulfate (about 2 mmol/L) was added to prevent coagulation of the emulsion due to the high dye content. To

shift the opal's band gap and thus the resulting reflection peak to the emission wavelength of the dye, the diameter of the colloids was increased by polymerizing MMA onto these particles. The size of the colloids was adjusted by the ratio of monomer to seed particles according to

$$d_\mathrm{c} = d_\mathrm{s} \sqrt[3]{1 + \frac{m_\mathrm{m} C_\mathrm{p}}{m_\mathrm{s}}}, \tag{4.1}$$

where d_c denotes the aspired colloidal diameter, d_s the diameter of the seed particles, m_s the mass of the seed particles, m_m the mass of the added monomer and C_p the conversion of the polymerization. The final diameter d_c of the colloids was determined based on the spectral position of the reflectance peak λ_peak, which are related by

$$d_\mathrm{c} = \frac{0.634}{\sqrt{2}} \lambda_\mathrm{peak} \tag{4.2}$$

for the first band gap in L-direction (centered at $\omega a / 2\pi c = 0.634$ with $a = \sqrt{2} d_\mathrm{c}$). Colloids with a final diameter of $d_\mathrm{c} = 267$ nm were used to match the emission spectrum of Rhodamine B.

For the preparation of opal films from the colloids, three different methods based on self-assembly were evaluated in this work: dip coating, spin coating and evaporation (see Figure 4.10).

Dip coated samples were obtained by pulling a glass substrate slowly out of an aqueous colloidal solution. During this process, the colloids aggregate at the meniscus and form a layer on the substrate surface due to adhesion and cohesion. The colloids thereby tend to form the thermodynamically favorable closest package of spheres (fcc). The number of sphere layers and the quality of the opal film

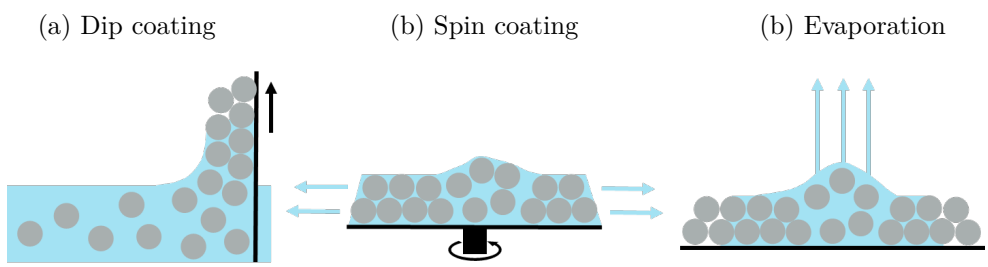

Figure 4.10: Sketches of the different methods evaluated in this work that were used to obtain opal film from an aqueous colloidal solution: (a) using dip coating, a glass substrate is slowly pulled out of the solution. (b) In the case of spin coating the solution is dispensed on the substrate and spread during the rotation process. (c) By wetting the substrate with the colloidal solution, the water slowly evaporates, yielding an opal film.

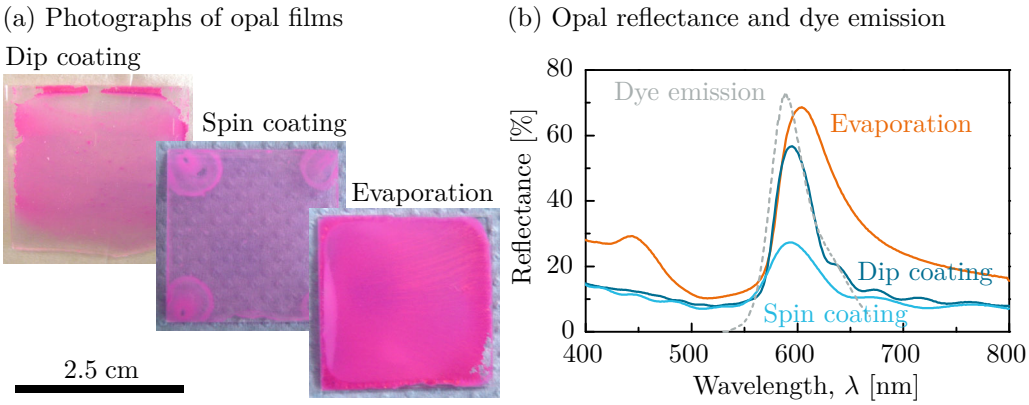

Figure 4.11: (a) Photographs of opal films from dip coating, spin coating and evaporation using PMMA colloids doped with the organic dye Rhodamine B (sample size of 2.5×2.5 cm^2). The film thickness and its homogeneity over the sample strongly depend on the process (parameters), as explained in detail in the text. (b) The colloid diameter was adjusted to match the reflectance peak (due to the opal's first band gap) with the emission spectrum of the dye.

mainly depend on the pulling speed and the colloid concentration, but also on the temperature, the humidity and the atmospheric pressure [179]. The dip coated samples used in this work were fabricated by Steidl at University of Mainz [180].

In the spin coating process, the aqueous colloidal solution was dispensed on a glass substrate and spread over the complete surface during the rotation process. During and after the spin coating process the water evaporates, resulting in an opal film. The thickness and quality of the films depend on the colloid concentration, the acceleration and final spin speed [172].

In the evaporation approach the colloid solution was dispensed to wet a glass substrate. The water then evaporated slowly over several days. The film thickness and quality depend on the concentration and volume of colloid solution as well as the surrounding temperature and humidity [177, 181]. To stabilize the humidity conditions, the samples were covered with a petri dish.

For the spin coating and the evaporation approach, the $25 \times 25 \times 1$ mm^3 glass substrates were hydrophilized using a sodium hydroxide solution (25 %) previous to the deposition of the opal films. The film quality was found to be enhanced when the colloidal solution was put in an ultrasonic bath for ca. 2 h before the deposition to break up aggregated colloids.

The fabricated samples were characterized by means of optical measurements. Typical reflectance curves for the different processes are shown in Fig. 4.11 (b). The reflectance of opals features a strong specular reflection peak related to the first band gap. Towards shorter wavelengths the reflectance typically increases

(a) Optical micrograph of dip coated opal (b) SEM graph of opal (by evaporation)

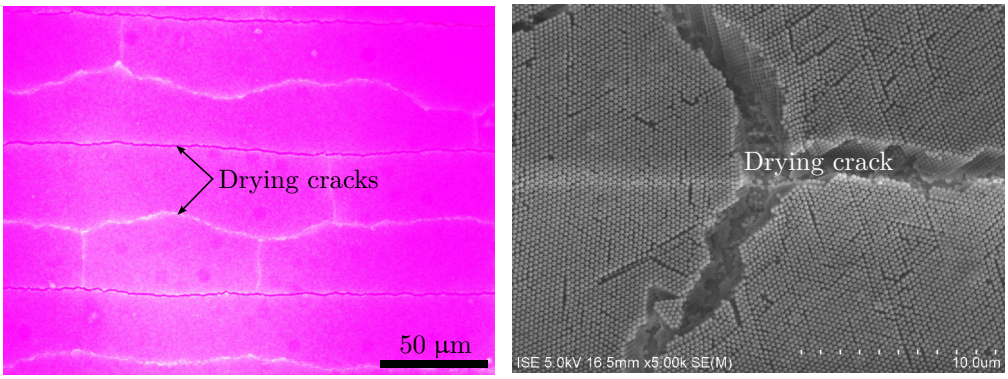

Figure 4.12: Opal films typically feature cracks from shrinking due to the evaporation of the water. (a) Using optical microscopy, the crack density and film quality in terms of orientation defect could be assessed in a non-destructive way. The color of the micrograph is due to the selective reflectance and the emission of the embedded dye. (b) Higher resolution and detailed information were obtained using SEM, which allowed for the imaging of single colloids.

due to scattering effects. This increase was found only in the diffuse, not in the specular reflectance, which confirms that it arises from diffuse scattering.

Furthermore, optical microscopy was found to be able to examine crystalline defects in a non-destructive way (in contrast to SEM, for example). As a well-known phenomenon, opal films feature cracks that arise from shrinking due to the evaporation of the water (or other solvents), as shown in Fig 4.12. These cracks were found to be very detrimental to the use of these opal films as LSCs due to unwanted out-coupling of light, as discussed in Sec. 6.2.2.

The processes of spin coating and evaporation were optimized in a comprehensive study to obtain homogeneous films of high quality with low crack density. Table 4.2 summarizes the process parameters that yielded the best results for the different processes. While the detailed analysis and process development can be found in the thesis of Posdziech [148], the main findings are summarized in the following.

Dip coating was able to produce samples with relatively low crack density: ordered regimes with a size of up to 100 µm were found. A peak reflectance of around 60 % could be achieved with low diffuse part, i.e. low scattering due to crystalline defects. The homogeneity of the film over the sample (ca. 2.5 cm), however, was rather poor (see Fig. 4.11 (a)).

Spin coated samples featured many cracks with ordered regimes of only 10 µm. Some of the grains were grown in other orientations than the desired $\langle 111 \rangle$. A low peak reflectance of merely up to 30 % was obtained, though with a low fraction

Table 4.2: Optimized process parameters for the fabrication of opal film using the spin coating and evaporation methods.

General	
Glass hydrophilization	2 h in 25 % sodium hydroxide solution
Colloidal solution treatment	2 h in ultrasonic bath before deposition
Spin coating	
Spin speed Ω	500 RPM
Spinning duration (plateau time)	120 s
Ramp up time (acceleration)	10 s
Colloid concentration	18.4 w%
Dispensed volume	200 µL
Dispensing mode	static
Evaporation	
Colloid concentration	9.2 w%
Dispensed volume	100 µL

of scattered light. The reason for the low reflectance is the small thickness of the film, which can be increased with a higher colloid concentration of the solution and lower spin speed. While the maximum concentration available in this work was 18.4 w%, low spin speeds resulted in artifacts at the edges of the substrate surface, as shown in Fig. 4.11 (a). Nevertheless, apart from the edges the film was found to be homogeneously distributed.

Samples from evaporation featured a low crack density similar to that of dip coated samples (ordered regimes of 100 µm). Due to the thick films, large reflectance (ca. 70 %) were found, but with a large fraction of scattered light, indicating many small defects in the crystalline structure. The homogeneity of the film over the sample was also rather poor as the solution did not dry homogeneously, but retracted with time to one point of the sample (Fig. 4.11 (a)).

Overall, the best results were obtained using the dip coating process due to the low crack density and low scattering. The quality of the samples in terms of cracks and homogeneity, however, was not satisfactory. Further work is necessary to improve the processes. Possible approaches to reduce the crack density could be the use of fluid substrates for crystallization [182] or the preparation of inverted opals with low-shrinking material [183]. Large area opals have been obtained using melt compression [176, 184] and spray coating [185]; however, they are still not free of defects.

4.3 Characterization

This section covers the essential methods for the investigation of the optical properties of the fabricated samples. I focus on methods and setups that were used and developed specifically for the purpose of this work, omitting common and well-known techniques such as scanning electron microscopy (SEM), atomic force microscopy (AFM), etc..

4.3.1 Reflectance, transmittance, absorptance and concentrator quantum yield

The reflectance $R(\lambda_\mathrm{i})$, transmittance $T(\lambda_\mathrm{i})$ and absorptance $A(\lambda_\mathrm{i})$ of a sample state the fraction of incident light that is reflected, transmitted and absorbed, respectively, as a function of the incident wavelength λ_i. These optical properties were obtained using the commercial spectrophotometer Cary5000 from Varian with an integrating sphere. In this setup, monochromatic light is selected from a "white" light source using a double grating monochromator to illuminate the sample with a spot size of ca. 1×1 cm^2 in reflectance, transmittance or center-mount configuration (Fig 4.13).

The inner surface of the sphere diffuses all light inside the sphere, where its intensity is detected by a photomultiplier or InGaAs-detector (depending on the spectral range of interest). Alternately measuring the sample beam and a reference beam at each incident wavelength allows one to correct for the spectral intensity and temporal stability of the light source. Using a reference sample with known optical properties, the detector signal can be calibrated for the spectral characteristics of the integrating sphere and the detector sensitivity, which allows for the measurement of absolute fractions of the incident light.

The reflectance can be measured in two configurations: as the sample is slightly tilted with respect to the sample beam (ca. 7°), both specular (R_s) and diffuse reflectance (R_d) are detected. The diffuse reflectance can be measured when a small port of the sphere is removed so that the specular reflection beam leaves the integrating sphere undetected. Similarly, the specular (T_s) and diffuse (T_d) parts of transmittance can be separated by an additional transmittance measurement without the integrating sphere, where the specularly transmitted beam is detected by a second detector. In the center-mount measurement C all light that is reflected, transmitted or guided to the edges is collected by the sphere. To capture specularly reflected light, the sample is tilted by ca. 8°.

When measurements from the different configurations are compared or used to calculate other quantities, the fact that they were obtained with different angles of incidence needs to be considered for samples whose optical properties show a strong angular dependence, such as the photonic structures investigated in this work. The typical shift of reflectance and transmittance peak wavelengths λ_peak

of photonic structures to shorter wavelengths with oblique incidence angles ϕ_i can be modeled using Bragg's law

$$\lambda_\mathrm{peak}(\phi_\mathrm{i}) = \lambda_\mathrm{peak}(0)\sqrt{1 - \frac{\sin^2\phi_\mathrm{i}}{n_\mathrm{eff}^2}}, \tag{4.3}$$

where the effective refractive index n_eff can be obtained by the volume-averaged refractive indices of the structure. As an approximation, the wavelength axis was rescaled accordingly for the tilted measurements to obtain the spectral characteristics for normal incidence, while the reflectance and transmittance values were kept constant.

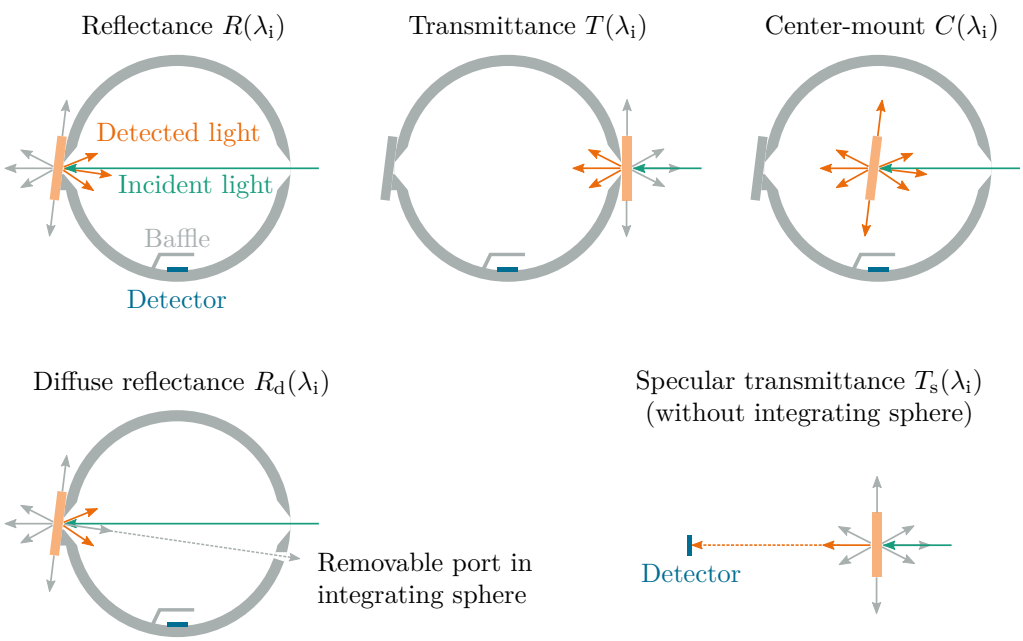

Figure 4.13: Sketch of the different configurations for the optical measurements using the CARY5000 setup with an integrating sphere: depending on the type of measurement, only the reflected, transmitted or all light including the light guided to the edges of a sample (center-mount) are detected. To distinguish between specular and diffuse reflectance, a small port in the integrating sphere can be removed to couple out the specular reflection (sample is slightly tilted). The specular transmittance is obtained without the integrating sphere using a second detector.

Absorption in non-luminescent samples

In non-transparent samples, not all incident light is reflected or transmitted. The absorbed fraction can be obtained from the difference

$$A(\lambda_\mathrm{i}) = 1 - R_\mathrm{s}(\lambda_\mathrm{i}) - T_\mathrm{s}(\lambda_\mathrm{i}). \tag{4.4}$$

Assuming a planar and homogeneously absorbing sample with thickness d (>> coherence length), the absorption coefficient $\alpha(\lambda)$ can be obtained via

$$\alpha(\lambda) = -\frac{1}{d}\ln\left(\frac{T_\mathrm{s}^2 - R_\mathrm{s}^2 + 2R_\mathrm{s} - 1 + \sqrt{4T_\mathrm{s}^2 + (T_\mathrm{s}^2 - R_\mathrm{s}^2 + 2R_\mathrm{s} - 1)^2}}{2T_\mathrm{s}}\right), \tag{4.5}$$

as shown in Sec. 3.3.2.

In samples with significant amounts of scattering, light is also diffusely reflected and transmitted and eventually guided to the edges. In this case the absorbed fraction without scattering can be obtained from $1 - R - T$ or $1 - C$. Applying both methods allows one to separate the absorption and scattering coefficients, as described by Rist [146].

Absorption in luminescent samples

In luminescent samples incident light is not only parasitically absorbed and scattered by the matrix material, but predominantly absorbed by the luminescent species. This absorbed light is subsequently emitted and can leave the sample at the surface or edge faces to fall onto the detector. To determine the total absorption A_tot of a luminescent sample, it is reasonable to use the specular components of reflectance and transmittance according to Eq. (4.4). The diffuse components in R and T and the light guided to the edges (in C) mainly arise from the emitted light (assuming low scattering).

To separate the fractions of light absorbed by the dye and by the matrix material, the total absorption needs to be split up. For samples that can be treated incoherently and that feature homogeneous distributions of the dye and parasitic absorption within the same material, the absorbtances by the dye A_dye and the matrix material A_ref are given by

$$A_\mathrm{dye} = \frac{\alpha_\mathrm{dye}}{\alpha_\mathrm{tot}} A_\mathrm{tot} = \left(1 - \frac{\alpha_\mathrm{ref}}{\alpha_\mathrm{tot}}\right) A_\mathrm{tot} \quad \text{and} \quad A_\mathrm{ref} = \frac{\alpha_\mathrm{ref}}{\alpha_\mathrm{tot}} A_\mathrm{tot}, \tag{4.6}$$

where the absorption coefficient of the dye α_dye can be obtained from the total absorption coefficient α_tot (from measuring the luminescent sample) and the absorption coefficient of the matrix material α_ref (from measuring an identical reference sample but without any dye). This stands in contrast to the incorrect method used in Ref. 186, as it is not the absorptances A of two materials which add up, but rather their absorption coefficients ($\alpha_\mathrm{tot} = \alpha_\mathrm{dye} + \alpha_\mathrm{ref}$).

The samples analyzed in this work, however, feature sub-wavelength structures for which this incoherent treatment based on simple Lambert-Beer absorption is not valid anymore. Thus absorption depends on the local electromagnetic field inside the sample (see Sec. 2.2.3). Furthermore, the dye and the material(s) causing parasitic absorption may be spatially separated. Therefore, the separation of the absorbed fractions is very complex and not accessible by these means. To estimate the absorptance by the dye for the samples used in this work, however, A_{dye} was approximated by A_{tot}, as the absorption by the matrix material (PMMA) is much smaller than that of the dye in the relevant spectral range ($\lambda > 400$ nm).

Concentrator quantum yield

The spectrophotometer setup can further be used to measure the concentrator quantum yield (CQY) $\eta(\lambda_{\mathrm{i}})$ of (P)LSCs. The CQY is the ratio of the number of photons guided to the edge faces of a sample to the total number of incident photons with wavelength λ_{i}. As the center-mount measurement contains the guided light, the CQY is given by subtracting the reflectance and transmittance [186]

$$\eta(\lambda_{\mathrm{i}}) = C(\lambda_{\mathrm{i}}) - R(\lambda_{\mathrm{i}}) - T(\lambda_{\mathrm{i}}). \tag{4.7}$$

In more detail, measurement data from luminescent samples need to be corrected. In contrast to non-luminescent samples, the light falling on the detector is not monochromatic (with λ_{i}) but also contains emitted light with longer wavelengths (due to the Stokes shift). Thus the calibration with the spectral sensitivity of the measurement system at the incident wavelength can result in erroneous results. Goldschmidt therefore proposed a correction method [186], which, however, does not involve all necessary correction, as shown by Posdziech [148]: A thorough correction requires detailed knowledge about the commercial setup, which was inaccessible.

In spectral regions with strong changes in detector efficiency (in the near IR, for example) the concentrator quantum yield thus cannot be measured satisfactorily. In the range of visible light in which the dyes used in this work operate, however, the effect is rather small and the result from Eq. (4.7) can be used as a qualitative measure of a sample's light guiding property, allowing for a comparison of samples with spectrally similar emission.

4.3.2 Spectroscopic ellipsometry

Ellipsometry was used to obtain the thickness and refractive index of thin layers. It relies on the polarization dependence of the reflection coefficients: monochromatic light (λ_{i}) with known s- and p-polarization components hits the sample surface at a certain angle. The polarization of the reflected light is measured to obtain the

change in polarization

$$\frac{r_\mathrm{p}(\lambda_\mathrm{i})}{r_\mathrm{s}(\lambda_\mathrm{i})} = \tan\left(\Psi(\lambda_\mathrm{i})\right)e^{i\Delta(\lambda_\mathrm{i})}, \tag{4.8}$$

where r_p and r_s are the complex reflection coefficients of s- and p-polarization, respectively. The complex ratio is typically expressed with the real parameters Ψ (measure of amplitude ratio) and Δ (phase shift difference).

Only for an ideal sample with infinite thickness can the refractive index be obtained analytically. For more complex systems the sample is modeled based on assumptions (range of thickness(es) and refractive indices). This model is then fit to the measurement data.

In the spectroscopic ellipsometry setup used in this work (M-2000 from J.A. Woollam Co., Inc.), incident light is varied in wavelength λ_i, which allows one to determine the material dispersion of the investigated material(s). Typically, this spectral dependence of the refractive index is modeled using an analytical expression, thus reducing fitting degrees of freedom.

For the materials used in this work, mainly the *Cauchy*-model was used, which is applicable for dielectric materials without significant absorption in the considered spectral range. Thus,

$$n(\lambda) = C_1 + \frac{C_2}{\lambda^2} + \frac{C_3}{\lambda^4} \tag{4.9}$$

with the three fit parameters C_1, C_2 and C_3 was used to describe the real part of the material's refractive index n.

4.3.3 Angular resolved photoluminescence

To investigate the influence of the photonic crystal on the emission of an embedded fluorescent dye, the emitted light was spectrally analyzed. The detected photoluminescence (PL) strongly depends on the specific modes that are detected and therefore on the actual detection setup. This measured spectrum is very sensitive to emission changes induced by a photonic crystal, as theoretically shown in Sec. 5.1.4. Here, a setup was built to measure the spectrum of the light escaping through the sample's surface as well as the light guided to the edge face, both as a function of the detection angle.

In both cases, the sample is mounted on a rotation platform together with the green excitation laser ($\lambda = 532$ nm, diode-pumped solid-state (DPSS) laser module RLTMGS-532 from Roithner LaserTechnik), as shown in Fig. 4.14 (a). In this configuration the angle of incidence of the excitation onto the sample and thus the absorptance is kept constant for all detection angles. The emitted light is collected using a fiber (Ø 1 mm, see Fig. 4.14 (b)), which is connected to a spectrometer (SP2300i from Princeton Instruments, equipped with a PIXIS-CCD

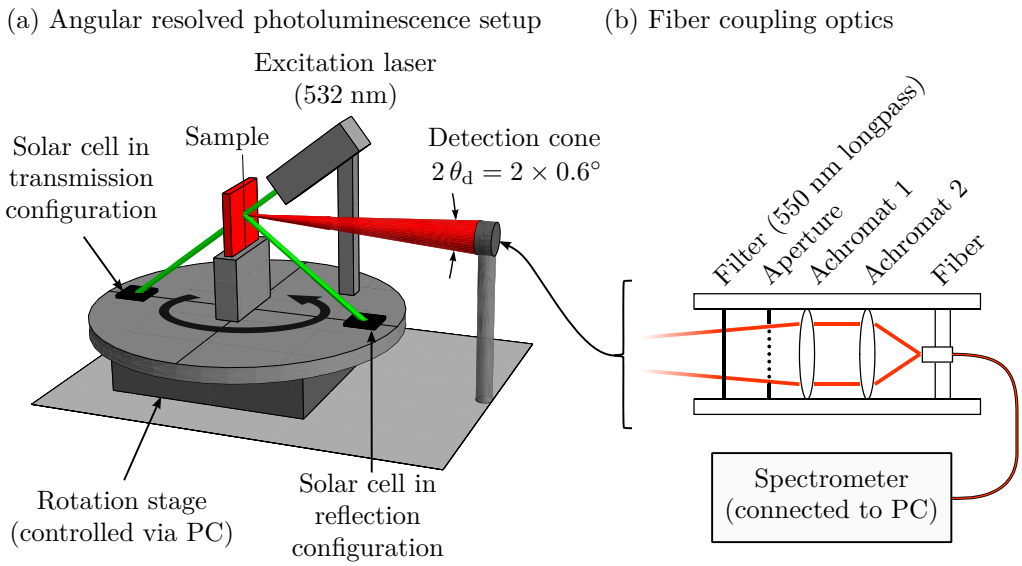

Figure 4.14: (a) Sketch of the automated angular photoluminescence setup. Both sample and excitation laser are mounted on a rotating platform to ensure constant excitation and detection conditions when rotating. The emitted light is coupled to a fiber (Ø 1 mm), which is connected to a spectrometer, as shown in (b).

camera). This way, the detection fiber was fixed during the measurements to avoid bending-related changes in its spectral transmission characteristic.

Given the geometry of the setup and the chosen fiber coupling optics, a detection cone with half-angle $\theta_d = 0.6°$ was obtained, which defines the angular resolution. The spectral sensitivity of the whole detection system (optical components, fiber transmission, grating efficiency and detector quantum yield) was calibrated using a tungsten-halogen lamp with a known emission spectrum.

Angular resolved surface PL

To measure the light escaping from the sample's surface, the configuration shown in Fig. 4.15 (a) was used. The sample was mounted with the point of excitation at the surface placed in the center of rotation. Light was detected for detection angles ϕ_d from $-10°$ to $90°$ in increments of $1°$. For $\phi_d \geq 85°$, however, shading by the sample holder occurred and no light was detected.

To quantitatively compare measurements of different samples that absorb more or less of the incident light, the absorption was measured during the luminescence measurement using a silicon solar cell as a photodetector. Connected to a current-voltage amplifier, the cell's short circuit current was recorded as a measure of intensity. The 5×5 mm^2 large concentrator solar cell was placed behind and in

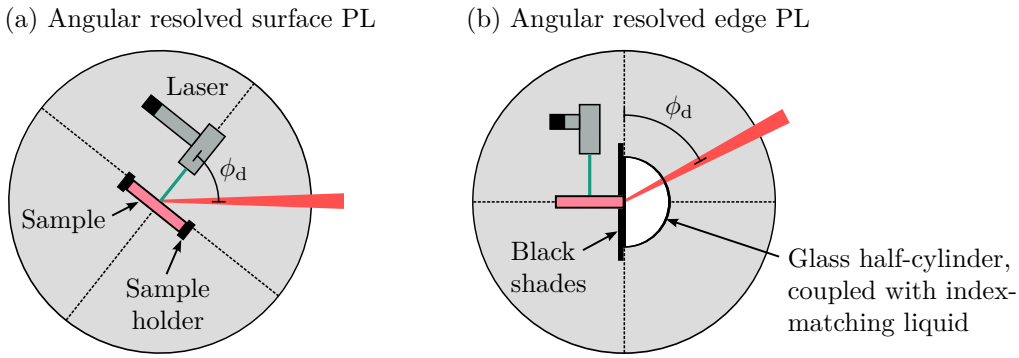

Figure 4.15: Top view of the two configurations used to measure the angular resolved photoluminescence (a) escaping from the sample's surface and (b) coupled out at the edge face. In (a) the excitation spot on the surface of the sample is centered on the rotation platform. In (b) the sample's edge face is mounted in the center of rotation and coupled to a glass half-cylinder using index-matching liquid to couple out the guided light.

front of the sample to detect the transmitted laser beam without the sample (T_{laser}) and with the sample (T_{sample}) as well as the reflected beam (R_{sample}), as shown in Fig. 4.14. The measured spectra $\Pi_{\text{meas}}(\lambda)$ were divided by the absolute absorption to obtain the normalized spectra

$$\Pi_{\text{norm}}(\lambda) = \Pi_{\text{meas}}(\lambda)/(T_{\text{laser}} - T_{\text{sample}} - R_{\text{sample}}). \tag{4.10}$$

This way, the measurements were also corrected for the absolute intensity of the excitation laser, which was found to be stable during one measurement of all angles (a few minutes), but drifted over longer times (hours). The influence of light emitted by the sample on the solar cell signal can be neglected due to the small size of the cell and the distance to the sample. Strongly scattering samples, however, may lead to erroneous absorption values as only the specular components of the reflected and transmitted laser light are detected. Furthermore, multiple internal reflections in some samples led to multiple spatially shifted transmission and reflection spots, not all of which fell on the cell area. In these cases the absorption is over-estimated, which should be noted for the interpretation of the results.

Angular resolved edge PL

To measure the angular distribution of the light guided to the sample's edge face, a half-cylinder of glass was coupled to the edge face using index-matching liquid (see Fig. 4.15 (b)). In this way all light is coupled out as no (total) reflection at the edge face occurs. In contrast to the surface measurement, the angle of detection in

this configuration corresponds to the angle of propagation inside the sample. The edge face of the sample was centered on the rotation platform while the sample was excited at 1 cm distance from the edge. Black shades were used to ensure that only light from the edge face is detected. Light was detected for detection angles ϕ_d from $-5°$ to $185°$ in $1°$ steps.

4.3.4 Integrated photoluminescence

In addition to angular resolved measurements, the photoluminescence was measured in different configurations using an integrated sphere to study the effect of the photonic crystal on the emission of light (Fig. 4.16). The integrating sphere 819C-SL-5.3 from Newport was connected to the spectrometer SP2300i from Princeton Instruments using an optical fiber. The spectral sensitivity was calibrated with a tungsten-halogen lamp. For excitation, the green laser ($\lambda = 532$ nm) described in the previous section was employed.

First, the spectral composition of the light coupling out at a sample's edge face was measured using a customized sphere port with a slit to fit the edge face dimensions of the PLSC samples (length of 2.5 cm). This way, the sample was excited with the green excitation laser outside the sphere while light guided to the edge was coupled into the sphere (see Fig. 4.16 (a)).

Second, all light emitted as well as reflected, transmitted and scattered by a sample was detected inside the sphere (Fig. 4.16 (b)). For this purpose a custom-made sample holder of diffusely reflecting PTFE was designed to position the

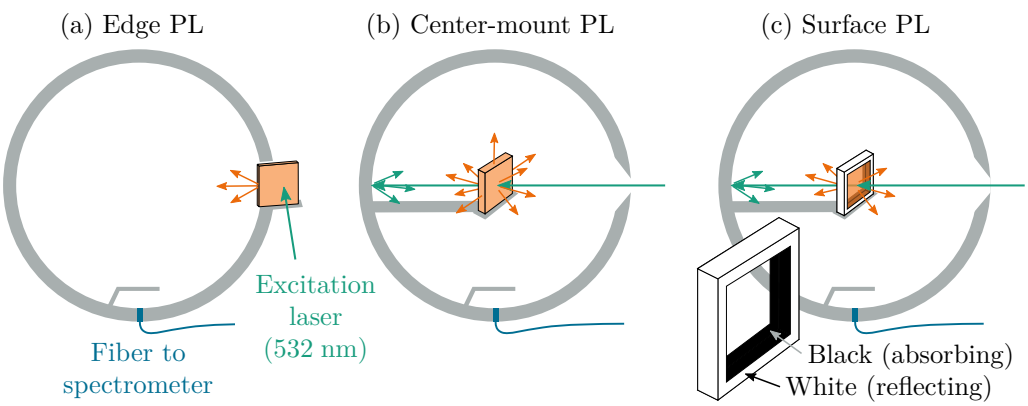

Figure 4.16: Different setups for integrated photoluminescence (PL) measurements using an integrating sphere connected to a spectrometer: in (a) the light guided to the sample's edge face is detected in the sphere. In (b) the sample is mounted inside the sphere to detect all light that is emitted. Similarly, in (c) all light escaping from the surfaces of a sample is detected, while the edge faces are covered with a cardboard frame to absorb the guided light.

sample inside the sphere ("center-mount" configuration). Apart from the luminescence signal, also a large signal from the excitation laser was detected. This background signal was removed using a reference measurement with no sample in the sample holder, though with the excitation laser turned on.

Similarly, the photoluminescence escaping through the front and back surface was measured: a frame of cardboard was constructed to cover the sample's edge faces, as shown in Fig. 4.16 (c). The inside of the frame was black to absorb all the light coupled out at the edges. The outside of the frame was white (i.e. diffusely reflective) to minimize a parasitic influence on the spectral collection characteristic of the integrating sphere setup.

Chapter 5

Effect of photonic crystals on emission

In this chapter the effect of a photonic crystal on the emission of a fluorescent dye is investigated. Results of theoretical calculations are presented using the modeling methods developed in this work. It is shown how the surrounding structure changes the emission spectrum, the PLQY and the fluorescence lifetime as well as the fraction of emitted light that is guided in the structure. Furthermore, experimental results of angular and integrated photoluminescence measurements are presented and compared to theoretical calculations. Using different reference experiments, I separate the influence of the photonic structure from other effects related to filter reflection, and show that the observations confirm the predicted effects.

5.1 Modeling results

5.1.1 Local density of photon states (LDOS)

The LDOS of photonic crystals is the decisive quantity when emission is studied. It determines the transition probability of spontaneous emission according to Fermi's golden rule. Here the LDOS was calculated for ideal, i.e. infinite and periodic photonic crystals using eigenmode calculations (see Sec. 3.1.1).

For the Bragg stack, refractive indices of $n_{\mathrm{lo}} = 1.5$ and $n_{\mathrm{hi}} = 2$ were used as realistic material properties for experiments. The unit cell size $a = 188$ nm was chosen as a result of an optimization of the overall concentrator performance for the considered dye Lumogen Red (see Sec. 6.1.2). The investigated opal consisted of spheres with refractive index $n_{\mathrm{sphere}} = 1.5$, surrounded by air ($n_{\mathrm{void}} = 1$). To match the emission of rhodamine B, a sphere diameter of $d_{\mathrm{sphere}} = 267$ nm

($a = 378$ nm) was chosen, which is consistent with the fabricated samples.

As the LDOS is a *local* quantity, it depends on the actual position $\boldsymbol{r}$ inside the photonic crystal's unit cell. This variation of the LDOS with $\boldsymbol{r}$, as reported in literature [98, 100], was confirmed in the calculations (see e.g. Fig. 3.2 for the Bragg stack) as well as the difference from the *total* DOS. The position dependence of the LDOS has to be considered when emitter ensembles are studied: especially when local absorption is not uniform, one has to account for the corresponding LDOS for each emitter position, as explained in Sec. 3.2.

To present results concisely, however, local absorption was neglected at this point and the LDOS was averaged over all relevant dye positions. In the Bragg stack, this means averaging over all positions in the low-refractive-index layer, in which the dye should be embedded. For the opal, all positions in an inner core of the sphere with diameter $d_{\text{core}} = 200$ nm are considered, which corresponds to the configuration realized in the experiments.

The resulting averaged LDOS are shown in Fig. 5.1 along with the undisturbed LDOS in the corresponding homogeneous medium and the ratio of the two curves. In both cases the overall LDOS variations are quite small and the curves roughly follow the quadratic behavior of the homogeneous-case LDOS. These results can be explained with the relatively low refractive index contrast and the non-omnidirectional band gaps in both structures. For small frequencies the data is distorted from "binning noise" due to the finite sampling of $\boldsymbol{k}$-space. This artifact can be reduced with higher resolution, resulting in higher computational effort. At the frequencies of interest around the band edges, however, the LDOS is obtained with sufficient accuracy.

For the Bragg stack, the LDOS lies above the corresponding LDOS in a homogeneous medium. This results in a LDOS ratio greater than one, indicating an enhancement of emission rates. Within the range of the band gap, the LDOS is reduced only slightly: there are many states with $\boldsymbol{k}$-vectors in other directions that have frequencies inside the gap. In the same way, the singularity-type enhancement at the band-edge of the one-dimensional LDOS in on-axis direction (see Fig. 3.2 (a)) vanishes in the three-dimensional LDOS. The LDOS within the band gap is largest at the lower-frequency band edge. This result can be understood with the shift of the band gap towards higher frequencies as wave vectors tilt towards off-axis directions. Thus the number of modes in the gap with frequencies near the upper-frequency band edge is reduced.

The LDOS of the opal lies below the homogeneous-case LDOS for the relevant frequencies, indicating a suppression rather than an enhancement of emission rates. Like in the Bragg stack, the LDOS does not drop to zero inside the band gap. Instead, it shows relatively small variations, as there are many states in other directions with frequencies in the band gap. The increase in the LDOS at the lower-frequency band edge can again be understood with the shift of the band gap towards higher frequencies as wave vectors tilt from the L- to the U-direction.

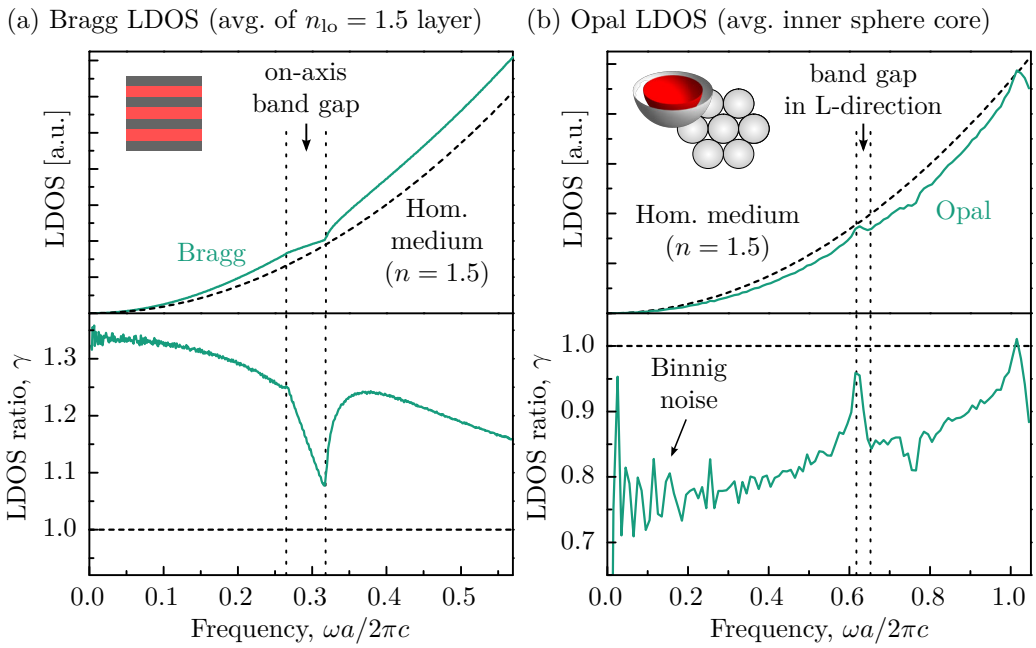

Figure 5.1: Position-averaged LDOS for (a) Bragg stack and (b) opal. The LDOS in the $n_{\mathrm{lo}} = 1.5$ layers is enhanced above its corresponding homogeneous-case LDOS, while the LDOS of the opal is reduced for positions in the inner core of the spheres (a configuration realized in the experiments). In both structures the overall LDOS variations are quite small and the curves roughly follow the quadratic behavior of the homogeneous LDOS as a result of the rather small refractive-index contrasts and therefore non-omnidirectional band gaps.

Similar results were found for an emitter positioned in the sphere center as well as averaged over the whole sphere, which I discuss in Ref. 129.

For the two structures, the LDOS was also studied in the respective other material (not shown here). It was found that in both cases the LDOS is enhanced in the lower-refractive index material and reduced in the higher-refractive index material compared to each corresponding homogeneous LDOS. This observation indicates that the material, in which emitters are embedded, should have the lower refractive index of the two materials to obtain an enhancement of spontaneous emission rates.

5.1.2 Emission spectrum, PLQY and fluorescence lifetime

To calculate the influence of the photonic crystal on the dye's emission, the LDOS results were combined with the rate-equation model of the emitter proposed in Sec. 3.2. It is particularly interesting to study fluorescent emitters such as the

organic dyes in this work: they typically exhibit broad emission spectra compared to the sharp features of the LDOS in photonic crystals. When emission at a certain frequency is suppressed, the excited electron can still decay to other ground state levels, thus emitting a photon with a different frequency. This leads to spectral redistribution: emission at frequencies with a relatively low LDOS ratio is suppressed and instead light is emitted at frequencies with higher LDOS ratios.

As an input to the calculations, the undistorted emission spectrum, i.e. the spectral shape function $g^0(\omega)$, was obtained initially in experiments: the photoluminescence spectra of LR and rhodamine B were measured from samples with a dye-doped PMMA film spin coated on a glass substrate. In this way the dye molecules experience the same chemical environment as in the photonic crystal. It is necessary to compare the emission in identical host materials to avoid other, chemical, effects that modify the emission.

Based on these homogeneous-case spectra, the emission spectra in the photonic crystal, i.e. the spectral shape functions g^{PC}, were calculated for the LR dye in the $n_{\mathrm{lo}} = 1.5$ layers of a Bragg stack as well as for the rhodamine B dye in the inner sphere core of the opal. For the conversion from normalized frequencies to wavelengths, the unit cell sizes of $a = 188$ nm for the Bragg stack (see optimization in Sec. 6.1.2) and $a = 378$ nm for the opal (to match the emission of rhodamine B) were chosen.

The resulting spectra are presented in Fig. 5.2 using the position-averaged

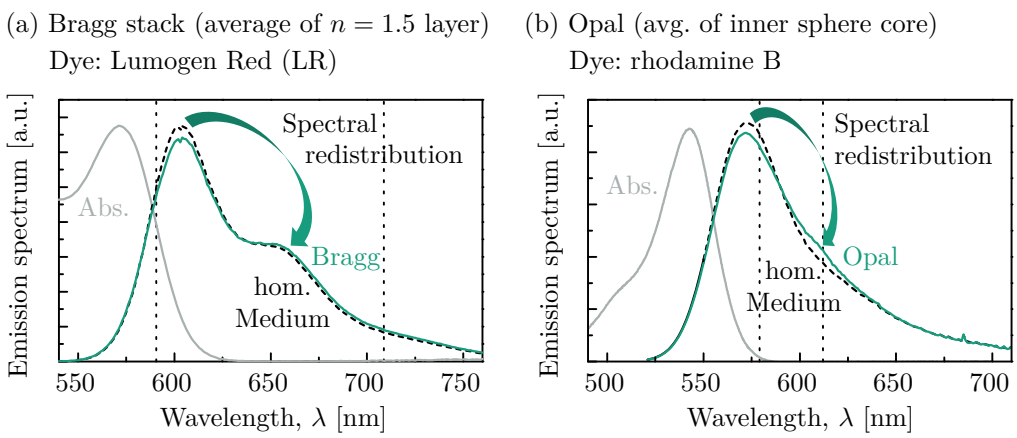

Figure 5.2: As a result of the modified LDOS inside the photonic crystals, the shape of the emission spectrum is changed for (a) the LR dye in the $n_{\mathrm{lo}} = 1.5$ layers of the Bragg stack and (b) the rhodamine B dye in the inner sphere core of the opal. In both structures emission is redistributed from shorter to longer wavelengths due to the elevated LDOS at these wavelengths (lower-frequency band edge), which can reduce reabsorption losses in LSCs.

Table 5.1: Calculated changes in emission probability, PLQY, and fluorescence lifetime induced by the photonic crystal for both the Bragg stack with the LR dye and the opal doped with rhodamine B.

	Bragg stack (LR)	Opal (rhodamine B)
Change in emission probability, ψ	1.148	0.873
PLQY, Φ^{PC}	98.3% ($\Phi^0 = 98\%$)	67.1% ($\Phi^0 = 70\%$)
Fluorescence lifetime, τ^{PC}	$0.873\,\tau^0$	$1.098\,\tau^0$

LDOS as discussed in the previous section. In both the Bragg stack and the opal, emission is redistributed from shorter to longer wavelengths due to the elevated LDOS at these wavelengths (at the lower-frequency band edge). This redistribution is beneficial for the application as a LSC, as it reduces reabsorption losses, which occur primarily the short-wavelength tail where emission and absorption overlap. However, the effect is rather small as the LDOS features only small variations.

I want to emphasize that these calculations yield the spectral distribution of all emitted light independent of the propagation direction. In experiments, this spectrum could be recorded using an integrating sphere when all modes (even trapped ones) are able to escape from a finite sample, for example at the edge faces, and reabsorption losses are negligible.

In most experiments, however, only part of the emitted light is detected. This fact explains why other experimental papers reported much stronger modifications of the emission spectrum for opals with a similar refractive index contrast [70–73]. To calculate the detected spectrum, e.g. for comparison with experiments, one needs to account for the exact measurement setup, as I will show in Sec. 5.1.4.

The shown emission spectra are the corresponding spectral shape functions, i.e. that they are normalized probability distributions ($\int_0^\infty g(\omega)d\omega = 1$). The absolute value of the spontaneous emission probabilities P_{SPE}, however, is changed by the factor ψ, as explained in Sec. 3.2.1. As a result, the key properties of a fluorescent material, the PLQY and the lifetime, are modified as well (see Tab. 5.1).

In the Bragg stack, the emission probability of the LR dye is enhanced by 14.8% due to the overall enhancement of the LDOS in the emission range. Therefore, the dye's PLQY is increased from $\Phi^0 = 98\%$ [151] to $\Phi^{\mathrm{PC}} = 98.3\%$ as this radiative decay channel is more favorable than in the homogeneous-medium case, compared to the unchanged non-radiative decay probability. This increase is beneficial for the LSC application as it reduces non-radiative losses. As a result of the higher transition probability, the fluorescence lifetime decreases by 12.7%.

In the opal, the emission probability of rhodamine B is reduced by 12.7% as a result of the overall lower LDOS when compared to a homogeneous medium. Thus the PLQY decreases from $\Phi^0 = 70\%$ [138] to $\Phi^{\mathrm{PC}} = 67.1\%$, which will also

decrease the LSC performance. The fluorescence lifetime in turn increases by 9.8% because the decay slows down due to the lower transition probability.

I want to point out that the measured fluorescence lifetime is independent of the exact way of measuring it: it does not matter if luminescence is recorded only for specific wavelengths or integrated over the full spectrum, nor if only part of the emitted light is detected in a certain measurement setup. The fractional transition probabilities might be different in these cases and therefore the absolute signal level. The dynamics of the decay, however, depend only on the exponential decay of the excited state population $N_2(t)$. This decay and thus the lifetime τ are determined by all possible transitions originating from this state, and not only from those being monitored.

In contrast, the shape of the measured spectrum strongly depends on the exact measurement setup, as mentioned above. This means that at the same time a strong modification of the spectrum (large FLDOS variation) but only little change in lifetime (small LDOS variation) may be observed. Such behavior has been reported in previous experiments [70, 71] and can now be explained by this reasoning.

5.1.3 Light guiding efficiency

The light guiding efficiency (LGE) of a (P)LSC is of key importance for the application as it states how much of the emitted light is able to couple out at the front and back surface and is thus lost. In conventional LSCs, this fraction is determined by total internal reflection (TIR) according to Snell's law. Accordingly, the LGE is given by $\sqrt{1-(1/n)^2}$ for the case of a homogenous medium with refractive index n, i.e. one minus the escape cone loss (Eq. (1.1)), which is independent of the emitter location and wavelength (when material dispersion is neglected).

In photonic crystals, however, the LGE is determined by the FLDOS of all modes that fulfill the out-coupling condition as described in Sec. 3.1.4. Remember, that the LGE is always referred to a certain surface of out-coupling that needs to be specified. Here, the surface parallel to the layer interfaces was considered for the Bragg stack. For the opal, the (111)-surface was used that is perpendicular to the L-direction, which features the band gap. In fact, this surface is typically obtained in experiments.

Same as the LDOS and the FLDOS, the LGE depends on the location of the emitter inside the structure. Here, the LGE for the Bragg stack and the opal is shown in Fig. 5.3 averaged over all emitter positions. Inside the Bragg stack, the LGE is strongly enhanced over TIR guiding in material with $n_{\mathrm{lo}} = 1.5$ (74.5%), especially inside the band gap with up to 95.0% at the upper-frequency band edge. Within the band gap, less light is emitted which is able to escape from the structure as a result of the reduced number of available states due to the band gap in the direction of the classical escape cone. Instead, light is *direction-*

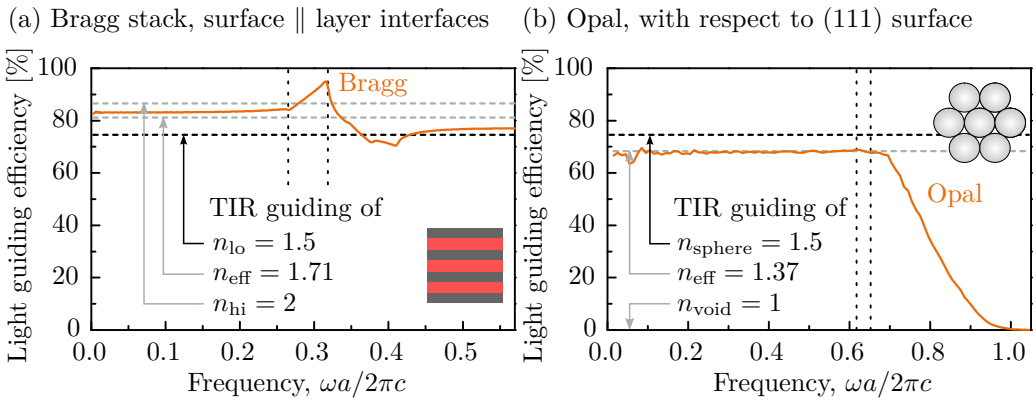

Figure 5.3: (a) The light guiding efficiency (LGE) inside the Bragg stack (averaged for emitter positions in $n_{lo} = 1.5$ layer) is strongly compared to the guiding through TIR in conventional LSCs (74.5%), especially within the band gap (indicated with dotted lines) with up to 95.0%. (b) In the opal, the LGE (avg. for emitters in sphere core) is similar to TIR guiding with the structure's effective refractive index (68.4%) for frequencies up to the band edge, but significantly below the value for the sphere material (74.5%). For frequencies above the band gap, the LGE drops to zero, as modes of higher band can couple out at the (111)-surface to "diffracted" orders, as explained in Fig. 5.4.

ally redistributed in guided modes. This increase in LGE is very beneficial to the LSC application: Even for large concentrator dimensions, the guided modes cannot escape for fundamental reasons (and not because of a high but non-perfect reflection).

For low frequencies, the LGE lies slightly above the TIR value corresponding to the volume-averaged effective refractive index $n_{eff} = 1.71$. In more detail, I calculated the LGE separately for modes with TE and TM polarization: the LGE for TM modes converges at low frequencies to the value of the effective material, also for emitter positions in the high-refractive-index material. In the case of TE polarization, however, the LGE is enhanced for emitters in the low- and reduced in the high-refractive-index material. This difference is a result of the distribution of the electrical energy of the modes: while TM modes concentrate in the high-refractive-index layers, the fields of TE modes cross both high- and low-refractive-index regions, leading to different effective refractive indices for the two polarizations. Considering the average of both polarizations, the LGE in the low-frequency regime thus lies slightly above the TIR guiding of $n_{eff} = 1.71$.

In the opal, the LGE is similar to the TIR guiding for the structure's effective refractive index $n_{eff} = 1.71$ (68.4%) for frequencies up to the band edge. This indicates that light with long wavelengths probes the opal as an effective material with n_{eff}, where the propagation direction or polarization plays a minor role.

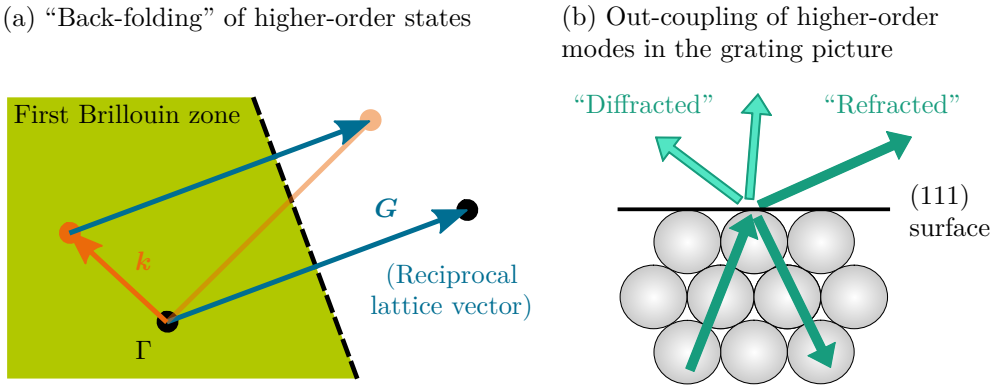

Figure 5.4: The strong decrease in the LGE of the opal for frequencies above the band gap can be explained with the modes of higher bands, whose wave vector is folded back into the FBZ due to the Bloch theorem, as illustrated in (a). (b) More intuitively, this effect can be understood with out-coupling in different diffraction orders as the considered (111)-surface represents a periodically structured surface, hence a grating.

In additional LGE calculations for another opal with $n_{\text{sphere}} = 2$, $n_{\text{void}} = 1$ as well as for an inverted opal ($n_{\text{sphere}} = 1$, $n_{\text{void}} = 1.5$), good agreements with TIR guiding for the corresponding n_{eff} were also obtained. The LGE for the opal studied here, however, is thus significantly lower than in a homogeneous material with a refractive index of $n_{\text{sphere}} = 1.5$ corresponding to a conventional LSC. Despite the band gap perpendicular to the surface, the LGE is reduced, which is detrimental to the use as a LSC.

For higher frequencies above the band gap, the LGE of the opal drops to zero. The reason for this effect is that modes from higher bands start to contribute to the LGE. As a result from the Bloch theorem, those modes are “folded back” into the FBZ by the reciprocal lattice vector $\boldsymbol{G}$, as schematically shown in Fig. 5.4 (a). Thus their wave vector $\boldsymbol{k}$ becomes “shorter”. As the frequency ω increases at the same time, those modes are more and more likely to satisfy the out-coupling criterion (Eq. (2.9)); thus, the LGE decreases.

In a more intuitive picture, this effect can be understood in terms of diffraction: the (111)-surface of the opal is a periodically structured surface, a hexagonal *grating*. Therefore, modes of higher bands may be able to couple to more than one plane-wave mode outside the photonic crystal corresponding to different “diffraction” orders, as illustrated in Fig. 5.4 (b).

In the calculations presented here, it is assumed that every mode, which is able to couple out, will couple out (i.e. with an efficiency of 100%). Especially for the opal, individual out-coupling efficiencies were not calculated. To obtain these efficiencies rather complex rigorous calculations need to be employed. Within the

focus of this work, however, these out-coupling efficiencies are not relevant: with a non-zero out-coupling efficiency, light will escape from the structure at some point, when light "bounces" between the top and bottom surface multiple times. Thus, the presented results are worst-case results corresponding to large concentrator dimensions.

To conclude, the LGE for light emitted in the Bragg stack is strongly enhanced over the TIR guiding of conventional LSCs, which is very promising for the application as a PLSC. The opal, however, features a reduced LGE lower than in a conventional LSC. Thus, further calculations were focused on the Bragg stack.

5.1.4 Detected emission: Angular resolved surface PL

In measurements, only part of the emitted light is usually detected. This fraction must be able to couple out from the photonic crystal and fall into the detector's aperture. Thus the exact measurement setup plays a crucial role. When probing the photonic crystal's effect on emission, the changes in the total emission spectrum (spectral redistribution), PLQY and fluorescence lifetime are relatively small and hard to measure. The detected emission in specific directions, however, is very sensitive to the photonic effects, especially when band gaps occur in the direction of detection. In this work, the emission escaping from the sample surface was thus analyzed in detail with angular resolution.

For comparison of the theory with the experiments, the spectrum of the detectable modes was calculated as a function of the detection angle ϕ_d according to the measurement setup used for the angular resolved surface PL (Sec. 4.3.3).

These calculations were done for the Bragg stack, as this is the most promising structure for PLSCs. Out-coupling was considered at the surface parallel to the interfaces of the layers. For each detection angle ϕ_d from the experiments ($-10°$ to $90°$ in $1°$ steps), the FLDOS of the Bragg stack and the resulting detected spectra were calculated as described in detail in Sec. 3.1.4 and 3.2.3. It was averaged over emitter positions in the low-refractive-index layers of the Bragg stack. As a reference, the same FLDOS calculations were done for emission in a homogeneous medium corresponding to a conventional LSC. Matching to the experiments, a detection cone with half-angle $\theta_\mathrm{d} = 0.6°$ was assumed. This FLDOS approach implies that every mode, which is able to couple out, will couple out (i.e. with an efficiency of 100%), similar to the LGE calculations above. This worst-case scenario corresponds to large concentrator sizes.

For comparison, a third sample type was considered, which consists of a dye layer in the center of 3 mm-thick $n = 1.5$ material with Bragg stack filters on the top and bottom surfaces, named "TSR" (*triple stack reference*). This TSR sample corresponds to a conventional LSC with filters on the top and the bottom: emission is assumed to be isotropic as in the homogeneous material because the filter structures are relatively far away from the point of emission. The simulated

filters shown here correspond to the ones fabricated by spin coating, with 29 layers of $n_{\mathrm{lo}} = 1.5$ and $n_{\mathrm{hi}} = 2$ materials and thicknesses given through $\lambda_{\mathrm{design}} = 645$ nm. The same calculations were done for the IBS filters based on the refractive indices and a list of layer thicknesses provided by Laseroptik GmbH. The results for these IBS filters are shown in Sec. 5.2.1 for direct comparison to the experimental results.

The resulting angular surface PL for the TSR samples was calculated with the ray-tracing method proposed in Sec. 3.3.3, which considers individual out-coupling efficiencies. In this ray-optical model, the number of interactions with the filter and thus the escaping fraction as a function of the propagation direction is calculated for a certain surface dimension. A detection spot size of $l_{\mathrm{d}} = 2.5$ mm was chosen according to the experimental conditions. The angular surface PL was also calculated with this method for a conventional LSC. Even for small values of l_{d}, however, practically the same results were obtained as with the FLDOS method due to the low reflectivity at the surface to air for these structures.

The resulting spectra as a function of the detection angle are shown in Fig 5.5. In the "LSC" case, i.e. emission in a homogeneous medium, the shape of the detected spectrum is constant for all angles and corresponds to the undisturbed emission spectrum. The intensity, however, decreases for larger detection angles. This decrease is consistent with the theory presented in Appendix A.5: while inside the homogeneous medium emission is uniformly distributed over the internal angles (isotropic emission), refraction at the surface changes the angular distribution in air according to Snell's law.

In the case of the TSR sample, the detected spectrum becomes a function of the detection angle, as shown in Fig. 5.5 (b). The reflection peak around $\lambda_{\mathrm{design}} = 645$ nm prevents light from escaping. This reflection peak and thus the reduced escape shifts to shorter wavelengths with larger angles. For $\phi_{\mathrm{d}} = 0°$, the calculated spectrum is similar to the original dye spectrum. The reason for this is the singularity in the number of interactions of light with the filters for this angle: light bounces forth and back endlessly, so that all light can escape due to the non-unity filter reflectance.

Furthermore, the obtained PL was integrated over all angles and all wavelengths to get the total value of escaped light. Note that for the angular integration the weighting factor $\sin\phi_{\mathrm{d}}$ needs to be considered (see Eq. (3.66)). The integrated PL was normalized to the value of the LSC case for the sake of comparison. In the TSR case, the out-coupled light is reduced to 62% compared with the LSC. The reduction, however, is based on a finite number of interactions with the filters that occur within the detection area of $l_{\mathrm{d}} = 2.5$ mm. This does not mean that this light is perfectly guided to the edge faces: the photon's path to the edge involves many more filter interactions. Thus light may couple out at some point between the point of excitation (and detection) and the edge face. This can be modeled by choosing l_{d} according to the concentrator size. With increasing concentrator size,

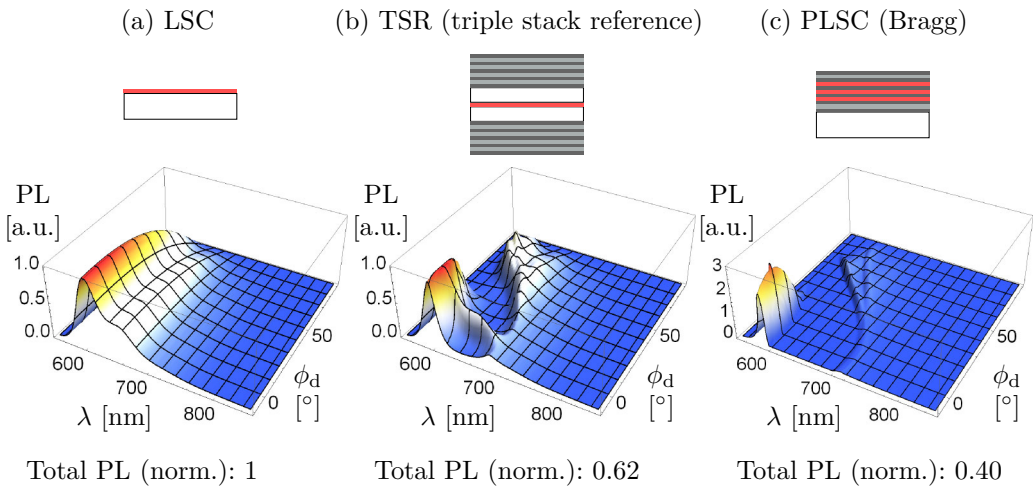

Figure 5.5: Calculated angular resolved surface PL as a function of the detection angle ϕ_d for the three sample types using FLDOS calculations (LSC and PLSC) and the ray-tracing method (TSR): (a) For the LSC, the detected spectra for all detection angles have the same shape corresponding to the undisturbed emission spectrum. The intensity decreases with oblique detection, as expected. (b) For the TSR sample, part of the undisturbed and isotropic emission is prevented from out-coupling through the reflectance of the filters that shifts to shorter wavelengths with larger angles. For $\phi_d = 0°$, a characteristic "shoulder" is visible as a result of endless back- and forth-propagation of light at that angle. (c) In the PLSC, however, only little light escapes as a result of the modified emission induced by the LDOS of the Bragg stack. Due to an enhanced FLDOS at the band-edge at 600 nm, an emission peak three-times higher than that in the LSC occurs. In total, the escape cone loss is reduced by 60% as a result of the fundamental LDOS effect, independent of the concentrator size.

the amount of escaped light converges to the value of the conventional LSC.

The out-coupled light from the Bragg PLSC also features a strong spectral and angular dependence, as shown in Fig. 5.5 (c). For most wavelengths and angles, no emitted light is expected to be detected. The reason for this inhibition is not a result of isotropic, but partly filtered emission as in the TSR. Instead, the emission itself is modified and becomes "anisotropic": less modes exist in the photonic crystal that are able to couple out, as discussed in the previous section.

The suppression of detected emission follows the spectral range of the band gap that shifts to shorter wavelengths for oblique angles in the same way as the reflectance of the TSR filters does. In contrast to the TSR sample, no light is emitted at $\phi_d = 0°$ between 600 nm and 700 nm as a result of the absence of photonic states. Eye-catchingly, a peak of out-coupled emission is predicted for wavelengths below 600 nm and for small angles. In fact, the absolute peak height is more than three times larger than the peak in the LSC case. The reason for

this enhancement is a strongly elevated FLDOS at the band edges. This effect of enhanced emission with narrowed spectrum and confined directionality may be also interesting for other applications such as solid-state lighting.

Integrated over all angles and wavelengths, the escaped light is only 40% of the LSC. This, in turn, means that more light is trapped in the structure and guided to the edges. In contrast to the TSR, this value does not increase with concentrator size. In fact, it is already the worst-case value for large concentrators.

To conclude, the amount of out-coupled and thus lost emission is reduced for both TSR and PLSC compared to conventional LSCs. In the TSR sample emission is undisturbed and isotropic. The reduction is a pure reflection effect and thus converges to the value of a LSC for large concentrators. Emission in the PLSC, however, is modified by the LDOS in terms of spectral and directional redistribution. The escape cone loss reduction by 60% is a result of these fundamental effects and is therefore independent of the concentrator size.

5.2 Experimental results and comparison to theory

To investigate the influence of the photonic crystal on the fluorescent emission, several samples were prepared. Here I focus on the multilayer structures due to the very promising theoretical results for the Bragg stack in the previous section. Results of angular resolved surface PL measurements of opals can be found in my publication Ref. 187.

The different types of multilayer samples are schematically shown in Fig. 5.6. First, undisturbed emission was studied using conventional thin film LSCs. For comparison with the other spin coated samples, simply a dye-doped PMMA layer was spun onto a glass substrate. For comparison to the bonded filter structures, two glass substrates were each spin coated with a dye-doped PMMA layer and subsequently bonded using the same platen press process.

Second, "TSR" (*triple stack reference*) samples were fabricated. As mentioned in Sec. 5.1.4, these structures consist of a dye layer in $n = 1.5$ material where filters were deposited on the top and bottom surface. Thus these samples correspond to conventional LSCs with filters on the top and bottom: emission is assumed to be isotropic as in the homogeneous material because the filter structures are relatively far away from the point of emission. To realize such a structure, a dye-doped PMMA layer was deposited on a glass substrate. This part was joined to two undoped spin coated Bragg stack samples, or to two IBS filters, as shown in Fig. 5.6 (b) and (e), respectively. To achieve good optical contact, an optical index-matching liquid was used.

Third, PLSC samples were fabricated where the luminescent dye was embedded inside the photonic structures either by spin coating or by bonding in between two filters, as presented in Sec. 4.1.

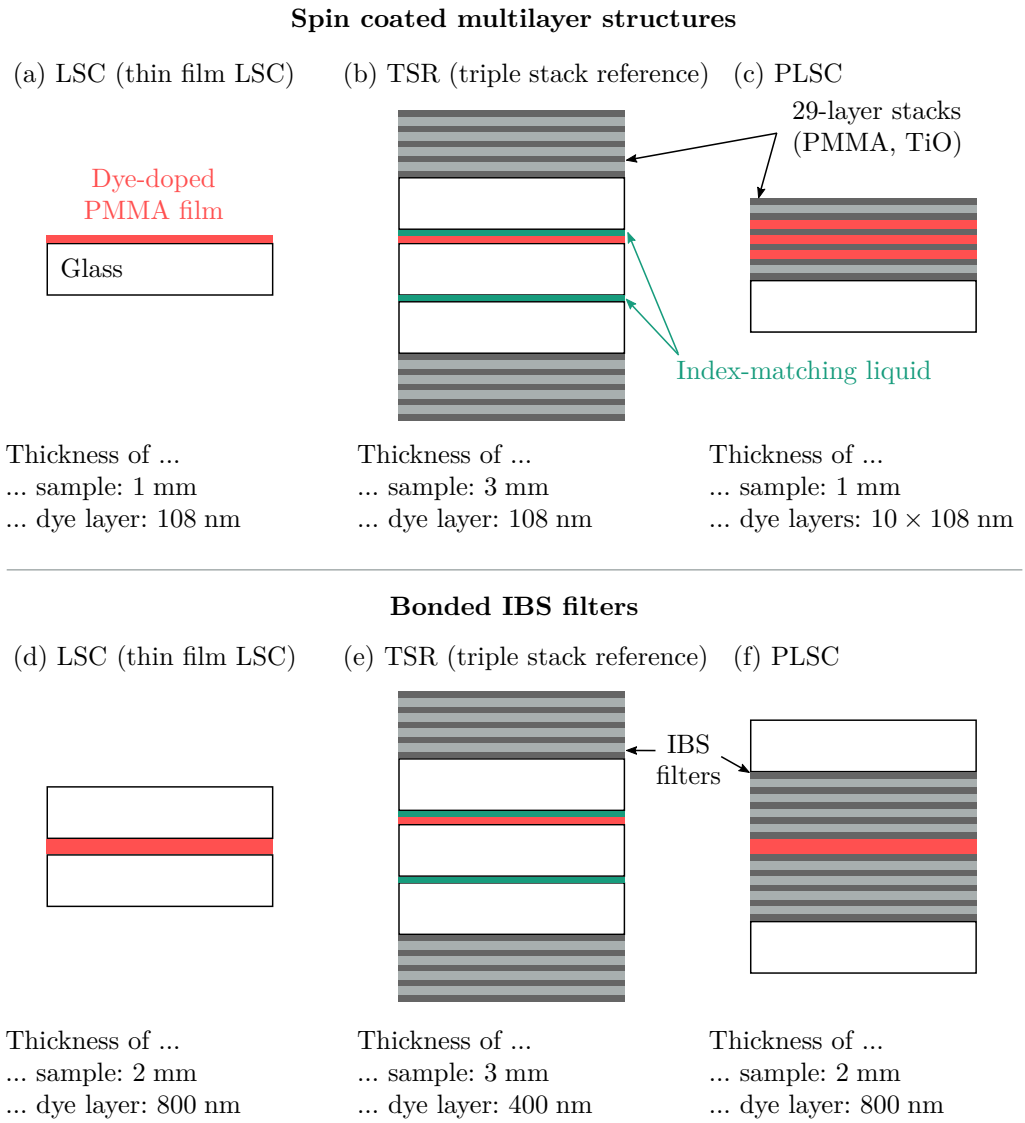

Figure 5.6: The three different types of samples investigated in this work for the two fabrication approaches of spin coating and filter bonding: (a) and (d) represent (thin film) LSCs that were used to study undisturbed emission and light guiding. As shown in (b) and (e), "TSR" (*triple stack reference*) samples were fabricated in which an inside dye layer was joined to filter stacks placed at the outer surfaces (optically coupled using index-matching liquid). These samples correspond to conventional LSCs with filters on the top and bottom where emission is undisturbed and isotropic. (c) and (f) show the PLSC samples where the luminescent dye was embedded inside the photonic structures either by spin coating or by bonding in between two filters.

Note that the thickness of the dye-doped layers in the spin coating LSC and TSR samples are relatively thin, thus the absorptance is rather low. However, this way the layers were deposited with the same processing conditions as the dye-doped layers in the PLSC, avoiding potential process-related parasitic influences.

5.2.1 Angular resolved surface PL

As mentioned before, the detected emission that escapes from the sample surface is very sensitive to the photonic effects on emission. Therefore, the spectra of this escaping light was measured using the angular resolved surface PL setup (Sec. 4.3.3) and the results were compared to theoretical calculations. This was done for both spin coated samples and bonded filters, as presented in the following.

Spin coated multilayer structures

Starting with the conventional LSC, the shape of the emission spectrum is constant for all detection angles ϕ_d and corresponds to the undisturbed emission spectrum, as shown in Fig. 5.7 (a). The absolute value decreases with increasing detection angles in the expected way. Thus the measurement of the LSC sample agrees very well with the corresponding calculation from Sec. 5.1.4, which is as well shown in Fig. 5.7 for direct comparison. This agreement indicates that emission inside the sample is indeed isotropic.

For the TSR sample, a good qualitative agreement with the calculation was obtained (Fig. 5.7 (b)): the characteristic influence of the reflection peak, which prevents emission from escaping and shifts to shorter wavelengths for larger detection angles, is clearly visible. Furthermore, enhanced out-coupling is observed for $\phi_\mathrm{d} = 0°$, especially within the range of high reflection (600–700 nm). This "shoulder", however, is less pronounced than in the calculation. This is due to the singularity of this effect at $\phi_\mathrm{d} = 0°$, where in the calculation emitted light bounces endlessly between the filters, allowing all of it to escape at some point. In the measurement, this effect is smoothed over the $2 \times 0.6°$ of the detection cone opening angle. However, the fact that this shoulder is clearly visible in the measurement strongly indicates isotropic emission of the dye: the spectral and angular dependence of the out-coupled light is a result of partial filtering by the Bragg stacks.

Moreover, minor differences between theory and experiment can be explained by imperfections in the fabricated filters, e.g. the faster decrease of the measured peak at 600 nm at small angles. The absolute values of the measurements, however, are not very reliable for the TSR sample: as mentioned in Sec. 4.3.3, multiple internal reflections in the relatively thick sample led to multiple spatially shifted transmission and reflection spots, which were not completely captured with the solar cell used to measure the intensity. Thus the absorption of the sample is over-

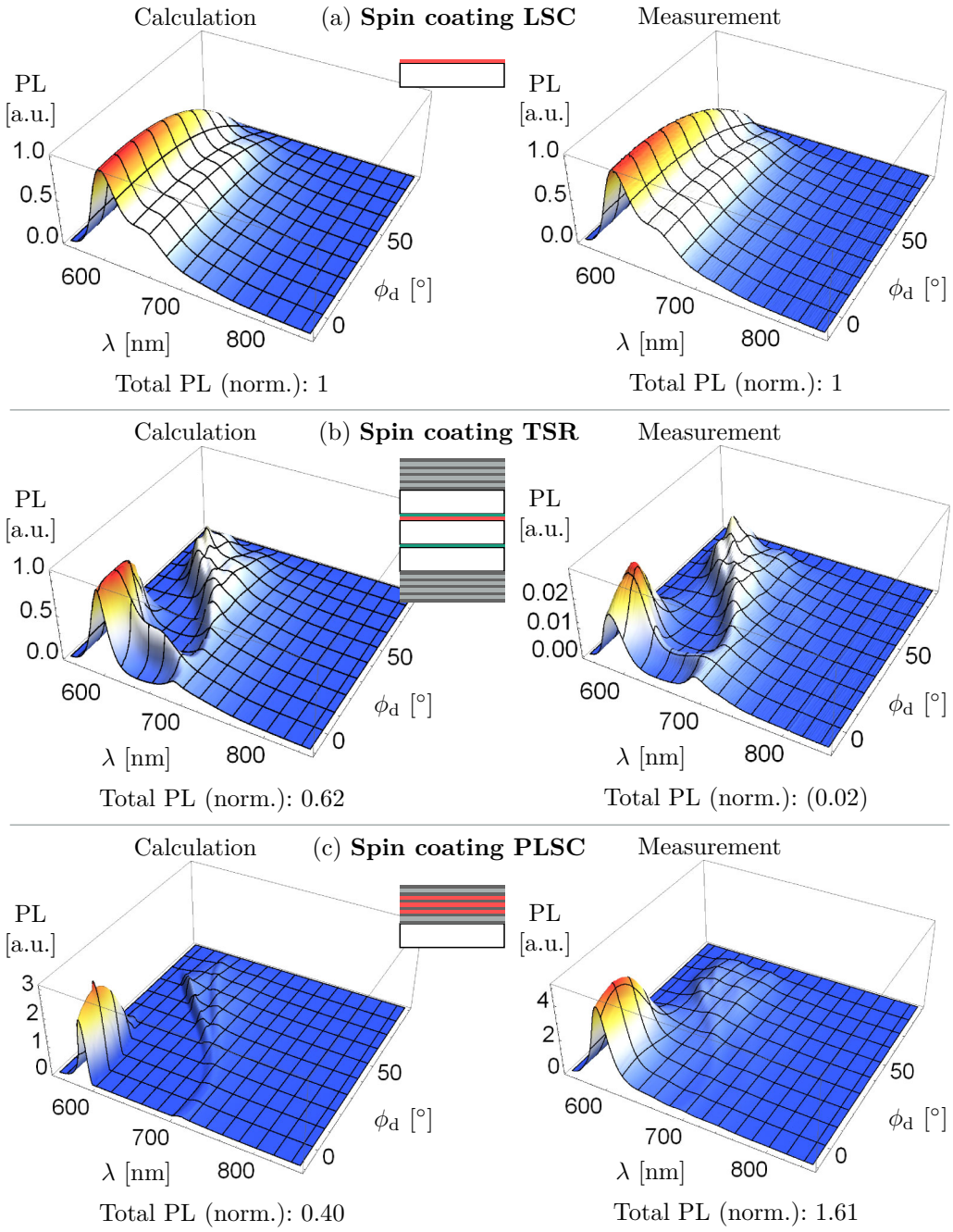

Figure 5.7: The calculated and measured angular surface PL spectra of the spin coating samples agree very well, especially for the (a) LSC and (b) TSR. For the PLSC in (c), the absence of the TSR-like shoulder at $\phi_d = 0°$ and the enhancement of the peak at 600 nm strongly indicate a modified emission induced by the LDOS, as predicted in theory.

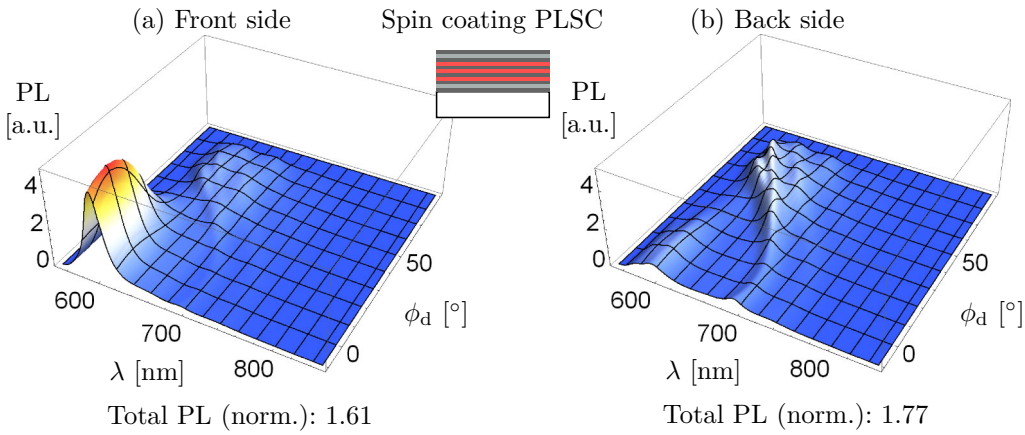

Figure 5.8: In contrast to the LSC and TSR samples, the detected angular surface PL of the spin coated PLSC was different from the (a) front side and from the (b) back side (glass substrate). While in theory these two measurements should be the same, the LDOS in the outer dye layers is presumably influenced by the surrounding air or glass material, causing this asymmetry. Indeed, this effect is strongly reduced in spin coated PLSCs with only one dye-doped layer in the center of the stack, as shown in Appendix A.6.

estimated and consequently the resulting absolute PL values are smaller than in reality. Therefore, also the total amount of escaped light integrated over all angles and wavelengths is quite small and allows no quantitative comparison.

The measurement result of the spin coated PLSC sample is shown in Fig. 5.7 (c). As predicted from theory, little escaping light is detected for most wavelengths and angles. This suppression follows the spectral range of the band gap with its shift to shorter wavelengths for larger detection angles. A significant amount of light with wavelengths of around 600 nm, however, escapes in directions close to normal incidence. This peak is strongly enhanced over the peak in the LSC sample, which was also predicted in the calculations.

In general, the characteristic features from theory appear to be smoothed and slightly less pronounced in the measurement. This difference may be caused by the finite nature of the fabricated sample compared to the ideal and infinitely periodic photonic crystal in the calculations. Especially for emitter positions in the outer dye layers of the structure, which are separated from the air or glass surface by only five other single layers, the LDOS effect is supposed to be not fully established. Further differences may be caused by out-coupling efficiencies lower than 100% in the experiment, while in the calculations all light escapes that is able to escape in principle.

All samples were measured from the front and back surface side. While for the LSC and TSR samples these two measurements did not differ significantly, the

detected signal of the two surfaces was different for the PLSC sample, as shown in Fig. 5.8. The resulting angular resolve surface PL from the back side (glass substrate) lacks the distinctive peak at 600 nm. Furthermore, at larger angles more light is detected compared to the front side. Integrated over all wavelengths and angles, a little more light is escaping from the back side.

In theory, the out-coupling condition does not change due to the glass substrate: While more modes couple from the photonic crystal to the glass in the first place, only those modes that fulfill the same criterion as for the front side will couple out from the glass into air (see Eq. (2.9)). There might occur, however, a lateral displacement of the point of out-coupling on the sample surface for oblique angles due to the propagation in glass. As a result, some modes might not be detected as they escape outside the detection area. In measurements, however, changing the detection area by defocusing the fiber-coupling optics had no influence on the detected signal.

Further differences of light escaping from the front and back might be related to different out-coupling efficiencies for the two sides. Additionally, the local absorption might differ in the two measurements as also the direction of excitation is changed. Thus, different dye positions do not contribute to the measured PL in the exact same way in the two measurements.

Most importantly, the theoretical consideration of same emission through the front and back side is based on the assumption that the dye experiences the full LDOS of the photonic crystal that results in symmetric emission. In the finite fabricated structures, however, the LDOS effect might be not fully established in all dye-doped layers, especially in the outer layers. Furthermore, the surrounding air and glass might influence the LDOS in those layers. Therefore, the distribution of states may become asymmetric due to the asymmetry of the sample, which results in different emission towards the front and back surfaces.

To investigate the difference in the front and back side measurements further, another set of samples was analyzed: samples with only one dye-doped layer in the center of the stack were compared with samples containing 10 dye-doped layers (like the PLSC from above). Although the peak reflectance wavelength of these samples was unfortunately slightly detuned by process variations, an interesting observation could be made: while the samples with multiple dye layers also showed large differences for the front and back side, this difference was strongly reduced for the samples with only a single dye layer, as discussed in detail in Appendix A.6. This result supports the above explanation that especially the LDOS in the outer dye layers is influenced by the surrounding air or glass, leading to an asymmetric distribution of photonic states.

The total amount of escaped light from the PLSC sample is larger than in the LSC despite the strong reduction for most angles and wavelengths: for the front side, 61% more light is detected, for the back side as much as 77% more light escapes. Even though the accuracy of the absolute values is rather poor due to

scattering of incident light, this increase is far from the theoretically predicted decrease by 60%. While for other applications this result is very promising, for example to increase the extraction of emitted light in LEDs, the increase indicates a reduced light guiding efficiency. The discrepancy between theory and experiment is presumably again due to the finite size of the fabricated structure, such that the LDOS of the photonic crystal is not fully established, especially in the outer layers. In fact, the measurements of the single dye layer sample mentioned above yielded much lower amounts of escaping light compared to the corresponding samples with multiple dye layers (see Appendix A.6). Additionally, the observed increase in escaping light might be promoted by microscopic cracks that were found at the surface of the PLSC sample, as discussed in Sec. 6.2.1. A better performance is therefore expected from optimizing the fabrication process to further reduce cracks and to deposit more doped inner and undoped outer layers.

To conclude, however, the measured angular surface PL for the LSC and TSR samples agreed very well with the calculations from theory. For the PLSC, the absence of the TSR-like shoulder at $\phi_\mathrm{d} = 0°$ and the enhancement of the peak at 600 nm both strongly indicate that the measurement is not a result of isotropic emission and filtering as in the TSR case, but that emission inside the sample is modified due to an altered LDOS, as predicted in the theoretical models.

Bonded IBS filters

Similar to the LSC sample from the spin coating process, the spectra of the detected light escaping from the bonded LSC sample correspond to the undisturbed dye emission spectrum, as shown in Fig. 5.9 (a). The decrease in intensity with larger detection angles ϕ_d follows the theoretical calculation. The good agreement with theory indicates isotropic emission inside the sample as expected.

A good agreement with theory was also obtained for the TSR sample, as shown in Fig. 5.9 (b): out-coupling of light is suppressed for the broad spectral range of high filter reflectivity, which shifts to shorter wavelengths for oblique detection angles. In detail, two pairs of side lobes are visible in both the measurement and the calculation with different spectral shifts for increasing detection angles. As validated in further calculations, the side lobes with the stronger spectral shift originate from the reflectance for p-polarized light while the other side lobes with the weaker shift correspond to s-polarization.

The “shape” of the peak at 600 nm is slightly different in the measurement than in the calculations, which is presumably caused by small differences in the modeled and the real filter characteristics. In particular, the shoulder at $\phi_\mathrm{d} = 0°$ in the calculation is almost not visible in the measurement. As for the spin coated sample, this feature is over-estimated in the calculation. The absolute values of the TSR measurements, however, are not very reliable due to multiple internal reflections. As for the spin coated TSR sample, the absorptance is over-estimated and thus

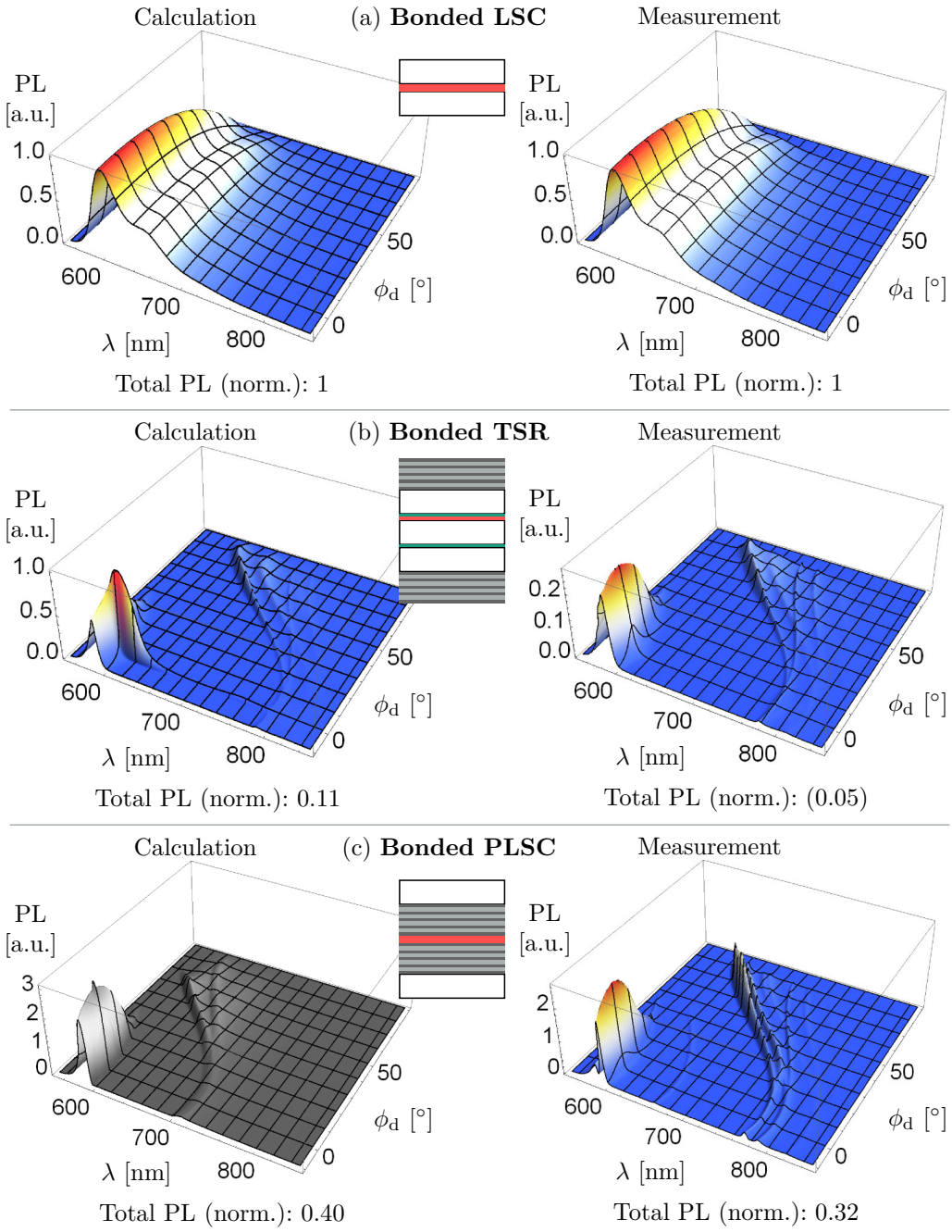

Figure 5.9: The measured and calculated angular resolved surface PL from the bonded samples shows very good agreement for (a) the LSC as well as for (b) the TSR samples. While the calculation of the PLSC is not directly applicable to the bonded PLSC, the enhanced peak at 600 nm in the measurement indicates the LDOS influence on emission.

the PL values are smaller than in reality and cannot be compared quantitatively. The calculation predicts that the out-coupled light is only 11% of that of the LSC due to the high reflectance of the filter. For larger l_{d}-values, i.e. for larger concentrator dimensions, this value increases as more light couples out on the path to the edges.

Besides the absolute values, however, the measurement and calculation agree very well, which indeed indicates isotroptic emission inside the structure. The spectral and angular dependence results from the partial filtering of emitted light.

The measured angular surface PL of the PLSC sample is shown in Fig. 5.9 (c): for most wavelengths and detection angles, almost no light is detected. This suppression follows the spectral range of the band gap, which is related to the filter reflectance with its typical spectral shift at larger angles. Besides the suppression, a spectrally very sharp peak was measured at 600 nm, which is 2.6-times higher than the peak of the LSC sample. This enhancement indicates a modification of the emission inside the structure as it cannot be explained by filtered isotropic emission, as in the TSR samples, for example.

Despite the peak, the integrated amount of out-coupled light is reduced by 68% compared to the LSC, which is more than for the calculation of the ideal Bragg photonic crystal (40%). This reduction in escape cone loss is beneficial to the light guiding efficiency.

The theoretical calculation of the Bragg stack, however, is not directly applicable to the bonded PLSC sample: first, the fabricated filters have a larger difference in refractive indices, resulting in a broader band gap and reflectance. Second and even more importantly, though, the fabricated structure is very non-periodic, especially due to the relatively thick dye-doped layer in between the two filter structures. For these reasons, the corresponding angular surface PL cannot be calculated with the eigenmode approach. Instead, the calculated angular surface PL of the Bragg stack is shown in grayscale for comparison only.

For all three samples, measurements from the front and back surface were conducted. The results, however, did not differ significantly, as expected for the nearly symmetric samples. To conclude, very good agreements of measurements and calculations were found for the bonded LSC and TSR structures, which indicates isotropic and undisturbed emission. For the bonded PLSC, however, the enhancement of the peak at 600 nm indicates a modification of emission due to the LDOS.

5.2.2 Angular resolved edge PL

Only part of the emitted light escapes at the surface. Most light is trapped within the samples and guided to the edge faces as desired for the LSC application. Therefore, this guided light was measured using the angular resolved edge PL setup described in Sec. 4.3.3 as a function of the propagation angle inside the sample, denoted as ϕ_{d} according to Fig. 4.15 (b).

These measurements address two important questions: first, what is the spectral distribution of the guided light? Especially for the TSR it is interesting to see whether light, which was not able to escape due to the filter reflection, is guided to the edges. This would in turn confirm undisturbed and isotropic emission. This point will be discussed in more detail in Sec. 5.2.3. Second, what is the angular distribution of the guided light? In particular, it is interesting to see whether light is guided to the edges at angles that lie within the classical escape cone.

Please note, that in contrast to the angular resolved surface PL the absolute values have little significance as the PL signal was not normalized to the individual absorptance of the samples.

In general, the light guided to the edges of a LSC has a certain non-trivial angular distribution, which depends on the type of concentrator, its geometry, and the way of excitation. As explained in Sec. 3.3.4, for samples with the dye confined in layers much thinner than the overall thickness, the resulting angular pattern features alternating "on"/"off" regions, whose spacing is determined by the sample thickness and the distance from the excitation spot to the edge face.

Spin coated multilayer structures

The measurement results for the spin coated sample are shown in Fig 5.10 as a 3D-plot (for intuitive information about spectral distributions) as well as a density-plot (for detailed angular information). Furthermore, the calculated angular patterns according to the individual sample thickness are depicted for comparison (see Sec. 3.3.4).

The guided light from the LSC sample features spectral distributions similar to the undistorted emission spectrum. The angular distribution shows the characteristic "on"/"off" pattern typical for thin film LSCs. Its spacing is well described by the calculated pattern. Interestingly, almost no light is guided directly to the edge, i.e. with angles close to 90°, which was however not further investigated. As expected, no light with angles inside the escape cone, i.e. $\phi_\mathrm{d} < 41.8°$ and $\phi_\mathrm{d} > 138.2°$, was detected. Thus, all light that is able to escape has escaped through the front and back surfaces before reaching the edge face, which confirms the angular surface PL results from above.

The TSR sample features an angular pattern that is roughly similar to the theoretical one with large spacing due to the large sample thickness. Within the expected angular regions of guiding, however, the measurement shows an additional internal structure and smoothed features. This difference was attributed to additional reflections at the two internal interfaces despite the index-matching liquid. The asymmetry of the pattern is caused by the asymmetry of the sample.

The spectra of the guided light in the TSR sample agree mostly with the undistorted emission spectrum. This is expected since most of the light is guided to the edge face by TIR, which does not change the spectral distribution. From the

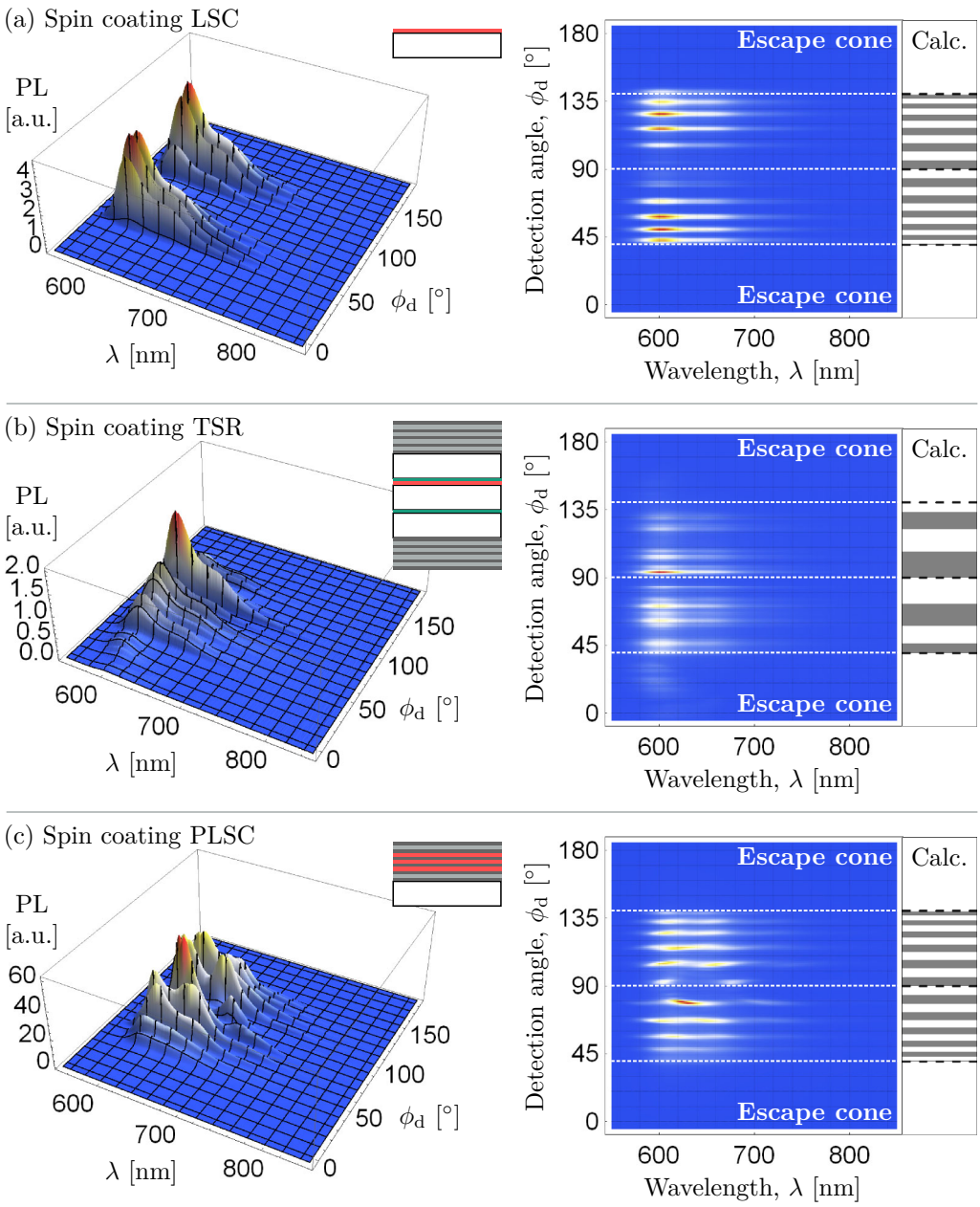

Figure 5.10: Measurement results for the angular resolved PL from the edge face of the spin coated samples. (a) The guided light in the LSC features undistorted spectra with the expected angular "on"/"off" pattern. (b) In the TSR, also light with angles in the escape cone is detected, which is guided by the reflection of the filters, though it can escape for larger path lengths. (c) In the PLSC, strong spectral variations and the absence of light in the escape cone strongly support the hypothesis of LDOS-induced emission modification.

angular distribution, it can be seen that also light with angles inside the escape cone reach the edge face. For the distance of 10 mm from the point of excitation to the edge face, the ray-tracing method from Sec. 3.3.3 yields that 7.6% of the light is guided by filter reflection in the escape cone. In the measurement, 12.9% of the guided photons were found in the escape cone. The measured fraction, however, should be interpreted rather qualitatively since scattering of light in the attached glass cylinder or small angular offsets can easily distort the measured fraction. The significant amount of guided light within the escape cone supports the hypothesis that the filters partly keep the isotropically emitted light in the sample for a certain lateral distance. With increasing distance, the amount of light guided by the filters was found to vanish using ray-tracing calculations.

The spacing of the angular pattern of the PLSC sample resembles the calculated pattern. The measured spectra, however, vary strongly and differ from the undistorted dye emission spectrum, which is presumably a result of the modified LDOS. Importantly, no light is detected at angles within the classical escape cone. Together with the results from the surface PL, in which almost no light escaped within the band-gap region, this observation strongly supports the hypothesis that no light with these wavelengths and angles was emitted by the dye. This in turn is a strong indication of the LDOS effect of directional redistribution.

Bonded IBS filters

The measured angular resolved edge PL for the bonded multilayer samples is shown in Fig 5.11 in the same way as for the spin coated sample above.

The bonded LSC sample features a regular angular pattern with an undistorted spectral distribution of guided light. Compared to the spin coated sample, the angular pattern is much more symmetric around the detection angle of $\phi_\mathrm{d} = 90°$ as the sample is symmetric with the dye layer in the center (which was not considered in the calculated pattern). The angular spacing of the measured "on"/"off" pattern, however, is twice as frequent as calculated. This might be caused by additional reflections at the internal interface from the bonding process. As expected, no light reaches the edge face at angles within the escape cone.

The angular pattern of the TSR sample oscillates strongly and hardly corresponds to the calculated pattern. Again, the asymmetry of the sample and internal reflections may be the reason for these deviations. The spectra of the guided light in the TSR sample, however, are similar to the undistorted emission spectrum, as expected for the TIR-guided as well as for the filter-guided light (due to the broad-band reflectance). A large amount of 34.7% of the guided light was detected within the angular range of the escape cone due to the high reflectance of the IBS filters. In ray-tracing calculation with $l_\mathrm{d} = 10$ mm, 22.2% of the guided light results from the filter reflection in the escape cone. In both cases, a significant amount of the guided light lies in the escape cone, which again confirm the

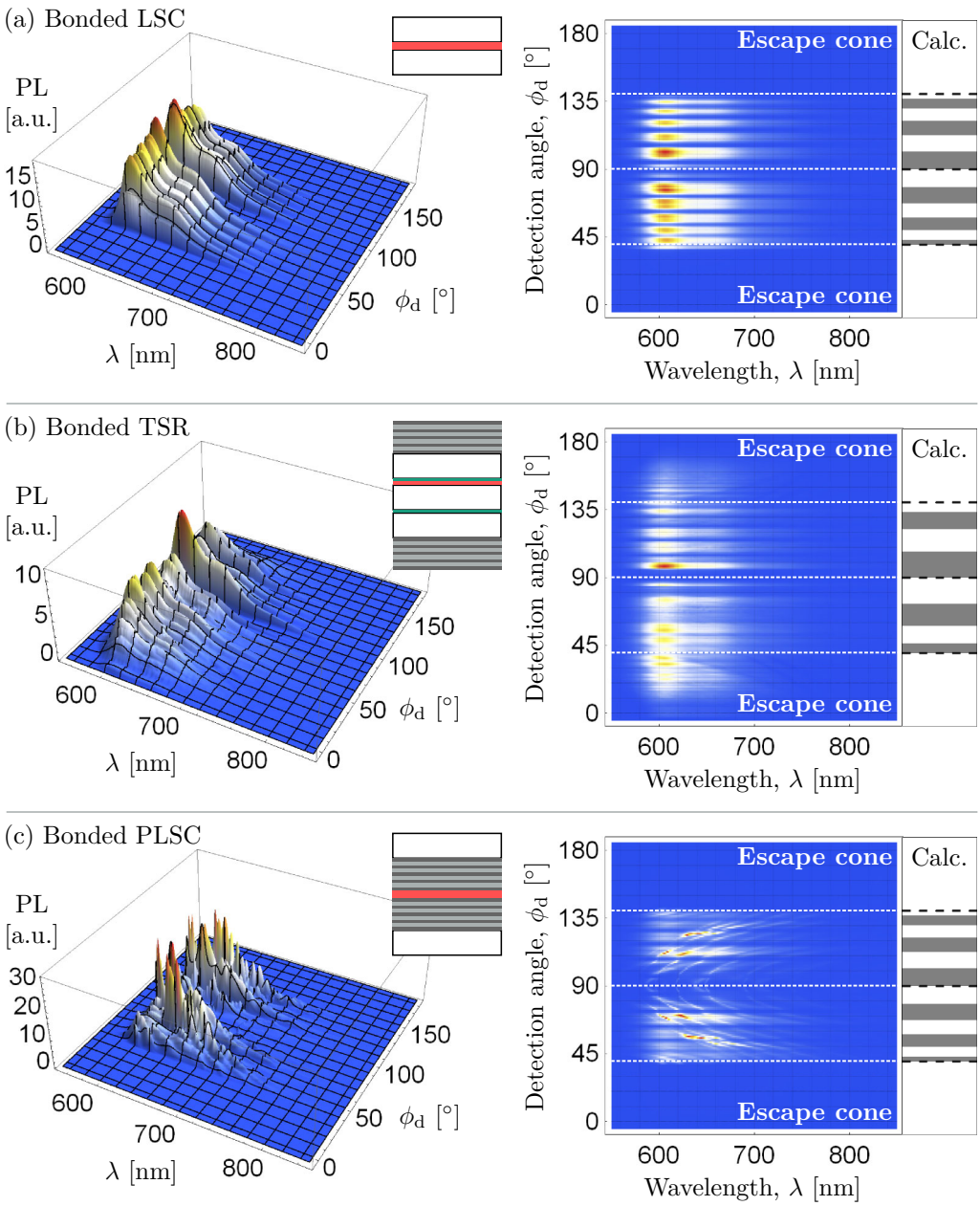

Figure 5.11: The measured angular resolved PL from the edge face of the bonded LSC (a) features an angular spacing twice as frequent as expected due to internal reflections at the bonding interface. (b) In the TSR, much light is detected within the escape cone due to the high reflectivity of the filters. (c) The PLSC features strong spectral variations that form an overlay pattern in the angular distribution. No light is detected in the escape cone, which indicates that emission at these angles was suppressed due to the (F)LDOS.

hypothesis of isotropic emission that is guided by the filters' reflection.

The measured angular pattern of the PLSC sample is similar to the pattern of the LSC with half of the calculated spacing. The sample has a strongly reflective internal interface that might cause this pattern. Remarkably, the spectral distribution is heavily distorted with very sharp features. As seen from the density plot, the spectral variations form an overlay pattern that is parabola-shaped. This pattern might be a result of guided modes within the 800 nm thick dye layer between the filters, which was not investigated in detail. Similar to the spin coated sample, no light is detected with angles in the escape cone. Therefore, no light was emitted at all at these angles with wavelengths in the region of high filter reflectance as it was neither detected in the angular surface PL nor in the edge PL measurements. This finding again indicates LDOS-induced redistribution of emission in other directions and to other wavelengths.

5.2.3 Integrated PL

Besides angular resolved measurements, the integrated PL of the samples was measured in the configurations presented in Sec. 4.3.4 to detect all light escaping at the surfaces, at the edge faces, and all escaping light in general ("center-mount" PL). These measurements were compared with the results from the angular resolved measurements, which were numerically integrated aver all angles. Note that for the integration of the angular surface PL the weighting factor $\sin\phi_\mathrm{d}$ needs to be considered (see Eq. (3.66)). The sum of both front and back side measurements was taken as the contributions of both sides are detected in the integrating sphere. Furthermore, the expected spectra from theory corresponding to the measurement were calculated.

The absolute values of the different measurements and calculations are not comparable since not all of them could be corrected for the absorptances of the samples. More importantly, however, is the shape of the spectra. Therefore, all spectra were normalized to one at $\lambda = 700\,\mathrm{nm}$, which has been found to be a reasonable procedure as at this wavelength no strong influence of the different effects is expected.

Surface PL

The (integrated) surface PL comprises all light that escapes at the front and back surfaces. For the spin coated and bonded LSC samples the results of the different measurement methods agree well with the theoretical spectrum that is given by the undisturbed emission spectrum ($(1-\sigma^0)\,g^0(\lambda)$), as shown in Fig. 5.12 (a) and (d), respectively. The minor deviation of the integrating sphere measurements (blue lines) is most likely due to the removal of the background signal of the excitation laser: as the samples absorb only little, the emission signal was rather

low compared to the strong background signal. The subsequent normalization at $\lambda = 700$ nm can cause differences in the height of the emission peak at $\lambda = 600$ nm, which is typically around 7-times higher than the value at $\lambda = 700$ nm. Overall, however, the three different curves agree quite well, confirming the finding from above of undisturbed and isotropic emission in the LSC samples.

The results for the spin coated and bonded TSR samples are presented in Fig. 5.12 (b) and (e), respectively. For the spin coated sample, both measured spectra are reduced in the spectral range of 600–700 nm compared to the undisturbed emission spectrum as the filters prevent part of the emitted at these wavelengths from escaping. The integrating sphere measurement (blue line), however, is higher at these wavelengths than the integrated angular surface PL measurement (red line). This difference is also visible in the two spectra calculated with the ray-tracing method (see Eq. (3.66)) for $l_\mathrm{d} = 12.5$ mm (whole sample surface) and $l_\mathrm{d} = 2.5$ mm (detection spot of angular resolved measurement setup) corresponding to the two measurement configurations. The difference can be explained as follows: the longer the path of propagation, the more interactions occur with the non-perfect filters, which leads to an increasing out-coupling of light. Since the integrated angular surface PL measurement considers out-coupled light from a small spot size, less light is detected, while additional out-coupling on the whole sample surface contributes to the integrating sphere measurement.

For the bonded TSR sample, the measured spectra differ strongly from the dye's emission spectrum, but agree very well with the calculated spectra. The integrating sphere measurements suffered from a low signal level, resulting in an artifactory spike at 695 nm. Despite the poor signal quality of this measurement, the difference in the calculations with $l_\mathrm{d} = 12.5$ mm and $l_\mathrm{d} = 2.5$ mm around 570–610 nm is qualitatively confirmed by the two different measurements.

The results for the spin coated and bonded PLSC samples are shown in Fig. 5.12 (c) and (f), respectively. In both cases the spectra from the two different measurement methods coincide very well. This confirms on the one hand the consistency of the methods in general. On the other hand, it indicates that on the way to the edges no (spectrally different) light is out-coupled other than the light escaping from the detection spot of the angular resolved measurement setup. This supports the hypothesis that the angular surface PL discussed above is a result of the modified emission due to the LDOS, and not a result of the filters partly keeping the emitted light inside like in the TSR samples.

For both samples the theoretical spectrum for the escaping emission from the ideal Bragg stack is shown. It is given by the product of the modified emission spectrum $g^\mathrm{PC}(\lambda)$ and the "inverse" light guiding efficiency $1 - \sigma^\mathrm{PC}(\lambda)$. The exact same spectrum was obtained by integrating the theoretical angular surface PL, which shows the consistency of both methods. The differences in measured and calculated spectra are most likely caused by the non-idealities of the samples: in the spin coated sample not all dye layers experience the full LDOS effect, as

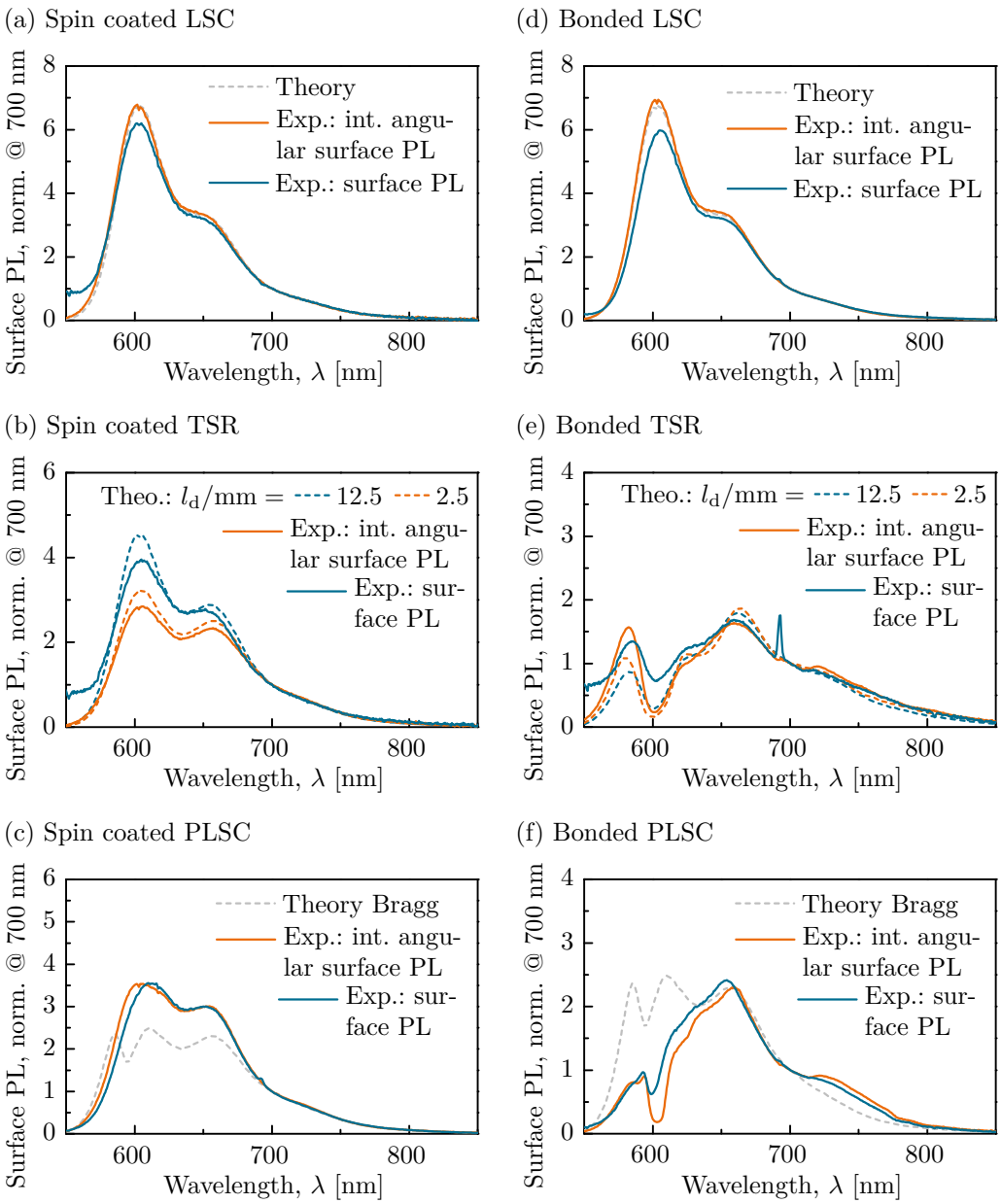

Figure 5.12: Spectra of the light escaping from the surface of the LSC, TSR and PLSC samples of both fabrication processes. The integrating sphere measurement, the numerically integrated angular resolved surface PL and theoretical calculations were normalized at $\lambda = 700$ nm for comparison. While the two measurement methods agree well for the LSC and PLSC samples, the differences for the TSRs reveal that part of the emission missing in the angular resolved measurement escapes at some point towards the edges.

discussed above. For the bonded filters the Bragg stack theory is not directly applicable due to the non-periodic structure and the different refractive indices.

Edge PL

The (integrated) edge PL comprises all light that is guided to edges. The measured edge PL spectra of the six samples are shown in Fig. 5.13 together with the integrated angular edge PL measurements and theoretical calculations. The excitation conditions in the two measurement methods are comparable: the laser spot hit the sample at 1 cm-distance from the edge face that was analyzed. This correspondence is confirmed in the very good agreement of the two measured spectra for all samples with only minor deviations.

The theoretical spectrum of the LSCs is given by the undisturbed emission spectrum ($\sigma^0 g^0(\lambda)$). For the TSR sample it was obtained with the ray-tracing calculations with $l_\mathrm{d} = 10\,\mathrm{mm}$ (see Eq. (3.67)). The measurements of all LSC and TSR samples are very similar to the corresponding theoretical spectrum. For the bonded samples, slight deviations occur at the short-wavelength part of the spectrum, which may be caused by reabsorption due to the higher dye content compared to the spin coated samples.

For the PLSC samples significant differences were observed at the short-wavelength part compared to the theoretical spectra. The latter were calculated from the modified emission spectrum inside the Bragg $g^\mathrm{PC}(\lambda)$ multiplied by the light guiding efficiency $\sigma^\mathrm{PC}(\lambda)$. Thus, it is not directly applicable for the bonded PLSC sample, as explained above. The deviation from the calculation is confirmed in both measurement methods. There are two possible explanations for the missing photons at around 600 nm: first, the modification of emission might be stronger than calculated such that less light is emitted at the upper-frequency band edge. Second, reabsorption can drastically re-shape the spectrum at these wavelengths.

For the bonded sample there may indeed be a stronger LDOS effect than in the Bragg stack calculation due to the higher refractive index contrast of the filters. Deviations from the Bragg stack calculations at the short-wavelength part of the spectrum were also observed in the surface PL of the bonded PLSC. Due to the large dye layer thickness of 800 nm, however, reabsorption might also play a role. For the spin coated sample, the speculation of a stronger LDOS effect is contradictory to the good agreement between theory and experiments in the surface PL. As the sample contains 10-times more dye than the corresponding LSC and TSR, reabsorption may be the major mechanism responsible for the deviation of this sample.

Reabsorption within the PLSC is quite hard to calculate: I present results for a propagation-based model in Sec. 6.1.2. However, the reality might be even more complex: light is guided within both the glass substrate and the Bragg stack layers. In the layers, the modes cannot be treated with ray-optics; instead, their exact

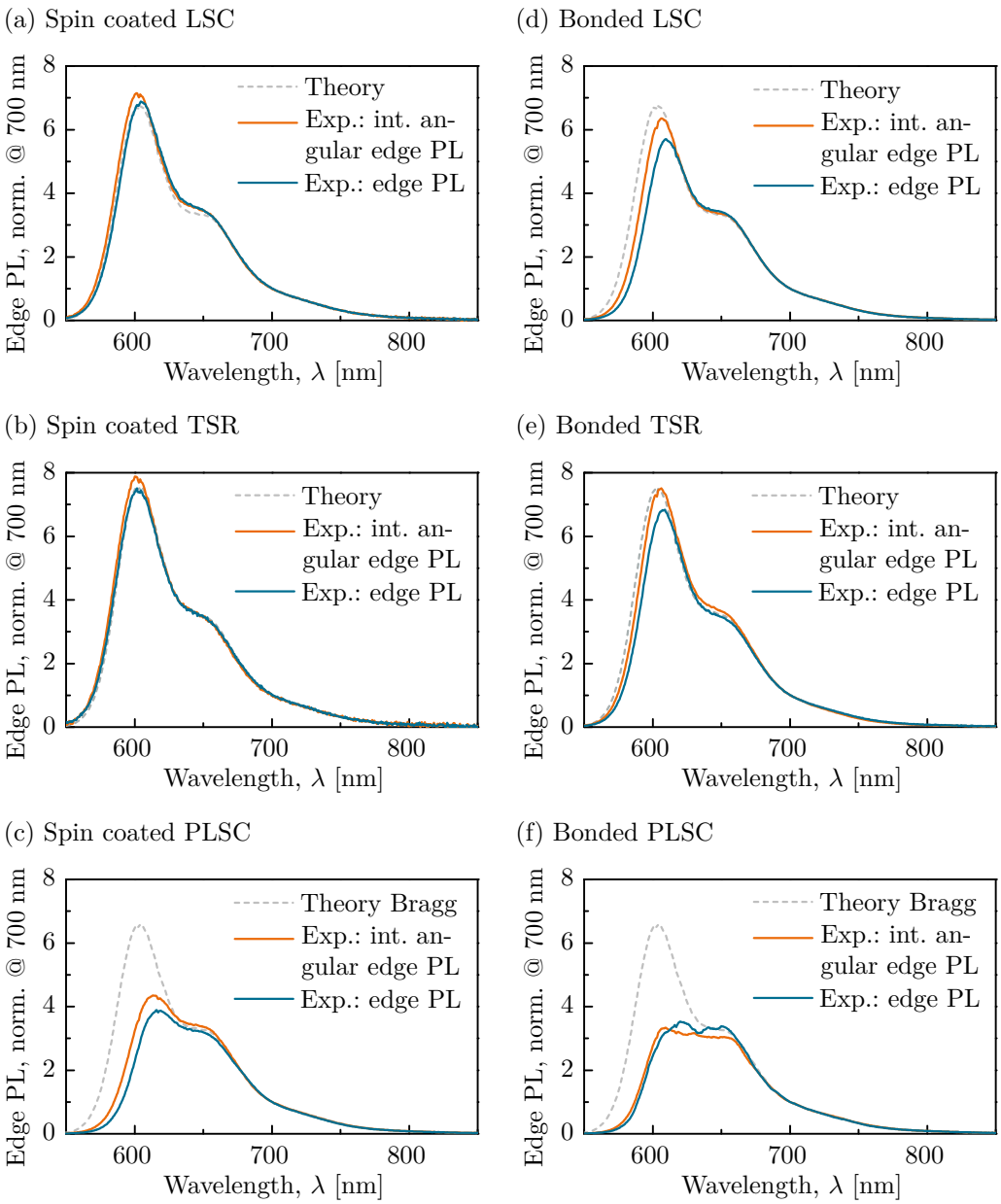

Figure 5.13: Measured and calculated PL spectra of the light guided to the edges of the different samples, normalized at $\lambda = 700$ nm for comparison. The integrating sphere measurement and the numerically integrated angular edge PL agree very well for all samples. The differences between measurements and calculations at the short-wavelength part of the spectrum for the PLSC samples may be caused by reabsorption and a potentially stronger LDOS effect than was calculated.

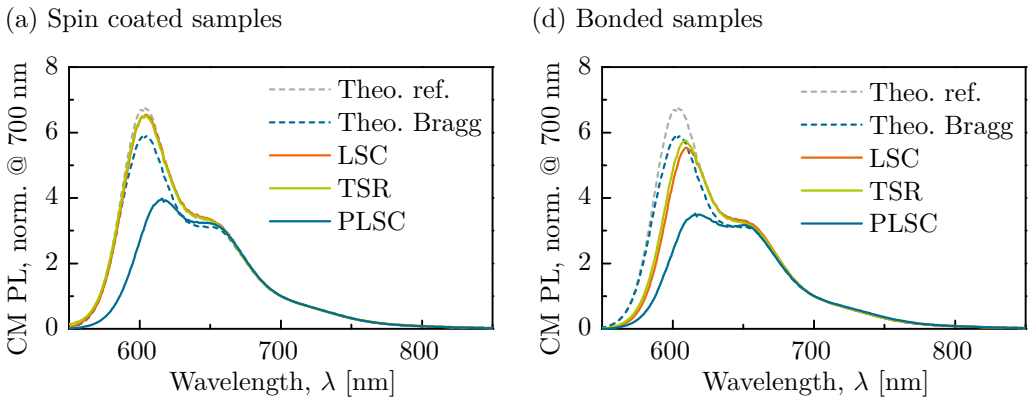

Figure 5.14: Measured center-mount (CM) PL spectra, in which all light escaping from the sample (through surfaces and edge faces) is detected. It is compared to the total emission spectra for undisturbed emission ("Theo. ref.") and the modified emission in the Bragg stack. Again, the PLSC samples deviate from the calculated spectra at the short-wavelength tail as seen in the edge PL measurements. Due to the higher dye content in these samples, these differences might be caused by reabsorption of the guided light.

field distribution in the dye-doped and undoped layers need to be considered. However, reabsorption losses become less detrimental to the LSC performance when the light guiding efficiency is enhanced like in the PLSC. Details about these concentrator performance aspects are discussed in Ch. 6.

Center-mount PL

As the third integrating-sphere measurement method, the PL in the center-mount configuration was measured for all samples. In this way, all light escaping from the sample, i.e. through front and back surface as well as from the edge faces, is detected, as show in Fig. 5.14. The measured spectra were compared to the total emission spectra g^0 (undisturbed emission) and g^{PC} in the Bragg stack.

The spin coated LSC and TSR samples agree very well with the theoretical spectrum. The PLSC sample, however, strongly deviated at the short-wavelength part of the spectrum, as also observed in the edge PL. Following the argumentation from above, this difference is most likely caused by reabsorption of the guided light.

The measurements of the bonded LSC and TSR samples show minor deviations from the theoretical spectrum at the short-wavelength tail, as also seen in their edge PL measurements. Again, this is presumably caused by reabsorption. The center-mount PL of the bonded PLSC confirms the results of the surface and edge PL measurements: less light is detected at around 600 nm than in the Bragg stack calculation, which might be due to a stronger LDOS effect and reabsorption, as discussed above.

Chapter 6

Effect on concentrator performance

A photonic structure affects the performance of an LSC in many aspects: on the one hand, it influences the spectral and directional distribution of emission and the light guiding efficiency, as discussed previously. On the other hand, the structure has an effect on the absorption of incident light and on reabsorption of emitted light, both being crucial aspects for the concentrator performance. In the first part of this chapter, the absorption of incident light and the overall performance are investigated theoretically for multilayer (P)LSCs. I will show that the PLSC's concentrator quantum yield is superior to conventional LSCs due to an increased absorption and an enhanced light guiding. In the second part, experimental results of the multilayer and opal samples are discussed.

6.1 Modeling results for multilayer structures

6.1.1 Absorption of incident light

An important factor for the performance of a PLSC is the absorption of incident light: when no photons are absorbed, no photons can be emitted and guided to the edge, independent of the improvements in quantum yield and light guiding efficiency. To study the absorptance of PLSC structures, the scattering matrix method was applied (see Sec. 3.3.1). To model the absorptance of the dye-doped layers, their complex refractive index was extracted from the dye's extinction coefficient that was obtained in the dye-concentration study (Sec. 4.1.1).

In the following I compare the absorptance of multilayer PLSCs and conventional LSCs, study how many layers are needed to absorb large parts of incoming light, and investigate how oblique incidence affects the absorptance.

Comparison of PLSC and conventional LSC

To compare the absorptance of a realistic multilayer PLSC, the structure depicted in Fig. 6.1 (a) was modeled: following the fabricated spin coating samples, a Bragg stack with 29 individual layers was used where the inner 10 low-refractive-index layers were doped with the Lumogen Red (LR) dye ($\zeta_{\text{dye}} = 1$ w%). The layer thicknesses were given by $\lambda_{\text{design}} = 645$ nm, for which optimum collection of absorbed light was found (see Sec. 6.1.2).

The stack was modeled on top of a comparatively thick glass substrate (n=1.5) that was treated incoherently, i.e. reflected light from the back surface was considered for the (local) absorptance inside the stack by superposition of intensities (cf. Sec. 3.3.2). In this way the calculated absorption represents the realistic case of non-coherent incident light.

For comparison an LSC with the same amount of dye was modeled as a thin film LSCs, as shown in Fig. 6.1 (b). Thus one dye-doped layer as thick as all the dye-doped layers of the PLSC was put on top of an incoherently treated glass substrate. Both systems were surrounded by air ($n = 1$) and light was incident normal to the surface from the top.

Fig. 6.1 (c) shows the resulting absorptance for the two structures. The shape of the two spectra differ significantly: while the LSC's absorptance corresponds to the dye's extinction, the spectrum of the PLSC features sharp peaks. The absorptance of incident light is strongly increased compared to the LSC case, especially for wavelengths from 550–600 nm.

This enhancement can be explained with slow light modes at the edge of the photonic crystal's band gap: at the upper-frequency band edge the energy of the electromagnetic fields is concentrated in the regions of low refractive index, i.e. in the dye-doped layers, as seen in the 1D LDOS in the direction of incidence, as depicted in Fig. 3.2 (a). This enhancement in the local energy density amplifies the absorption and causes, together with the parasitic reflection of incident light, the sharp peaks in the absorptance spectrum.

In more detail, the local distribution of intensity ($\propto |\boldsymbol{E}(\boldsymbol{r})|^2$) in the dye-doped PLSC layers and the corresponding "slices" of the LSC's dye-doped block were compared. Their ratio, as shown in Fig. 6.1 (d), reveals the increase in local intensity, especially at the band edge near 600 nm. But also for shorter wavelengths, the intensity is rather enhanced than suppressed. For longer wavelength outside the spectral range of dye absorption, the intensity in the PLSC is much lower as in the LSC due to the reflection of incident light within the band gap. As the local absorptance is directly proportional to $|\boldsymbol{E}(\boldsymbol{r})|^2$, i.e. to the intensity (see Eq. (2.25)), the absorptance is also locally enhanced by a factor of up to six in the modeled PLSC system, which results in the enhancement of the overall absorptance.

This result shows that the emission-related improvements such as the enhanced light guiding efficiency do not come at the cost of worse absorptance. In fact, the

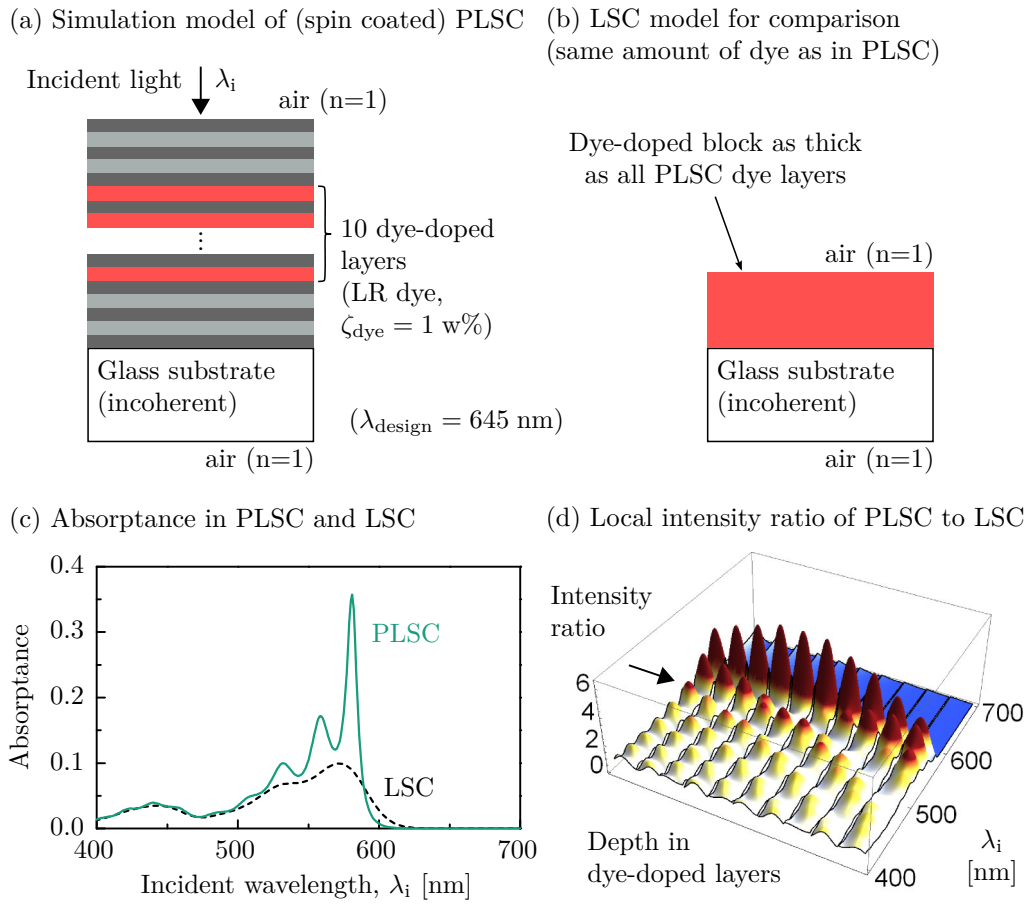

Figure 6.1: The absorptance of (a) a PLSC and (b) a conventional LSC was calculated using the scattering matrix method. As in the fabricated spin coating PLSC, a Bragg stack of 29 individual layers with 10 dye-doped layers was modeled, on top of a "thick" glass substrate that was treated incoherently. To allows for comparison, the corresponding thin film LSC contains the same amount of dye. As shown in (c), the absorptance of the PLSC is strongly increased especially near the band edge at 600 nm. This enhancement is caused by the local concentration of the energy of slow-light modes in the low-refractive-index layers as shown in (d).

photonic structure is even beneficial for the absorption of incident light for the PLSC analyzed here although it was not optimized for low parasitic reflectance of incident light in the dye's absorption range. The overall absorptance of the modeled structures, however, is rather low in view of the application for harvesting solar energy. To increase the overall absorptance of a PLSC, more dye-doped layers are necessary as discussed in the following.

Variation of the number of dye-doped layers

To study the absorptance as a function of the number dye-doped layers, an idealized PLSC structure was used, as illustrated in Fig. 6.2 (a). To ensure that the dye doped layers experience the full LDOS effect of the periodic Bragg stack, a structure was modeled with several undoped outer layers. Corresponding to the results of the simulations from my publication Ref. 171, 20 bi-layers on the top and bottom were used. The number of dye-doped layers m in between was varied between one and 1000.

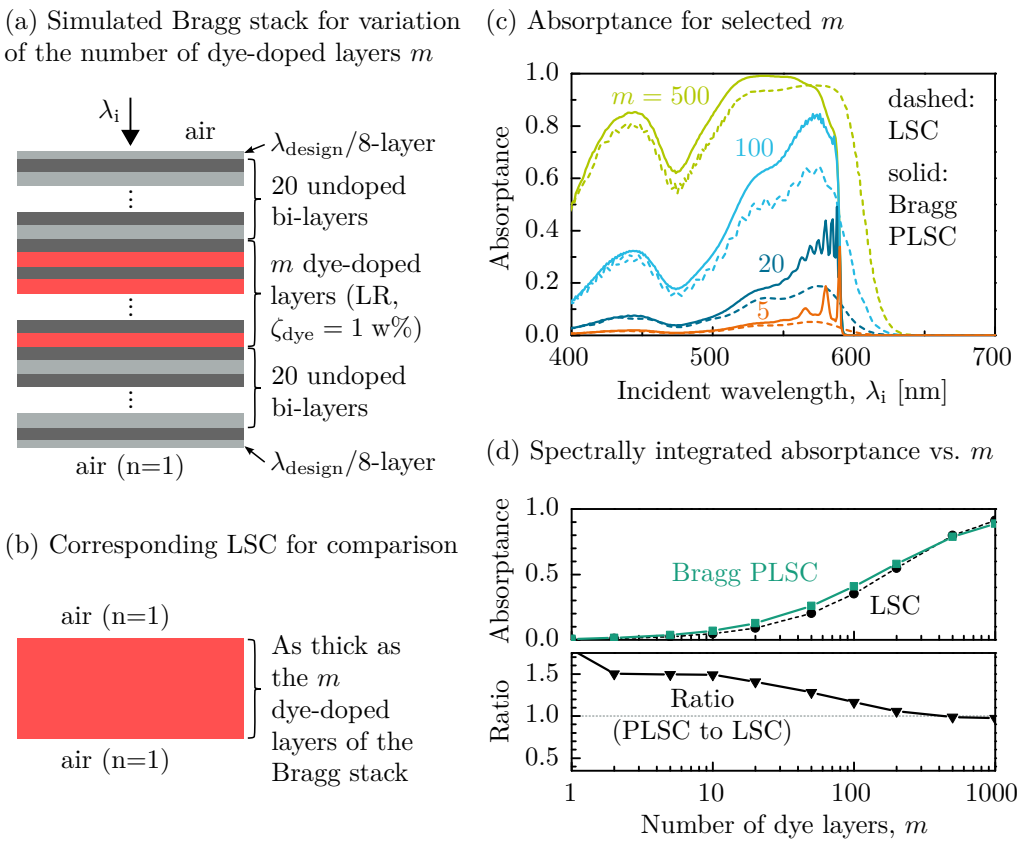

Figure 6.2: To investigate the absorptance for different number of dye-doped layers m, an idealized PLSC was modeled with 20 undoped Bragg bi-layers on top and bottom to establish the full LDOS effect, and with outer λ_{design}/8-layers to suppress parasitic reflection, see (a). An LSC with same dye content was used for comparison, as illustrated in (b). As shown in (c) for selected m, the PLSC's absorptance is again enhanced at the band edge. This increase is quantified in the spectrally integrated absorptance in (d), where the difference in absorptance of PLSC and LSC vanishes for several hundred dye layers, which are necessary to absorb significant amounts of the incident light.

To optimize the transmission of incident light in the absorption range, a low-refractive-index layer with a thickness of $\lambda_{\text{design}}/8$ was placed on top and bottom of the complete stack. As a well-known filter design strategy, such simple $\lambda_{\text{design}}/8$-layers can effectively suppress reflection side lobes [139, 149]. At the same time, the LDOS in the inner layers is still determined by the periodic Bragg stack. For comparison, an LSC with the same amount of dye was modeled as a dye-doped slab as thick as the m dye-doped layers of the PLSC (Fig. 6.2 (b)). Both structures were modeled without a glass substrate that might be necessary in experiments.

Selected absorptance spectra for certain values of m are shown in Fig. 6.2 (c): similar to the results of the PLSC calculation from above, the absorptance of the Bragg stacks is enhanced over the LSC, especially near the band edge close to $\lambda_{\text{i}} = 600$ nm. Interestingly, the absorptance of the PLSC is not capped at 96% as for the LSC due to the reflectance of 4% at the air-to-polymer surface: as a result of the anti-reflection effect of the $\lambda_{\text{design}}/8$-layer the PLSC's absorptance can approach 100%. In contrast to the enhancement for wavelengths below the band edge, the PLSC's absorptance drops to zero for $\lambda_{\text{i}} > 590$ nm. In the LSC, however, significant absorption also occurs at these wavelengths above the band edge, in particular for thick dye layers.

To compare the total amount of absorbed light for both systems, the absorptance spectra were integrated from 400–600 nm and normalized by dividing by the corresponding integral over a maximum absorptance of one. This integrated absorptance is shown in Fig. 6.2 (d) for the Bragg PLSC and the LSC, along with its ratio of PLSC to LSC for comparison. In the PLSC, the integrated absorptance is enhanced over the LSC by up to 50% for a few dye-doped layers. To absorb significant fractions of the incident light, however, more than 100 dye-doped layers are needed in both systems. For this many layers, the integrated absorptance of PLSC and LSC become similar as the enhancement below the band edge saturates and it is compensated by the LSC's absorptance tail at $\lambda_{\text{i}} > 590$ nm.

To conclude, several hundred dye-doped layers would be necessary to absorb most of the incident light, which is challenging for the fabrication of such stacks. For this many layers the enhanced absorption of the PLSC saturates and approaches similar values as corresponding LSCs. The improvements of the PLSC with regard to emission and light guiding, however, are still beneficial to the overall performance, even without additional enhancement of absorption.

Oblique incidence of light

In contrast to other concentrating photovoltaic technologies that work with mirrors or lenses, one advantage of LSCs is that they can concentrate not only direct (normal incidence) but also diffuse radiation with no need for tracking. In conventional LSCs light with all angles of incidence can enter the concentrator to be absorbed. The reflectance at the surface, which is defined by the Fresnel equations,

(a) Angular absorptance in Bragg PLSC (b) Spectrally integrated absorptance

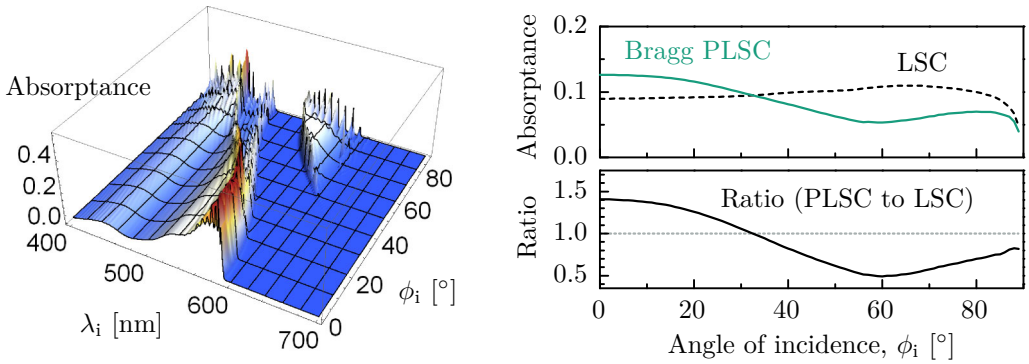

Figure 6.3: As the reflectance of the Bragg stack shifts with oblique incident angles to shorter wavelengths, less light can be absorbed inside the structure as depicted in (a). The spectrally integrated absorptance shown in (b) reveals this decrease for the PLSC while the angular absorptance of the LSC is relatively constant for most angles. The reduced absorptance of the PLSC at oblique angles of incidence may be over-compensated by the enhancement at near-normal angles, depending on the specific application scenario.

increases only slowly with larger angles of incidence.

In the PLSC, however, the reflectance strongly depends on the incident angle: the broad reflection peak resulting from the band gap of the Bragg stack shifts to shorter wavelengths for oblique incident angles. Accordingly, high reflectance occurs at wavelengths where the dye absorbs, which in turn reduces the absorptance at oblique incidence angle, as shown in Fig. 6.3 (a).

To investigate the angular dependence in detail, the absorptance of the Bragg stack from Fig. 6.2 (a) with $m = 20$ dye-doped layers was calculated for incident angles from 0–89° and compared to the corresponding LSC slab. As in the previous section, the absorptance was spectrally integrated from 400–600 nm and normalized to the maximum integrated absorptance. As shown in Fig. 6.3 (b), the integrated absorptance of the PLSC is enhanced by 40% for normal incidence ($\phi_i = 0°$). For increasing angles of incident the absorptance decreases until $\phi_i = 60°$. For even larger angles the PLSC's absorptance recovers slightly as the reflection peak has passed the wavelengths of strongest absorption.

The amount of absorbed light in the LSC is more or less constant for angles up to ca. 80°, as the increase in reflection of s-polarized light is compensated by the reduced reflection near the Brewster angle for the p-polarized fraction of the incident light. In theory, the absorptance of a "thick" i.e. incoherently treated LSC is maximum for normal incidence but with a very shallow decrease to larger angles. Due to the microscopic LSC slab thickness in this calculation, however, interference effects increase the absorptance slightly at oblique incidence over the

value of normal incidence, resulting in the maximum absorptance around 60–70°.

The reduced absorptance of the PLSC at large incident angles may be overcompensated by the enhancement at near-normal angles at which typically most energy from the sun is received on earth (around noon). To quantitatively calculate the impact of the angular dependence of absorptance on the performance of a (non-tracked) (P)LSC system, however, detailed knowledge about the specific application scenario is necessary, such as the geographic location and how the (P)LSC "module" is mounted.

6.1.2 Overall concentrator performance

In Chapter 5, the influence of the photonic crystal on the emission was studied in detail. Most importantly for the LSC application, the emitted spectrum, the fluorescence quantum yield and the light guiding efficiency are affected as a result of an altered LDOS. Furthermore, as seen in the previous section, the absorption of incident light is changed in PLSCs. To predict the overall influence of all these individual effects on the performance of the concentrator, I propose a model for the device performance combining the different mechanisms.[1]

Similarly to Ref. 13, the path of an incident photon through the concentrator is modeled as a chain of probabilities, as shown in Fig. 6.4. This way, the concentrator quantum yield η (CQY), i.e. the probability that a photon incident on the device reaches the edge face, can be calculated. The CQY is a quantity that is also accessible in measurements using the optical characterization methods introduced in Sec. 4.3.1.

First, an incident photon with wavelength λ_i needs to be absorbed in the concentrator by a dye molecule, which is described by the probability $p_{abs}(\lambda_\mathrm{i})$. This probability is given by the absorptance as calculated in the previous section and it depends on the exact PLSC configuration. In the following, I analyze the PLSC structure depicted in Fig. 6.1 (a) that corresponds to the fabricated structures from spin coating.

If an incident photon has been absorbed, the dye emits a red-shifted photon with a certain probability that is given by the dye's PLQY Φ. If a photon is emitted, it may be trapped and guided inside the concentrator with the probability p_g, which is determined by the spectral average of the light guiding efficiency $\sigma(\lambda)$, weighted with the spectral distribution $g(\lambda)$ of the emitted light:

$$p_\mathrm{g} = \frac{\int g(\lambda)\,\sigma(\lambda)d\lambda}{\int g(\lambda)d\lambda}. \tag{6.1}$$

A guided photon faces a certain probability to be reabsorbed on its path through the concentrator to the edge face. If reabsorbed, the photon is fed back in the

[1] Parts of this section are adopted from one of my publications, Ref. 188.

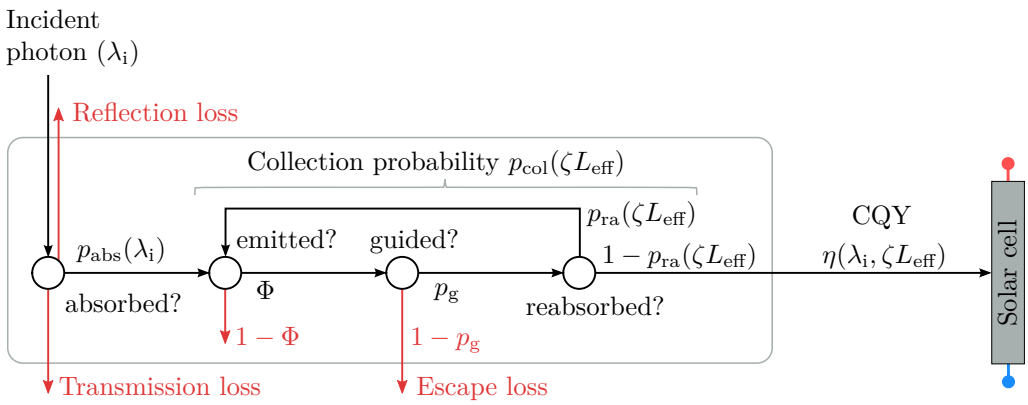

Figure 6.4: The overall concentrator performance is modeled as a chain of probabilities: an incident photon needs to be absorbed, subsequently emitted and guided to reach the edge face. Depending on the concentrator size, photons may be reabsorbed on the path to the edge with a certain probability, which is implemented as a feedback loop back to the emission process.

probability chain to the point of emission, as indicated in Fig. 6.4. This reabsorption probability $p_{ra}(\zeta L_{eff})$ is the average of a *spectral* reabsorption probability $p_{ra,s}(\lambda, \zeta L_{eff})$, weighted with the spectral distribution of the guided light that is given by $g(\lambda)\,\sigma(\lambda)$. Thus,

$$p_{ra}(\zeta L_{eff}) = \frac{\int g(\lambda)\,\sigma(\lambda)\,p_{ra,s}(\lambda, \zeta L_{eff})d\lambda}{\int g(\lambda)\,\sigma(\lambda)d\lambda}. \tag{6.2}$$

The phenomenon of reabsorption is quite complex to model. To account for the positions of reabsorption events, often methods like monte-carlo ray-tracing are employed [146]. For a simplified treatment here, an analytical approach is used to estimate the spectral reabsorption probability based on the Lambert-Beer absorption law:

$$p_{ra,s}(\lambda, \zeta L_{eff}) = 1 - \mathrm{e}^{-\epsilon(\lambda)\zeta L_{eff}}, \tag{6.3}$$

where $\epsilon(\lambda)$ is the dye's extinction coefficient, ζ is the dye concentration, and the "effective length" L_{eff} models the path length to the edge face. This effective length is related to the actual concentrator dimensions and thus allows investigating the influence of the LSC size qualitatively. Absolute values, however, depend on the specific LSC system geometry (e.g. how the solar cells are placed). Furthermore, L_{eff} needs to be considered for different spatial positions (similar to the treatment in Ref. 56) and one needs to account for possible reabsorption events at other positions (with subsequent emission).

The overall concentrator quantum yield η can be obtained from the individual

probabilities by adding up the different contributions resulting from the reabsorption loop:

$$\begin{aligned}\eta(\lambda_\mathrm{i}, \zeta L_\mathrm{eff}) = p_{abs}(\lambda_\mathrm{i})\{&\Phi\, p_\mathrm{g}\,[1 - p_\mathrm{ra}(\zeta L_\mathrm{eff})] \\ &+ p_\mathrm{ra}(\zeta L_\mathrm{eff})\,\Phi\, p_\mathrm{g}\,[1 - p_\mathrm{ra}(\zeta L_\mathrm{eff})] \\ &+ p_\mathrm{ra}^2(\zeta L_\mathrm{eff})\,\Phi\, p_\mathrm{g}\,[1 - p_\mathrm{ra}(\zeta L_\mathrm{eff})], \\ &+ \dots\},\end{aligned} \tag{6.4}$$

which is a geometric series and can thus be written as

$$\eta(\lambda_\mathrm{i}, \zeta L_\mathrm{eff}) = p_{abs}(\lambda_\mathrm{i})\, \underbrace{\frac{\Phi\, p_\mathrm{g}\,[1 - p_\mathrm{ra}(\zeta L_\mathrm{eff})]}{\Phi\, p_\mathrm{g}\, p_\mathrm{ra}(\zeta L_\mathrm{eff})}}_{p_\mathrm{col}(\zeta L_\mathrm{eff})} = p_{abs}(\lambda_\mathrm{i})\, p_\mathrm{col}(\zeta L_\mathrm{eff}), \tag{6.5}$$

where the collection probability $p_\mathrm{col}(\zeta L_\mathrm{eff})$ summarizes the emission-related probabilities. This collection probability states the ratio of the number of photons reaching the edges to number of absorbed photons. It is determined only by the photonic crystal's LDOS and the undisturbed properties of the dye $g^0(\lambda)$ and Φ^0.

Spatially resolved probabilities and averaging

When calculating the collection probability in the PLSC, it needs to be considered that both absorption and emission depend on the exact position of an emitter. The PLQY, the LGE, the emission spectrum, and therefore also the reabsorption probability are derived from the (F)LDOS. Therefore, these quantities depend on the emitter position $\boldsymbol{r}$ in the layer. The *local* probabilities $\Phi(\boldsymbol{r})$, $p_\mathrm{g}(\boldsymbol{r})$, $p_\mathrm{ra}(\zeta L_\mathrm{eff}, \boldsymbol{r})$, and the resulting $p_\mathrm{col}(\zeta L_\mathrm{eff}, \boldsymbol{r})$ are shown in Fig. 6.5 (c), (d), (e), and (b), respectively. While the individual $\Phi(\boldsymbol{r})$, $p_\mathrm{g}(\boldsymbol{r})$, and $p_\mathrm{ra}(\zeta L_\mathrm{eff}, \boldsymbol{r})$ show different variations with $\boldsymbol{r}$ in strength and curvature, the combined overall collection probability $p_\mathrm{col}(\zeta L_\mathrm{eff}, \boldsymbol{r})$ is clearly enhanced for emitter positions in the center of the layer.

Light is emitted where it is absorbed. The *local* absorptance of incident light was studied in detail in the beginning of Sec. 6.1.1 for the PLSC structure considered here. Consequently, a spatial resolved absorption distribution $w_\mathrm{abs}(\boldsymbol{r})$ was calculated by averaging the local absorptance over all wavelengths and layers from Fig. 6.1 (d), resulting in the curve shown in Fig. 6.5 (a). Beneficially for the concentrator performance, light is absorbed most likely in the center of a dye-doped layer, where also emitted light is collected most efficiently. Besides the local absorption of incident light, dye molecules are also excited from reabsorption of emitted light. The spatial distribution of excitation through reabsorption was not studied in detail and assumed to be similar to $w_\mathrm{abs}(\boldsymbol{r})$.

Given the local collection probability $p_\mathrm{col}(\zeta L_\mathrm{eff}, \boldsymbol{r})$ and the local absorption distribution $w_\mathrm{abs}(\boldsymbol{r})$, the average collection probability $p_\mathrm{col}(\zeta L_\mathrm{eff})$ was calculated as

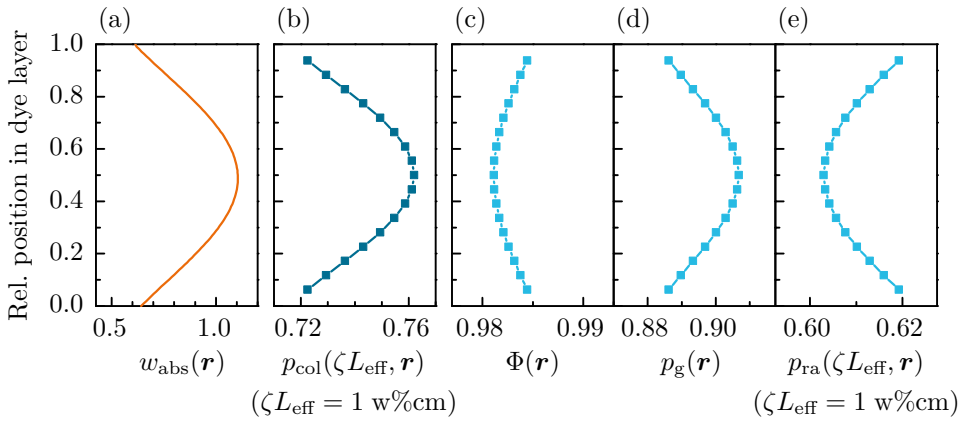

Figure 6.5: (a) The local distribution of absorption $w_{\mathrm{abs}}(\boldsymbol{r})$ obtained from the local absorptance calculation in Fig. 6.1 is enhanced in the center of the layers. As they are derived from the (F)LDOS, the emission-related probabilities depend of the emitter position $\boldsymbol{r}$, as shown in (c), (d), and (e). The resulting local collection probability $p_{\mathrm{col}}(\zeta L_{\mathrm{eff}}, \boldsymbol{r})$ is also increased in the center, as shown in (b). As light is emitted only where it is absorbed, the local absorption distribution $w_{\mathrm{abs}}(\boldsymbol{r})$ was used as weights to average p_{col}.

a weighted average, where the weights were given by $w_{\mathrm{abs}}(\boldsymbol{r})$. In the case of no reabsorption ($\zeta L_{\mathrm{eff}} = 0$), $p_{\mathrm{col}}(0) = 0.883$ was obtained for the PLSC, i.e. 88.3% of the absorbed photons can be guided to the edge faces in this case. The corresponding collection probability of a conventional LSC is simply the product of the dye's PLQY ($\Phi^0 = 98\%$) and the LGE due to TIR (74.5%), thus $p_{\mathrm{col}}(0) = 0.730$.

From these numbers, one can see that the losses from non-radiative processes and due to the escape cone are strongly reduced by 56.7% in the PLSC. This result is in accordance with the calculated reduction in the escape cone loss by 60% from the angular resolved surface PL study (see Sec. 5.1.4), which however did not account for the locally different absorption and the changes in PLQY.

Reabsorption

To illustrate the impact of reabsorption, Fig. 6.6 (a) shows the spectral reabsorption probability $p_{\mathrm{ra,s}}(\lambda, \zeta L_{\mathrm{eff}})$ for selected values of ζL_{eff}. The higher the dye concentration or the larger the concentrator dimensions, the higher the spectral reabsorption probability and its overlap with the emission spectrum. Thus, the reabsorbed fraction of the emitted light and therefore the corresponding reabsorption probability $p_{\mathrm{ra}}(\zeta L_{\mathrm{eff}})$ increase with ζL_{eff}.

As one result, the collection probability decreases with ζL_{eff} as discussed in the following section. Note, however, that reabsorption itself is not a loss mechanism: photons may be lost by not being emitted or by emission into non-guided modes,

(a) Spectral reabsorption probabilities for certain ζL_{eff}

(b) Spectra of light reaching the edge face for certain values of ζL_{eff}

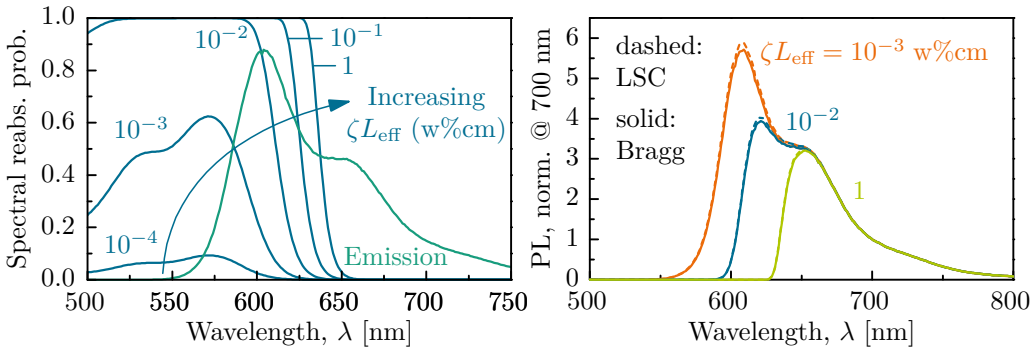

Figure 6.6: (a) With larger values of ζL_{eff}, i.e. larger concentrator dimensions, the spectral reabsorption probability $p_{\text{ra,s}}(\lambda, \zeta L_{\text{eff}})$ increases. (b) As a result, the spectral distribution of the light reaching the concentrator's edge face depends on ζL_{eff}: with increasing reabsorption, i.e. ζL_{eff}, the short-wavelength part of the original emission spectrum vanishes. This effect is well-known from experiments.

but part of the reabsorbed light can still contribute to the overall CQY.

As a second result, the spectral shape of the light reaching the concentrator's edge face can be strongly altered. Given by the product $g(\lambda)\,\sigma(\lambda)\,p_{\text{ra,s}}(\lambda, \zeta L_{\text{eff}})$, the resulting spectrum is shown for three ζL_{eff}-values in Fig. 6.6 (b). To compare the spectral shapes, the spectra were normalized to one at $\lambda = 700$ nm, as were the experimental results in Sec. 5.2.3. With increasing ζL_{eff}, the short-wavelength part of the emission spectrum vanishes. This well-known effect (see e.g. Ref. 18) is similar to the experimentally observed spectra from the sample's edge faces (Fig. 5.13), which supports the hypothesis of reabsorption effects discussed in that section.

Collection probability

To show the influence of the photonic crystal on the emission process and light guiding, the collection probability p_{col} is plotted in Fig. 6.7 (a) as a function of the effective path length ζL_{eff} for a comparison of the LSC and PLSC independent of the exact concentrator dimensions. In the regime with no relevant reabsorption ($\zeta L_{\text{eff}} < 10^{-4}$ w%cm) the collection probability is limited by the corresponding PLQY and LGE as mentioned above. Mainly due to the enhanced LGE the escape cone losses in the PLSC are reduced by 60% compared to the conventional LSC.

In the application relevant regime with $\zeta L_{\text{eff}} >> 10^{-2}$ w%cm (a typical dye concentration of 0.01 w%cm [51] and LSC sizes of 100 cm yield $\zeta L_{\text{eff}} \approx 1$ w%cm) the collection probability decreases with ζL_{eff} for both LSC and PLSC due to

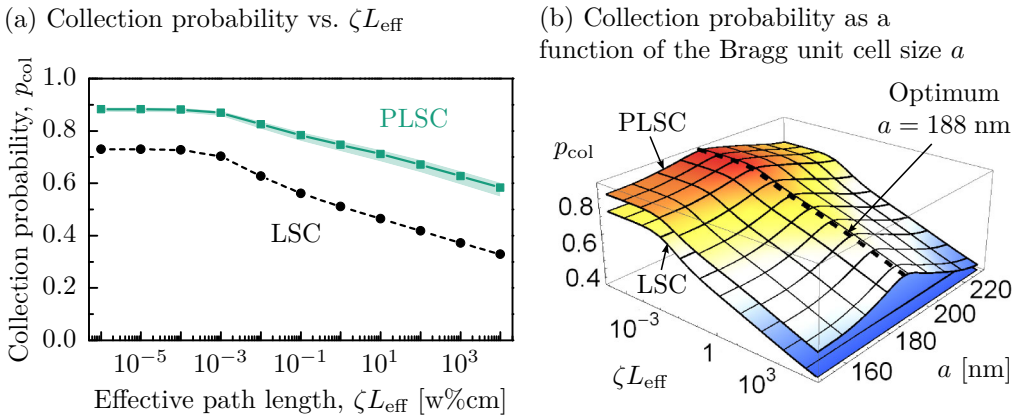

Figure 6.7: (a) The collection probability p_{col} decreases for both PLSC and LSC with increasing effective path length ζL_{eff}, i.e. device dimensions, due to reabsorption. Mainly due to the enhanced light guiding efficiency, however, p_{col} is strongly increased for the PLSC by more than 50% for application-relevant device dimensions. For the PLSC, the green-shaded region marks the minimum and maximum values for all emitter positions $\boldsymbol{r}$, where the drawn line represents the absorption-weighted averaged $p_{\text{col}}(\zeta L_{\text{eff}})$. (b) To optimize the overall performance of the PLSC, $p_{\text{col}}(\zeta L_{\text{eff}})$ was evaluated for different unit cell sizes a of the Bragg stack. The maximum collection efficiency for the LR dye was found for $a = 189$ nm ($\lambda_{\text{design}} = 645$ nm), independent of ζL_{eff}.

increasing reabsorption losses. As in the PLSC part of the emitted light is redistributed to longer wavelengths (see Fig. 5.2) that are less prone to reabsorption, the decrease in p_{col} is not exactly as steep as in the conventional LSC.

More importantly, however, the absolute values of the collection probability are strongly enhanced for the PLSC. For relevant concentrator dimensions ($\zeta L_{\text{eff}} >$ 1 w%cm), p_{col} is increased by 50% and more compared to a conventional LSC.

The LDOS of the Bragg stack and thus the effects on the emission spectrum, PLQY, and LGE can be spectrally shifted by tuning the unit cell size a. Therefore, also the probabilities Φ, p_{g}, and $p_{\text{ra}}(\zeta L_{\text{eff}})$ depend on this parameter a. To optimize the overall performance, the collection probability $p_{\text{col}}(\zeta L_{\text{eff}})$ of the PLSC was evaluated for values of a from 150–230 nm, as shown in Fig. 6.7 (b). The maximum collection efficiency for the LR dye was found for $a = 189$ nm independent of ζL_{eff}, which corresponds to $\lambda_{\text{design}} = 645$ nm. Interestingly, for this value of a the lower-frequency band edge and thus the transition wavelength from transmission to reflection of the Bragg stack coincides with the crossing of the dye's absorption and emission spectra. Thus incident light can be transmitted and absorbed effectively, although the absorptance was not considered in the optimization with regard to p_{col}. This optimized unit cell size was used for the target thicknesses of the fabricated samples and also for all calculations presented in this work.

Concentrator quantum yield

Combining the results of the collection probability $p_{\mathrm{col}}(\zeta L_{\mathrm{eff}})$ with the absorption probability $p_{\mathrm{abs}}(\lambda_{\mathrm{i}})$ (from Fig. 6.1 (c)), the concentrator quantum yield (η) is shown in Fig. 6.8 for an example value of $\zeta L_{\mathrm{eff}} = 1$ w%cm. The CQY follows the absorptance spectrum and is strongly increased in the PLSC for the whole spectral range due to both absorption enhancement and the higher collection probability.

Considering the solar spectrum, maximum currents of 0.312 mA/cm^2 (LSC) and 0.654 mA/cm^2 (PLSC) can be obtained from these systems assuming ideal solar cells (external quantum yield of one). Thus, the system efficiency would be 2.1-times larger for the PLSC than for a conventional LSC.

The absolute values of the CQY and the potential currents, however, are rather low due to the low absorptance of the PLSC studied here with only 10 dye-doped layers. The absorptance and thus the CQY can be increased with more dye-doped layers, as shown in Sec. 6.1.1. Note, that even if the advantage of increased absorption vanishes for large numbers of dye layers or for oblique incidence, the enhancement in collection efficiency $p_{\mathrm{col}}(\zeta L_{\mathrm{eff}})$ is still maintained. The collection efficiency is determined only by the LDOS of the ideal Bragg stack and the dye, independent of the specific realization (number of layers, $\lambda_{\mathrm{design}}/8$-layers, etc.).

To conclude, the collection of absorbed photons in the PLSC is strongly enhanced based on the proposed device model, mainly due to the better light guiding efficiency. Additionally, the absorptance is typically increased especially near the band edge at 590 nm as the energy of the incident fields concentrates in the dye-doped layers. These two beneficial influences can improve the concentrator quantum yield drastically.

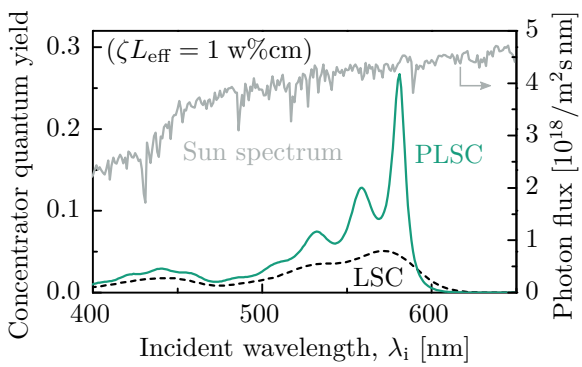

Figure 6.8: The concentrator quantum yield of the PLSC is strongly enhanced over the conventional LSC due to enhancements in both absorption and collection probability. Here, results for the PLSC model from Fig. 6.1 (c) are shown with $\zeta L_{\mathrm{eff}} = 1$ w%. The potential system efficiency of the PLSC is 2.1-times larger than for the conventional LSC.

6.2 Experimental results

To study the concentrator performance in experiments, the absorptance of incident light and the concentrator quantum yield of both the fabricated multilayer and opal samples were assessed, using the optical characterization methods from Sec. 4.3.1.

6.2.1 Multilayer structures

For the multilayer structures, the LSC, TSR, and PLSC samples from both fabrication methods (spin coating and bonding of filters) were characterized. For the exact structure and composition of these samples please refer to Fig. 5.6 and the first part of Sec. 5.2.

Spin coated multilayer structures

The absorptance of the multilayer samples fabricated using the spin coating approach is shown in Fig. 6.9 (a). The PLSC sample features significant absorption of incident light with up to 20%. The shape of the absorptance spectrum exhibit the characteristic distortions of the dye's original absorption spectrum due to parasitic reflection of incident light and local field enhancements, similar to the calculations (Fig. 6.1). Although the peaks are not as pronounced as calculated (most likely due to non-ideal layer thicknesses of the fabricated structures), the absorption is clearly enhanced over the calculated absorptance of an LSC with the same amount of dye shown in Fig. 6.1 (c).

The experimentally fabricated LSC, however, features only a very small absorptance, due to the very thin dye-doped layer (10-times thinner than the total thickness of all dye-doped layers of the PLSC). For the TSR sample with the same thin dye layer, no significant absorptance can be identified as well. Instead, its absorptance curve is heavily distorted: the waviness is a result of adding and subtracting the measurements of the diffuse and total reflectance and the specular transmittance, although angular corrections were applied (cf. Sec. 4.3.1). Furthermore, the curve features an offset that may be caused by broad-band parasitic absorption. More likely, however, the offset results from the uncertainty of the measurement method (stated with 1% absolute, for each individual measurement). This result reveals the weakness of the optical characterization method in accurately measuring weakly absorbing samples that feature strong spectral and angular dependence of their optical properties.

The extracted concentrator quantum yield of the three samples is shown in Fig. 6.9 (b). For the LSC sample, no significant amount of guided light was measured, which is due to the very low absorptance of the sample.

For the same reason, no CQY can be identified in the TSR. Instead, the resulting curve slightly oscillated as a result of superposition of the results of the three dif-

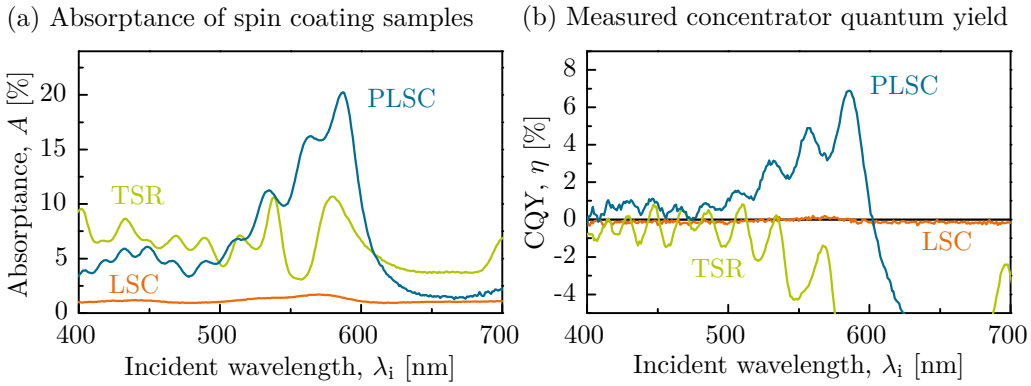

Figure 6.9: (a) Absorptance measurements of the spin coating samples show an absorptance of the PLSC similar than in calculations. In contrast, no significant absorption of incident light could be identified for the LSC and TSR sample that contain 10-times less dye than the PLSC. The TSR measurement furthermore revealed weaknesses of the characterization method for weakly absorbing samples with strong spectral and angular dependence of their optical properties. (b) Accordingly, only for the PLSC reasonable concentrator quantum yield was obtained. Negative values of the CQY, especially in regions of high reflectance, are unphysical measurement artifacts as discussed in the text.

ferent measurement configuration (center-mount, reflectance and transmittance), although the different measurement angles were corrected for. Furthermore, the TSR's CQY drops to negative values that are unphysical. These negative values occur at wavelengths from 600 nm onwards where the sample is highly reflective. For these wavelengths the center-mount measurement drops by some percent points from the expected value at 100% although no absorption should occur at these wavelengths. The reason for this drop is presumably out-coupling of specularly reflected light through a port of the integrating sphere, even though the samples were tilted by 8° with respect to the incident beam. In a detailed study, strongly different measurement results for the highly reflective wavelengths were found for multiple measurement of the same sample that was each time dismounted and re-mounted in the sample holder. Thus, only slight differences in mounting (angle) cause large uncertainties of the center-mount measurement for wavelengths, where a sample features high specular reflectance.

The PLSC features a significant CQY that qualitatively follows its absorptance. With the peak value of 7%, a collection probability (ratio of CQY to absorptance) of roughly $7/20 = 35\%$ was obtained. In contrast to the enhancement in calculations, this value is lower than the values of around 50% obtained for samples with same dimensions in the dye concentration study (see Fig. 4.3 (d)).

This deviation can have several reasons. First, the light guiding efficiency in the fabricated sample could be lower than calculated: the LDOS effect may not

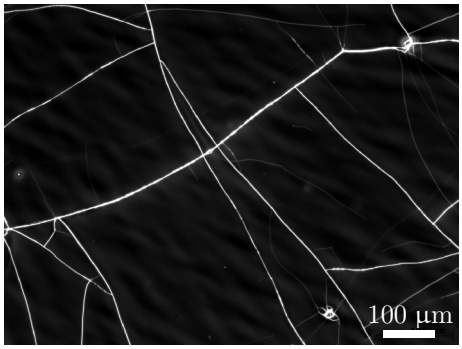

Figure 6.10: Fluorescence micrograph of the spin coated PLSC sample. The fluorescence signal was strongly increased along cracks in top layers of the stack. Originating from mechanical stress in the layers during tempering, guided light may scatter at these cracks and exit the PLSC, thus reducing the CQY.

be fully established due to finite size of the structure, especially in the outer dye-doped layers.

Second, the light guiding efficiency could be reduced by imperfections of the fabricated sample. For a detailed investigation, the PLSC sample was examined using a fluorescence microscope, where the sample is excited with short-wavelength light and only the filtered fluorescence is detected.[2] Indeed, cracks in top layers of the spin coated PLSC were found, along which the fluorescence signal was strongly increased, as shown in Fig. 6.10. These cracks might originate from mechanical stress in the different layers during tempering, as discussed in Sec. 4.1.1. Although the cracks occur at a scale of several hundred µm (much less dense as in the opal samples), guided light may scatter at these cracks and exit the PLSC. While the results from the integrated surface PL (see Fig. 5.12 (c)) indicate that on the way to the edges no significant amount light is lost, the out-coupling of guided light at the cracks could explain the large amount of light detected in the angular resolved surface PL as well as the reduced collection probability obtained here. The exact amount of light lost due to the cracks, however, cannot be quantified by this means.

Third, the collection probability of only 35% could be a result of reabsorption in the PLSC that is stronger than expected. This explanation is supported by the reabsorption indicated in the edge PL measurements (see Fig. 5.13 (c)).

Additionally to these fundamental reasons, the relatively low collection proba-

[2] The microscope Axio Imager.A2 Vario from Zeiss was used, equipped with the HXP120C light source (mercury short-arc lamp). Using the filter set FS09 from Zeiss, samples were excited with $\lambda = 450$–490 nm while only light with $\lambda > 515$ nm was detected by a monochromatic camera.

bility may be caused by the inaccuracy of the measurement method, which is also apparent in the negative values of CQY that are unphysical and result from the measurement artifacts as explained above for the TSR sample.

In conclusion, these measurements revealed the weaknesses of the optical characterization method, especially for weakly absorbing samples with strong spectral and angular dependence of their optical properties and high specular reflectance in the center-mount configuration. For the PLSC, however, a significant amount of incident light was absorbed and guided to the concentrator edge faces, demonstrating the desired functionality.

More reliable quantitative results, especially regarding possible enhancements in collection probability, require further investigations. On one hand, crack-free samples containing much more dye molecules could be fabricated, similar to the simulated stacks from Fig. 6.2 (a). To achieve this, the spin coating process needs to be optimized for reproducibility and layer quality, and partly automated to deposit hundreds of single layers efficiently. On the other hand, the characterization method could be improved, for example by modifying the spectrophotometer setup for spectral resolved detection. Alternatively, samples could be connected to solar cells for electrical characterization, which, however, would introduce other measurement uncertainties due to the optical coupling and non-homogeneous solar cell characteristics.

Bonded IBS filters

The measurement results for the absorptance and the concentrator quantum yield of the samples fabricated by bonding of the IBS filters are presented in Fig. 6.11. For all samples, significant absorptance and light guiding was obtained.

The absorptance in the PLSC follows the one of the LSC sample. Although the PLSC contains twice as much dye as the LSC, the absolute values of the absorptance are comparable. The PLSC, however features strong spectral oscillations although the individual measurements were corrected for their tilt angle. The absorptance of the TSR sample also follows the shape of the other samples' spectrum, but with slightly lower absolute values. Overall, the measurements yield low absolute values with potentially large measurement uncertainties, as discussed above. The uncertainty is for example visible in the small offsets of the spectra for wavelengths from 600–700 nm, where no absorptance should occur.

The concentrator quantum yield of the samples follows the absorptance curves: PLSC and LSC are comparable while the TSR lies slightly lower. As in the measurements of the spin coating samples, the extracted CQY of PLSC and TSR drops to negative values due to artifacts in the center-mount measurements.

Overall, the results indicate neither an increase nor a decrease in the collection probability (i.e. the ratio of CQY to absorptance) of PLSC and TSR compared to the conventional LSC. The reliability of the absolute values, however, is lim-

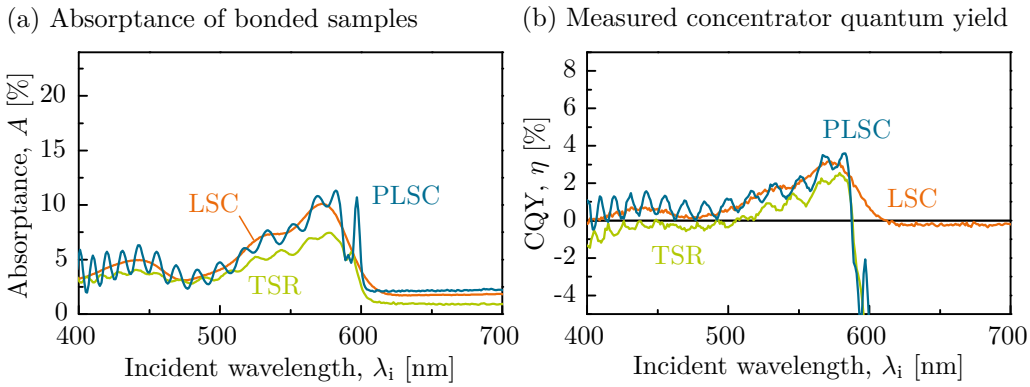

Figure 6.11: For all bonded samples, significant amounts of incident light were absorbed and guided to the edge faces: (a) the absorptances of PLSC and LSC are comparable while the TSR's curve lies slightly below. The concentrator quantum yield in (b) follows the absorptance curves of the samples, indicating similar collection probabilities of PLSC, TSR, and conventional LSC. The reliability of the absolute values, however, is limited due to the measurement uncertainties of the optical characterization method.

ited due to the uncertainties of the measurement method. Samples containing much more dye would help to quantitatively study absorptance, CQY and thus the possible enhancement in collection probability. The dye concentration, however, should not be increased to avoid self-quenching of the luminescence (see Sec. 4.1.1). Increasing the thickness of the dye-doped bonding layer, on the other hand, decreases the LDOS effect on emission as show in the simulations in my publication in Ref. 171. Therefore, the bonding approach is not suitable to fabricate PLSCs with large absorptance.

6.2.2 Opal structures

The absorptance of incident light as well as the concentrator quantum yield were obtained for the opal PLSCs fabricated using dip coating, spin coating, and evaporation (see Sec. 4.2). Due to the large diffuse reflectance and transmittance of the opals, the absorptance was calculated from $A(\lambda_\mathrm{i}) = 1 - C(\lambda_\mathrm{i})$ (instead of the specular parts of reflectance and transmittance).

The obtained absorptance and CQY are shown in Fig. 6.12 (a), (b), and (c) for a dip coated sample, a spin coated sample, and a sample from evaporation, respectively. All samples absorb a significant amount of the incident light. The opal from the evaporation process absorbs more than 60%, which is considerably more than the dip and spin coated samples, corresponding to the opaqueness of the samples from visual inspection. This difference can be attributed to the different thicknesses of the films, as discussed in Sec. 4.2. While the spectral shape of

the absorptance of dip and spin coated samples is similar to the Rhodamine B extinction spectrum, the large amount of dye in the relatively thick sample from evaporation leads to saturation of the absorptance from 500–600 nm.

All samples feature a broad band elevated CQY, even apart from the spectral range of absorption. This offset is likely to be caused by scattering of incident light to the sample's edge faces. This effect was also observed in measurements of undoped opals (not shown here). Furthermore, artifacts of the optical measurement method also contribute to the CQY curve, for example in form of the dip at $\lambda_i = 590$ nm: as discussed above for the multilayer samples, the CQY signal drops at these wavelengths of high specular reflectance (cf. Fig. 4.11 (b)) due to

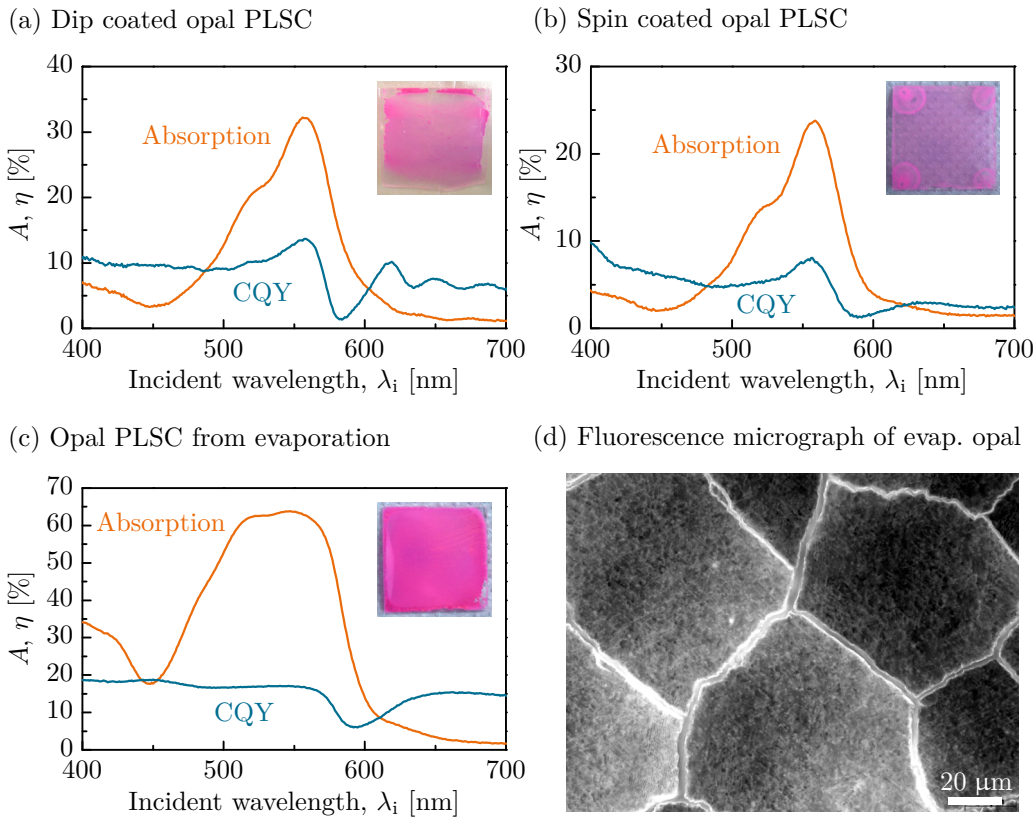

Figure 6.12: The opal PLSCs from dip coating, spin coating and evaporation were optically characterized to obtain the absorptance and CQY, as shown in (a)–(c). Although the samples absorb large fractions of the incident light, only little light guiding was found to originate from fluorescence. This poor performance was attributed to the unwanted outcoupling of guided light at the films' drying cracks, where strongly increased fluorescence signals were found, as shown in (d) for the opal from evaporation.

unintentional out-coupling of reflected light in the center-mount measurement. Additionally, the measurement spots on a sample varied slightly between the different measurement configurations due to manual mounting. As the films are not perfectly homogeneous, additional measurement errors might be introduced by adding and subtracting the optical properties of not exactly the same spots.

A contribution to the CQY due to absorption of incident light and subsequent emission and light guiding, however, should follow the spectral shape of the absorptance. For the dip coated and the spin coated samples a characteristic peak is observed that indicates a certain amount of light guiding through fluorescence. The absolute values of the CQY and the resulting collection probability (i.e. η/A), however, are rather small and cannot compete with conventional LSCs, although large absorptances were achieved.

This poor performance cannot be explained only with the a slightly reduced PLQY and LGE in theory, as calculated in Sec. 5.1.2 and 5.1.3. The drying cracks of the opal film discussed in Sec. 4.2 were therefore investigated using fluorescence microscopy.[3] For all opal samples, strongly increased fluorescence signals were found at the edges of the cracks, as shown in Fig. 6.12 (d) for the sample from evaporation as an example. This observation indicates that at these cracks light, which was guided within the grains, exits the PLSC and is thus lost.

Although the fabrication processes were optimized to reduce the crack density, they could not be totally avoided. As discussed in the end of Sec. 4.2, even more sophisticated fabrication approaches reported in literature yield these defects. As also the theoretical calculations indicated no improvements over conventional LSCs, the concept of opal PLSCs does not seem to be suitable for the intended application.

[3] For details of the experimental setup see Footnote 2 on p. 126

Chapter 7

Conclusion and outlook

In this work, I have investigated the concept of a photonic luminescent solar concentrator (PLSC), in which the luminescent material is embedded in a photonic crystal. I have studied the influence of the surrounding environment on the emission of light and demonstrated that the dominant loss mechanisms of conventional luminescent solar concentrators (LSC) can be mitigated: the shape of the emission spectrum can be tailored to reduce reabsorption, the light guiding efficiency can be strongly improved through directional redistribution of emission, and enhanced radiative emission rates lead to an increase in photoluminescence quantum yield (PLQY). In particular, the 1D-periodic Bragg stack and the 3D-periodic opal were investigated in detail.

Based on the fundamental physics of photonic crystals and light-matter interaction, I developed theoretical methods to quantitatively model the relevant processes of absorption and emission. It was shown how changes in the local density of photon states (LDOS) induced by the photonic environment modify the spectral distribution of the emitted light, the PLQY, and the excited state lifetime of a certain fluorescent species. Moreover, I demonstrated that it is important to consider certain subsets of all modes: for example only those modes that can escape from an (P)LSC, or those modes that can be detected in a specific measurement setup. By introducing a fractional LDOS (FLDOS) for these subsets, the guided fraction of the emitted light (the light guiding efficiency), and the detected emission in angular resolved photoluminescence measurements can be modeled.

The calculations revealed that both Bragg stack and opal feature only relatively small variations in the LDOS of ca. 10% around their incomplete band gaps due to the weak refractive index contrasts. This in turn results in rather small changes in the PLQY, and in only little spectral redistribution: a small part of the emitted

light is shifted to longer wavelengths, which slightly reduces the probability of reabsorption in PLSCs.

More important, however, is the directional redistribution of the emitted light from lossy modes, which can escape from the concentrator, to modes that are guided within the structure: similar to total internal reflection in classic optics, these modes are guided due to the fundamental behavior of light at interfaces. In this understanding, light guiding is independent of the path length to the edges and thus of the concentrator size.

For the opal, the calculations revealed that light guiding is less efficient than in conventional LSCs because of the smaller effective refractive index and because of out-coupling of light at the structured surface due to diffraction (cf. Sec. 5.1.3). Moreover, the fabrication of defect-free opals was found to be challenging. For these reasons, advanced investigations were focused on the Bragg stack.

The theoretical results for the Bragg stack are very promising: as its band gap points in the direction of the classical escape cone, emission is effectively suppressed in this direction. Accordingly, a strong improvement in light guiding efficiency was obtained when the emission spectrum overlaps with the band gap: for the investigated Bragg stack with refractive indices $n_{\mathrm{lo}} = 1.5$, $n_{\mathrm{hi}} = 2$ and the dye Lumogen F Red 305, the escape cone loss was reduced by 60% compared to a conventional LSC.

Using simulations, I have demonstrated that this gain in light guiding efficiency does not come at the cost of worse absorption of incident light. In fact, typical Bragg stacks absorb up to 50% more incident light than conventional LSCs that contain the same amount of dye. The reason for the absorption enhancement is the local concentration of the incident field's energy in the low-refractive-index layers, where the dye is located.

To predict the overall influence of these different effects on the performance of the concentrator, I proposed a device model that also considers reabsorption. Due to the small spectral redistribution of emission, the Bragg stack PLSC suffers from reabsorption only slightly less than a conventional LSC. Because of the strongly enhanced light guiding efficiency, however, the probability for emitted photons to reach the edge faces is increased by more than 50% for application-relevant device dimensions. Combined with the enhancement in absorption, the system efficiency of a typical Bragg stack PLSC was estimated to be 2.1-times larger than that of a comparable LSC.

To compare the calculations with experiments, novel fabrication methods were developed to realize photonic crystals with an embedded fluorescent dye. By optimizing a spin coating process of alternating titania and partly dye-doped PMMA layers, Bragg stacks with up to 29 layers and a peak reflectance of 98.9% were obtained. As as alternative approach, high-quality thin film filters from ion beam sputtering were bonded using a dye-doped intermediate layer. To obtain opals of PMMA colloids that contain luminescent material, different self-assembly pro-

cesses were evaluated, aiming at a reduction of detrimental cracks that originate from the drying of the solvent. At these cracks, parasitic out-coupling of guided light was found, resulting in a poor performance of opal PLSCs.

Consequently, the detailed characterization was focused on the promising Bragg stack. To examine the emission characteristics of the embedded dye, a measurement setup was developed to resolve the photoluminescence as a function of the propagation direction. These angular resolved photoluminescence measurements are sensitive to the spectral and directional redistribution induced by the photonic crystal.

The measured emission escaping from the surface of the Bragg stack was found to be in very good agreement with the calculations: in most directions of the escape cone, emission was strongly reduced and redistributed in other directions. The characterization of the light escaping from the edge faces confirmed that this observation indeed results from suppression of emission in certain directions, and is not caused by the filter behavior of the Bragg stack. This important finding was further verified using reference samples, where the emission of the dye remains undisturbed while Bragg stacks at the surfaces filter part of the out-coupled light.

It was shown that the Bragg stack's LDOS is not fully established in the outer PMMA layers due to boundary effects. This should be considered in the design of PLSCs by embedding dye only in the inner layers. Furthermore, for the light that was guided to the edge faces of the PLSC, difference between the calculations and measurements were found at the short-wavelength part of the spectrum. These deviations might be caused by under-estimated reabsorption losses in the Bragg stack. This propagation-related aspect should be studied in detail in future work. However, the very good overall agreement of the calculated and measured angular emission for the Bragg stack as well as for the reference structures provides clear evidence of the photonic effects on fluorescent emission and confirms the theoretical framework and the modeling methods developed in this work.

Using optical characterization, the absorption of incident light and the guiding of the subsequently emitted light to the edge faces were demonstrated for the first time in a PLSC, stating a proof-of-principle. The measured ratio of absorbed light and guided emission, however, was found to be similar to that of a conventional LSC. A reliable and exact determination of this collection probability and the concentrator quantum yield in the experiments was however difficult due to the relatively weak absorption of the samples and systematic uncertainties of the used measurement setup.

To quantitatively investigate the theoretically predicted enhancement in concentrator performance and the effect of reabsorption, future work should focus on the fabrication of samples with larger absorptance. As the dye concentration was shown to be limited by self-quenching, more dye content can only be achieved through multiple dye-doped layers, which in principle can be realized using the proposed spin coating approach. However, hundreds of layers are necessary to ab-

sorb most of the incident sunlight. The deposition of such a large number of layers with precise and reliable control of the layer properties might require further optimization of the fabrication process. Additionally, for the intended use of PLSCs for solar harvesting, the fabrication needs to be very cost-effective to be able to compete with solar cells that are getting cheaper continuously. The fabrication under these boundary conditions remains a challenging task for future work.

Apart from LSCs, the findings of this work can also be applied to many other applications, in which one wants to influence the emission of light: triggered by this work, our group at Fraunhofer ISE studied how the "upconversion" of sub-bandgap photons can be improved through photonic effects to enhance the efficiency of solar cells using Bragg-stack-like structures [124]. Furthermore, the unwanted radiative recombination of charge carriers in solar cells can be partly suppressed with the concept of a photonic solar cell, as also studied at Fraunhofer ISE [189, 190]. Beyond photovoltaics, this work can have an impact on applications such as distributed feedback lasers [81–87] and (organic) light emitting diodes [88–92], which face the reverse problem of LSCs: how to couple out most of the emitted light? More generally, the presented comprehensive theoretical treatment of controlling the emission of light through photonic structures provides significant physical understanding and insight in the field of light-matter interaction.

Appendix

A.1 Derivation of the wave equation

Maxwell's equations for a non-magnetic ($\mu_r = 0$), charge and current-free dielectric with no material dispersion ($\varepsilon \neq \varepsilon(\omega)$) read

$$\boldsymbol{\nabla} \cdot (\varepsilon(\boldsymbol{r})\boldsymbol{E}(\boldsymbol{r},t)) = 0, \tag{A.1}$$

$$\boldsymbol{\nabla} \cdot \boldsymbol{H}(\boldsymbol{r},t) = 0, \tag{A.2}$$

$$\boldsymbol{\nabla} \times \boldsymbol{E}(\boldsymbol{r},t) = -\mu_0 \frac{\partial}{\partial t}\boldsymbol{H}(\boldsymbol{r},t), \tag{A.3}$$

$$\boldsymbol{\nabla} \times \boldsymbol{H}(\boldsymbol{r},t) = \varepsilon_0 \varepsilon(\boldsymbol{r}) \frac{\partial}{\partial t}\boldsymbol{E}(\boldsymbol{r},t). \tag{A.4}$$

With the ansatz of a harmonic time dependence of the fields

$$\boldsymbol{E}(\boldsymbol{r},t) = \boldsymbol{E}(\boldsymbol{r})\,\mathrm{e}^{-i\omega t} \tag{A.5}$$

$$\boldsymbol{H}(\boldsymbol{r},t) = \boldsymbol{H}(\boldsymbol{r})\,\mathrm{e}^{-i\omega t} \tag{A.6}$$

with frequency ω, Eqn. (A.1) and (A.2) yield

$$\boldsymbol{\nabla} \cdot (\varepsilon(\boldsymbol{r})\boldsymbol{E}(\boldsymbol{r})) = 0, \tag{A.7}$$

$$\boldsymbol{\nabla} \cdot \boldsymbol{H}(\boldsymbol{r}) = 0, \tag{A.8}$$

which means that there are no point sources or sinks of the magnetic and displacement field [66].

Inserting the ansatz for the fields into Eq. (A.3), we obtain

$$\begin{aligned} \mathrm{e}^{-i\omega t}\,\boldsymbol{\nabla} \times \boldsymbol{E}(\boldsymbol{r}) &= -\mu_0 \boldsymbol{H}(\boldsymbol{r})\,\mathrm{e}^{-i\omega t}(-i\omega) \\ \Leftrightarrow \boldsymbol{\nabla} \times \boldsymbol{E}(\boldsymbol{r}) &= i\omega\mu_0 \boldsymbol{H}(\boldsymbol{r}). \end{aligned} \tag{A.9}$$

Inserting the ansatz into Eq. (A.4), dividing by $\varepsilon(\boldsymbol{r})$, and taking the curl yields

$$\begin{aligned} \boldsymbol{\nabla} \times \boldsymbol{H}(\boldsymbol{r}) &= -i\omega\varepsilon_0\varepsilon(\boldsymbol{r})\boldsymbol{E}(\boldsymbol{r}) \\ \Leftrightarrow \boldsymbol{\nabla} \times (\frac{1}{\varepsilon(\boldsymbol{r})}\boldsymbol{\nabla} \times \boldsymbol{H}(\boldsymbol{r})) &= -i\omega\varepsilon_0\boldsymbol{\nabla} \times \boldsymbol{E}(\boldsymbol{r}). \end{aligned} \tag{A.10}$$

Replacing $\boldsymbol{\nabla} \times \boldsymbol{E}(\boldsymbol{r})$ on the right hand side of this equation with Eq. (A.9), we arrive at the wave equation of the $\boldsymbol{H}$-field, the so-called master equation:

$$\begin{aligned} \boldsymbol{\nabla} \times \left(\frac{1}{\varepsilon(\boldsymbol{r})}\boldsymbol{\nabla} \times \boldsymbol{H}(r)\right) &= \omega^2\varepsilon_0\mu_0\boldsymbol{H}(\boldsymbol{r}) \\ \Leftrightarrow \boldsymbol{\nabla} \times \left(\frac{1}{\varepsilon(\boldsymbol{r})}\boldsymbol{\nabla} \times \boldsymbol{H}(\boldsymbol{r})\right) &= \left(\frac{\omega}{c}\right)^2 \boldsymbol{H}(\boldsymbol{r}) \end{aligned} \tag{A.11}$$

where we used $1/c = \sqrt{\varepsilon_0\mu_0}$.

This wave equation can be read as an eigenvalue problem

$$\hat{\Theta}\boldsymbol{H}(\boldsymbol{r}) = \left(\frac{\omega}{c}\right)^2 \boldsymbol{H}(\boldsymbol{r}) \tag{A.12}$$

with eigenvectors $\boldsymbol{H}(\boldsymbol{r})$ and corresponding eigenvalues $(\omega/c)^2$. The operator

$$\hat{\Theta}\square = \boldsymbol{\nabla} \times \left(\frac{1}{\varepsilon(\boldsymbol{r})}\boldsymbol{\nabla} \times \square\right) \tag{A.13}$$

is linear and Hermitian [66], like the Hamiltonian operator from quantum mechanics. As a consequence, several analogies exist between "real" crystals in solid state physics and photonic crystals.

A.2 Definitions of polarization at interfaces and in photonic crystals

In classic optics, the polarization of light is defined with respect to a certain interface. For a plane wave incident on the interface, two cases are distinguished: when the electric field vector $\boldsymbol{E}$ is aligned parallel to the interface, the wave is called TE polarized (transverse electric), which is also denoted as s polarization (from the german word *senkrecht* - perpendicular). In contrast, the TM (transverse magnetic) polarization is characterized by an interface-parallel magnetic field vector $\boldsymbol{H}$, also known as the p polarization (from *parallel*) [191].

In the field of photonic crystals, the polarization of light is defined differently: the modes are separated based on mathematical symmetry considerations. Given a 1D or 2D photonic crystal, the structure is uniform along one axis that is perpendicular to the plane of periodicity; let this axis be the z-axis. Accordingly,

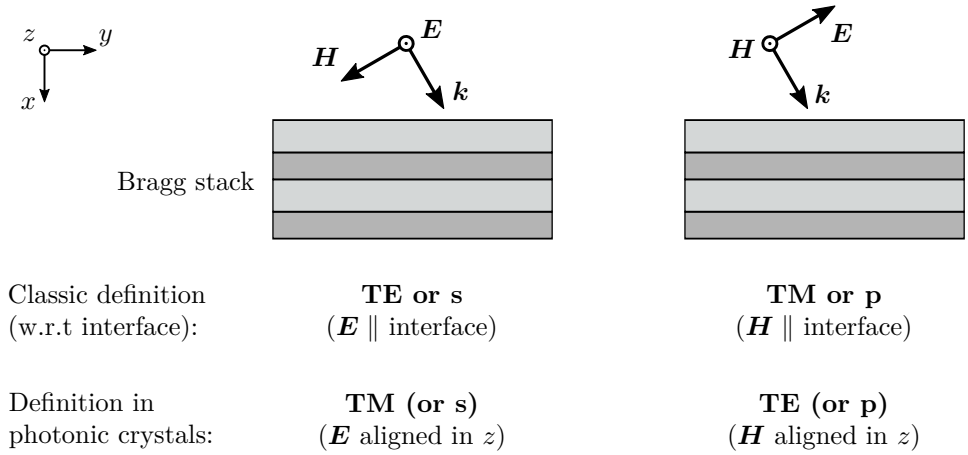

Figure A.1: There are different definitions of the polarization of light: classically, depending on the orientation of the electric and magnetic fields $\boldsymbol{E}$ and $\boldsymbol{H}$ with respect to a certain interface, waves are classified as transverse electric (TE) or transverse magnetic (TM). In photonic crystal literature, these polarization are defined based on symmetry considerations. In case of the Bragg stack as an example, the two definitions are contradictory. The alternative notation of s and p polarization, however, is consistent and is thus used in this work.

there are "odd" modes whose $\boldsymbol{E}$ field is aligned in z-direction, while the corresponding $\boldsymbol{H}$-field can have components in x and y. These modes are denoted as TE polarized. On the other hand, so-called "even" modes feature an $\boldsymbol{H}$-field only in z-direction and an $\boldsymbol{E}$-field in the x, y-plane, defining the TM polarization [66].

Lets compare the two definitions of polarization for the Bragg stack as an example (1D photonic crystal). Considering the interfaces of the alternating layers, modes can be separated in TE and TM modes according the classical definition as illustrated in Fig. A.1. When applying the second definition from photonic crystals literature, however, the same waves are assigned the opposite term TE and TM. This reveals that the two different definitions of polarization - (a) at interfaces and (b) in photonic crystals - are contradictory, which has to be kept in mind.

In photonic crystals literature also the terminology of s and p polarization is used. In contrast to the classic optics, s is assigned to TM-polarized light, and p denotes the TE polarization [66]. As a result, the notation of s and p polarization is consistent in classic optics and in photonic crystals. Consequently, this s and p terminology was used in this work to avoid misconceptions.

A.3 Fresnel equations

At the interface of two media, the reflected and transmitted fractions of light are determined by the boundary conditions of the electromagnetic fields at the interface. For the interface between two homogeneous materials, the tangential field components are continuous [107]. Accordingly, the reflected and transmitted electric field amplitudes E_r, E_t can be derived in form of the coefficients r_s, r_p depending on the polarization (s or p), known as the Fresnel equations [191]:

$$r_\mathrm{s} = \frac{E_\mathrm{r}}{E_\mathrm{i}} = \frac{n_\mathrm{i}\cos\phi_\mathrm{i} - n_\mathrm{t}\cos\phi_\mathrm{t}}{n_\mathrm{i}\cos\phi_\mathrm{i} + n_\mathrm{t}\cos\phi_\mathrm{t}}, \tag{A.14}$$

$$t_\mathrm{s} = \frac{E_\mathrm{t}}{E_\mathrm{i}} = \frac{2\,n_\mathrm{i}\cos\phi_\mathrm{i}}{n_\mathrm{i}\cos\phi_\mathrm{i} + n_\mathrm{t}\cos\phi_\mathrm{t}} \tag{A.15}$$

for s-polarized light and

$$r_\mathrm{p} = \frac{E_\mathrm{r}}{E_\mathrm{i}} = \frac{n_\mathrm{t}\cos\phi_\mathrm{i} - n_\mathrm{i}\cos\phi_\mathrm{t}}{n_\mathrm{t}\cos\phi_\mathrm{i} + n_\mathrm{i}\cos\phi_\mathrm{t}}, \tag{A.16}$$

$$t_\mathrm{p} = \frac{E_\mathrm{t}}{E_\mathrm{i}} = \frac{2\,n_\mathrm{i}\cos\phi_\mathrm{i}}{n_\mathrm{t}\cos\phi_\mathrm{i} + n_\mathrm{i}\cos\phi_\mathrm{t}} \tag{A.17}$$

for p-polarized light. Here, E_i denotes the incident amplitude and the refractive indices n and propagation angles ϕ correspond to the sketch in Fig. 2.1 (a).

Based on these equations, the fractions of reflected and transmitted power, the reflectance R and the transmittance T, are given by

$$R = r^2, \tag{A.18}$$

$$T = \frac{n_\mathrm{t}\cos\phi_\mathrm{t}}{n_\mathrm{i}\cos\phi_\mathrm{i}} t^2 \tag{A.19}$$

for both polarizations.

Note that $R + T = 1$ (conservation of energy), while $r + t \neq 1$.

A.4 Effect of the LDOS on the line shape of individual transitions

In Sec. 3.2.1, the effect of the LDOS on the emission spectrum is modeled as a modulation of the spectral shape function $g^0(\omega)$ with the LDOS ratio $\gamma(\boldsymbol{r}, \omega)$ (see Eq. (3.29)). The spectral shape function is basically the sum of numerous possible transitions to the different vibrational (and rotational) levels of the ground state. Depending on their frequency, some of these transitions may be enhanced by the LDOS, others may be suppressed.

In more detail, each individual transition has its own line shape function $g_l(\omega)$. For a discrete two-level system, the line shape function is proportional to [192]

$$\frac{\Gamma_{21}/2}{(\omega - \omega_{21} - \Delta_{21})^2 + (\Gamma_{21}/2)^2}, \tag{A.20}$$

where Γ_{21} and ω_{21} are the rate and frequency of the transition from excited state 2 to ground state 1, respectively. Δ_{21} describes the Lamb shift due to interaction of the electron with the vacuum fluctuations.

Due to the finite lifetime of a transition, its linewidth is broadened as a result of Heisenberg's time-energy uncertainty principle. This effect is called *natural* or *lifetime broadening*. Being defined as the full width at half maximum (FWHM) of the line shape function, the linewidth $\Delta\omega$ is given by Γ_{21} for this Lorentzian function. As the photonic crystal changes the transition rate Γ_{21}, the linewidth $\Delta\omega$ is changed proportionally.

For the fluorescent dyes that were studied in this work, typical lifetimes are in the range of several ns. Assuming $\tau = 1$ ns and a quantum yield of $\Phi = 1$, the linewidth due to the natural broadening is $\Delta\lambda = 0.0002$ nm for emission at $\lambda_0 = 600$ nm. This is very small compared to the width of typical dye emission spectra, which are in the range of 100 nm. Even for large suppression or enhancement of a transition due to variations of the LDOS, the linewidth of the individual transitions is still negligible compared to the emission spectrum width. Thus, this effect can be neglected when calculating the influence of the photonic crystal on fluorescent emission (spectral redistribution etc.).

Another influence on individual transition could arise from the Lamb shift Δ_{21}, which shifts the line shape function on the frequency axis. The classic Lamb shift for the splitting of the $2S_{1/2} - 2P_{1/2}$ energy levels of the hydrogen atom is about 1.06 GHz [193]. As the LDOS modifies the vacuum fluctuations, the Lamb shift is also affected [194, 195]. The calculation of this effect in fluorescent molecules is out out the scope of this work. However, compared to the width of the emission spectrum, the change in Lamb shift Δ_{21} is expected to be negligible (1 GHz corresponds to $\Delta\lambda = 0.0012$ nm at $\lambda_0 = 600$ nm).

A.5 Propagation of probability distributions

In this section, I derive the probability distribution of one quantity, which is a function of a second variable for which the probability distribution is known. While the result can be applied to arbitrary variables in different contexts, I present the derivation for the incident and transmitted angles at an optical interface from a higher to a lower refractive index as an example that I used in the calculations in Sec. 3.3.3.

Thus, the probability distribution function $f_{\phi_t}(\phi_t)$ of the transmitted angle ϕ_t is what we are looking for. The distribution of the angles ϕ_i incident on the optical

interface is uniform when the light results from (2D) isotropic emission in this higher refractive index medium. Therefore,

$$f_{\phi_\mathrm{i}}(\phi_\mathrm{i}) = s, \tag{A.21}$$

where s is constant.

The incident angles ϕ_i are translated into the transmitted angles ϕ_t with the function h, which in this case is given by Snell's law:

$$\phi_\mathrm{t} = h(\phi_\mathrm{i}) = \sin^{-1}\left(\frac{n_\mathrm{i}}{n_\mathrm{t}}\sin(\phi_\mathrm{i})\right), \tag{A.22}$$

where n_i and n_t are the refractive indices of medium of incidence and transmission, respectively (w.l.o.g. $n_\mathrm{i} > n_\mathrm{t}$).

Given that the function h is bijective, the probability p that ϕ_t lies between ϕ_1 and ϕ_2 is equal to the probability that ϕ_i lies between $h^{-1}(\phi_1)$ and $h^{-1}(\phi_2)$. Therefore,

$$p\left\{\phi_\mathrm{t} \in [\phi_1, \phi_2]\right\} = p\left\{\phi_\mathrm{i} \in \left[h^{-1}(\phi_1), h^{-1}(\phi_2)\right]\right\} = \int_{h^{-1}(\phi_1)}^{h^{-1}(\phi_2)} f_{\phi_\mathrm{i}}(\phi_\mathrm{i})\, d\phi_\mathrm{i}. \tag{A.23}$$

Using integration by substitution one obtains

$$\int_{h^{-1}(\phi_1)}^{h^{-1}(\phi_2)} f_{\phi_\mathrm{i}}(\phi_\mathrm{i})\, d\phi_\mathrm{i} = \int_{\phi_1}^{\phi_2} f_{\phi_\mathrm{i}}(h^{-1}(\phi_\mathrm{t})) \times \left(h^{-1}\right)'(\phi_\mathrm{t})\, d\phi_\mathrm{t}, \tag{A.24}$$

with $\left(h^{-1}\right)'$ being the derivative of the inverse function of h with respect to ϕ_t. Combining Eqs. (A.23) and (A.24), we find

$$p\left\{\phi_\mathrm{t} \in [\phi_1, \phi_2]\right\} = \int_{\phi_1}^{\phi_2} \underbrace{f_{\phi_\mathrm{i}}(h^{-1}(\phi_\mathrm{t})) \times \left(h^{-1}\right)'(\phi_\mathrm{t})}_{f_{\phi_\mathrm{t}}(\phi_\mathrm{t})}\, d\phi_\mathrm{t}, \tag{A.25}$$

where the probability density function of the transmitted light $f_{\phi_\mathrm{t}}(\phi_\mathrm{t})$ can be identified:

$$f_{\phi_\mathrm{t}}(\phi_\mathrm{t}) = f_{\phi_\mathrm{i}}(h^{-1}(\phi_\mathrm{t})) \times \left(h^{-1}\right)'(\phi_\mathrm{t}). \tag{A.26}$$

With $f_{\phi_\mathrm{i}}(\phi_\mathrm{i})$ from isotropic emission (Eq. (A.21)) and inserting Snell's law as h (Eq. (A.22)), we find

$$f_{\phi_\mathrm{t}}(\phi_\mathrm{t}) = s\frac{n_\mathrm{t}}{n_\mathrm{i}}\frac{\cos(\phi_\mathrm{t})}{\sqrt{1 - \left(\frac{n_\mathrm{t}}{n_\mathrm{i}}\right)^2 \sin(\phi_\mathrm{t})}}. \tag{A.27}$$

If needed, $f_{\phi_\mathrm{t}}(\phi_\mathrm{t})$ can be normalized by choosing an appropriate value of s. To obtain $\int_{0^\circ}^{90^\circ} f_{\phi_\mathrm{t}}(\phi_\mathrm{t})\, d\phi_\mathrm{t} = 1$, it should be set to $s = 1/\sin^{-1}(n_\mathrm{t}/n_\mathrm{i})$.

A.6 Multilayer structure with single dye-doped layer

In Sec. 5.2.1, the angular resolved photoluminescence (PL) escaping from the concentrators' surfaces was discussed. In experiments, the samples were characterized from both the front and the back surface, which resulted in different measurement results for the investigated Bragg stack PLSC. This observation was mainly attributed to the structural asymmetry of this PLSC, where the inner 10 of the 14 PMMA layers were doped with the fluorescent dye. Accordingly, the LDOS in the outer dye-doped layers is expected to be significantly influenced by the surrounding, i.e. by the air at the front and by the glass substrate at the back, respectively. As a result, the emission towards the front and back surfaces can differ.

For a detailed experimental investigation of the deviations of the front and back side measurements, additional samples were fabricated and characterized. To examine the hypothesis that the dye in the outer dye-doped layers experiences an LDOS distorted by the surrounding, only one PMMA layer in the center of the stack was doped with the dye. This center layer has the largest distance to the surrounding and is thus expected to be influenced only little. For comparison also samples with 10 dye-doped layers (as before) were fabricated.

Unfortunately, the wavelength of peak reflectance of these additional samples was slightly detuned by 20 nm from the optimum $\lambda_{\text{design}} = 645$ nm, thus not perfectly matching with the dye spectrum. Although the light guiding efficiency of these sample is therefore less than with optimum layer thicknesses, the emission of the embedded dye is nevertheless strongly influenced by these structures, which allows investigating the asymmetric LDOS distribution mentioned above.

Fig. A.2 shows the measured angular surface PL of (a) the sample with 10 dye-doped layers and (b) the sample with only one dye-doped layer in the center. As for the sample from Sec. 5.2.1, the front and back side measurements of the sample with 10 dye-doped layers show large differences, especially at small angles ϕ_{d} near $\lambda = 600$ nm. The front and back side measurements of the sample with only a single dye-doped layer, however, agree much better. This result indicates that emission from the outer layers is less symmetric due to boundary effects, while emission in the center layer is mainly determined by the LDOS of the ideal Bragg stack with infinite layers.

Moreover, the spectra of this sample exhibits finer features than the relatively smooth spectra of the sample with 10 dye layers. This supports the hypothesis that the LDOS in the outer layers is different from the LDOS in the centered layer: an unequal LDOS in the different layers results in different emission spectra in each layer. Accordingly, the measured emission of the sample with 10 dye-doped layers is the sum of the contributions in the individual layers, resulting in a smoothed spectrum. This result supports the hypothesis that especially the LDOS in the outer dye layers is influenced by the surrounding air or glass, leading to an asymmetric distribution of photonic states.

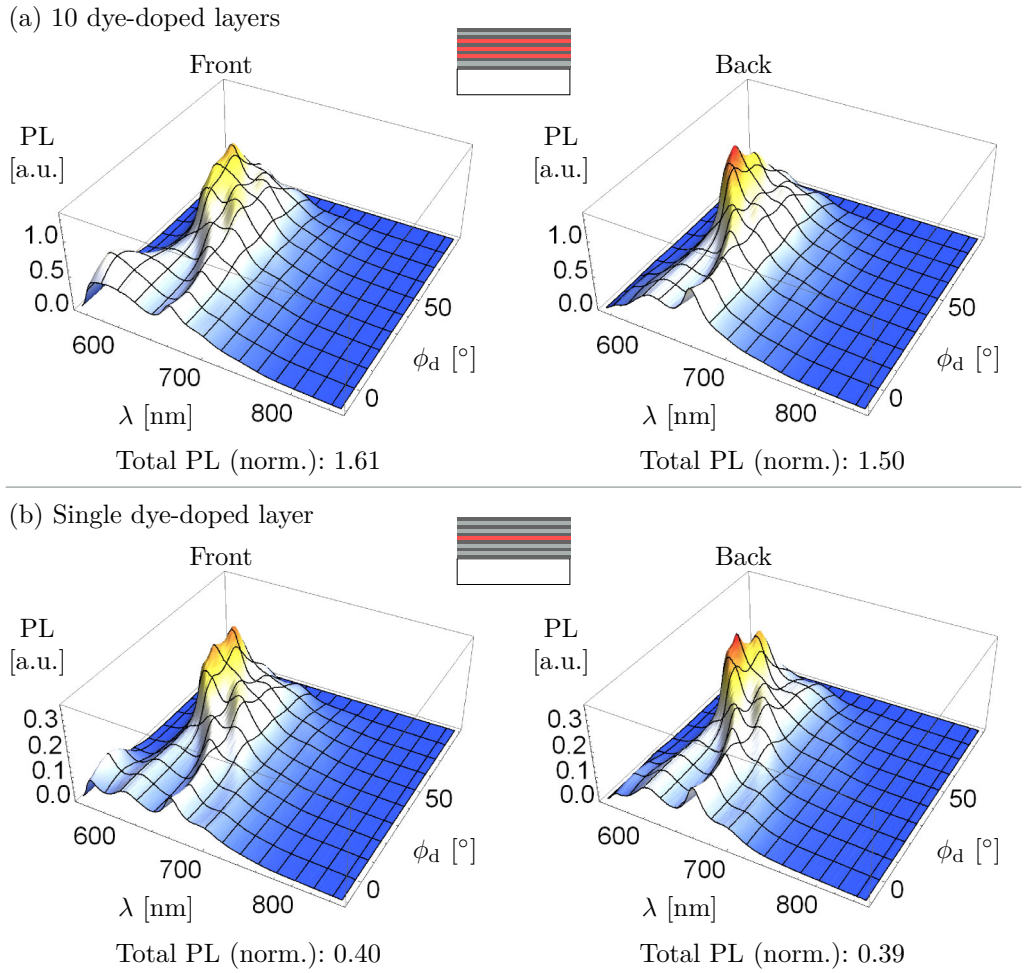

Figure A.2: The angular resolved photoluminescence escaping from the front and back surface was studied for (a) a sample with 10 dye-doped layers and (b) a sample with only one dye-doped layer in the center of the stack. While the front and back side measurements of the sample with 10 dye layers differ significantly, the results of the sample with one dye layer are quite similar and exhibit finer spectral features. These observations support the hypothesis that the surrounding (air or glass) influences emission especially in the outer layers of the stack and cause an asymmetric distribution of photonic states.

The normalized total amount of escaped light of the sample with 10 dye layers is around 50-60% higher that for a conventional LSC, which is similar to the result for the 10-dye-layer PLSC from Sec. 5.2.1. For the sample with only one dye-doped layer, however, the escape cone loss is reduced by around 60% compared to conventional LSCs. This result is in good agreement with a theoretical reduction

of 55% from calculations that accounts for the non-optimum layer thicknesses. The differences of these two samples strongly indicate that the deviations of the theory of an ideal Bragg stack and the measurements of samples with 10 dye-doped layers arise from the finite structure of the samples. In turn, the characteristic Bragg stack LDOS is not fully established in the structure, especially in the outer layers, as seen above.

References

[1] Intergovernmental Panel on Climate Change (IPCC), *Fourth Assessment Report: Climate Change 2007: The AR4 Synthesis Report.* Geneva: IPCC, 2007.

[2] J. Tsao, N. Lewis, and G. Crabtree, "Solar FAQs," 2006. Available online at http://www.sandia.gov/~jytsao/Solar%20FAQs.pdf (February 08, 2014).

[3] German Advisory Council on Global Change (WBGU), *World in Transition - A Social Contract for Sustainability.* Berlin: WBGU, 2011.

[4] M. G. Debije and P. P. C. Verbunt, "Thirty Years of Luminescent Solar Concentrator Research: Solar Energy for the Built Environment," *Advanced Energy Materials*, vol. 2, no. 1, pp. 12–35, 2012.

[5] J. Yoon, L. Li, A. V. Semichaevsky, J. H. Ryu, H. T. Johnson, R. G. Nuzzo, and J. A. Rogers, "Flexible concentrator photovoltaics based on microscale silicon solar cells embedded in luminescent waveguides," *Nature Communications*, vol. 2, p. 343, 2011.

[6] M. Buffa, S. Carturan, M. Debije, A. Quaranta, and G. Maggioni, "Dye-doped polysiloxane rubbers for luminescent solar concentrator systems," *Solar Energy Materials and Solar Cells*, vol. 103, pp. 114–118, 2012.

[7] A. Zastrow, *Physikalische Analyse der Energieverlustmechanismen im Fluoreszenzkollektor.* PhD thesis, University of Freiburg, 1981.

[8] G. Baur and W. Greubel, "Fluorescence-activated liquid-crystal display," *Applied Physics Letters*, vol. 31, no. 1, pp. 4–6, 1977.

[9] W. H. Weber and J. Lambe, "Luminescent greenhouse collector for solar radiation," *Applied Optics*, vol. 15, no. 10, pp. 2299–2300, 1976.

[10] A. Goetzberger and W. Greubel, "Solar energy conversion with fluorescent collectors," *Applied Physics A: Materials Science & Processing*, vol. 14, pp. 123–139, 1977.

[11] W. A. Shurcliff and R. C. Jones, "The Trapping of Fluorescent Light Produced within Objects of High Geometrical Symmetry," *Journal of the Optical Society of America*, vol. 39, no. 11, pp. 912–916, 1949.

[12] J. B. Birks, *The theory and practice of scintillation counting.* London: Pergamon, 1964.

[13] J. S. Batchelder, A. H. Zewail, and T. Cole, "Luminescent solar concentrators. 1: Theory of operation and techniques for performance evaluation," *Applied Optics*, vol. 18, no. 18, pp. 3090–3110, 1979.

[14] E. Yablonovitch, "Thermodynamics of the fluorescent planar concentrator," *Journal of the Optical Society of America*, vol. 70, no. 11, pp. 1362–1363, 1980.

[15] V. Wittwer, W. Stahl, and A. Goetzberger, "Fluorescent planar concentrators," *Solar Energy Materials*, vol. 11, no. 3, pp. 187–197, 1984.

[16] U. Rau, F. Einsele, and G. C. Glaeser, "Efficiency limits of photovoltaic fluorescent collectors," *Applied Physics Letters*, vol. 87, no. 17, p. 171101, 2005.

[17] A. Chatten, D. Farrell, A. Büchtemann, and K. Barnham, "Thermodynamic modelling of luminescent solar concentrators," in *Proceedings of the 21st European Photovoltaic Solar Energy Conference*, pp. 315–20, 2006.

[18] J. C. Goldschmidt, *Novel Solar Cell Concepts.* PhD thesis, University of Konstanz, 2009.

[19] K. Sakuta, S. Sawata, and M. Tanimoto, "Luminescent concentrator module of a practical size," in *Proceedings of the 1st World Conference on Photovoltaic Energy Conversion, 24th IEEE Photovoltaic Specialists Conference*, vol. 1, pp. 1115–1118, 1994.

[20] A. Goetzberger and O. Schirmer, "Second stage concentration with tapers for fluorescent solar collectors," *Applied physics*, vol. 19, no. 1, pp. 53–58, 1979.

[21] B. D. Markman, R. R. Ranade, and N. C. Giebink, "Nonimaging optics in luminescent solar concentration," *Optics Express*, vol. 20, no. S5, pp. A622–A629, 2012.

[22] W. Viehmann and R. L. Frost, "Thin film waveshifter coatings for fluorescent radiation converters," *Nuclear Instruments and Methods*, vol. 167, pp. 405–15, 1979.

[23] V. Wittwer, K. Heidler, A. Zastrow, and A. Goetzberger, "Theory of fluorescent planar concentrators and experimental results," *Journal of Luminescence*, vol. 24-25, Part 2, pp. 873–876, 1981.

[24] G. Seybold and G. Wagenblast, "New perylene and violanthrone dyestuffs for fluorescent collectors," *Dyes and Pigments*, vol. 11, no. 4, pp. 303–317, 1989.

[25] T. Förster, "Zwischenmolekulare Energiewanderung und Fluoreszenz," *Annalen der Physik*, vol. 437, pp. 55–75, 1948.

[26] D. L. Dexter, "A Theory of Sensitized Luminescence in Solids," *The Journal of Chemical Physics*, vol. 21, no. 5, pp. 836–850, 1953.

[27] S. T. Bailey, G. E. Lokey, M. S. Hanes, J. D. Shearer, J. B. McLafferty, G. T. Beaumont, T. T. Baseler, J. M. Layhue, D. R. Broussard, Y.-Z. Zhang, and B. P. Wittmershaus, "Optimized excitation energy transfer in a three-dye luminescent solar concentrator," *Solar Energy Materials and Solar Cells*, vol. 91, no. 1, pp. 67–75, 2007.

[28] M. J. Currie, J. K. Mapel, T. D. Heidel, S. Goffri, and M. A. Baldo, "High-Efficiency Organic Solar Concentrators for Photovoltaics," *Science*, vol. 321, no. 5886, pp. 226–228, 2008.

[29] R. Bose, M. Gonzalez, P. Jenkins, R. Walters, J. Morseman, M. Moss, C. McLain, P. Linsert, A. Büchtemann, A. Chatten, and K. Barnham, "Resonance energy transfer in luminescent solar concentrators," in *Proceedings of the 35th IEEE Photovoltaic Specialists Conference*, pp. 467–470, 2010.

[30] R. Reisfeld and Y. Kalisky, "Improved planar solar converter based on uranyl neodymium and holmium glasses," *Nature*, vol. 283, pp. 281–282, 1980.

[31] R. Reisfeld and Y. Kalisky, "Nd^{3+} and Yb^{3+} germanate and tellurite glasses for fluorescent solar energy collectors," *Chemical Physics Letters*, vol. 80, no. 1, pp. 178–183, 1981.

[32] R. Reisfeld and S. Neumann, "Planar solar energy converter and concentrator based on uranyl-doped glass," *Nature*, vol. 274, pp. 144–145, 1978.

[33] B. Jezowska-Trzebiatowska, E. Lukowiak, W. Strek, A. Buczkowski, S. Patela, J. Radojewski, and J. Sarzynski, "Neodymium-chromium doped phosphate glasses as luminescent solar concentrators," *Solar Energy Materials*, vol. 13, no. 4, pp. 267–277, 1986.

[34] K. Barnham, J. Marques, J. Hassard, and P. O' Brien, "Quantum-dot concentrator and thermodynamic model for the global redshift," *Applied Physics Letters*, vol. 76, no. 9, pp. 1197–1199, 2000.

[35] A. Chatten, K. Barnham, B. Buxton, N. Ekins-Daukes, and M. Malik, "Novel quantum dot concentrators," in *Proceedings of the 17th European Photovoltaic Solar Energy Conference*, pp. 200–3, 2001.

[36] A. Chatten, K. Barnham, B. Buxton, N. Ekins-Daukes, and M. Malik, "The quantum dot concentrator: theory and results," in *Proceedings of the 3rd World Conference on Photovoltaic Energy Conversion*, vol. 3, pp. 2657–2660, 2003.

[37] A. J. Chatten, K. W. J. Barnham, B. F. Buxton, N. J. Ekins-Daukes, and M. A. Malik, "Quantum Dot Solar Concentrators and Modules," in *Proceedings of the 19th European Photovoltaic Solar Energy Conference*, pp. 109–112, 2004.

[38] V. Sholin, J. D. Olson, and S. A. Carter, "Semiconducting polymers and quantum dots in luminescent solar concentrators for solar energy harvesting," *Journal of Applied Physics*, vol. 101, no. 12, p. 123114, 2007.

[39] A. Schüler, M. Python, M. V. del Olmo, and E. de Chambrier, "Quantum dot containing nanocomposite thin films for photoluminescent solar concentrators," *Solar Energy*, vol. 81, no. 9, pp. 1159–1165, 2007.

[40] S. Reda, "Synthesis and optical properties of CdS quantum dots embedded in silica matrix thin films and their applications as luminescent solar concentrators," *Acta Materialia*, vol. 56, pp. 259–64, 2008.

[41] G. V. Shcherbatyuk, R. H. Inman, C. Wang, R. Winston, and S. Ghosh, "Viability of using near infrared PbS quantum dots as active materials in luminescent solar concentrators," *Applied Physics Letters*, vol. 96, no. 19, p. 191901, 2010.

[42] R. Bose, D. Farrell, A. Chatten, M. Pravettoni, A. Buchtemann, J. Quilitz, A. Fiore, L. Manna, and R. Barnham, K. W Jacobsson, "Luminescent solar concentrators: Nanorods and raytrace modeling," in *Proceedings of the 33rd IEEE Photovoltaic Specialists Conference*, pp. 1–5, 2008.

[43] N. D. Bronstein, L. Li, L. Xu, Y. Yao, V. E. Ferry, A. P. Alivisatos, and R. G. Nuzzo, "Luminescent Solar Concentration with Semiconductor Nanorods and Transfer-Printed Micro-Silicon Solar Cells," *ACS Nano*, vol. 8, no. 1, pp. 44–53, 2014.

[44] S. Gallagher, B. Norton, and P. Eames, "Quantum dot solar concentrators: Electrical conversion efficiencies and comparative concentrating factors of fabricated devices," *Solar Energy*, vol. 81, no. 6, pp. 813–821, 2007.

[45] D. K. G. de Boer, D. J. Broer, M. G. Debije, W. Keur, A. Meijerink, C. R. Ronda, and P. P. C. Verbunt, "Progress in phosphors and filters for luminescent solar concentrators," *Optics Express*, vol. 20, no. S3, pp. A395–A405, 2012.

[46] Y. Zhao and R. R. Lunt, "Transparent Luminescent Solar Concentrators for Large-Area Solar Windows Enabled by Massive Stokes-Shift Nanocluster Phosphors," *Advanced Energy Materials*, vol. 3, no. 9, pp. 1143–1148, 2013.

[47] F. Meinardi, A. Colombo, K. A. Velizhanin, R. Simonutti, M. Lorenzon, L. Beverina, R. Viswanatha, V. I. Klimov, and S. Brovelli, "Large-area luminescent solar concentrators based on "Stokes-shift-engineered" nanocrystals in a mass-polymerized PMMA matrix," *Nature Photonics*, vol. 8, no. 5, pp. 392–399, 2014.

[48] C. S. Erickson, L. R. Bradshaw, S. McDowall, J. D. Gilbertson, D. R. Gamelin, and D. L. Patrick, "Zero-Reabsorption Doped-Nanocrystal Luminescent Solar Concentrators," *ACS Nano*, vol. 8, no. 4, pp. 3461–3467, 2014.

[49] J. Goldschmidt, M. Peters, F. Dimroth, A. Bett, L. Steidl, R. Zentel, M. Hermle, S. Glunz, and G. Willeke, "Developing Large and Efficient Fluorescent Concentrator Systems," in *Proceedings of the 24th European Photovoltaic Solar Energy Conference*, pp. 207–212, 2009.

[50] J. C. Goldschmidt, "Fraunhofer ISE achieves new world record efficiency for fluorescent collectors," 2008. Available online at http://www.ise.fraunhofer.de/en/press-and-media/pdfs-zu-presseinfos-englisch/bis-2008/press-release-fraunhofer-ise-achieves-new-world-record-efficiency-for-fluorescent-collectors.pdf (June 18, 2014).

[51] L. H. Slooff, E. E. Bende, A. R. Burgers, T. Budel, M. Pravettoni, R. P. Kenny, E. D. Dunlop, and A. Büchtemann, "A luminescent solar concentrator with 7.1% power conversion efficiency," *physica status solidi (RRL) - Rapid Research Letters*, vol. 2, pp. 257–259, 2008.

[52] L. Desmet, A. J. M. Ras, D. K. G. de Boer, and M. G. Debije, "Monocrystalline silicon photovoltaic luminescent solar concentrator with 4.2% power conversion efficiency," *Optics Letters*, vol. 37, no. 15, pp. 3087–3089, 2012.

[53] G. Smestad, H. Ries, R. Winston, and E. Yablonovitch, "The thermodynamic limits of light concentrators," *Solar Energy Materials*, vol. 21, pp. 99–111, 1990.

[54] B. S. Richards, A. Shalav, and R. Corkish, "A low escape-cone-loss luminescent solar concentrator," in *Proceedings of the 19th European Photovoltaic Solar Energy Conference*, pp. 113–116, 2004.

[55] J. C. Goldschmidt, M. Peters, L. Prönneke, L. Steidl, R. Zentel, B. Bläsi, A. Gombert, S. Glunz, G. Willeke, and U. Rau, "Theoretical and experimental analysis of photonic structures for fluorescent concentrators with increased efficiencies," *physica status solidi (a)*, vol. 205, pp. 2811–2821, 2008.

[56] M. Peters, J. C. Goldschmidt, P. Löper, B. Bläsi, and A. Gombert, "The effect of photonic structures on the light guiding efficiency of fluorescent concentrators," *Journal of Applied Physics*, vol. 105, p. 014909, 2009.

[57] S. Knabe, N. Soleimani, T. Markvart, and G. H. Bauer, "Efficient light trapping in a fluorescence solar collector by 3d photonic crystal," *physica status solidi (RRL) - Rapid Research Letters*, vol. 4, no. 5-6, pp. 118–120, 2010.

[58] D. K. G. de Boer, C.-W. Lin, M. P. Giesbers, H. J. Cornelissen, M. G. Debije, P. P. C. Verbunt, and D. J. Broer, "Polarization-independent filters for luminescent solar concentrators," *Applied Physics Letters*, vol. 98, no. 2, p. 021111, 2011.

[59] J. C. Goldschmidt, M. Peters, A. Bösch, H. Helmers, F. Dimroth, S. W. Glunz, and G. Willeke, "Increasing the efficiency of fluorescent concentrator systems," *Solar Energy Materials and Solar Cells*, vol. 93, no. 2, pp. 176–182, 2009.

[60] J. C. Goldschmidt, M. Peters, J. Gutmann, L. Steidl, R. Zentel, B. Bläsi, and M. Hermle, "Increasing fluorescent concentrator light collection efficiency by restricting the angular emission characteristics of the incorporated luminescent material - the 'nano-fluko' concept," in *Proc. SPIE 7725, Photonics for Solar Energy Systems III*, p. 77250S, 2010.

[61] N. C. Giebink, G. P. Wiederrecht, and M. R. Wasielewski, "Resonance-shifting to circumvent reabsorption loss in luminescent solar concentrators," *Nature Photonics*, vol. 5, pp. 694–701, 2011.

[62] I. Rousseau and V. Wood, "Nanophotonic luminescent solar concentrators," *Applied Physics Letters*, vol. 103, no. 13, p. 131113, 2013.

[63] E. M. Purcell, "Proceedings of the american physical society," *Physical Review*, vol. 69, pp. 674–674, 1946.

[64] E. Yablonovitch, "Inhibited Spontaneous Emission in Solid-State Physics and Electronics," *Physical Review Letters*, vol. 58, no. 20, pp. 2059–2062, 1987.

[65] S. John, "Strong Localization of Photons in Certain Disordered Dielectric Superlattices," *Physical Review Letters*, vol. 58, no. 23, pp. 2486–2489, 1987.

[66] J. D. Joannopoulos, S. G. Johnson, J. N. Winn, and R. D. Meade, *Photonic Crystals - Molding the Flow of Light*. Princeton: Princeton University Press, 2nd ed., 2008.

[67] V. P. Bykov, "Spontaneous emission in a periodic structure," *Soviet Physics JETP*, vol. 35, p. 269, 1972.

[68] S. G. Romanov, A. V. Fokin, and R. M. D. L. Rue, "Eu^{3+} emission in an anisotropic photonic band gap environment," *Applied Physics Letters*, vol. 76, no. 13, pp. 1656–1658, 2000.

[69] M. J. A. de Dood, A. Polman, and J. G. Fleming, "Modified spontaneous emission from erbium-doped photonic layer-by-layer crystals," *Physical Review B*, vol. 67, p. 115106, 2003.

[70] E. P. Petrov, V. N. Bogomolov, I. I. Kalosha, and S. V. Gaponenko, "Spontaneous Emission of Organic Molecules Embedded in a Photonic Crystal," *Physical Review Letters*, vol. 81, pp. 77–80, 1998.

[71] M. Megens, J. E. G. J. Wijnhoven, A. Lagendijk, and W. L. Vos, "Fluorescence lifetimes and linewidths of dye in photonic crystals," *Physical Review A*, vol. 59, pp. 4727–4731, 1999.

[72] M. Barth, A. Gruber, and F. Cichos, "Spectral and angular redistribution of photoluminescence near a photonic stop band," *Physical Review B*, vol. 72, p. 085129, 2005.

[73] P. Lodahl, A. Floris van Driel, I. S. Nikolaev, A. Irman, K. Overgaag, D. Vanmaekelbergh, and W. L. Vos, "Controlling the dynamics of spontaneous emission from quantum dots by photonic crystals," *Nature*, vol. 430, no. 7000, pp. 654–657, 2004.

[74] J. Li, B. Jia, G. Zhou, C. Bullen, J. Serbin, and M. Gu, "Spectral Redistribution in Spontaneous Emission from Quantum-Dot-Infiltrated 3D Woodpile Photonic Crystals for Telecommunications," *Advanced Materials*, vol. 19, no. 20, pp. 3276–3280, 2007.

[75] M. R. Jorgensen, J. W. Galusha, and M. H. Bartl, "Strongly Modified Spontaneous Emission Rates in Diamond-Structured Photonic Crystals," *Physical Review Letters*, vol. 107, p. 143902, 2011.

[76] M. D. Leistikow, A. P. Mosk, E. Yeganegi, S. R. Huisman, A. Lagendijk, and W. L. Vos, "Inhibited Spontaneous Emission of Quantum Dots Observed in a 3D Photonic Band Gap," *Physical Review Letters*, vol. 107, p. 193903, 2011.

[77] S. Ogawa, M. Imada, S. Yoshimoto, M. Okano, and S. Noda, "Control of Light Emission by 3D Photonic Crystals," *Science*, vol. 305, no. 5681, pp. 227–229, 2004.

[78] P. Vukusic and I. Hooper, "Directionally Controlled Fluorescence Emission in Butterflies," *Science*, vol. 310, no. 5751, p. 1151, 2005.

[79] E. V. Hooijdonk, C. Barthou, J. P. Vigneron, and S. Berthier, "Angular dependence of structural fluorescent emission from the scales of the male butterfly Troïdes magellanus (Papilionidae)," *Journal of the Optical Society of America B*, vol. 29, no. 5, pp. 1104–1111, 2012.

[80] J. V. Sanders, "Colour of Precious Opal," *Nature*, vol. 204, pp. 1151–1153, 1964.

[81] S. Nojima, "Optical-gain enhancement in two-dimensional active photonic crystals," *Journal of Applied Physics*, vol. 90, no. 2, pp. 545–551, 2001.

[82] R. Ozaki, T. Matsui, M. Ozaki, and K. Yoshino, "Electrically color-tunable defect mode lasing in one-dimensional photonic-band-gap system containing liquid crystal," *Applied Physics Letters*, vol. 82, no. 21, pp. 3593–3595, 2003.

[83] J. Yoon, W. Lee, and E. L. Thomas, "Optically Pumped Surface-Emitting Lasing Using Self-Assembled Block-Copolymer-Distributed Bragg Reflectors," *Nano Letters*, vol. 6, no. 10, pp. 2211–2214, 2006.

[84] K. Kiyota, T. Kise, N. Yokouchi, T. Ide, and T. Baba, "Various low group velocity effects in photonic crystal line defect waveguides and their demonstration by laser oscillation," *Applied Physics Letters*, vol. 88, no. 20, p. 201904, 2006.

[85] V. M. Menon, M. Luberto, N. V. Valappil, and S. Chatterjee, "Lasing from InGaP quantum dots in a spin-coated flexible microcavity," *Optics Express*, vol. 16, no. 24, pp. 19535–19540, 2008.

[86] D. P. Puzzo, F. Scotognella, M. Zavelani-Rossi, M. Sebastian, A. J. Lough, I. Manners, G. Lanzani, R. Tubino, and G. A. Ozin, "Distributed Feedback Lasing from a Composite Poly(phenylene vinylene)-Nanoparticle One-Dimensional Photonic Crystal," *Nano Letters*, vol. 9, no. 12, pp. 4273–4278, 2009.

[87] F. Scotognella, D. P. Puzzo, A. Monguzzi, D. S. Wiersma, D. Maschke, R. Tubino, and G. A. Ozin, "Nanoparticle One-Dimensional Photonic-Crystal Dye Laser," *Small*, vol. 5, no. 18, pp. 2048–2052, 2009.

[88] E. F. Schubert, Y.-H. Wang, A. Y. Cho, L.-W. Tu, and G. J. Zydzik, "Resonant cavity light-emitting diode," *Applied Physics Letters*, vol. 60, no. 8, pp. 921–923, 1992.

[89] A.-L. Fehrembach, S. Enoch, and A. Sentenac, "Highly directive light sources using two-dimensional photonic crystal slabs," *Applied Physics Letters*, vol. 79, no. 26, pp. 4280–4282, 2001.

[90] K. Saxena, V. Jain, and D. S. Mehta, "A review on the light extraction techniques in organic electroluminescent devices," *Optical Materials*, vol. 32, no. 1, pp. 221–233, 2009.

[91] C. Wiesmann, K. Bergenek, N. Linder, and U. T. Schwarz, "Photonic crystal LEDs - designing light extraction," *Laser & Photonics Reviews*, vol. 3, no. 3, pp. 262–286, 2009.

[92] Y.-S. Tyan, "Organic light-emitting-diode lighting overview," *Journal of Photonics for Energy*, vol. 1, no. 1, p. 011009, 2011.

[93] N. Ashcroft and N. Mermin, *Solid state physics*. Saunders College, 1976.

[94] S. G. Johnson and J. D. Joannopoulos, "Block-iterative frequency-domain methods for Maxwell's equations in a planewave basis," *Optics Express*, vol. 8, no. 3, pp. 173–190, 2001.

[95] A. F. Koenderink, *Emission and Transport of Light in Photonic Crystals*. PhD thesis, University of Amsterdam, 2003.

[96] T. F. Krauss, "Slow light in photonic crystal waveguides," *Journal of Physics D: Applied Physics*, vol. 40, no. 9, p. 2666, 2007.

[97] T. Baba, "Slow light in photonic crystals," *Nature Photonics*, vol. 2, no. 8, pp. 465–473, 2008.

[98] K. Busch and S. John, "Photonic band gap formation in certain self-organizing systems," *Physical Review E*, vol. 58, no. 3, pp. 3896–3908, 1998.

[99] R. Sprik, B. A. van Tiggelen, and A. Lagendijk, "Optical emission in periodic dielectrics," *Europhysics Letters*, vol. 35, no. 4, p. 265, 1996.

[100] I. S. Nikolaev, W. L. Vos, and A. F. Koenderink, "Accurate calculation of the local density of optical states in inverse-opal photonic crystals," *Journal of the Optical Society of America B*, vol. 26, no. 5, pp. 987–997, 2009.

[101] S. M. Barnett and R. Loudon, "Sum Rule for Modified Spontaneous Emission Rates," *Physical Review Letters*, vol. 77, pp. 2444–2446, 1996.

[102] S. Scheel, "Sum rule for local densities of states in absorbing dielectrics," *Physical Review A*, vol. 78, p. 013841, 2008.

[103] E. Pavarini, L. C. Andreani, C. Soci, M. Galli, F. Marabelli, and D. Comoretto, "Band structure and optical properties of opal photonic crystals," *Physical Review B*, vol. 72, p. 045102, 2005.

[104] R. Zengerle, "Light Propagation in Singly and Doubly Periodic Planar Waveguides," *Journal of Modern Optics*, vol. 34, no. 12, pp. 1589–1617, 1987.

[105] D. N. Chigrin, "Radiation pattern of a classical dipole in a photonic crystal: Photon focusing," *Physical Review E*, vol. 70, p. 056611, 2004.

[106] K. Sakoda, *Optical Properties of Photonic Crystals.* Berlin: Springer, 2004.

[107] M. Born and E. Wolf, *Principles of Optics.* Cambridge University Press, 7th ed., 2005.

[108] A. Einstein, "Zur Quantentheorie der Strahlung," *Physikalische Zeitschrift*, vol. 18, pp. 121–128, 1917.

[109] M. Fox, *Quantum Optics.* Oxford University Press, 2006.

[110] L. E. Ballentine, *Quantum Mechanics: A Modern Development.* Singapore: World Scientific Publishing Co. Pte. Ltd., 1998.

[111] D. J. Griffiths, *Introduction to Quantum Mechanics.* Upper Saddle River: Prentice Hall, Inc., 1995.

[112] R. Loudon, *The Quantum Theory of Light.* Oxford University Press, 3rd ed., 2000.

[113] J. P. Dowling and C. M. Bowden, "Atomic emission rates in inhomogeneous media with applications to photonic band structures," *Physical Review A*, vol. 46, pp. 612–622, 1992.

[114] W. L. Vos, A. F. Koenderink, and I. S. Nikolaev, "Orientation-dependent spontaneous emission rates of a two-level quantum emitter in any nanophotonic environment," *Physical Review A*, vol. 80, p. 053802, 2009.

[115] R. C. Hilborn, "Einstein coefficients, cross sections, f values, dipole moments, and all that," *American Journal of Physics*, vol. 50, no. 11, pp. 982–986, 1982.

[116] K.-H. Brenner, "Aspects for calculating local absorption with the rigorous coupled-wave method," *Optics Express*, vol. 18, no. 10, pp. 10369–10376, 2010.

[117] J. Lakowicz, *Principles of Fluorescence Spectroscopy.* London: Springer, 2009.

[118] R. Wang, X.-H. Wang, B.-Y. Gu, and G.-Z. Yang, "Local density of states in three-dimensional photonic crystals: Calculation and enhancement effects," *Physical Review B*, vol. 67, p. 155114, 2003.

[119] R. C. McPhedran, L. C. Botten, J. McOrist, A. A. Asatryan, C. M. de Sterke, and N. A. Nicorovici, "Density of states functions for photonic crystals," *Physical Review E*, vol. 69, p. 016609, 2004.

[120] D. P. Fussell, R. C. McPhedran, and C. Martijn de Sterke, "Three-dimensional Green's tensor, local density of states, and spontaneous emission in finite two-dimensional photonic crystals composed of cylinders," *Physical Review E*, vol. 70, p. 066608, 2004.

[121] S. J. Myers, D. P. Fussell, J. M. Dawes, E. Mägi, R. C. McPhedran, B. J. Eggleton, and C. M. de Sterke, "Manipulation of spontaneous emission in a tapered photonic crystal fibre," *Optics Express*, vol. 14, no. 25, pp. 12439–12444, 2006.

[122] E. V. Hooijdonk, S. Berthier, and J.-P. Vigneron, "Bio-inspired approach of the fluorescence emission properties in the scarabaeid beetle Hoplia coerulea (Coleoptera): Modeling by transfer-matrix optical simulations," *Journal of Applied Physics*, vol. 112, no. 11, p. 114702, 2012.

[123] P. Bermel, A. Rodriguez, J. D. Joannopoulos, and M. Soljacic, "Tailoring Optical Nonlinearities via the Purcell Effect," *Physical Review Letters*, vol. 99, p. 053601, 2007.

[124] B. Herter, S. Wolf, S. Fischer, J. Gutmann, B. Bläsi, and J. C. Goldschmidt, "Increased upconversion quantum yield in photonic structures due to local field enhancement and modification of the local density of states – a

simulation-based analysis," *Optics Express*, vol. 21, no. S5, pp. A883–A900, 2013.

[125] G. Lehmann and M. Taut, "On the Numerical Calculation of the Density of States and Related Properties," *physica status solidi (b)*, vol. 54, no. 2, pp. 469–477, 1972.

[126] J. Hama, M. Watanabe, and T. Kato, "Correctly weighted tetrahedron method for k-space integration," *Journal of Physics: Condensed Matter*, vol. 2, no. 36, p. 7445, 1990.

[127] A. Sinitskii, S. Klimonsky, S. Eliseeva, Y. Tretyakov, J. Li, P. Zhang, M. Li, and J. Zhou, "Directional radiation pattern of luminescent photonic crystals at frequencies near the second photonic stop band," *JETP Letters*, vol. 87, pp. 672–676, 2008.

[128] M. Li, P. Zhang, J. Li, J. Zhou, A. Sinitskii, V. Abramova, S. Klimonsky, and Y. Tretyakov, "Directional emission from rare earth ions in inverse photonic crystals," *Applied Physics B: Lasers and Optics*, vol. 89, pp. 251–255, 2007.

[129] J. Gutmann, H. Zappe, and J. C. Goldschmidt, "Quantitative modeling of fluorescent emission in photonic crystals," *Physical Review B*, vol. 88, p. 205118, 2013.

[130] K. Yee, "Numerical solution of initial boundary value problems involving maxwell's equations in isotropic media," *Antennas and Propagation, IEEE Transactions on*, vol. 14, no. 3, pp. 302–307, 1966.

[131] A. Taflove and S. C. Hagness, *Computational Electrodynamics: The Finite-Difference Time-Domain Method.* Norwood: Artech House, 3rd ed., 2005.

[132] M. G. Moharam and T. K. Gaylord, "Diffraction analysis of dielectric surface-relief gratings," *Journal of the Optical Society of America*, vol. 72, no. 10, pp. 1385–1392, 1982.

[133] D. M. Whittaker and I. S. Culshaw, "Scattering-matrix treatment of patterned multilayer photonic structures," *Physical Review B*, vol. 60, pp. 2610–2618, 1999.

[134] R. F. Chen and J. R. Knutson, "Mechanism of fluorescence concentration quenching of carboxyfluorescein in liposomes: Energy transfer to nonfluorescent dimers," *Analytical Biochemistry*, vol. 172, no. 1, pp. 61–77, 1988.

[135] K. A. Colby, J. J. Burdett, R. F. Frisbee, L. Zhu, R. J. Dillon, and C. J. Bardeen, "Electronic Energy Migration on Different Time Scales: Concentration Dependence of the Time-Resolved Anisotropy and Fluorescence

Quenching of Lumogen Red in Poly(methyl methacrylate)," *The Journal of Physical Chemistry A*, vol. 114, no. 10, pp. 3471–3482, 2010.

[136] N. Tanaka, N. Barashkov, J. Heath, and W. N. Sisk, "Photodegradation of polymer-dispersed perylene di-imide dyes," *Applied Optics*, vol. 45, no. 16, pp. 3846–3851, 2006.

[137] L. Bechger, A. F. Koenderink, and W. L. Vos, "Emission Spectra and Lifetimes of R6G Dye on Silica-Coated Titania Powder," *Langmuir*, vol. 18, no. 6, pp. 2444–2447, 2002.

[138] F. L. Arbeloa, P. R. Ojeda, and I. L. Arbeloa, "Flourescence self-quenching of the molecular forms of Rhodamine B in aqueous and ethanolic solutions," *Journal of Luminescence*, vol. 44, pp. 105–112, 1989.

[139] H. Macleod, *Thin-film optical filters.* Bristol: Adam Hilger, 2nd ed., 1986.

[140] P. Yeh, *Optical waves in layered media.* Wiley, 2005.

[141] L. Li, "Formulation and comparison of two recursive matrix algorithms for modeling layered diffraction gratings," *Journal of the Optical Society of America A*, vol. 13, no. 5, pp. 1024–1035, 1996.

[142] F. Bödicker, "Modellierung des strahlenden Emissionsverhaltens in einer photonischen Solarzelle," Bachelor's thesis, Technische Universität Darmstadt, 2012.

[143] R. Jacobsson, "V Light Reflection from Films of Continuously Varying Refractive Index," in *Progress in Optics* (E. Wolf, ed.), vol. 5, pp. 247–286, Elsevier, 1966.

[144] R. J. Potton, "Reciprocity in optics," *Reports on Progress in Physics*, vol. 67, no. 5, p. 717, 2004.

[145] S. Knabe, *Spectral photoluminescence for the characterization of excitation states in semiconductors and fluorescence solar collectors with manipulation of the in and out coupling of radiation.* PhD thesis, University of Oldenburg, 2011.

[146] T. Rist, "Modellierung und Charakterisierung von Fluoreszenzkonzentrator- und Hochkonvertersystemen," Diploma thesis, University of Freiburg, 2012.

[147] H. Sträter, S. Knabe, T. J. Meyer, and G. H. Bauer, "Spectrally and angle-resolved emission of thin film fluorescence collectors," *Progress in Photovoltaics: Research and Applications*, vol. 21, no. 4, pp. 554–560, 2013.

[148] J. Posdziech, "Herstellung und Charakterisierung von fortgeschrittenen Fluoreszenzkonzentratoren," Diploma thesis, University of Freiburg, 2011.

[149] J. Löffler, "Photonische Vielschichtsysteme für Fluoreszenzkonzentratoren," Diploma thesis, University of Freiburg, 2013.

[150] BASF, "Lumogen® F Yellow 083." Available online at www2.basf.us/additives/pdfs/lumyel083.pdf (March 12, 2012).

[151] BASF, "Lumogen® F Red 300." Available online at www2.basf.us/additives/pdfs/lumred300.pdf (March 12, 2012).

[152] L. H. Slooff, N. J. Bakker, P. M. Sommeling, A. Büchtemann, A. Wedel, and W. G. J. H. M. van Sark, "Long-term optical stability of fluorescent solar concentrator plates," *physica status solidi (a)*, vol. 211, no. 5, pp. 1150–1154, 2014.

[153] C. B. Walsh and E. I. Franses, "Ultrathin PMMA films spin-coated from toluene solutions," *Thin Solid Films*, vol. 429, no. 1-2, pp. 71–76, 2003.

[154] M. E. Calvo, O. Sánchez-Sobrado, S. Colodrero, and H. Míguez, "Control over the Structural and Optical Features of Nanoparticle-Based One-Dimensional Photonic Crystals," *Langmuir*, vol. 25, no. 4, pp. 2443–2448, 2009.

[155] B. Walter, "Die Aenderung des Fluorescenzvermögens mit der Concentration," *Annalen der Physik*, vol. 270, no. 6, pp. 316–326, 1888.

[156] W. L. Lewschin, "Die Auslöschung der Fluoreszenz in festen und flüssigen Farbstofflösungen," *Zeitschrift für Physik A Hadrons and Nuclei*, vol. 43, pp. 230–253, 1927.

[157] T. Förster, *Fluoreszenz organischer Verbindungen.* Göttingen, 1951.

[158] F. Perrin, "Loi de decroissance du pouvoir fluorescent en fonction de la concentration," *Comptes Rendus de l'Académie des Sciences*, vol. 178, pp. 1978–1980, 1924.

[159] L. R. Wilson, *Luminescent Solar Concentrators: A Study of Optical Properties, Re-absorption and Device Optimisation.* PhD thesis, Heriot-Watt University Edinburgh, 2010.

[160] BASF, "Lumogen® F Technical Information," 1997. Available online at www2.basf.us/additives/pdfs/p3201e.pdf (March 12, 2012).

[161] C. J. Brinker and G. W. Scherer, *Sol-Gel Science.* San Diego: Academic Press, 1990.

[162] M. Alam and D. Cameron, "Preparation and Characterization of TiO2 Thin Films by Sol-Gel Method," *Journal of Sol-Gel Science and Technology*, vol. 25, no. 2, pp. 137–145, 2002.

[163] W. Drotning and E. Roth, "Effects of moisture on the thermal expansion of poly(methylmethacrylate)," *Journal of Materials Science*, vol. 24, no. 9, pp. 3137–3140, 1989.

[164] K. V. K. Rao, S. V. N. Naidu, and L. Iyengar, "Thermal Expansion of Rutile and Anatase," *Journal of the American Ceramic Society*, vol. 53, no. 3, pp. 124–126, 1970.

[165] T. J. Rehg and G. Higgins, "Spin coating of colloidal suspensions," *AIChE Journal*, vol. 38, no. 4, pp. 489–501, 1992.

[166] J. Yoon, W. Lee, J.-M. Caruge, M. Bawendi, E. L. Thomas, S. Kooi, and P. N. Prasad, "Defect-mode mirrorless lasing in dye-doped organic/inorganic hybrid one-dimensional photonic crystal," *Applied Physics Letters*, vol. 88, no. 9, p. 091102, 2006.

[167] Z. Wang, J. Zhang, J. Xie, Y. Yin, Z. Wang, H. Shen, Y. Li, J. Li, S. Liang, L. Cui, L. Zhang, H. Zhang, and B. Yang, "Patterning Organic/Inorganic Hybrid Bragg Stacks by Integrating One-Dimensional Photonic Crystals and Macrocavities through Photolithography: Toward Tunable Colorful Patterns as Highly Selective Sensors," *ACS Applied Materials & Interfaces*, vol. 4, no. 3, pp. 1397–1403, 2012.

[168] D. P. Puzzo, L. D. Bonifacio, J. Oreopoulos, C. M. Yip, I. Manners, and G. A. Ozin, "Color from colorless nanomaterials: Bragg reflectors made of nanoparticles," *Journal of Materials Chemistry*, vol. 19, pp. 3500–3506, 2009.

[169] S. Colodrero, M. Ocana, and H. Miguez, "Nanoparticle-Based One-Dimensional Photonic Crystals," *Langmuir*, vol. 24, no. 9, pp. 4430–4434, 2008.

[170] L. D. Bonifacio, B. V. Lotsch, D. P. Puzzo, F. Scotognella, and G. A. Ozin, "Stacking the Nanochemistry Deck: Structural and Compositional Diversity in One-Dimensional Photonic Crystals," *Advanced Materials*, vol. 21, no. 16, pp. 1641–1646, 2009.

[171] J. Gutmann, M. Peters, B. Bläsi, M. Hermle, A. Gombert, H. Zappe, and J. C. Goldschmidt, "Electromagnetic simulations of a photonic luminescent solar concentrator," *Optics Express*, vol. 20, no. S2, pp. A157–A167, 2012.

[172] A. Mihi, M. Ocaña, and H. Míguez, "Oriented Colloidal-Crystal Thin Films by Spin-Coating Microspheres Dispersed in Volatile Media," *Advanced Materials*, vol. 18, no. 17, pp. 2244–2249, 2006.

[173] C. López, "Materials Aspects of Photonic Crystals," *Advanced Materials*, vol. 15, no. 20, pp. 1679–1704, 2003.

[174] J. F. Bertone, P. Jiang, K. S. Hwang, D. M. Mittleman, and V. L. Colvin, "Thickness Dependence of the Optical Properties of Ordered Silica-Air and Air-Polymer Photonic Crystals," *Physical Review Letters*, vol. 83, no. 2, pp. 300–303, 1999.

[175] H. Fudouzi and Y. Xia, "Photonic Papers and Inks: Color Writing with Colorless Materials," *Advanced Materials*, vol. 15, no. 11, pp. 892–896, 2003.

[176] P. Spahn, *Kolloidale Kristalle aus monodispersen Silika-Polymer Hybridpartikeln.* PhD thesis, Technische Universität Darmstadt, 2008.

[177] M. Egen and R. Zentel, "Surfactant-free emulsion polymerization of various methacrylates: Towards monodisperse colloids for polymer opals," *Macromolecular Chemistry and Physics*, vol. 205, no. 11, pp. 1479–1488, 2004.

[178] M. Müller, R. Zentel, T. Maka, S. G. Romanov, and C. M. Sotomayor Torres, "Dye-Containing Polymer Beads as Photonic Crystals," *Chemistry of Materials*, vol. 12, no. 8, pp. 2508–2512, 2000.

[179] P. Jiang, J. F. Bertone, K. S. Hwang, and V. L. Colvin, "Single-Crystal Colloidal Multilayers of Controlled Thickness," *Chemistry of Materials*, vol. 11, no. 8, pp. 2132–2140, 1999.

[180] L. Steidl, *Kolloide und ihre Überstrukturen als Bausteine zur Herstellung funktioneller Materialien.* PhD thesis, University of Mainz, 2013.

[181] C. Dushkin, G. Lazarov, S. Kotsev, H. Yoshimura, and K. Nagayama, "Effect of growth conditions on the structure of two-dimensional latex crystals: experiment," *Colloid and Polymer Science*, vol. 277, no. 10, pp. 914–930, 1999.

[182] B. Griesebock, M. Egen, and R. Zentel, "Large Photonic Films by Crystallization on Fluid Substrates," *Chemistry of Materials*, vol. 14, no. 10, pp. 4023–4025, 2002.

[183] B. Lange, J. Wagner, and R. Zentel, "Fabrication of Robust High-Quality ORMOCER® Inverse Opals," *Macromolecular Rapid Communications*, vol. 27, no. 20, pp. 1746–1751, 2006.

[184] T. Ruhl, P. Spahn, and G. Hellmann, "Artificial opals prepared by melt compression," *Polymer*, vol. 44, no. 25, pp. 7625–7634, 2003.

[185] A. N. Sprafke, D. Schneevoigt, S. Seidel, S. L. Schweizer, and R. B. Wehrspohn, "Automated spray coating process for the fabrication of large-area artificial opals on textured substrates," *Optics Express*, vol. 21, no. S3, pp. A528–A538, 2013.

[186] J. C. Goldschmidt, M. Peters, M. Hermle, and S. W. Glunz, "Characterizing the light guiding of fluorescent concentrators," *Journal of Applied Physics*, vol. 105, no. 11, p. 114911, 2009.

[187] J. Gutmann, J. Posdziech, M. Peters, L. Steidl, R. Zentel, H. Zappe, and J. C. Goldschmidt, "Emission of Rhodamine B in PMMA opals for luminescent solar concentrators," in *Proc. SPIE 8438, Photonics for Solar Energy Systems IV*, p. 84381O, 2012.

[188] J. Gutmann, H. Zappe, and J. Goldschmidt, "Predicting the performance of photonic luminescent solar concentrators," in *Proceedings of the 39th IEEE Photovoltaic Specialists Conference*, pp. 1864–1868, 2013.

[189] M. Peters, J. Christoph Goldschmidt, and B. Bläsi, "Efficiency limit and example of a photonic solar cell," *Journal of Applied Physics*, vol. 110, p. 043104, 2011.

[190] O. Höhn, T. Kraus, U. T. Schwarz, and B. Bläsi, "The photonic solar cell: system design and efficiency estimations," in *Proc. SPIE 9140, Photonics for Solar Energy Systems V*, pp. 91400B–91400B–7, 2014.

[191] E. Hecht, *Optics*. Addison Wesley, 4th ed., 2002.

[192] C. Cohen-Tannoudji, J. Dupont-Roc, and G. Grynberg, *Atom-Photon Interactions: Basic Process and Appilcations*. New York: Wiley, 1998.

[193] M. I. Eides, H. Grotch, and V. A. Shelyuto, "Theory of light hydrogenlike atoms," *Physics Reports*, vol. 342, no. 2–3, pp. 63–261, 2001.

[194] S. John and J. Wang, "Quantum optics of localized light in a photonic band gap," *Physical Review B*, vol. 43, pp. 12772–12789, 1991.

[195] X.-H. Wang, Y. S. Kivshar, and B.-Y. Gu, "Giant Lamb Shift in Photonic Crystals," *Physical Review Letters*, vol. 93, p. 073901, 2004.

Notation

List of symbols

Note: boldface type symbols denote vector quantities.

Symbol	Meaning	Unit
a	Size of unit cell of photonic crystal	m
$\boldsymbol{a}$	Amplitude vector of forward propagating wave (scattering matrix method)	V/m
A	Absorptance	–
A_{dye}	Absorptance by the dye	–
A_{ref}	Absorptance by the matrix material	–
A_{tot}	Total absorptance of sample	–
$\mathcal{A}$	Einstein coefficient for emission	1/s
b	Band index	–
$\boldsymbol{b}$	Amplitude vector of backward propagating wave (scattering matrix method)	V/m
$\mathcal{B}$	Einstein coefficient for absorption	$\mathrm{m}^3/\mathrm{Js}^2$
c	Speed of light in vacuum (299792458 m/s)	m/s
C	Center-mount measurement	–
C_1	Coefficient for Cauchy model of refractive index	–
C_2	Coefficient for Cauchy model of refractive index	m^2
C_3	Coefficient for Cauchy model of refractive index	m^4
C_{p}	Conversion of the polymerization (opal)	–
d	Thickness (of layer or sample)	m
d_{c}	Diameter of colloids (opal)	m
d_{s}	Diameter of the seed particles (opal)	m
d_{p}	Thickness of PMMA layers	m

Symbol	Meaning	Unit
d_{TiO}	Thickness of titania layers	m
$\boldsymbol{d}$	Direction vector of detection cone ($\boldsymbol{k}$-space)	1/m
D, D'	Intersection points of detection cone, see. Fig. 3.3	1/m
$\boldsymbol{E}$	Electric field	V/m
E_{r}, E_{t}, E_{i}	Amplitudes of the reflected, transmitted, and incident electric field at an interface	V/m
$\mathcal{E}$	Energy	J
f	Probability density function (Appendix A.5), e.g. the angular distribution function in Sec. 3.3.3	–
F	Set of modes in $\boldsymbol{k}$-space, see Sec. 3.1.4	1/m
g	Spectral shape function	–
g_{f}	Spectral shape function of detected light	–
g_{l}	Line shape function (atomic line broadening)	–
$\boldsymbol{G}$	Reciprocal lattice vector	1/m
$\mathcal{G}$	Degeneracy of a state	–
h	Function connecting two random variables, see Appendix A.5	–
$\hbar$	Reduced Planck constant (1.05×10^{-34} Js)	Js
$\boldsymbol{H}$	Magnetic field	A/m
i	Imaginary unit $\sqrt{-1}$	–
I	Intensity	W/m^2
j	Index variable	–
J_{f}, J_{b}	Number of summands in Eq. (3.62)	–
$\boldsymbol{k}$	Wave vector	1/m
$k = \lvert\boldsymbol{k}\rvert$	Absolute value of wave vector	1/m
$\tilde{k}$	Normalized wave vector ($k\,a/2\pi$)	–
$\boldsymbol{k}_{\mathrm{out}}$	Wave vector of out-coupled plane wave	1/m
$\boldsymbol{k}_{\parallel}$	Wave vector component parallel to interface	1/m
Δk	Spacing of sampled grid in $\boldsymbol{k}$-space	1/m
k_{B}	Boltzmann constant (1.380648810^{-23} J/K)	J/K
K	Set of modes in $\boldsymbol{k}$-space, see Eq. (3.1)	1/m
K	Crystallographic orientation in $\boldsymbol{k}$-space, see Fig. 1.2 (d)	1/m
l_{d}	Detection spot radius in ray-tracing calculations	m
l_{e}	Distance between point of excitation and edge face, see Sec. 3.3.4	m
L	Crystallographic orientation in $\boldsymbol{k}$-space, see Fig. 1.2 (d)	1/m
L_{eff}	Effective path length to edge face	m
m	Number of dye-doped layers	–
m_{s}	Mass of the seed particles (opal)	kg
m_{m}	Mass of the added monomer (opal)	kg

Symbol	Meaning	Unit
M	Number of sampled modes, see Sec. 3.1.2	–
M_w	Weight average molecular weight (of polymer)	kg
n	Refractive index	–
$\tilde{n}$	Complex refractive index	–
n_{eff}	Effective refractive index	–
n_{p}	Refractive index of PMMA layers	–
n_{TiO}	Refractive index of titania layers	–
n_{i}	Refractive index of medium of incidence	–
n_{t}	Refractive index of medium of transmission	–
n_{in}	Refractive index of internal medium (of sample)	–
n_{out}	Refractive index of surrounding medium	–
$\boldsymbol{n}$	Interface normal	m
N_j	Population of state j of emitter	–
$p\{X\}$	Probability of event X	–
p_{abs}	Probability of absorption of incident light	–
p_{g}	Probability of guiding	–
p_{ra}	Reabsorption probability	–
$p_{\mathrm{ra,s}}$	Spectral reabsorption probability	–
p_{col}	Collection probability	–
P_{fi}	Probability for transition from state f to i	1/s
P_{ABS}	Transition probability of absorption	1/s
P_{STE}	Transition probability of stimulated emission	1/s
P_{SPE}	Transition probability of spontaneous emission	1/s
$P_{\mathrm{SPE,f}}$	Fractional transition probability of spontaneous emission	1/s
$\mathcal{P}_{\mathrm{ABS}}$	Absorbed power	W
q	Attenuation due to absorption in Sec. 3.3.2	–
$\boldsymbol{r}$	Position (vector)	m
r_{s}, r_{p}	Reflection coefficient of electric fields for s-, p-polarized light at interfaces	–
R	Reflectance	–
R_{d}	Diffuse reflectance	–
R_{s}	Specular reflectance	–
$\boldsymbol{R}$	Lattice vector	m
s	Normalization constant of the probability density function in Appendix A.5	–
$\boldsymbol{\mathcal{S}}$	Scattering matrix	–
t	Time	s
t_{s}, t_{p}	Transmission coefficient of electric fields for s-, p-polarized light at interfaces	–

Symbol	Meaning	Unit
T	Transmittance	–
T_d	Diffuse transmittance	–
T_s	Specular transmittance	–
$\boldsymbol{\mathcal{T}}$	Transfer matrix	–
u	Spectral energy density	$\mathrm{Js/m^3}$
$\boldsymbol{u}$	Bloch function	A/m
U	Crystallographic orientation in $\boldsymbol{k}$-space, see Fig. 1.2 (d)	1/m
v_g	Group velocity ($d\omega/dk$)	m/s
V	Volume	$\mathrm{m^3}$
$\mathcal{V}_\mathrm{fi}$	Perturbation Hamiltonian	J
w_abs	Spatial resolved distribution of absorptance	–
W	Crystallographic orientation in $\boldsymbol{k}$-space, see Fig. 1.2 (d)	1/m
x, y, z	Spatial coordinates	m
X	Crystallographic orientation in $\boldsymbol{k}$-space, see Fig. 1.2 (d)	1/m
α	Absorption coefficient	1/m
α_dye	Absorptance coefficient of the dye	1/m
α_ref	Absorptance coefficient of the matrix material	1/m
α_tot	Total absorptance coefficient	1/m
β	Enhancement factor of absorption probability	–
γ	Ratio of LDOS in photonic crystal to that in homogeneous media	–
δ	Dirac delta function	–
ϵ	Extinction coefficient	1/m
ε	Relative permittivity (real part)	–
ε''	Imaginary part of the complex relative permittivity	–
ε_0	Vacuum permittivity (8.85×10^{-12} F/m)	F/m
ζ, ζ_dye	Dye concentration	–
ζ_p	Polymer concentration	–
η	Concentrator quantum yield (CQY)	–
θ_d	Half-angle of detection cone (angular resolved PL)	–
ϑ	Absolute temperature	K
κ	Imaginary part of complex refractive index	–
$\varkappa$	Normalization factor in Eq. (3.41)	–
λ_0	Vacuum wavelength	m
λ	Wavelength (in media)	m
λ_design	Design wavelength of Bragg stack, where the reflection peak occurs; determines thickness of layers.	m
λ_peak	Wavelength where a reflection peak occurs	m

Symbol	Meaning	Unit
λ_i	Incident wavelength	m
μ	Relative permeability	–
μ_0	Vacuum permeability ($4\pi \times 10^{-7}$ Vs/Am)	Vs/Am
ν	Frequency	1/s
ξ	Excited-state population factor, see Eq. (3.37)	–
ρ	Local density of photon states (LDOS)	–
$\hat{\rho}$	Binned local density of photon states	–
$\hat{\rho}_\mathrm{f}$	Binned fractional LDOS (FLDOS)	–
ϱ	Density of photon states (DOS)	–
$\hat{\varrho}$	Binned density of photon states	–
σ	Light guiding efficiency (LGE)	–
τ	Fluorescence lifetime	s
ϕ_c	Critical angle of total internal reflection	–
ϕ_d	Detection angle (angular resolved PL)	–
ϕ_in	Internal propagation angle	–
ϕ_i	Angle of incident light	–
ϕ_t	Angle of transmitted light	–
ϕ_k	Angle of wave vector of out-coupled plane wave, see Fig. 2.1	–
φ_k	Angle of wave vector inside a photonic crystal, see Fig. 2.1	–
χ	Detectable fraction of emission in homogeneous media, i.e. ratio of FLDOS to LDOS	–
ψ	Enhancement factor of emission probability	–
ω	Angular frequency	1/s
$\Delta\omega$	Binning width of histogram	1/s
$\tilde{\omega}$	Normalized angular frequency ($\omega a/2\pi c$)	–
Γ	Origin in $\boldsymbol{k}$-space, see Fig. 1.2 (d)	1/m
Γ_fi	Rate for transition from state f to i	1/s
Γ_ABS	Transition rate of absorption	1/s
Γ_STE	Transition rate of stimulated emission	1/s
Γ_SPE	Transition rate of spontaneous emission	1/s
$\Gamma_\mathrm{SPE,f}$	Fractional transition rate of spontaneous emission	1/s
Δ	Phase shift difference (Ellipsometry)	–
Δ_{21}	Lamb shift	1/s
$\hat{\Theta}$	Hermitian operator of wave equation	$1/\mathrm{m}^2$
Π_0	Angular resolved emission spectrum (Sec. 3.3.3)	–
Π_d	Detected angular resolved surface PL (Sec. 3.3.3)	–
Π_s	Integrated angular resolved surface PL (Sec. 3.3.3)	–
Π_e	Integrated edge PL (Sec. 3.3.3)	–

Symbol	Meaning	Unit
Π_{meas}	Raw measurement signal for angular resolved surface PL (Sec. 4.3.3)	a.u.
Π_{norm}	Measurement signal for angular resolved surface PL normalized by absorptance of sample (Sec. 4.3.3)	a.u.
Φ	Photoluminescence quantum yield (PLQY)	–
Ψ	Measure of amplitude ratio (Ellipsometry)	–
Ω	Spin speed	1/s
$\square$	Placeholder for the field in Eq. (A.13)	–
$\sphericalangle(\boldsymbol{v}_1, \boldsymbol{v}_2)$	Angle included between vectors $\boldsymbol{v}_1$ and $\boldsymbol{v}_2$	–
$\lfloor x \rfloor$	Gives the greatest integer less than or equal to x	–
$\boldsymbol{v}^{\mathrm{T}}$	Transpose of vector $\boldsymbol{v}$	–
$\boldsymbol{\nabla}$	Nabla operator, $(\frac{\partial}{\partial x}, \frac{\partial}{\partial y}, \frac{\partial}{\partial z})^{\mathrm{T}}$	1/m
$\boldsymbol{\nabla}_{\boldsymbol{k}}$	Nabla operator in $\boldsymbol{k}$-space, $(\frac{\partial}{\partial k_x}, \frac{\partial}{\partial k_y}, \frac{\partial}{\partial k_z})^{\mathrm{T}}$	m

List of abbreviations

Abbreviation	Meaning
1D	One-dimensional
2D	Two-dimensional
3D	Three-dimensional
a.u.	Arbitrary units
ABS	Absorption
AFM	Atomic force microscopy
AIBN	Azobisisobutyronitrile
CM	Center-mount
CQY	Concentrator quantum yield
DOS	Density of photon states
FBZ	First Brillouin zone
fcc	Face centered cubic
FDTD	Finite-difference time-domain
FLDOS	Fractional local density of photon states
(F)LDOS	*Short notation for* “FLDOS and LDOS”
FWHM	Full width at half maximum
IBS	Ion beam sputtering
LED	Light emitting diode

Abbreviation	**Meaning**
LDOS	Local density of photon states
(L)DOS	*Short notation for* “LDOS and DOS”
LGE	Light guiding efficiency
LR	Lumogen dye F Red 305
LSC	Luminescent solar concentrator
LY	Lumogen dye F Yellow 083
MMA	Methyl methacrylate
MPB	MIT Photonic-Bands
NIR	Near-infrared
NRD	Non-radiative decay
PC	Photonic crystal
PECVD	Plasma enhanced chemical vapor deposition
PL	Photoluminescence
PLQY	Photoluminescence quantum yield
PLSC	Photonic luminescent solar concentrator
(P)LSC	*Short notation for* “PLSC and LSC”
PTFE	Polytetrafluoroethylene
PMMA	Poly(methyl methacrylate)
q3D	Quasi-3D
SEM	Scanning electron microscope
SPE	Spontaneous emission
TE	Transverse electric
TIR	Total internal reflection
TM	Transverse magnetic
TSR	Triple stack reference
w%	Weight percent (concentrations)
w.l.o.g.	Without loss of generality
w.r.t.	With respect to
WSC	Wigner-Seitz cell

List of Figures

1.1 Working principle of (conventional) luminescent solar concentrators 2
1.2 Concept and structure of Bragg stack and opal PLSCs 7

2.1 Light at interfaces: refraction and out-coupling in $\boldsymbol{k}$-space 15
2.2 Illustration of absorption, and stimulated and spontaneous emission 17
2.3 Typical spectra and energetic structure of a fluorescent dye 21

3.1 Discretization of reciprocal space for opal and Bragg stack 25
3.2 Results for the 1D, 2D, and 3D LDOS and DOS of the Bragg stack 30
3.3 Evaluation of FLDOS for angular resolved surface PL 33
3.4 Quasi-two-level rate-equation model for fluorescent emitters 36
3.5 Principles of the transfer and scattering matrix methods 45
3.6 Derivation of incoherent optical properties of “thick” layers 47
3.7 Ray tracing method to calculate angular resolved surface PL . . . 49
3.8 Angular pattern of light out-coupled at edge face 52

4.1 Fabrication approaches for dye-doped multilayer structures 54
4.2 Thickness and refractive index of spin coated PMMA layers 55
4.3 Dye concentration study to investigate self-quenching 57
4.4 Thickness and refractive index of spin coated titania layers 58
4.5 Defects in spin coated stacks with non-optimum process parameters 60
4.6 Position and height of reflectance peak of spin coated stacks 61
4.7 SEM and reflectance of optimized spin coated stacks 63
4.8 Refractive indices and reflectance of IBS filters 64
4.9 Evaluation of bonding techniques for filters 66
4.10 Self-assembly approaches for the fabrication of opals 67
4.11 Photographs and reflectances of different opal films 68

4.12 Optical micrograph and SEM graph of drying cracks in opals . . . 69
4.13 Configurations of the CARY5000 setup for optical characterization 72
4.14 Sketch of the automated angular photoluminescence setup 76
4.15 Configurations for angular resolved surface and edge PL 77
4.16 Measurement setups for the angular integrated PL 78

5.1 LDOS in Bragg stack and opal averaged over relevant dye positions 83
5.2 Spectral redistribution of emission in the Bragg stack and opal . . 84
5.3 Light guiding efficiency for emission in the Bragg stack and opal . 87
5.4 Illustration of the out-coupling of higher-band modes in opal . . . 88
5.5 Calculated angular resolved surface PL of multilayer structures . . 91
5.6 Structure of the three multilayer sample types: LSC, TSR, PLSC . 93
5.7 Angular resolved surface PL for spin coated multilayer samples . . 95
5.8 Angular surface PL of front and back side of Bragg stack PLSC . . 96
5.9 Angular resolved surface PL for bonded multilayer samples 99
5.10 Angular resolved edge PL for spin coated multilayer samples . . . 102
5.11 Angular resolved edge PL for bonded multilayer samples 104
5.12 Integrated surface PL for all multilayer samples 107
5.13 Integrated edge PL for all multilayer samples 109
5.14 Integrated center-mount PL for all multilayer samples 110

6.1 Comparison of calculated absorptance of LSC and Bragg stack PLSC113
6.2 Absorptance of PLSC for different numbers of dye-doped layers . . 114
6.3 Absorptance of Bragg stack PLSC at oblique incident angles . . . 116
6.4 Model for the overall concentrator performance of (P)LSCs 118
6.5 Spatial resolved absorption and emission changes 120
6.6 Modeled reabsorption for different effective concentrator sizes . . . 121
6.7 Collection probability in PLSC for optimum performance 122
6.8 Enhanced concentrator quantum yield of Bragg stack PLSC 123
6.9 Measured absorptance and CQY of spin coated multilayer structures125
6.10 Fluorescence micrograph of spin coated PLSC with cracks 126
6.11 Measured absorptance and CQY of bonded multilayer structures . 128
6.12 Measured absorptance and CQY of different opal samples 129

A.1 Comparison of the different definitions for the polarization of light 137
A.2 Comparison of the PL of samples with one and 10 dye-doped layers 142

List of Tables

3.1 Overview of (fractional) transition rates and spectral shape functions 43

4.1 Optimized spin coating parameters to deposit PMMA/titania stacks 62
4.2 Optimized process parameters for the fabrication of opals 70

5.1 Calculated changes in emission inside Bragg stack and opal 85

Acknowledgments

I would like to thank Prof. Dr. Hans Zappe for giving me the possibility of pursuing my PhD project under his supervision. I am thankful for his regular feedback and for regarding me – being an "external" PhD student – as part of the micro-optics group.

I am very thankful to PD Dr. Andreas Gombert for being the co-examiner and for sharing his expertise on photonics in several valuable discussions.

I want to thank Dr. Jan Christoph Goldschmidt for his guidance of my PhD project as my adviser at Fraunhofer ISE. I am thankful for the numerous discussions about physical and technical aspects as well as for giving me the opportunity to present my research at project meetings and at international conferences.

This work was supported by the Reiner Lemoine Stiftung through a doctoral scholarship, thank you very much for the generous support!

I am thankful to Dr. Stefan Glunz for the great opportunity to work in his division and his inspiration and motivation. Furthermore, I want to thank Dr. Martin Hermle for his support, and Dr. Benedikt Bläsi and Dr. Marius Peters for the many interesting discussions.

Janina Posdziech and Janina Löffler contributed significantly to the experimental part of this work through their master theses, thank you very much!

I want to thank my companion Stefan Fischer not only for his help in the PL lab: sharing the office for most of the time during my PhD, we had plenty of inspiring technical and non-technical discussions. For the many fruitful discussions and the outstanding work atmosphere I want to thank all other colleges in the team "Novel solar cell concepts" at Fraunhofer ISE, especially Johannes Eisenlohr, Benjamin Frölich, Barbara Herter, Dominik Pelzer, Tim Rist, Linda Schmidt, Heiko Steinkemper, and Sebastian Wolf. I further want to thank all "Hiwis" for their support in the lab; special thanks goes to Bissera Dimitrova, who spent numerous hours at the spin coater and at the CARY setup.

For the excellent administrative support I want to thank Birgit Stadel (ISE) and Nadja Katthagen (IMTEK).

Last but not least I want to thank my parents Judith and Roland, and my wife Theresa for the continuous support and encouragement in the past years.

Curriculum vitae

Johannes Gutmann

Born April 4, 1985 in Freiburg

Education

02/2010 - 10/2014	PhD (Dr. rer. nat.) at the Gisela and Erwin Sick Chair of Micro-optics (Prof. Dr. Hans Zappe), Dept. of Microsystems Engineering (IMTEK), University of Freiburg, in cooperation with the Fraunhofer Institute for Solar Energy Systems (ISE), Freiburg
10/2004 - 12/2009	"Diplom" (equivalent to MSc) in Microsystems Engineering at Dept. of Microsystems Engineering (IMTEK), University of Freiburg
02/2007 - 08/2008	"Vordiplom" (intermediate exam) in Economics at University of Freiburg
1995 - 2004	"Abitur" at Faust-Gymnasium, Staufen (high school)

Professional experience

since 01/2014	R&D-Engineer at Micronas, Freiburg
02/2010 - 12/2013	Researcher at Fraunhofer Institute for Solar Energy Systems ISE, Freiburg
11/2008 - 03/2009	Intern at Robert Bosch LLC, Research and Technology Center, Palo Alto, CA, USA
08/2007	Student trainee at Bosch Sensortec GmbH, Reutlingen

Awards & Scholarships

01/2011 - 12/2013	Doctoral scholarship from the Reiner Lemoine Stiftung
03/2007 - 12/2009	Scholarship from the Robert Bosch GmbH
08/2007	First prize in the business game "NewBizCup 2008"
07/2006	International Students' Invention Exhibition Award (ISIE 2006), Seoul, Korea
07/2005	Lucent Global Science Scholar Award 2005, Murray Hill, NJ, USA
2004, 2005	"Jugend forscht" (German contest for young scientists): first prize in the Baden-Württemberg state competition in 2004, "Preis des Gastgebers" (special prize) at the nationwide competition in 2005
2002, 2003, 2004	Winner of the "VDE invent a chip" contests in 2002, 2003, and 2004

Publications of the author

List of publication in reverse chronological order, with peer-reviewed journals emphasized in boldface:

- J. C. Goldschmidt, L. Prönneke, A. Büchtemann, J. Gutmann, L. Steidl, M. Dyrba, M.-C. Wiegand, B. Ahrens, A. Wedel, S. Schweizer, B. Bläsi, R. Zentel, and U. Rau, "Fluorescent concentrators for photovoltaic applications," in R. Wehrspohn, U. Rau, and A. Gombert (eds.), *Photonmanagement in Solar Cells*, Weinheim: Wiley-VCH, in print.

- A. L. Martínez Díez, J. Gutmann, J. Posdziech, T. Rist, D. Gómez Plaza, and J. C. Goldschmidt, "Optimized scalable stack of fluorescent solar concentrator systems with bifacial silicon solar cells," ***Journal of Applied Physics***, vol. 116, p. 154507, 2014.

- C. Hofmann, B. Herter, J. Gutmann, J. Löffler, S. Fischer, S. Wolf, R. Piper, N. Ekins-Daukes, N. Treat, and J. C. Goldschmidt, "Organic upconverters embedded in a Bragg structure," in *Proc. SPIE 9140, Photonics for Solar Energy Systems V*, p. 91400H, 2014.

- J. C. Goldschmidt, S. Fischer, B. Fröhlich, J. Gutmann, B. Herter, C. Hofmann, J. Löffler, F. C. J. M. van Veggel, and S. Wolf, "Photon management with luminescent materials and photonic structures," in *Proc. SPIE 9140, Photonics for Solar Energy Systems V*, p. 91400G, 2014.

- J. Gutmann, H. Zappe, and J. C. Goldschmidt, "Quantitative modeling of fluorescent emission in photonic crystals," ***Physical Review B***, vol. 88, p. 205118, 2013.

- B. Herter, S. Wolf, S. Fischer, J. Gutmann, B. Bläsi, and J. C. Goldschmidt, "Photonic structures for enhanced upconversion," in *Proc. SPIE 8824, Next Generation (Nano) Photonic and Cell Technologies for Solar Energy Conversion IV*, p. 88240A , 2013.

- B. Herter, S. Wolf, S. Fischer, J. Gutmann, B. Bläsi, and J. C. Goldschmidt, "Increased upconversion quantum yield in photonic structures due to local field enhancement and modification of the local density of states – a simulation-based analysis," ***Optics Express***, vol. 21, no. S5, pp. A883–A900, 2013.

- J. Gutmann, H. Zappe, and J. Goldschmidt, "Predicting the performance of photonic luminescent solar concentrators," in *Proceedings of the 39th IEEE Photovoltaic Specialists Conference*, pp. 1864–1868, 2013.

- J. Gutmann, H. Zappe, and J. C. Goldschmidt, "Using Photonic Crystals to Modify the Emission in Luminescent Solar Concentrators," in *Proceeding of the OSA Congress Renewable Energy and the Environment Optics and Photonics, Optics for Solar Energy*, p. ST2A.4, 2012.

- J. Löffler, J. Gutmann, and J. C. Goldschmidt, "Fabrication of One-Dimensional Photonic Crystals for Luminescent Solar Concentrators," in *Proceeding of the OSA Congress Renewable Energy and the Environment Optics and Photonics, Optics for Solar Energy*, p. ST2A.5, 2012.

- J. Gutmann, J. Posdziech, M. Peters, L. Steidl, R. Zentel, H. Zappe, and J. C. Goldschmidt, "Emission of Rhodamine B in PMMA opals for luminescent solar concentrators," in *Proc. SPIE 8438, Photonics for Solar Energy Systems IV*, p. 84381O, 2012.

- J. Gutmann, M. Peters, B. Bläsi, M. Hermle, A. Gombert, H. Zappe, and J. C. Goldschmidt, "Electromagnetic simulations of a photonic luminescent solar concentrator," ***Optics Express***, vol. 20, no. S2, pp. A157–A167, 2012.

- J. Gutmann, M. Peters, B. Bläsi, M. Hermle, H. Zappe, and J. C. Goldschmidt, "Towards photonic luminescent solar concentrators," in *Proc. SPIE 8111, Next Generation (Nano) Photonic and Cell Technologies for Solar Energy Conversion II*, p. 81110K, 2011.

- J. Gaspar, J. Gutmann, B. Lemke, and O. Paul, "Nonlinear piezoresistance of silicon at large stresses," in *Proceeding of the 24th IEEE International Conference on Micro Electro Mechanical Systems (MEMS)*, pp. 469–472, 2011.

- J. C. Goldschmidt, M. Peters, J. Gutmann, L. Steidl, R. Zentel, B. Bläsi, and M. Hermle, "Increasing fluorescent concentrator light collection efficiency by restricting the angular emission characteristics of the incorporated luminescent material - the 'nano-fluko' concept," in *Proc. SPIE 7725, Photonics for Solar Energy Systems III*, p. 77250S, 2010.

- B. Lemke, M. E. Schmidt, J. Gutmann, P. Gieschke, P. Alpuim, J. Gaspar, and O. Paul, "Nonlinear piezoresistance of silicon," in *Proceeding of the 2010 IEEE Sensors Conference*, pp. 1950–1953, 2010.

- G. Lammel, J. Gutmann, L. Marti, and M. Dobler, "Indoor Navigation with MEMS sensors," ***Procedia Chemistry***, vol. 1, no. 1, pp. 532–535, 2009.

- J. Gutmann, L. Marti, and G. Lammel, "Multipath Detection and Mitigation by Means of a MEMS Based Pressure Sensor for Low-Cost Systems," in *Proceedings of the 22nd International Technical Meeting of The Satellite Division of the Institute of Navigation*, pp. 2077–2087, 2009.

Luminescent solar concentrators are semi-transparent plates that are able to concentrate incident sunlight on its edge faces, where solar cells are attached. This work studies how the dominant loss mechanisms of conventional devices can be mitigated by embedding the luminescent material in a photonic crystal to tailor its emission characteristics. In such a photonic luminescent solar concentrator emission is redistributed spectrally and directionally, which can strongly improve the guiding of light to the edge faces and thus increase the concentrator's efficiency.

To quantitatively describe the effects of a photonic crystal on luminescent emission, new theoretical models are proposed in this work. This theoretical treatment provides significant physical understanding and insight in the interaction of light and matter, and is of large interest also for other applications that deal with the emission of light (e.g. LEDs, lasers). Furthermore, novel fabrication methods were developed to realize photonic crystals in form of Bragg stacks and opals with embedded organic dye molecules. Using dedicated photoluminescence measurements with angular resolution, an excellent agreement of calculations and experiments was found, which confirms the theoretical models presented in this work.

UNI FREIBURG

ISBN 978-3-8396-0833-3